UiT The Arctic University of Norway

Faculty of Science and Technology

Department of Chemistry

Expanding the toolbox for the study of antimicrobial peptides

Developing and adapting *in vitro* methods WIND-PVPA and MST to characterise the mode of action of membrane active antibacterial agents and their properties

Philip Ben Rainsford

A dissertation for the degree of Philosophiae Doctor

April 2022

All figures and illustrations throughout the thesis were created using BioRender.com by Philip Rainsford

Sometimes science is more art than science…a lotta people don't get that

Acknowledgements

Me. I thank me.

I jest of course.

Where to begin?

The road to this point has been long and winding, seldom smooth, and frequently bumpy, but I made it here. This is in no short part down to many of you who are currently reading this, and many who won't.

I'm currently writing this train of thought on a late Friday evening while I distract myself from the final tweaks of what you're about to read - so I guess I'm not quite 'here' just yet, but this feels like as good a time as any to reflect on everything that has come before this point.

Firstly, my supervisor Johan deserves a great deal of thanks, not just for hiring me, but for putting together an exciting and fulfilling project, for fruitful side-projects along the way, for the freedom granted to explore my own ideas, and for the vital guidance and input to help form those ideas into the work that you will soon read.

Martin, thank you for reading this 'thing' more than anybody else. I feel that without your input this would have been much longer, and much messier than it otherwise is. More importantly, you provided motivation at a time when it was sorely lacking.

A special thanks to John-Sigurd for being foolish enough to fund me and enable me to finish off this work without having to resort to living under a bridge.

To friends made along the way, Fredrik and Eric, Eskil, and Marte, to old friends from 'before', Tone and Marc, and others great and small not mentioned (there are a quite a few of you after all). Thank you for the good times we had over the years and for those that are hopefully still to come.

Mom, Dad and Nick, I'm sorry for not calling as much as I should, I've been a little bit busy, I guess. I promise I'll call more now that I'm done (hopefully).

To the 'boys' back home, I don't know if you'll ever actually read this, but thank you for making home feel like home on the all too rare occasions that I visit and making sure I don't forget that I don't have a real job.

Thank you to Rufus and Regulus for being the coolest cats.

And finally, to Andreea, and the one part that you won't have proof-read for me. I love you. I would never have made it to this point without you by my side. I owe more of this to you than any other one person.

Now, the final changes and finishing touches beckon. See you on the other side.

Abstract

There is an urgent lack of new antibiotics in the face of an ever-expanding antimicrobial resistance crisis. The fact that fewer new classes of antibiotics are being developed, and resistance soon follows newly available antibiotics, only serves to underline the urgency of the matter. There is a clear need of a paradigm shift with regards to antibiotics, and one such hope is antimicrobial peptides (AMPs). AMPs are an integral part of the innate immune systems of most organisms within the domains of life; since their discovery they have become of significant interest as a new type of antimicrobial agent, due in part to the low capacity of bacteria to develop resistance mechanisms towards them. Despite their potential, and lengthy study so far, establishing the specifics of the mechanism of action of many AMPs remains difficult– particularly of those that target the bacterial cell membrane. This lack of understanding limits the ability to rationally design new AMPs with a view to developing new antimicrobial agents.

The aim of this work was to help identify new potential hit compounds through NMR structure elucidation, and to develop new methods that would give greater insight into the activity of membrane active AMPs. This in turn could help enable the rational design of new AMPs.

WIND-PVPA, a method to quantify permeabilities of water and ions as a means to evaluate the disruptive capabilities of AMPs, was developed. This was demonstrated on a number of AMPs, and it was shown that WIND-PVPA can identify AMPs that have strong, selective, membrane disruptive activities such as the AMP WRWRWR, as well as more modestly disruptive AMPs such as KP-76. The WIND-PVPA was further used with a non-AMP membrane active natural product – lulworthinone – that was characterised over the course of the project. The findings of the study helped classify lulworthinone as a non-disruptive membrane active agent. In addition, microscale thermophoresis (MST) was shown to be a viable method by which the binding and partition coefficients of Trp-rich AMPs can be determined, and it was shown that the derived lipid-bindings of the AMPs correlates well with their bactericidal activity. Both WIND-PVPA and MST have expanded the toolbox available to the study of AMP-lipid interactions and can be used synergistically to give greater insight into the possible mechanism by which AMPs act, by helping to identify interesting cases, such as non-disruptive AMPs with potent activities.

In summary, the methods developed have great potential that can be further refined into robust methods that can greatly assist in the deconvolution of AMP activity and can open up possibilities of the rational design of membrane active AMPs as a new generation of antimicrobial agents.

Scientific Environment

All the work undertaken within this thesis was done at UiT the Arctic University of Norway Dept. Chemistry, at both Realfagsbygget, and Norstruct/Siva innovasjonssenter labs, with a brief stay at the Niels Bohr institute, Copenhagen University. As such a great deal of thanks needs to be given to the engineering staff at all locations, as well as administration and faculty members, without which the work could not have taken place.

The work conducted within this thesis was done as part of work package (WP) 4 of the DigiBiotics project (NFR-project: 269414). DigiBiotics is a cross-disciplinary project that is seeking to unite multiple disciplines and bring together synthetic and analytical chemists, molecular biologists, and computer scientists to develop a pipeline for the discovery, isolation, characterisation of structure and mode-of-action, and development of new marine-based antimicrobial agents. The focus of the DigiBiotics project is on AMPs, and their potential as a new generation of antimicrobial agents with a reduced capacity for resistance development. AMPs that are active on the bacterial membrane are of highest interest as there is a poor understanding of the specific mode by which AMPs disrupt the bacterial membrane.

The collaborators from the other WPs have been integral to the success of my work, with the natural products supplied through WP1, the synthetic AMPs supplied by WP 2, the calculations from WP 3 and 5, and the biological results of WP 6. The work herein would not have been possible without this collective input, as well as the insight and leadership of the respective PIs.

List of Publications

Paper I. WIND-PVPA: Water/Ion NMR Detected PVPA to assess lipid barrier integrity *in vitro* through quantification of passive water- and ion transport.
Biochimica et Biophysica Acta (BBA) – Biomembranes, **2022** doi**:** 10.1016/j.bbamem.2022.183911
Philip Rainsford, Ravdna Sarre, Margherita Falavigna, Bjørn Olav Brandsdal, Gøril Eide Flaten, Martin Jakubec and Johan Isaksson

Paper II. Novel application of label free MST: Measurement of AMP affinity (K_D) and partitioning (K_P) to lipid vesicles and SMA-lipid nanodiscs
(manuscript)
Philip Rainsford, Martin Jakubec, Mitchell Silk, Richard Engh, Johan Isaksson

Paper III. Lulworthinone, a New Dimeric Naphthopyrone From a Marine Fungus in the Family Lulworthiaceae With Antibacterial Activity Against Clinical Methicillin-Resistant Staphylococcus aureus Isolates.
Front. Microbiol., **2021** doi: 10.3389/fmicb.2021.730740
Marte Jenssen, **Philip Rainsford**, Eric Juskewitz, Jeanette H. Andersen, Espen H. Hansen, Johan Isaksson, Teppo Rämä and Kine Ø. Hansen

Paper IV. Lulworthinone: *In vitro* mode of action investigation of an antibacterial dimeric naphthopyrone isolated from a marine fungus.
MDPI (*submitted manuscript* **2022**)
Eric Juskewitz, Ekaterina Mishchenko, Vishesh K. Dubey, Marte Jenssen, Martin Jakubec, **Philip Rainsford**, Johan M. Isaksson, Jeanette H. Andersen and Johanna U. Ericson

Paper V. Isolation and characterization of St-CRPs: Cysteine-rich peptides from the Arctic marine ascidian Synoicum turgens.
(*manuscript*)
Ida K. Ø. Hansen, **Philip B. Rainsford**, Johan Isaksson, Kine Ø. Hansen, Klara Stensvåg, Anastasia Albert, Terje Vasskog and Tor Haug

Summary of papers and Author contributions

Paper I - WIND-PVPA: Water/Ion NMR Detected PVPA to assess lipid barrier integrity *in vitro* through quantification of passive water- and ion transport.

Biochimica et Biophysica Acta (BBA) – Biomembranes, **2022**

Philip Rainsford, Ravdna Sarre, Margherita Falavigna, Bjørn Olav Brandsdal, Gøril Eide Flaten, Martin Jakubec and Johan Isaksson

Paper I serves as an introduction to the WIND-PVPA method. WIND-PVPA allows for the monitoring of water, and Ca^{2+} and Mg^{2+} ions. The change in the permeability of the water and ions is used to determine the disruptive effects of AMPs. Two lipid compositions are used to show the selectivity of AMPs; in particular, WRWRWR was shown to exert a large disruptive effect on the anionic barrier, while having little effect on the zwitterionic barrier. The method is backed up in silico studies of two of the AMPs in the presence of zwitterionic and anionic bilayers.

Author Contributions

PR, MJ and JI designed and planned the project. PR and MJ established NMR procedures under the supervision of JI. MF prepared PVPA barriers under the supervision of GF. Modelling was done by RS under the supervision of JI and BOB. Figures were prepared by PR and RS. Original draft was written by PR, MJ, RS and JI. Funding for this project was acquired by JI. All authors interpreted data and commented on the final version of the manuscript.

Paper II - Novel application of label free MST: Measurement of AMP affinity (K_D) and partitioning (K_P) to lipid vesicles and SMA/lipid nanodiscs.

(Manuscript)

Philip Rainsford, Martin Jakubec, Mitchell Silk, Richard Engh, Johan Isaksson

Paper II describes the application microscale thermophoresis (MST) to evaluate the K_D and K_P of a set of five AMPs to different lipid model systems – vesicles and SMA-nanodiscs. The paper serves as a demonstration of how one can use MST to obtain such parameters to which surface plasmon resonance (SPR) serves as a more established technique to compare the findings. The findings show that MST is a viable method to these ends, along with facilitating a discussion on the relative suitability of both vesicles and SMA-nanodiscs to evaluate peptide-lipid interactions, and the influence the choice of model system can have. Furthermore, it was shown that both K_D and K_P correlate well with AMP activity.

Author Contributions

Conceptualisation: PR. Peptide synthesis and purification: MS. Nanodisc and vesicle preparation, and MST: PR. Vesicle preparation and SPR: MJ. Data analysis: PR and MJ. Original draft: PR. Visualisation: PR. Writing and editing: PR, MJ, MS, JI. Supervision: RE and JI. All authors reviewed and approved final version.

Paper III - Lulworthinone, a New Dimeric Naphthopyrone From a Marine Fungus in the Family Lulworthiaceae With Antibacterial Activity Against Clinical Methicillin-Resistant Staphylococcus aureus Isolates.

Front. Microbiol., **2021**

Marte Jenssen, **Philip Rainsford**, Eric Juskewitz, Jeanette H. Andersen, Espen H. Hansen, Johan Isaksson, Teppo Rämä and Kine Ø. Hansen

Paper III describes the isolation and elucidation of a new dinapthopyrone – Lulworthinone. Two separate isolations were performed, and the structures determined showed dissimilarities in behaviour. The first preparation was done in the presence of formic acid and produced readily interpretable data; however, the second preparation was done in the absence of any acid and resulted in spectra that showed signs of aggregation. The structures of the two forms of lulworthinone were elucidated, with the second form exhibiting good bactericidal activity.

Author Contributions

MJ was responsible for conducting experiments, data analysis, and writing and revising the draft manuscript. PR and JI were responsible for the NMR analysis of the compound and the writing related to this. EJ conducted the antibacterial testing against the clinical bacterial isolates, wrote this section in the "Materials and Methods," and contributed to the writing of the MIC results. KH assisted in writing and revision of the manuscript and contributed to the experiment design. TR did the initial isolation of the fungus and the phylogenetic analysis, contributed to the experiment design by selecting this fungus for the study, and revised the manuscript. JA and EH contributed to the conceptualization of the work, supervised the work, and revised the manuscript. All authors reviewed and approved the final manuscript.

Paper IV - Lulworthinone: *In vitro* mode of action investigation of an antibacterial dimeric naphthopyrone isolated from a marine fungus.

MDPI (*under revision* **2022**)

Eric Juskewitz, Ekaterina Mishchenko, Vishesh K. Dubey, Marte Jenssen, Martin Jakubec, **Philip Rainsford**, Johan M. Isaksson, Jeanette H. Andersen and Johanna U. Ericson

Paper IV recounts the efforts to determine the mode of action of lulworthinone. Having previously been identified as having antimicrobial activity, the aggregatory properties and mode of action of lulworthinone were explored. A number of assays were utilised, including WIND-PVPA, and it was shown that lulworthinone is active on the bacterial membrane without disrupting it, and that it ultimately prevents cell division. The activity of lulworthinone was shown to be reliant on its ability to aggregate.

Author Contributions

Conceptualization, EJ and JE; data curation, EJ; formal analysis, EJ, VK, MJA; investigation, EJ, EM, VD, MJA and PR, project administration, EJ; resources, MJE; software, EJ, VK, MJA; supervision, EM and JE; visualization, EJ; writing - original draft preparation, EJ; writing review and editing, EJ, EM, MJE, MJA, PR, JA, JI and JE. All authors have read and agreed to the published version of the manuscript

Paper V – Isolation and characterization of St-CRPs: Cysteine-rich peptides from the Arctic marine ascidian Synoicum turgens.

(*Manuscript*)

Ida K. Ø. Hansen, **Philip B. Rainsford**, Johan Isaksson, Kine Ø. Hansen, Klara Stensvåg, Anastasia Albert, Terje Vasskog and Tor Haug

Paper V describes the isolation and structure elucidation of a pair of cysteine rich AMPs st-CRP-1 and 2. The CRPs were 18 and 19 residues in length, with a 1/6-2/4-3/5 disulfide connectivity. There was only sufficient material of St-CRP-1 available to yield a full NMR derived structure. A 3D structure of st-CRP-1 was determined using experimentally constrained simulated annealing and it was shown to be moderately bactericidal.

Author Contributions

IK, TH, KS and TV were responsible for the concept and idea behind the study. IK, AA, TV and JI designed the study and the methods within. Data gathering and interpretation was completed by IK, PR, JI, KH, TV, and AA. The manuscript was worked on by IK, PR, JI, TV, and TH, with all authors and contributors giving final approval of the manuscript.

Table of Contents

Abbreviations

ADME	Absorption, Distribution, Metabolism and elimination properties
AMP	Antimicrobial Peptide
AMR	Antimicrobial Resistance
APD3	Antimicrobial Peptide Database 3
CAC	Critical Aggregation Concentration
CL	Cardiolipin
COSY	Correlated Spectroscopy
CSP	Chemical Shift Perturbation
DIBMA	Diisobutylene-maleic acid
DLS	Dynamic Light Scattering
DMSO	Dimethylsulfoxide
DOFI	Declaration of Invention
EDTA	Ethylenediamine tetra acetic acid
FITC	Fluorescein isothiocyanate
GFP	Green Fluorescent Protein
GL	Glycolipid
GUV	Giant Unilamellar Vesicle
HDP	Host Defence Peptide
HDX	Hydrogen Deuterium Exchange
HMBC	Heteronuclear Multiple Bond Correlation
HPLC	High-Performance Liquid Chromatography
HSQC	Heteronuclear Single Quantum Coherence
ITC	Isothermal Calorimetry
LPS	Lipopolysaccharide
LTA	Lipoteichoic acid
LUV	Large Unilamellar Vesicle
MIC	Minimum Inhibitory Concentration
MLV	Multilamellar Vesicle
MOA	Mode of Action
MSP	Membrane Scaffold Protein
MST	Microscale Thermophoresis
NMR	Nuclear Magnetic Resonance
NOE	Nuclear Overhausen Effect
NOESY	Nuclear Overhauser Effect Spectroscopy
OM	Outer Membrane
Omp	Outer Membrane Protein
P:L	Peptide:Lipid ratio
PAMPA	Parallel Artificial Membrane Permeation Assay
PC	Phosphatidylcholine
PDB	Protein Database
PE	Phosphatidylethanolamine
PG	Phosphatidylglycerol
PI	Phosphatidylinositol

PS	Phosphatidylserine
PVPA	Phospholipid Vesicle-based Permeation Assay
SA	Simulated Annealing
SM	Sphingomyelin
SMA	Styrene-maleic acid
SPE	Solid Phase Extraction
SPR	Surface Plasmon Resonance
STD	Saturation Transfer Difference
SUV	Small Unilamellar Vesicles
TFA	Trifluoroacetic acid
TOCSY	Total Correlation Spectroscopy
TRIC	Temperature Related Intensity Change
TRIS	Tris(hydroxymethyl)aminomethane
WIND-PVPA	Water/Ion NMR Detected-Phospholipid Vesicle-based Permeation Assay

1 Introduction

1.1 Antimicrobial Resistance

> *"Mr. X. has a sore throat. He buys some penicillin and gives himself, not enough to kill the streptococci but enough to educate them to resist penicillin. He then infects his wife. Mrs. X gets pneumonia and is treated with penicillin. As the streptococci are now resistant to penicillin the treatment fails. Mrs. X dies."*
>
> *Sir Alexander Flemming, 1945*

In his 1945 Nobel lecture, Alexander Flemming outlined this hypothetical scenario[1]. He had, in his initial work with lysozyme and penicillin, observed that when bacteria were subjected to sub-lethal doses, they would eventually develop a resistance to an antibacterial agent. In the years following his Nobel lecture, cases of penicillin-resistant infections continued to rise and started to become common place[2].

The following decades became known as the 'golden age of antibiotics', with new classes being identified, and the rate of discovery remained able to outpace resistance development[3]. This golden age eventually drew to a close, and the discovery of new antibiotics and novel classes waned, with increasing costs of development and low profitability of new antimicrobial agents cited as common reasons[4]. This, alongside the widespread use of antibiotics in agriculture[5, 6], and antibiotic misuse and poorly fulfilled prescriptions[7], has clarified a very real antimicrobial resistance (AMR) crisis[8]. The O'Neill and WHO reports of 2011 outlined the headline figures of both the human and financial costs that have defined AMR discourse, with a forecast of AMR being the leading cause of death by 2050, overtaking cancer[9].

Since this initial report, WHO have released multiple updates outlining the efforts so far to curb and combat AMR, describing it as one of the top ten global public health threats in 2021[10]. The Global Antimicrobial Resistance and Use Surveillance System (GLASS) was established in

2015 by WHO to monitor the use of antibiotics and AMR around the world, as well as assist in data gathering in areas where there was previously a deficit[11].

Enterococcus faecium, Staphylococcus aureus, Klebsiella pneumonia, Acinetobacter baumannii, Pseudomonas aeruginosa, and *Enterobacter* species make up the ESKAPE pathogens. These pathogens are multi-drug resistant bacteria that are designated by the WHO as being of particular concern for healthcare and should have a high priority when it comes to concerning the development of new antimicrobials[12].

To truly tackle antimicrobial resistant bacteria, it is first important to address the bacteria themselves. Bacteria are single-celled prokaryotic organisms that are differentiated from eukaryotic organisms by the absence of a membrane bound nucleus. Bacteria are classified into two groups: gram-negative and gram-positive. At a surface level, gram-positive and negative bacteria are differentiated by their response to the Gram stain: gram-positive retain the stain, while gram-negative do not. This difference in response to the Gram stain is a result of difference in structure of the cell walls of gram-negative and gram-positive bacteria, whereby gram-negative bacteria possess an additional outer membrane that is rich in lipopolysaccharide (LPS) and which sits above a thinner peptidoglycan layer (Figure 1)[13,14].

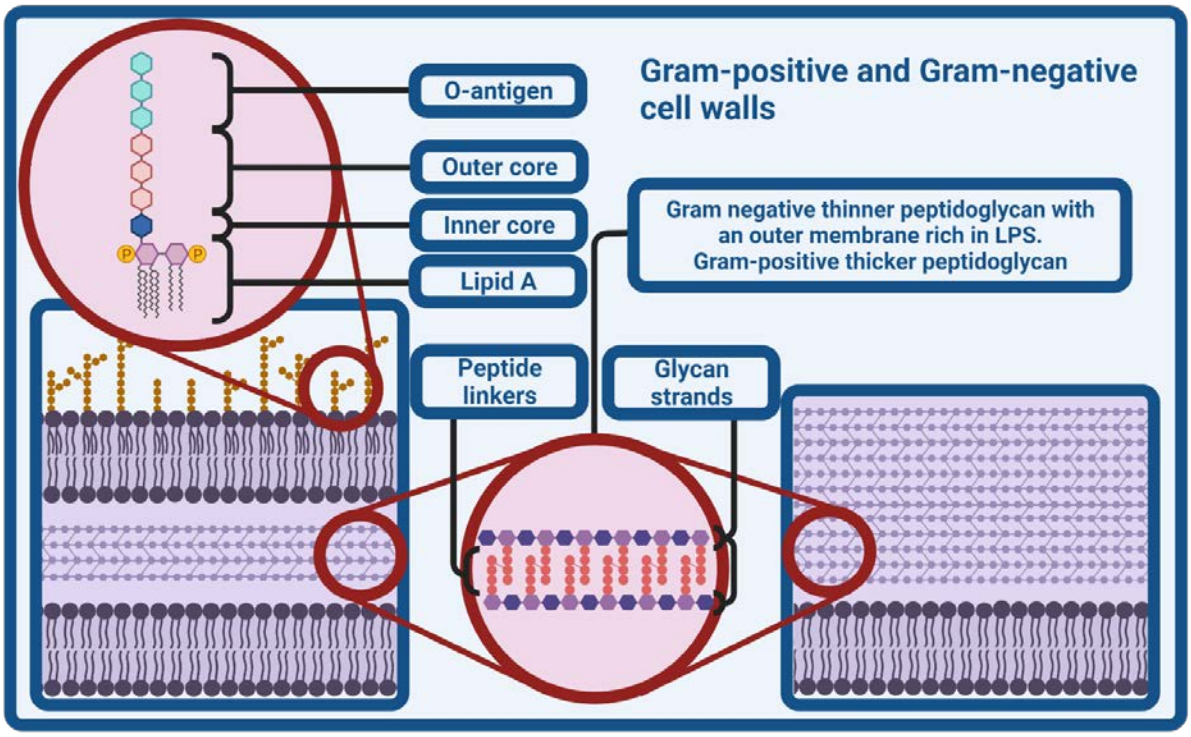

Figure 1: The simplified cell wall structures of gram-negative (left) and gram-positive (right) bacteria. Highlighted is the structure of LPS (only present in gram-negative) and the difference in the thickness of the peptidoglycan layer.

The extra barrier to entry that gram-negative bacteria possess is crucial to its resistance to many antibiotics[15]. Of the six ESKAPE pathogens, four are gram-negative bacteria[12]. Furthermore, on the 2017 WHO priority list of resistant bacteria, nine of twelve are gram-negative strains, of which three are of critical priority, and four are of high priority (there are no critical priority and two high priority gram-positive strains)[16].

There is therefore a pressing need for new antimicrobial agents, specifically those that are active against gram-negative bacteria, and pipelines to increase the efficiency on the development of such agents. Crucially, emphasis should be placed on strategies addressing resistance development.

1.2 Antimicrobial Peptides

AMPs encompass a broad church of peptides that possess antimicrobial activity. AMPs are found in nature as host-defence peptides (HDPs), where they are classified by their role in host immune response but possess no activity towards the host organism's cells. In the form of HDPs, AMPs form the backbone of innate immune systems of organisms across the domains of life, from micro-organisms such as viruses[17] and bacteria themselves[18], through to larger organisms including humans[19], other mammals[20], and reptiles[21]. AMPs are produced in nature by several mechanisms, including the cleavage of the active sequence from larger proteins, ribosomally by mRNA, and non-ribosomally[22, 23].

One of the key reasons for AMPs becoming of great interest as antimicrobial agents is due to a low expectation of resistance development. As noted previously AMPs as HDPs are a key part of the immune defences of a vast number of organisms and have been for millennia. During this time bacteria have found no adequate defence, in contrast to many other agents where resistance development is swift. Several reasons are proposed for this reduced capacity for resistance including the general pharmokinetic properties of AMPs whereby they demonstrate a quick onset of activity in a small dose-response range with fast killing, leaving limited concentration ranges within which resistance can develop. There is a high fitness cost of adapting the bacterial membrane (a common AMP target), and the broad range of additional targets that AMPs are active against depresses resistance development[24].

Peptides are characterised by the peptide bond - the amide linkage between the carboxylic acid and amide groups of two amino acids (Figure 2). The peptide bond is a strong linkage and derives its strength from the delocalised pi-system across the carbonyl and amine groups. This delocalised character gives the bond a fixed angle of 180º. The primary structure of a peptide is described by the number and sequence of amino acid residues that make up a given peptide, with the number of residues typically below 50-60 but able to be considered up to 100 residues; larger sequences would typically be classed as proteins. Peptides with sufficient length and correct sequence can form specific secondary structural elements, such as alpha-helix or beta-sheet. Secondary structure of peptides is imparted through the phi and psi angles around the alpha position of the backbone.

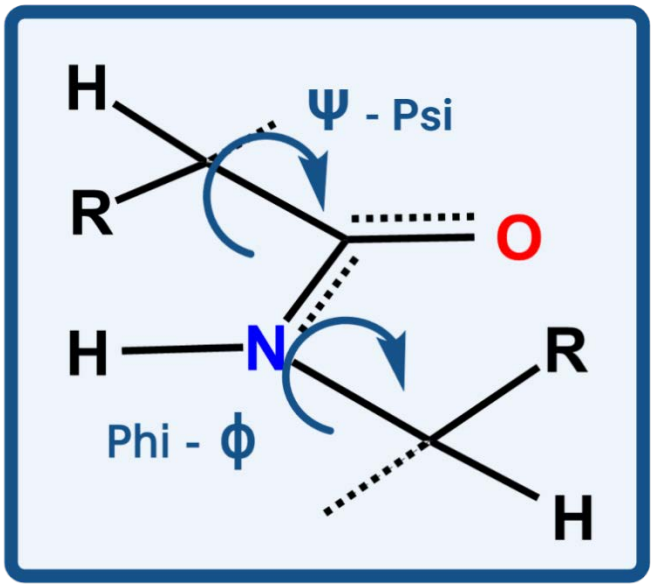

Figure 2: The peptide bond. The strength of the peptide bond is imparted by the delocalised NHCO pi-system. While the phi and psi angles describe the shape of the backbone and the secondary structure of the linked amino acid residues.

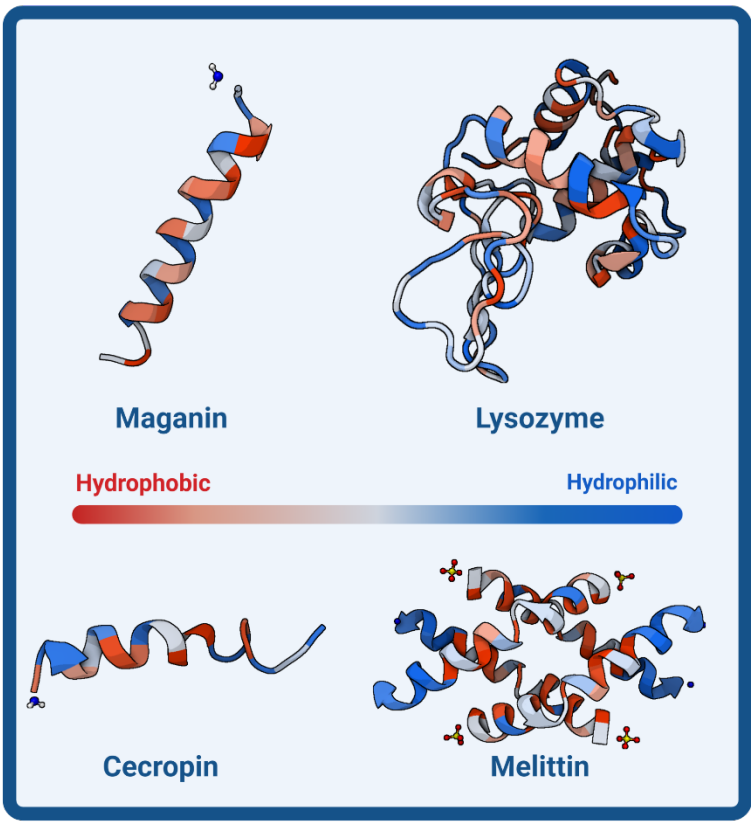

Figure 3: The 3D structures of early and important AMPs. The amphipathic nature of the structures is highlighted by the colour coding of the residues (red-blue - hydrophobic-hydrophilic) whereby the hydrophobic residues group together in space.

One of the early instances of the identification of AMPs was in 1981 by Hans Boman and colleagues, working out of Stockholm and Uppsala[25]. From the pupae of the silk moth H*yalophora cecropia*, the group identified two structurally similar 37 and 35 residue peptides, that they named cecropin A and B, respectively. Comparisons were made with other proteins and peptides with bactericidal properties, including melittin, a peptidic toxin from bee venom[26], and lysozyme[27]. Although both the cecropins and melittin are structurally similar, containing large hydrophobic and hydrophilic regions, they showed significant deviations in activity. While bactericidal activity against *E. coli* was observed for the cecropins and melittin, melittin also showed lytic properties towards human liver cells – something that was absent in the cecropins, and it was therefore noted that there must be some degree of recognition by the cecropins to prevent the lysis of the insects' own cells[28].

Later in 1986, Michael Zasloff isolated a pair of closely related peptides from the skin of the African claw frog, *Xenopus laevis*[29]. Zasloff found that they exhibited a broad range of anti-microbial activity against gram-positive and gram-negative bacteria and had little impact on mammalian cells. It was later identified that the magainins also killed bacterial cells through the lysis and permeabilisation of the cell membrane[29, 30].

Advancements in the tools available to researchers at the time, both analytical and computational, allowed for greater progress to be made in the identification and classification of HDPs, and as a result in the decades that followed a series of cysteine rich HDPs were identified in rabbits[31], sheep[32] , and monkeys[33]. These discoveries helped to shape the α-,β-, and θ-defensins – mammalian cysteine rich HDPs that are differentiated from one another by their disulfide bridge connectivities[34]. The additional discoveries of the plant-defensins[35], and insect-defensins[36] further solidified the importance of the role AMPs as HDPs have in the immune response of organisms across numerous kingdoms.

The broad variety in sequence length and composition, as well as diverse source, means there is no universally agreed upon method of classification of AMPs; rather, there exist a number of ad-hoc classifications, the use of which typically depends upon the context in which AMPs are being discussed. Common modes split AMPs based upon derived organism (insect, bacterial, mammalian), activity (anti-microbial, anti-fungal), the amino-acid composition (Trp-, Pro-, Arg-rich peptides) or by mode-of-action/target.

1.3 AMP Targets

1.3.1 The bacterial membrane

A common observation for many of the early AMPs such as the cecropins, the magainins, and toxins such as alamethicin and melittin, was that they were membrane lytic – they destroyed the cell membrane. Many other peptides, with large differences in size and sequence have also been shown to have strong membrane targeting activities.

Both gram-positive and –negative bacteria possess a negatively charged, phospholipid membrane. This lipid bilayer is constructed by amphipathic phospholipids, where the hydrophobic lipid tails interact with one another to form the core of the bilayer.

The exact phospholipid composition of the membrane varies between gram-positive and –negative bacteria, as well as bacterial species, however, some common lipid species are present in many bacteria. These include the zwitterionic phosphatidylethanolamine (PE) and more rarely phosphatidylcholine (PC) species, of which PE is generally the most richly abundant, and makes up the bulk, typically between 75-95% of the bacterial phospholipid membrane of *E. coli* [37, 38]. Anionic phospholipids such as phosphatidylglycerol (PG) and cardiolipin (CL) provide the negative charge of the membrane and usually account for at least 15% of the lipids in the membrane[14].

The presence of a negative charge on the outer leaflet of bacterial membranes is a significant differentiator between bacterial cells and mammalian cells (Figure 4). While anionic phospholipids are similarly present in mammalian cells (17%), the species are different, typically phosphatidylserine (PS) and phosphatidylinositol (PI)[39], and there is significant asymmetry in the mammalian bilayer[40]; the anionic PS and PI reside on the inner leaflet of the membrane, with the outer leaflet mostly comprised of zwitterionic PC, glycolipids (GL), and sphingomyelin (SM), and remaining neutral[39].

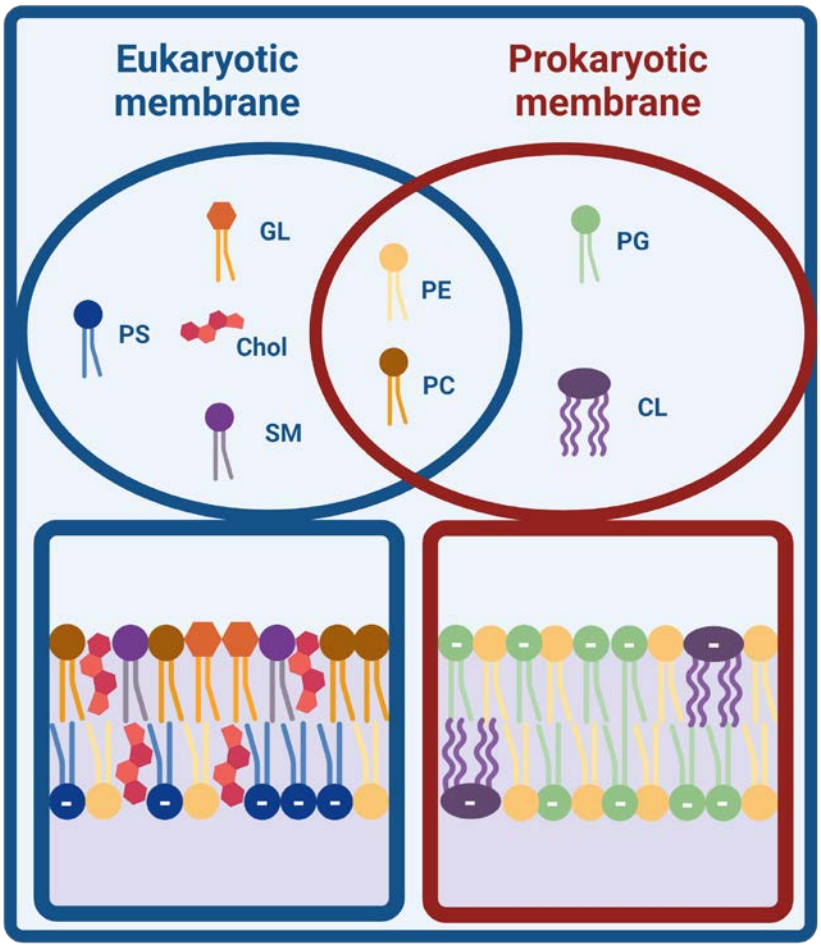

Figure 4: Common components of the lipid membranes of eurkaryotic and prokaryotic organisms.

As described previously, while some AMPs showed a general membrane lytic behaviour, such as melittin, some AMPs demonstrated little-to-no lytic behaviour towards host cells, while retaining significant bacteriolytic activity. It was therefore put forward that AMPs, and specifically HDPs, must have a method of differentiating between host cells and invading bacterial cells[28].

The presence of anionic lipids has been demonstrated to have a positive impact on the interactions between AMPs and lipid models[41, 42]. However, it is not just the anionic lipids that are a point of differentiation: PE and CL, are both common lipids in bacterial membranes, that are not as prevalent in mammalian membranes. It has been demonstrated that due to their cone-like structure, the bacterial membrane has a higher propensity towards saddle-like curvatures (so-called 'saddle-splay') that can manifest in a number of ways, either as pores, or protrusions known as blebs[43]. These saddle-splay curvatures are points of weakness in the membranes due to the curvature stress[44].

A further difference between mammalian and bacterial cells is the presence of cholesterol in the leaflet of mammalian cells (Figure 4). Cholesterol has been demonstrated to have a negative impact on the binding of AMPs to lipid models, due to changes in membrane packing. Cholesterol is one of the reasons why the mammalian membrane is more rigid and inaccessible, when compared to the more fluid environment of bacteria[45]. The targeting of bacteria by AMPs, and the differentiation from host cells is therefore not solely charge based, but due to a combination of several factors.

There are two main effects of membrane targeting AMPs: membrane disruption, and membrane lysis. Membrane disruption can be categorised as the reduction in stability and integrity of the lipid membrane, that eventually leads to membrane lysis. Membrane lysis is a far more catastrophic effect and represents a total loss of membrane integrity.

One of the early effects of AMPs binding to the membrane is a thinning of the membrane, as the membrane expands laterally[46]. This results in the formation of previously mentioned saddle-splay curvatures[43]. Such effects can further be encouraged by the formation of lipid rafts[47]; lipid rafts are clusters of structurally similar lipids such as charged lipids, or lipids with a similar phase[48]. As lipid rafts begin to form and there is a reduction in membrane fluidity, membrane protein activity can be lost[49]. Highly asymmetric membranes can be produced by the formation of anionic lipid rafts, that are promoted by an increase in lipid flip-flop, bringing more anionic lipids from the inner leaflet to the outer leaflet[46]. AMPs such as magainin and melittin are known to increase lipid flip-flop and increase asymmetry[50, 51].

When membrane lysis takes place, the membrane is dissolved as lipids are removed. The result is a significant increase in the permeability of the membrane, and the loss of cell contents and metabolites[52]. Several models have been proposed for this process and will be discussed in more detail in a chapter 1.4.

1.3.2 Membrane-bound Targets

While the MOA of membrane targeting AMPs is generally considered to be centred on the disruption of the lipid bilayer, there are specific targets, such as membrane bound proteins, that are present on the lipid bilayer. For instance, defensins from a number of sources have been demonstrated to inhibit potassium ion channels by binding to different regions of potassium channels[53]. The lipid A component of LPS has also been shown to be the target of AMPs and stronger binding to Lipid A has been shown to have a correlation with AMP activity[54].

Thanatin, a 21-residue AMP isolated from the spined soldier bug (*Podisus maculiventris)*[55], binds to LPS and the LPS transporter proteins LptA and LptD, preventing the uptake of LPS

into the OM, and destabilising it[56]. As a result of the absence of LPS on the outer membrane of gram-positive bacteria, thanatin possess no activity against gram-positive bacteria.

1.3.3 Intracellular targets

Many AMPs have been demonstrated to have intracellular targets. Buforin II, an amphibian derived AMP, does not lyse cells but rather accumulates intracellularly by strongly binding to DNA (Figure 5B)[57]. Indolicidin was also shown to inhibit the biosynthesis of DNA, and to a lesser extent RNA synthesis resulting in the filamentation of the *E. coli* and interrupting the cell division process (Figure 5A) [58].

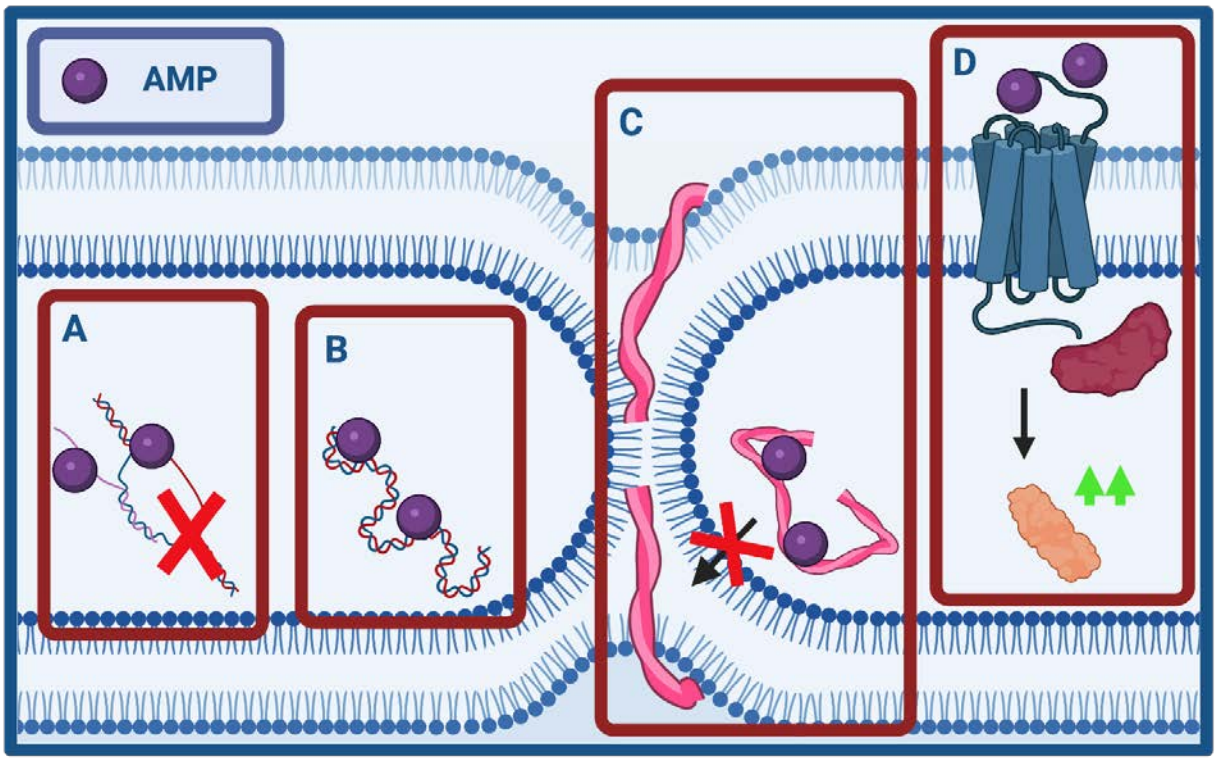

Figure 5: Intracellular AMP targets that prevent cell division. A: DNA and RNA synthesis. B: binding of DNA. C: Z-ring disruption by FtsZ binding. D: PhoQ/PhoP regulatory system upregulation of QueE.

Cell division is also interrupted by the AMPs through the disruption of multiple areas in the divisome complex – an organisation of over 20 proteins that is responsible for cell division in bacterial cells[59]. In *E. coli* the divisome two-component regulatory system PhoQ/PhoP is

sensitive to the presence of cationic AMPs, and upon detection of AMPs, upregulates QueE, preventing cell division (Figure 5D)[60]. Temporin L, another frog derived AMP (*Rana temporaria*), binds with the enzyme FtsZ, forming a ring-like structure (the z-ring) which is integral to the early steps of cell division in both gram-positive and gram-negative bacteria(Figure 5C)[59, 61].

Other AMPs can disrupt protein biosynthetic pathways. Fragments of the bovine AMP Bac5 are able to exert this effect without lysing the bacterial membrane. Bac5 is able to enter *E. Coli* using the membrane transporter protein SmbA, as demonstrated by a strain lacking SmbA to which activity was greatly reduced, and no inhibition of protein synthesis was observed[62]. Fragments of another bovine AMP, Bac7, demonstrate similar activity to that of Bac5[63] (Figure 6A).

An interesting example is attacin, an insect derived AMP, which inhibits the synthesis of numerous specific outer membrane proteins (Omps). This is achieved by preventing the incorporation of the Omps into the outer membrane and is induced without entering the cell. Rather, it is suggested that Omp synthesis is inhibited as a result of signalling events that arise due to the build-up of Omps in the periplasm[64] (Figure 6B).

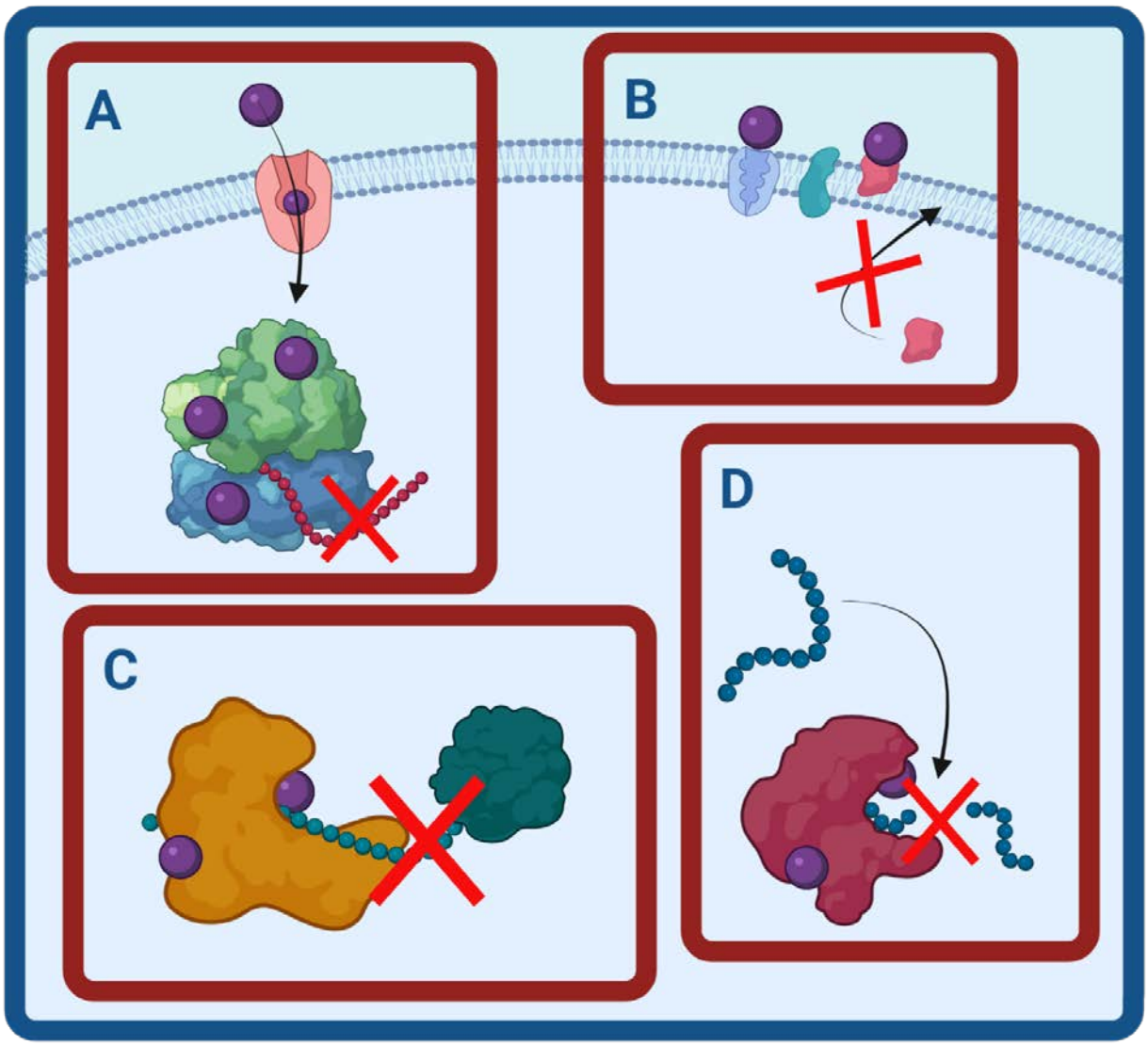

Figure 6: AMP protein based targets. A: SmbA transport and biosynthesis inhibition. B: accumulation of Omps in the periplasm. C: Chaperone inhibition. D: Protease inhibition.

Abaecin, apidaecin, drosocin, oncocin, and pyrrhocoricin [65-69] are AMPs that have been demonstrated to interrupt the activity of DnaK, which is a key component of the chaperone network of *E. coli*[70]. Without a chaperone to assist in their proper folding, proteins can improperly aggregate with potentially fatal consequences for the cell[71] (Figure 6C).

Proteases are enzymes that catalyse the degradation of proteins and peptides, by hydrolysing the peptide bond[72]. Histatin 5, a human AMP, has been shown to inhibit different proteases,

both host-based and bacterial[73, 74]. An equine AMP, eNAP-2, however, can selectively inhibit bacterial serine proteases, with no inhibitory effect on mammalian serine proteases[75] (Figure 6D).

1.3.4 Non-antimicrobial activities

The activity of some AMPs is not solely limited to bacteria, with some AMPs showing a diverse array of complimentary properties such as anti-fungal activities[76] (Figure 7). Many of the previously discussed AMPs have documented antifungal activities; the magainins[29], human defensins[77], the cecropins[78, 79], and thanatin[55] have been shown to have fungicidal properties, some of which lyse the fungal cells, as in the case of the magainins and cecropins[76]. APD3, a database of antimicrobial peptides, has 1220 peptides displaying antifungal properties[80].

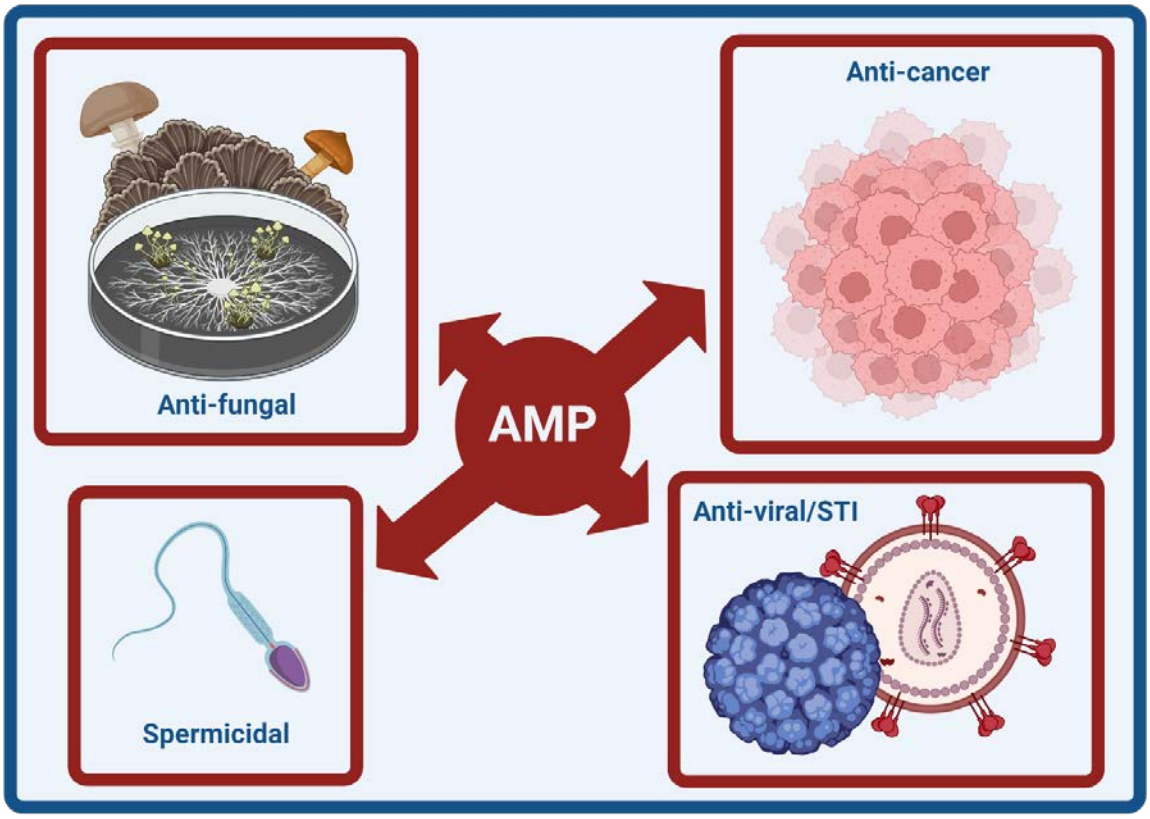

Figure 7: The additional activities of AMPs.

Similarly, a number of AMPs are also antiviral, with APD3 listing 193 and 109 antiviral and anti-HIV AMPs, respectively (December 2021)[80]. AMPs have become of interest due to anti-

STI activities[81], including the anti-HIV activities of human defensins[82], cecropins, and mellitin[82], though these activities do not rely on the lytic properties of the AMPs, and are able to inhibit viral transcription.

Previously noted was the importance of the anionic lipids to the specificity of AMPs activity, and that this is afforded by the asymmetry of the lipid membrane in mammalian cells. However, in certain cancers for instance, this asymmetry is lost alongside an overexpression of some anionic glycoproteins[40,83]. As a result, the previously zwitterionic mammalian outer leaflet becomes negatively charged, making cancer cells a viable target for AMPs. Due to their selectivity, rate of action, and low-side effects, AMPs with anti-cancer properties have become of interest as a new type of cancer therapy[84].

In addition, AMPs have further attracted attention as potential contraceptives due to the spermicidal properties of some peptides[81, 85]. In particular cathelicidin/LL-37, a human AMP with noted anticancer properties[86], has been studied as a possible contraceptive[87].

1.3.5 Important structural properties

In the study of the effect of the cecropins, Boman noted the structural similarities between cecropin A and B, and the bee venom toxin melittin; both the cecropins and melittin possessed distinct regions of hydrophobicity, and basicity/hydrophilicity, i.e. they were amphipathic[28].

These domains of hydrophobicity and hydrophilicity have been observed for a large majority of AMPs, regardless of their organism of origin[88]. The specific amino acid sequence does not need to be amphipathic; rather, the peptide needs to have the ability to adopt a conformation that is amphipathic in the presence of a lipidic environment[25]. That amphipathicity is a common thread between such a diverse array of sequence and origin, suggests that it is key to the activity of AMPs.

The importance of the amphipathic properties of AMPs arises from the different characteristics that are present in the environment of and surrounding the cell membrane. The cell membrane, as described previously, is primarily made up of lipids (though other important non-lipidic constituents are present), which comprise of hydrophobic alkyl-chain tails that pack together, driven by hydrophobic forces, and hydrophilic head groups that face outwards to the aqueous environment. The amphipathicity of AMPs allows them to access the interface between the aqueous surroundings and head groups, and the hydrophobic core of the membrane, and it has been shown that many AMPs prefer this interfacial region of the membrane[89, 90].

Some AMPs demonstrate their amphipathicity as a 'reveal' of their hydrophobicity through changes in conformation when they encounter the hydrophobic membrane[29, 91]. One of the early focuses of AMP MOA were the conformational properties of magainin, melittin, and the cecropins that adopted an alpha-helix conformation when they approached the membrane. It was this alpha-helical structure that possessed amphipathicity, with one side of the helix clustering the hydrophobic residues counter to the hydrophilic residues[29, 92]. The positioning of the hydrophobic residues towards the hydrophobic lipid core allows the AMPs to exert their disruptive activities, by interfering with lipid packing.

The hydrophobic residues include glycine (G/Gly), alanine (A/Ala), and the leucines (L/Leu and I/Ile), however, the most relevant residues for membrane disrupting AMPs are phenylalanine (F/Phe) and tryptophan (W/Trp). The hydrophobic nature of the sidechains of Trp and Phe results in their preference to sit in the hydrophobic lipid bilayer and the bulk of these sidechains, meaning that their presence in the bilayer disrupts the ability of the lipids to

pack together[90, 93]. On the AMP database (APD3), 81%[1] of peptides with recorded activity against gram-negative or gram-positive bacteria contain at least one Trp or Phe residue.

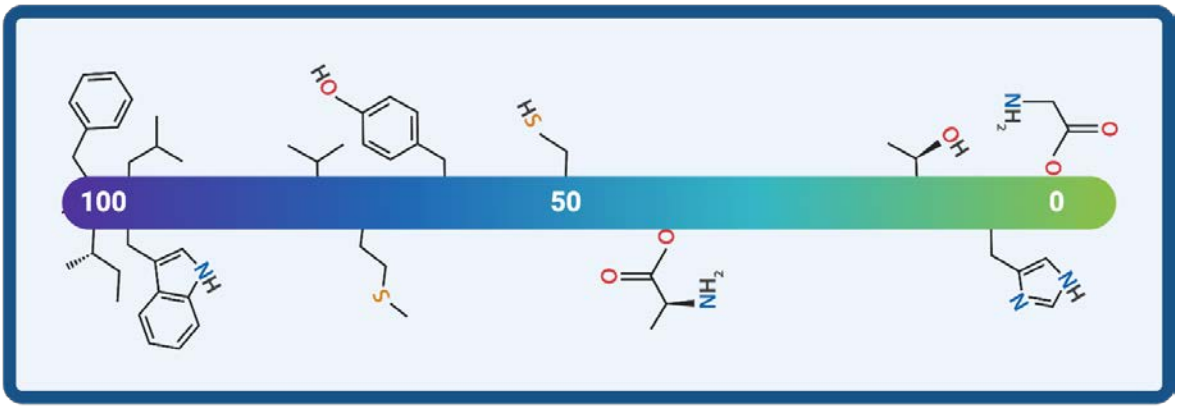

Figure 8: The relative hydrophobicity of amino acid side-chains. Adapted taken from SigmaAldrich[94].

Phe is the most prevalent hydrophobic residue in AMPs hosted on APD3, with 69%[1] of AMPs containing at least one Phe residue. Trp is present in 35%[1] of AMPs recorded in APD3, and it is also one of the more unique hydrophobic residues. The sidechain of Trp is a 'paddle-like' indole group, and as well as the source of the bulk, the aromatic nature of the indole and its amine group lends Trp a degree of amphipathicity, as well as some unique properties. Trp has been identified as having a strong preference to be in the vicinity of the first position of the fatty acid tail where a hydrogen bond can be formed between the NH of the indole and the lipid C=O[89]. Overall, the planar and bulky nature of both Phe and Trp means that they can insert perpendicular to the lipid bilayer, between the tail groups of the lipids, and interrupt lipid-lipid interactions.

The importance of the presence of anionic lipids on the outer leaflet of bacterial membranes has been discussed in previous sections as one of the modes by which AMPs are able to selectively target bacteria. From the point of view of the AMP, this selectivity comes from the cationic residues in the hydrophilic region. At pH 7 the cationic amino acids are arginine

[1] Data extracted from sequence data of peptides that have reported activity against Gram-positive, or Gram-negative bacteria archived on ADP3. Accurate as of Dec 21

(R/Arg) and lysine (K/Lys). Additionally, histidine (H/His) with a pKa of 6 can be partially protonated at neutral pH[95]. The overriding significance of cationic residues is highlighted by their near-universal presence in AMPs; 95%[1] of APD3 peptides with bactericidal activity contain at least one Arg and/or Lys – this increases to 96.5%[2] if His is also included.

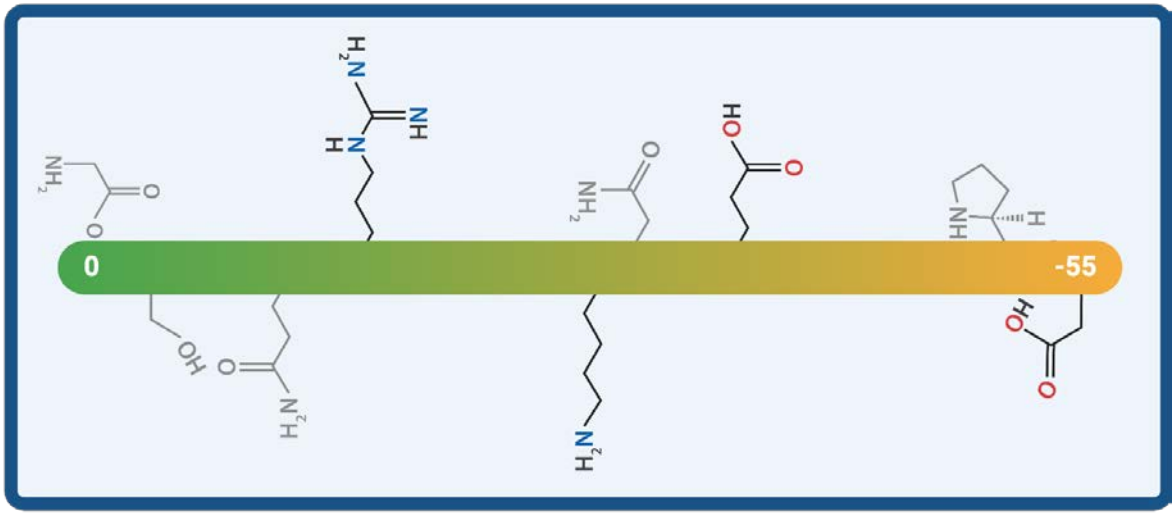

Figure 9: The relative hydrophilicity of amino acid side-chains. Adapted taken from SigmaAldrich[94]

[1] Data extracted from sequence data of peptides that have reported activity against Gram-positive, or Gram-negative bacteria archived on ADP3. Accurate as of Dec 21

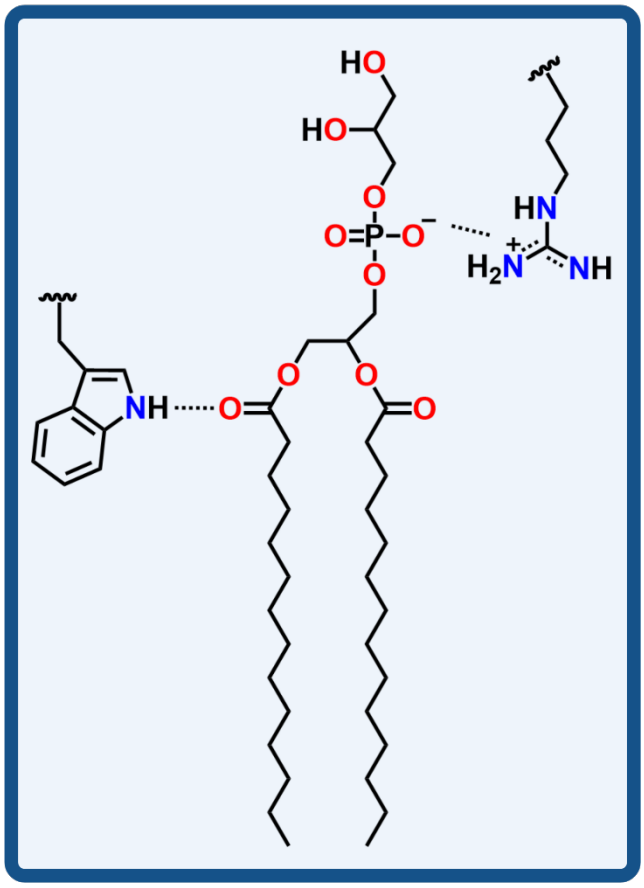

Figure 10: Preferential sites of Trp and Arg interactions illustrated using DMPG

Lys is more common in AMPs on APD3, being present in 86%[1] of peptides. The positive charge on Lys is provided by an ammonium that is terminal of a 5-membered alkyl chain. The position of the charged moiety on the end of the chain gives Lys a great deal of flexibility to take up favourable conformations. A common point of interaction for Lys, as well as Arg, is the lipid phosphate group[96, 97]. The phosphate group is deprotonated, and therefore carries a negative charge - this is also true of zwitterionic lipids such as phosphaticholines (PC), where the phosphate is counter to a trimethylammonium group.

Arg, like Lys, has its cationic group terminal of an alkyl chain, however in Arg the cationicity is supplied by the pi-rich guanidinium ion. In so far as cationicity is concerned, Arg behaves much as Lys, however its pi-rich nature enables pi-pi interactions, or pi-stacking, with both lipids and other residues. A surprising consequence of the pi-rich guanidinium is the formation of pi-pi interactions with other Arg residues, stabilising a highly cationic species – in contrast the charges on Lys are repulsive to one another, and therefore detrimental to Lys-Lys interactions.

[1] Data extracted from sequence data of peptides that have reported activity against Gram-positive, or Gram-negative bacteria archived on ADP3. Accurate as of Dec 21

The selectivity of AMPs towards bacteria is an electrostatic attraction between the cationic residues on the AMP and anionic lipids on the bacterial leaflet. *In silico* studies suggest that the notion of one positive charge from an AMP, meeting a negative charge from a lipid in a one-to-one interaction is an oversimplification; instead, the electrostatic interaction between AMP and anionic lipids drives an initial interaction that enhances interaction with all lipids in the membrane, both anionic and neutral – 0.8 lipids bound per Arg in PC, versus 1.4 lipids per Arg in PC/PG[42].

The cationicity on both Lys and Arg not only enhances the electrostatic interactions with the anionic lipids, but it also enables pi-cation interactions between Trp and Phe, and Lys and Arg. In an analysis of the PDB, it was shown that 25% of all Trp present are involved in pi-cation interactions[98]. While Lys can form a stronger interaction with six-membered pi-ring systems (-15.3 kcal/mol) compared to Arg (-4.1 kcal/mol when parallel or -10.6 kcal/mol when perpendicular), 40% of Lys are located near aromatic residues, in comparison to 70% of Arg[99]. Trp-Arg rich sequences in particular have been demonstrated to be a potent pharmacophore in short AMPs[100].

1.4 Membrane-based modes of action

As previously described, the membrane has been known to be a common target of AMPs from the earliest instances of AMPs. However, the exact mechanism of how AMPs disrupt membranes is a matter of dispute, with many models put forth that seek to explain AMP activity. This section will be an overview some of the more prominent models, though it will not be an exhaustive list, and how the models have evolved from one-another to overcome the short comings of the previous models.

1.4.1 Pore-formation

One of the most influential AMPs was isolated from the fungus *Tricoderma viride* in 1967 by Meyer and Reusser and initially identified as a polypeptide named Antibiotic U-22324[101]. It

was later renamed to alamethicin and the sequence and structure were confirmed as a 20 residue linear peptide that adopt a helical conformation in a membrane environment[102,103,104]. While alamethicin is not strictly a HDP, as it is better characterised by its non-specific lytic behaviour[105], its oligomeric barrel-stave pores formed through strict peptide-peptide interactions proved a source of significant interest[106]. After its initial discovery, magainin was also demonstrated to adopt an alpha-helical conformation that formed pores. However, unlike alamethicin, it forms pores in concert with membrane lipids to produce so-called toroidal pores[30] (Figure 11).

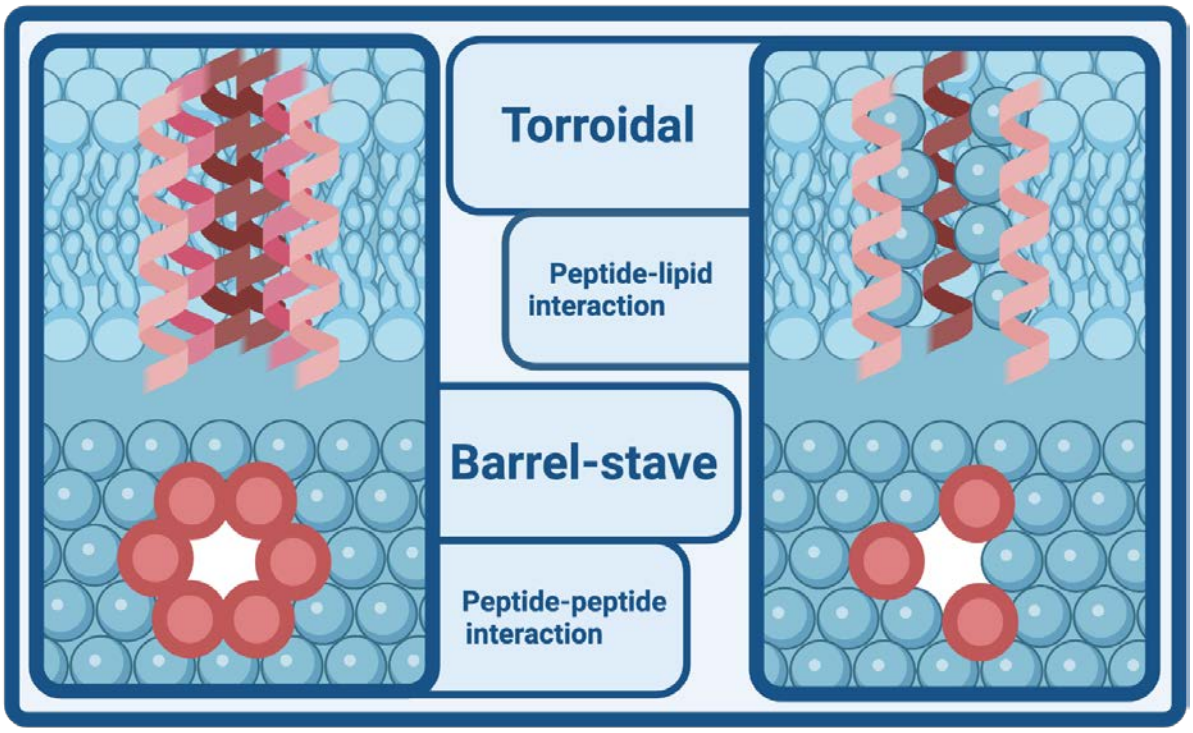

Figure 11: The dominant models of AMP pores. The barrel-stave pore is characterised by its strict peptide-peptide interactions and best embodied by alamethicin. The toroidal pore is characterised by the presence of peptide-lipid interactions, where the lipid is co-opted by the AMP in the formation of the pore, and is best described by magainin.

The pore-forming properties of magainin and alamethicin, as well as their similarity in sequence length, helped establish pore-formation as one of the key models in the bactericidal process of AMPs, in particular alpha-helical peptides[105]. Much study has been done on the pores of magainin and alamethicin, with a view to design new antimicrobial agents with similar

properties; however, the specific pore structure, i.e. barrel-stave vs. toroidal, has come under question, with differing conclusions being drawn by different methods[107].

The primary method of differentiating the pore types is the measurement of conductance across a membrane[108]. In the case of barrel-stave pores formed by alamethicin, voltage gating occurs, whereby distinct voltage levels can be observed to coincide with the change in the number of peptides that participate in the pore. In the case of toroidal pores, a more continuous and varied voltage is observed that lacks general reproducibility[107]. It was soon noted though that no other pore-forming peptides were able to reliably replicate the barrel-stave model, and that rather than alamethicin-like barrel-stave pores being the rule, they were the exception[25, 107].

1.4.2 Carpet Model

The carpet model was first proposed by Shai in 1992 in an attempt to explain the activity of non-pore-forming AMPs (Figure 12). Shai noted, through the fluorescence measurement of numerous membrane-lytic peptides, that such AMPs did not tend to insert fully into the hydrophobic core; furthermore, contemporary models and the methods to describe them often yielded conflicting results as to the specific mode of action[109].

The carpet model starts with the AMP initially binding to the surface of the membrane, followed by conformational adjustment so that the hydrophilic residues face out towards the water layer, and the hydrophobic residues towards the membrane (Figure 12A). The AMP continues to bind and aggregate ‘carpeting’ the membrane, and at a sufficient local concentration causes disruption of the curvature of the membrane. This disruption allows the formation of transient holes in the membrane that enable the passage of small molecules, and eventually the disintegration of the membrane once a sufficient threshold of membrane bound AMP is reached (Figure 12B). Importantly, no specific conformation is required of the peptide, nor does the peptide fully insert into the membrane, unlike the pore-based models[110].

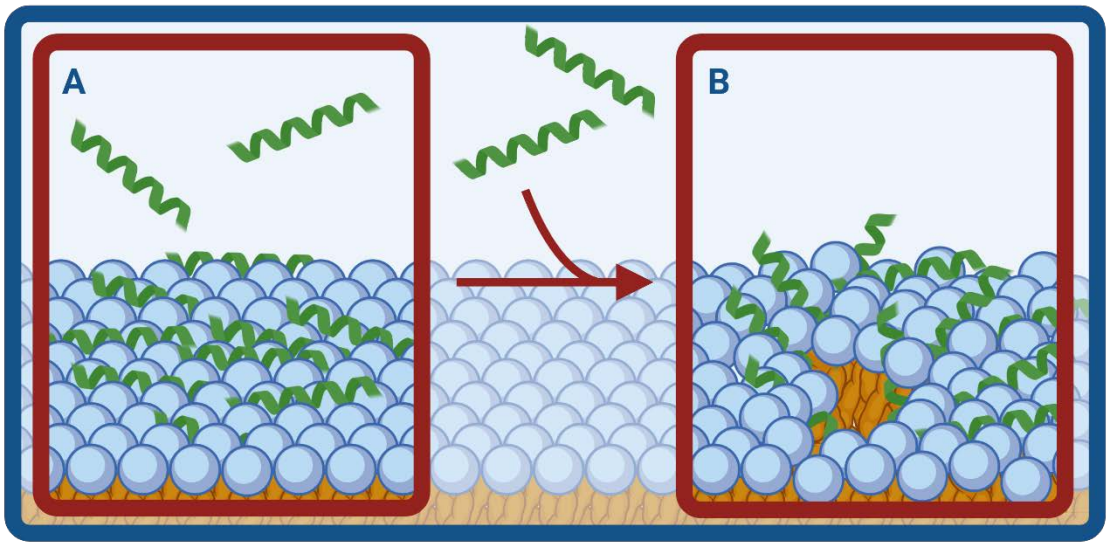

Figure 12: The carpet model. A: initial binding and adoption of a perpendicular position. B: loss of membrane integrity after a threshold concentration is reached.

1.4.3 Detergent Model

One of the criticisms of the carpet model is its reliance on the AMP reaching a threshold concentration before it can exert its activity; however, peptides have been demonstrated to exert membrane disruptive effects at much lower peptide:lipid ratios than those expected by the carpet model. To account for this, Bechinger and Lohner proposed the detergent model in 2006[111] (Figure 13).

The detergent model, as the name indicates, treats the peptides as though they are detergent-like molecules. Detergents, like AMPs, are amphipathic and can form aggregates with themselves, often micelles, that are able to solubilise hydrophobic molecules such as lipids and other fatty acids. The detergent model describes the AMPs permeabilising the membrane by forming stable aggregates with other AMP molecules and lipids that are removed from the membrane as micelles or bicelles (Figure 13B). This results in large holes, which like pores, allow for less-restricted movement of matter in and out of the cell; this destabilises, and eventually kills the bacteria[111].

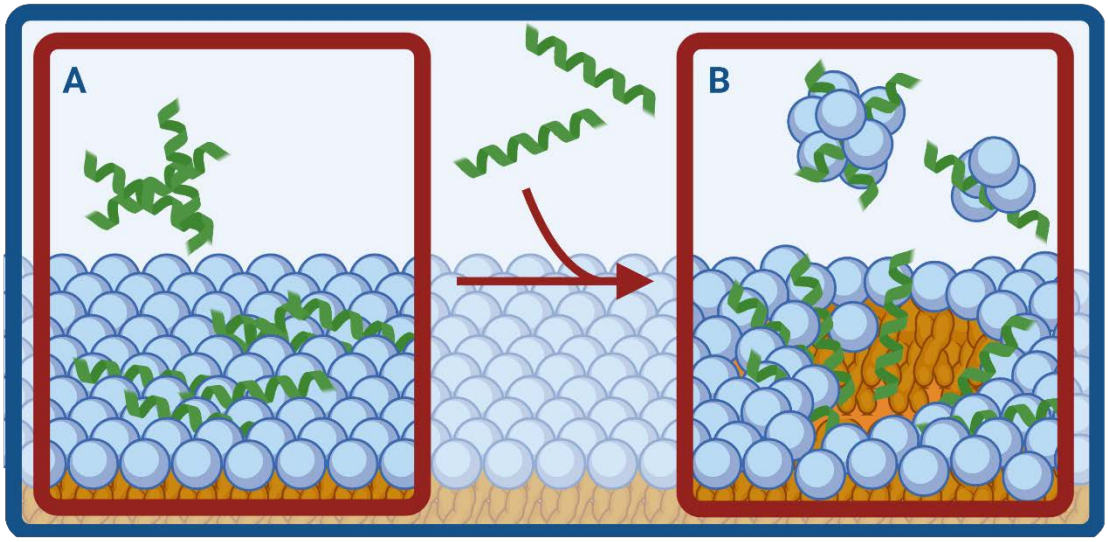

Figure 13: The detergent model. A: initial binding and formation of AMP aggregates. B: loss of membrane integrity as AMP-lipid aggregates form and remove lipids from the membrane.

The model also predicts a difference in the activity of oligomers of AMPs and their respective monomers. Using the aggregation of detergents as an example, as well as some AMPs, Bechinger and Lohner describe the possibility of AMPs forming micelles/aggregates before interacting with the membrane (Figure 13A). Such oligomers could enhance selectivity and insert into the membrane to incorporate membrane lipids into the oligomer, removing them from the membrane, or enable the oligomer to position itself into the membrane and form a discrete pore. As a result, Bechinger and Lohner suggest that the previous pore and carpet models are actually specific cases within the detergent model, and further suggest that AMP activity may be better described by a detergent-like phase diagram where such cases could occur if the correct conditions are satisfied[111].

1.4.4 Other Models

The barrel-stave and toroidal pores, detergent, and carpet models represent the most popular models of AMP membrane disruption. However, other models of AMP activity have been proposed.

The interfacial model of activity was proposed by Wimley et al. as a means of explaining the differences in the performances of the limited number of pore-forming AMPs and most other AMPs[25]. Similar to the carpet model, it focuses on the tendency of AMPs to sit in the interfacial region between the lipid membrane and aqueous surrounding, a phenomenon which has already been discussed. It is while the AMPs are in the interfacial region that they are able to disturb the membrane by interfering with lipid packing.

An alternative mode of action was suggested for the cyclic peptide cWFW, but described and observed previously for other AMPs[49]. This model has the AMP inducing the formation of clustered domains, or rafts, of anionic lipids, as well as clusters of differently ordered lipid fluidities. The result can be a rigidification of the phase of the lipids in these domains, interrupting Omp activity by reducing the density of Omps in the rigid domains. The boundaries between such domains of lipids can also enhance the permeability of the membrane[47].

2 A Toolbox For Antimicrobial Peptide Design

Rational design is a methodology by which alterations to a substrate are made with the intention of achieving a desired outcome based on observations or expectations of modelling, physical or otherwise. Typically, one could think of inhibitors for a specific enzyme where the active site is studied and defined, and based on the shape, size, and residues present, substrates that fit within and could feasibly interact with the active site can be proposed. In the instance of membrane active substrates this poses a problem: there is no single defined target with which a one-to-one interaction can take place, instead the target is an amorphous lipid barrier that plays host to a number of proteins (both membrane-bound, and trans-membrane), sterols and

carbohydrates, that is highly variable between strains and species of bacteria. Therefore, the typical tools and models used need to be adapted to suit AMPs and lipids.

2.1 Common Features of AMP MOA

While the previously described models differ on the specific details of how membrane targeting AMPs disrupt the lipid membrane, they do share common features that will be further discussed:

- An initial binding
- Build up on the surface
- Disruption of the lipid membrane resulting in greater permeability

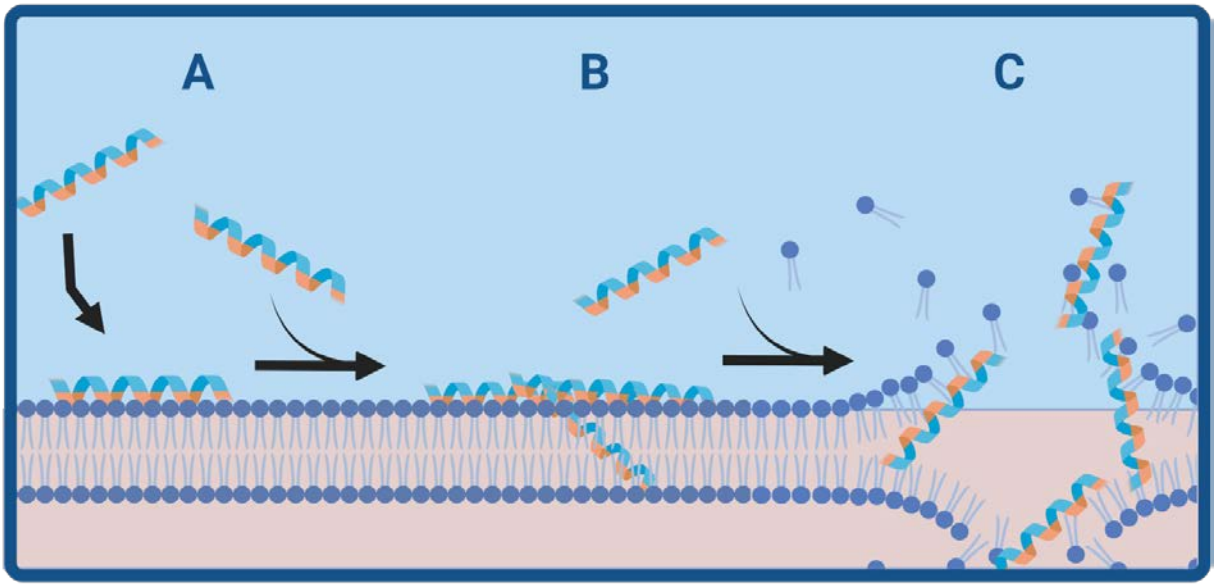

Figure 14: Generalised mechanism of AMP action. A: Initial binding of AMP to the membrane. B: Build up of AMP on the surface. C: Disruption of the membrane.

These common features can be described in measurable, experimentally testable metrics. There are many other properties of AMPs and AMP-lipid interactions that can be investigated, both quantitatively and qualitatively. However, this discussion of common methods will focus on

the two properties that are most relevant to the work undertaken: the binding of AMPs to lipids (Figure 14A), and quantification of permeability/leakage (Figure 14C).

2.2 Binding

There are many methods by which one can assess the binding properties of AMPs to lipids. As these methods were primarily developed for receptor/ligand type complexes, in such cases as are pertinent to the discussion, the lipids will be considered as the receptor, and the AMP as the ligand. Binding is typically described by the dissociation constant K_D. K_D describes the equilibrium between the rate constants k_{on} and k_{off} (Equation 1), with a lower K_D describing a stronger binding[112].

$$K_D = \frac{k_{off}}{k_{on}}$$

Equation 1

K_D is further related to the thermodynamic measures of the Gibbs free energy change ΔG, enthalpy change ΔH, and entropy change ΔS through Equations 2 and 3.

$$K_D = \frac{1}{\Delta G}$$

Equation 2

$$\Delta G = \Delta H - T\Delta S$$

Equation 3

Alternatively, the partition coefficient K_P can be used to describe the preference of an AMP towards a lipidic environment over an aqueous one. K_P is typically used to describe the concentration of a drug in tissue versus the surrounding blood[113]. However, it can more generally be applied as a measure of the ratio of the relative concentrations of a drug in an aqueous and lipidic environment[114].

$$K_P = \frac{[Concentration\ in\ Lipids]}{[Concentration\ in\ Water]}$$

Equation 4

K_P can be considered complimentary to K_D, in that K_P describes the preference for the hydrophobic environment of the lipids, while K_D describes the kinetics of the interaction between the AMP and the lipids. In the case of AMPs, the relationship between K_P and K_D is reasonably linear, with a higher K_P anticorrelating to a lower K_D for a given AMP in different lipid compositions[115].

2.2.1 NMR

Nuclear magnetic resonance (NMR) based methods use different phenomena to extract K_D, such as the transfer of magnetism between molecules. One such method is STD (Saturation Transfer Difference). In STD the receptor is irradiated by an 'on-resonance' selective pulse (I_{sat}). When the receptor is in contact with the ligand the saturation is transferred to the ligand, in the NOE enhancement of the protons which are involved in the binding. An additional spectrum is collected where the receptor is not irradiated - an 'off-resonance' spectrum (I_0). The off-resonance spectrum is subtracted from the on-resonance spectra to yield the STD spectra, whereby only the protons that had saturation transferred to them are visible[116].

$$\text{STD amplification factor} = \frac{I_{sat} - I_0}{I_0} \text{ x ligand excess}$$

Equation 5

$$STD_{AF} = \frac{[L]\alpha_{STD}}{K_D + [L]}$$

Equation 6

This process is repeated with an increasing concentration of ligand, and the STD amplification factor (STD_{AF}) is plotted against ligand concentration [L], such that α_{STD} is the max $STD_{AF.}$ From this plot KD can be extracted. Using STD, bindings within a mM-nM range can be probed.

Similarly, waterLOGSY utilises the transfer of saturation between molecules that interact, as well as the differences in the tumbling of large and small molecules. However, in the case of waterLOGSY, instead of the selective excitement of the ligand or receptor, the bulk water is excited, enhancing sensitivity[117].

Other NMR-based binding methods take advantage of chemical shift perturbation (CSP). Changes in chemical shift arise from (potentially minor) changes in conformation that occur when a ligand is bound by a receptor. The induced changes in chemical shift are monitored with an increasing ligand concentration, and from these parameters yield K_D[118].

One of the outstanding advantages of NMR-based binding measurements is the ability to extract more detailed information regarding the binding taking place, such as the specific parts of both the receptor and ligand that play the greatest role in the interaction. However, a common drawback of some NMR methods, such as CSP, is that they often require labelling to achieve optimal results[118, 119]. NMR methods also typically require larger amounts of sample, and the limit of detections often prevents the exploration of nM interactions. Case in point, while it is possible to determine K_P by NMR methods, large sample requirements compared to other non-NMR based methods mean it is not a common method for K_P determination, with optical methods favoured instead[119,120].

2.2.2 Fluorescence

Fluorescence based determination of binding properties K_D and K_P for AMPs often takes advantage of the intrinsic fluorescence of Trp, a conveniently common residue in many AMPs, and the resulting changes in quantum yields in aqueous and lipidic environments as a result of quenching[121].

When a fluorophore absorbs a photon of light of the correct wavelength, it reaches an excited state. Fluorescence occurs when the fluorophore leaves this excited state by emitting a photon at an altered wavelength – the difference in wavelength between the absorbed and emitted photon is known as the Stokes shift. The quantum yield of a fluorophore describes the efficiency by which absorbed photons are emitted – i.e. a fluorophore with a quantum yield of 1 emits every photon that it absorbs. The quantum yield of a fluorophore depends on many factors, one of which is the degree of quenching it is subjected to. Quenching describes a number of processes that prevent the fluorophore from emitting the photon, either by preventing the fluorophore from reaching an excited-state (static quenching), or by collision with a 'quencher' (such as a solvent molecule) that reverts the excited-state to the ground-state by energy transfer (dynamic quenching)[122].

For the determination of K_P, the fluorescent intensity is monitored in the presence of an increasing concentration of lipid[123]. As the AMP partitions into the lipidic environment an accompanying increase in intensity is expected as there is a reduction in dynamic quenching by the water[124] – it should be noted that there are special cases where self-quenching of the peptide occurs[125] .

$$I = \frac{I_0 + K_P \gamma_L [Lipid] I_L}{1 + K_P \gamma_L [Lipid]}$$

Equation 7

The measured intensity (I) can be used as a raw value, or normalised on the initial, aqueous, intensity I_0, and plotted against lipid concentration so as to fit to Equation 7 where γ_L is the lipid molar volume, and I_L is the fluorescence intensity of the AMP in the lipidic environment.

$$I = \frac{K_P \gamma_L [Lipid] I_L}{1 + K_P \gamma_L [Lipid] + K_2 K_p I_L} + \frac{I_0}{1 + K_p \gamma_L [Lipid]}$$

Equation 8

In this special self-quenching case a further term (K_2) is used to account for the decrease in fluorescence as a result of this phenomenon (Equation 8)[125].

2.2.3 Microscale Thermophoresis

Microscale thermophoresis (MST) is a more recent technique that is normally used to probe the binding of a substrate to a target, typically an enzyme and a ligand, pioneered by Nanotemper. Thermophoresis describes the movement of molecules along a temperature gradient, normally from hot to cold, and is defined by the Soret coefficient (S_T) which can be determined by the relative concentrations of a substrate in the 'cold' environment, and the concentration in the 'hot' environment. The binding is determined by small changes in the thermophoretic properties of the target as it is bound.

$$S_T = \frac{[\mathrm{Hot}]}{[\mathrm{Cold}]}$$

Equation 9

MST creates a temperature gradient by applying an IR laser to a capillary that contains the mixture of target and substrate. The laser is focused on a 50 μm area that is then heated by 4-6^{o}C, creating a small temperature gradient that the substrate and target can move along.

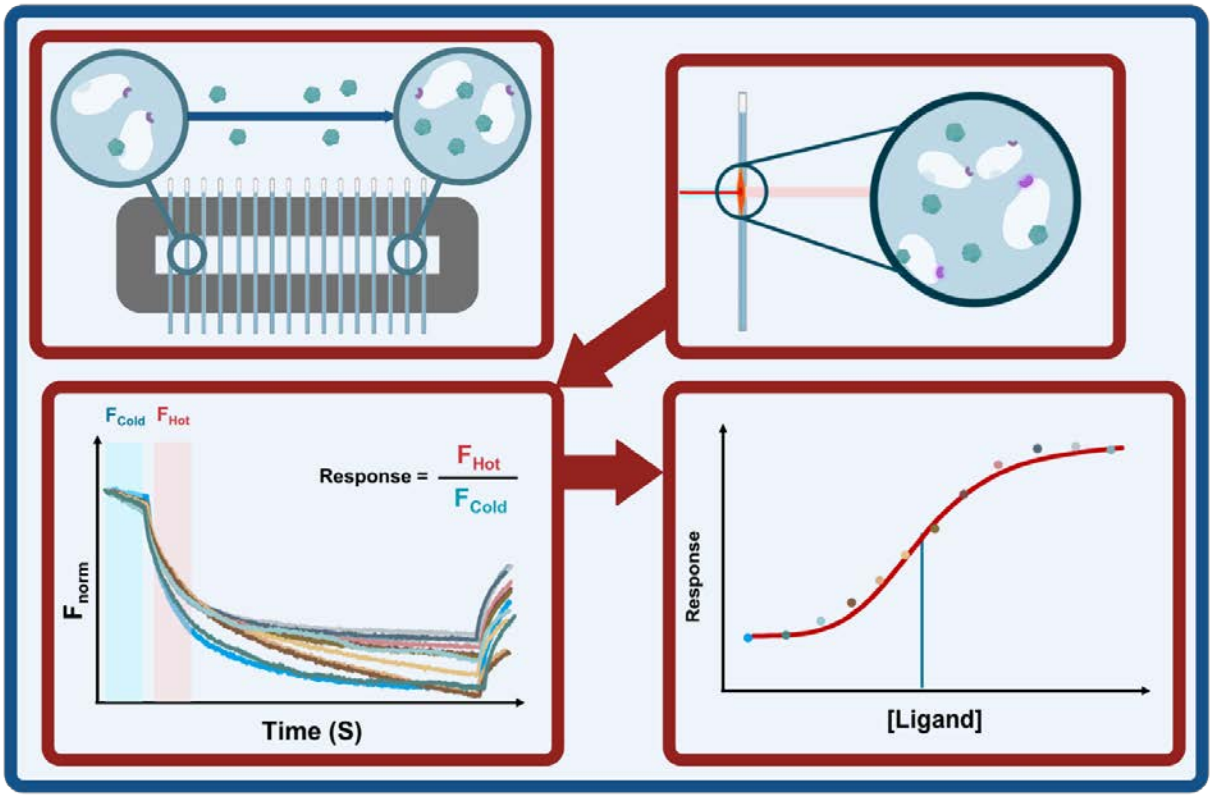

Figure 15:Overview of microscale thermophoresis. Capillaries of increasing concentration of ligand prepared. IR laser irradiates each capillary in turn, this causes an initial sudden drop in fluorescence intensity, followed by a slower decline to a steady state. The change in MST response is plotted against ligand concentration to yield a sigmoidal dose-response from which K_D can be extracted.

In MST, S_T is determined by observing the fluorescence of a target, either as the intrinsic fluorescence from Trp or Tyr residues, or from an attached fluorophore-tag. The initial fluorescence of the mixture of the target and substrate is monitored for 1-3 seconds before the activation of the IR laser. Upon the activation of the laser, a temperature-related intensity change (TRIC) occurs due to the dependence of the quantum yield of a fluorophore on temperature; the TRIC is observed within the first second, and is referred to as the T-Jump. After the initial 1-1.5 seconds, the TRIC has taken place and the thermophoresis of the target occurs until a steady state is reached - typically after 15-30 seconds. At this point the IR laser is deactivated, and a reverse T-Jump is observed, as the temperature gradient dissipates and the target returns.

S_T can then be determined from the relative fluorescent intensity of the fluorophore during the application of the laser compared (F_{Hot}) to before the application of the laser (F_{Cold}), where the intensity correlates with the relative concentrations in either environment; this is referred to as F_{norm} (Equation 10).

$$S_T = F_{norm} = \frac{F_{Hot}}{F_{Cold}}$$

Equation 10

A more detailed description of S_T can be shown in Equation 11,

$$S_T = \frac{A}{kT}\left(-s_{hyd} + \frac{\beta\sigma^2{}_{eff}}{4\varepsilon\varepsilon_0 T} \text{ x } \lambda_{DH}\right)$$

Equation 11

where s_{hyd} is the entropy of solvation of the complex, A is the size of the complex, and $\frac{\beta\sigma^2{}_{eff}}{4\varepsilon\varepsilon_0 T}$ describes the overall properties of the complex. The result of which is that the MST response is very sensitive to potentially small changes to the complex when binding takes place.

By selecting different regions from where F_{Hot} is sampled from, one can evaluate different properties of the bound/unbound complex. By selecting the T-jump region around 1.5 seconds, the changes in the environment of the fluorophore can be evaluated, and by sampling F_{Hot} once a steady-state of the MST trace is achieved, one can evaluate the thermophoretic properties of the fluorophore containing complex. Previous best practice focused on the evaluation of the steady-state region of the MST trace. However, the influence of the prolonged heat exposure from the IR laser on the stability of complexes has led to a re-evaluation, with the T-jump region analysis now consider best practice[126], with thermophoretic analysis best suited to sample stability determination[127].

The experimental setup for the determination of the binding has the protein/enzyme in a fixed concentration, as this is usually the location of the fluorophore, while the substrate concentration is varied over a serial dilution. Each point is a distinct sample; a control of substrate only and target only are also collected.

$$y = y_0 + \frac{B_{Max} \text{ x } K_D \text{ x } [\text{Ligand}]}{K_D \text{ x } [\text{Ligand}]}$$

Equation 12

The result should be a sigmoidal dose-response curve that can be fitted to the hill model (Equation 12), where y_0 is the response of the peptide on its own, and B_{Max} is the difference between y_0 and the maximum response. MST can be used to detect bindings down to the low nM and pM ranges.

MST has had limited application to peptide:lipid interactions previously. In an early MST study, the K_D of a 13 residue AMP, L-RW, to PC and PG lipids was determined in a number of different buffer conditions[45]. The determined K_Ds were in the low μM range, typical of many peptides. In order to obtain the bindings, a label, FITC, was covalently bound to the C-terminal of L-RW. While no binding of FITC on its own to the lipids was observable, the addition of a bulky label to the peptide, with its own physiochemical properties, will likely influence the properties of the peptide that it is bound to, therefore a label-free method would be more practical.

2.2.4 Other methods

Surface plasmon resonance (SPR) is a robust technique that has been used to study biophysical interactions, including drug/lipid membrane interactions[128]. In the SPR determination of binding parameters, a receptor is immobilised onto the surface of a chip. Once the chip has been successfully covered, stocks of ligand in increasing concentration are passed over the chip.

While the ligand moves across the chip, if it is able to interact with the receptor it will similarly be immobilised on the chip, changing the mass of material loaded on the chip, which is detected by an optical reader[129].

In the case of AMP-lipid interactions, the lipid is loaded onto the chip as vesicles[130]. SPR has been applied to AMPs and lipids in the determination of K_D[131] and K_P, as well as more detailed kinetic parameters including detailed k_{Off} rates. Some shortcomings of the SPR study of peptide-lipid interactions include instability of the lipid layer due to fusion of the loaded vesicles, potential accumulation of cell-penetrating peptides below the chip-bound vesicles, as well as an inability to accurately probe membrane dissociating detergent-like molecules[130].

Isothermal calorimetry (ITC) measures the heat created or used by a reaction, and has found use in the probing of biomolecular interactions, and as well as probing kinetic properties such as K_D, ITC is able to yield thermodynamic parameters of the interaction ΔH, ΔS and ΔG[132].

ITC has been used to assess the binding properties of AMPs to lipids in a number of different lipid compositions and models, including vesicles, nanodiscs and micelles[133-135]. Like SPR, ITC is able to function label-free, giving it an advantage over techniques such as NMR, however ITC has much greater sample requirements in comparison to fluorescence-based techniques[136].

2.3 Permeability/leakage

Membrane leakage can be considered in several different ways, either in terms of water and ions, which are held in an equilibrium in cells, or as the ability of small and large molecules to transport across the membrane, or for the agent that is disrupting the membrane to pass across. The permeability across a membrane is quantified by the apparent permeability P_{app}. P_{app} is the

rate at which a target moves across a membrane in cm/s^{-1}, that is normalised on the area of the membrane.

$$P_{app} = \frac{dQ}{dt}\ x\ \frac{1}{A\ x\ C_0}$$

Equation 13

Equation 13 is a derivation of Fick's law where $\frac{dQ}{dt}$ is the change in concentration over time, A is the area of the membrane, and C_0 is the starting concentration.

2.3.1 Vesicle Leakage

A common method of determining the disruptive capabilities of AMPs is through vesicle leakage assays. In vesicle leakage assays a reporter molecule is contained within the aqueous core of the vesicle; then, when the vesicle is disrupted by an AMP, the reporter is able to escape the vesicle and enter the bulk solvent, where it can be detected[137-139].

Reporters are captured in the vesicle by extrusion of a vesicle stock in the presence of a buffer solution in which the reporter is present and buffer exchange is performed to replace the reporter containing buffer with a reporter-free buffer[137]. The reporter used in vesicle leakage assays depends on the method of acquisition that is to be used. Fluorescence vesicle leakage assays typically make use of fluorescein[140], calcein[137], or derivatives thereof. NMR-based vesicle leakage can be performed with labelled molecules such as $H_2{}^{17}O$ for water leakage[141], or other nuclei such as 23Na to monitor ion transmission across the lipid bilayer[142, 143].

The reliability of vesicle leakage assays has been questioned, especially as a method to determine whether AMPs form pores or lyse cells as the MOA[25]. Wimley compared the MIC and vesicle leakage conditions as a function of peptide:lipid and demonstrated that MIC

conditions typically have 1000:1 P:L compared to 1:100 P:L in vesicle leakage studies. Furthermore, 'burst-release' behaviour can be exhibited in these experiments, whereby a short initial release of material upon addition of AMP is observed before a stabilisation where no reporter leakage is observed until a further addition of AMP or detergent. One explanation for this is an 'all-or-none' mechanism where rather than all vesicles losing some of their contents, some vesicles lose all of their contents, while the remaining vesicles are unaffected[144] – the interfacial model was proposed as an explanation for this[25].

2.3.2 PVPA

The Phospholipid Vesicle Permeation Assay (PVPA) is an assay developed to determine the apparent permeability (P_{app}) of drugs across a permeable lipid barrier[145]. PVPA has been used to predict the uptake of a given drug across the gastrointestinal barrier and is capable of increasing layers of complexity to enhance the biological relevance[146, 147].

The assay consists of a well-plate insert that has a cellulose support fused to the bottom. 300 nm E80 lipid vesicles are loaded into the pores of the cellulose support through centrifugation and drying. Larger 600 nm vesicles are then deposited on top of the cellulose, and affixed through centrifugation and drying[145] (Figure 16).

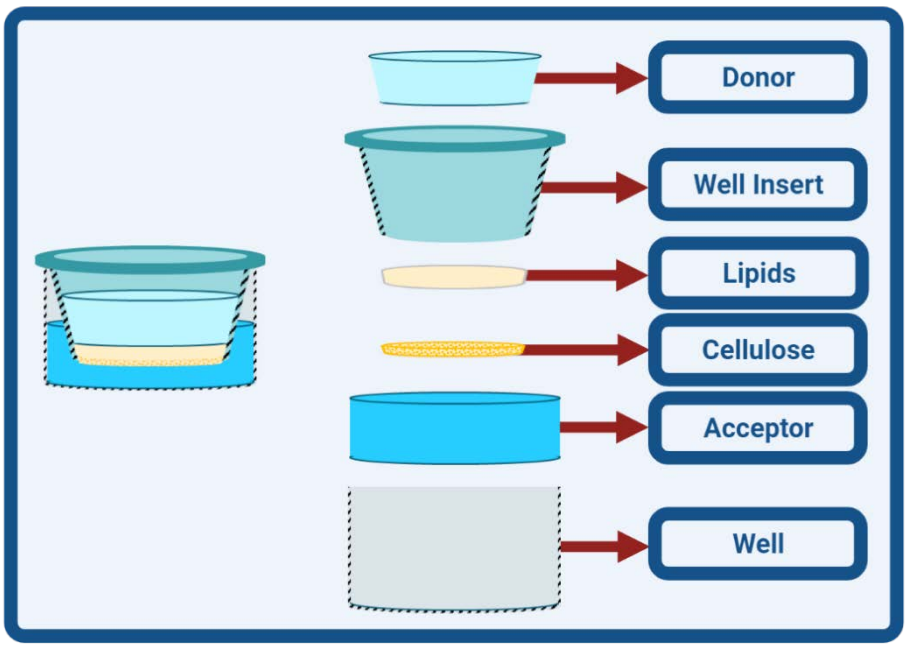

Figure 16: Exploded view of the PVPA barrier highlighting the construction of the PVPA barrier

A so-called donor buffer solution that contains the compound of interest is placed on top the barrier, which is in turn placed into a well that contains the acceptor buffer solution, that is identical to the donor but free of the guest molecule. The barrier is left in the well for a pre-defined time, typically 30 or 60 minutes, before being transferred to a new well where the process is repeated several times until 6 hours have elapsed.

The acceptor wells that have contained the barrier are checked by mass spectrometry to determine the amount of the guest molecule that has transferred across the barrier into the acceptor. The derivative of the line that describes concentration over time is taken, and the P_{app} is determined using Equation 13, where A is the area of the barrier (0.33 cm^2 for the barrier used in PVPA),C_0 is the initial concentration of the guest molecule and 1 is the volume of the acceptor well (in cm3).

2.3.3 Other Methods

Another common measure of permeability is through electrical current measurements across lipid membranes in membrane potential experiments[108]. In such experiments changes in voltage across the membrane are monitored over time with the addition of AMP, with AMPs that perturb the membrane causing an increase in the current across the membrane[148]. Such methods

were often used in the determination of whether toroidal and barrel-stave pores were formed, due to the voltage-gated behaviour of barrel-stave pores[107].

Other methods focus on the monitoring of the ability of the AMP itself to move across the lipid membrane. Hydrogen-deuterium exchange (HDX) was used in MALDI-HDX experiments where peptide insertion through liposomes was probed[149]. In a non-AMP context, the passive transport of peptidomimetics across phospholipid membranes has also been tested using Parallel Artificial Membrane Permeation Assay (PAMPA)[150] to determine absorption, distribution, metabolism and elimination (ADME) properties[151].

2.4 Membrane Modelling

An equally important choice to what method is to be used to assess peptide-lipid interactions is what model system of lipids is to be used. The decision on the model-system depends on the need of the user, with each system, while generally similar in so far as all will be lipid-based, having its own strengths and weaknesses, thus making them applicable to different interactions and techniques.

2.4.1 Lipid Composition

Most studies using model membrane systems use very simple compositions, often using just a small number of lipids, usually one or two classes of headgroup, typically a zwitterionic species, and an anionic species. More detailed models will utilise more complex lipid compositions using three or more lipids, as well as including other membrane components such as sphingomyelin, cholesterol, and LPS.

The most widely used class of zwitterionic lipid is phosphatidylcholine (PC). PC, particularly DMPC, is a cheap and widely available lipid that is abundant in mammalian cells. DMPC is robust in the applicability of a number of different lipid assemblies and compositions and is well studied[96, 130, 133, 138]. The combination of these factors makes PC ideal for use in method development[152, 153]. PC is often used as the zwitterionic bulk of most model membranes, both mammalian and bacterial. However, PC lipids are found sparingly in bacteria[154] - the more common zwitterionic species in bacteria is phosphatidylethanolamine (PE). As a result, some groups make use of POPE or DOPE lipids, and differences in the AMP affinities for PE and PC lipids has been demonstrated[96].

The use of PO or DO lipids has significant advantages over DM lipids. Firstly, PO and DO represent lipid tails with longer lengths, 16 and 18 carbons long (compared to 14 for DM lipids), but also contain a double bond along the chain (both chains in DO and one in PO). Secondly, PO and DO lipid tails are more prevalent lipid species compared to DM, which is otherwise quite rare[155]. The unsaturated chains of PO and DO have lower melting points compared to DM lipids, resulting in a more fluid lipid phase[156]. As such, the properties of the lipid species should be considered beyond the headgroup, especially when attempting to produce biologically-relevant lipid membrane models.

A common experimental setup uses two compositions: a wholly zwitterionic composition that is intended to represent mammalian/host or inert lipid membrane, and an anionic composition containing a percentage amount of anionic lipid that represents the bacterial membrane. This is done to highlight the role the anionicity of bacterial membranes has in the peptide-lipid interaction, and to effectively demonstrate the selectivity of AMPs – especially in the case of binding assays[124, 134].

The anionicity of the bacterial membrane is most often emulated with phosphatidylglycerol (PG) lipids, with more complex models including the addition of cardiolipin (CL). However, not all bacteria have the same content of anionic lipids, or even the same species; gram-positive

bacteria contain many PG derivatives and other charged, non lipids components, like LTA[157], while gram-negative bacteria have an outer membrane that is rich in the highly negative LPS[158]. The result is there is no standardised model; instead there are a great many proposed compositions, ranging from 5% anionic content up to 50%, or even 100%, all of which are derived with reasonable rationale [25, 37, 159, 160].

One possible solution to the lack of a standardised model is the use of native lipid preparations. Native lipid preparations (sometimes named membrane vesicles) are vesicles that have been directly obtained from bacteria, and as such much more closely resemble the bacterial membrane of a given species, or a given strain. Such preparations can be produced by mutant strains, or by direct extraction as nanodiscs from bacteria using SMA, and contain not only lipids, but also membrane bound proteins and lipid-precursors[161-163].

2.4.2 *In Vitro* Models

Liposomes are a common membrane model system that was discussed in the leakage assays. Liposomes are vesicles constructed of lipid bilayers and can vary significantly in size. Liposomes are classified by their vesicle structure in one of two of ways: size, or number of bilayers.

Unilamellar vesicles consist of a single bilayer and are further classified by size, as either small, large, or giant unilamellar vesicles, shortened to SUV, LUV and GUV, respectively. The specific sizes of the categories can vary, but SUVs are typically below 100/250 nm, LUVs up to 500-1000 nm, and GUVs are vesicles considered greater than 1000-5000 nm[164, 165]. The particular size of vesicle influences the curvature of the bilayer – the larger the vesicle, the less curved the bilayer. GUVs are large enough that they have a locally flat bilayer which can be advantageous for a number of studies[166]. The large size of GUVs means that individual vesicle events can be more closely observed[167, 168].

The more widely-used vesicles are SUVs and LUVs. The main advantage of vesicles of these sizes are the ease of preparation. Unilamellar vesicles are normally prepared from multilamellar vesicles (MLV). MLVs, in contrast to UVs, and consist of many bilayers that could be considered as vesicles-in-vesicles-in-vesicles. By sonication, extrusion, or freeze-thawing preparation methods, one can yield a vesicle stock of a SUV of desired size[165]. The heterogeneity of the suspensions of SUVs and LUVs means that individual events cannot be observed, instead averaged steady-state observations must be used[167]. Due to their smaller size, LUVs have an increased surface curvature that can have a significant impact on the peptides' influence[166]; this, coupled with the heterogenous nature of SUV/LUV preparations and constant slow fusion, can result in poorly reproducible studies[25].

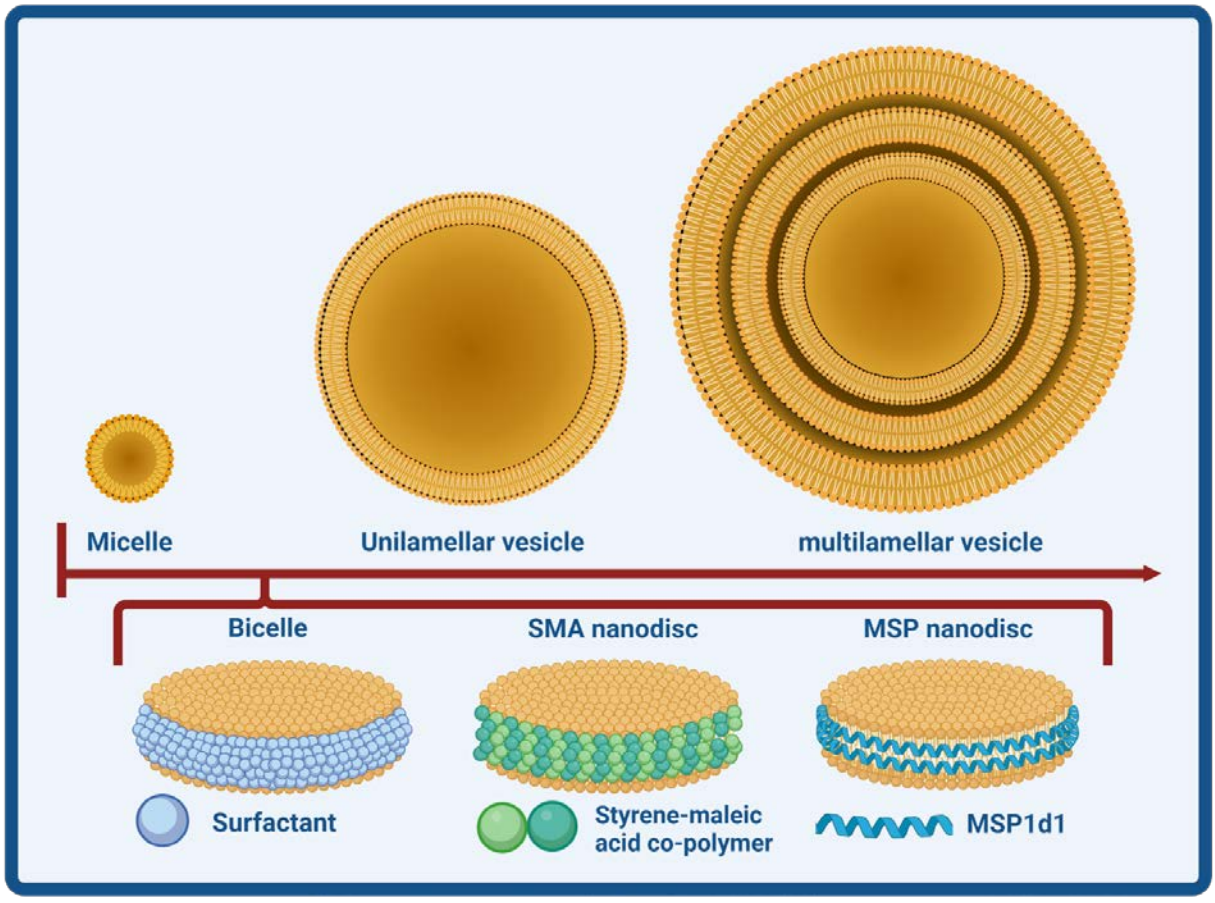

Figure 17: Size comparison of different lipid model systems, and nanodisc constructions

A more homogenous model system are nanodiscs. Nanodiscs are circular planar lipid bilayers that are supported by a belt molecule and prepared through self-assembly. First produced by Sligar et al[169], nanodiscs are commonly used to solubilise membrane proteins for further study[152, 170]. Nanodiscs offer greater size homogeneity over vesicles and a planar surface with no curvature stress, as well as greater stability – convenient for the longer experiment times, such as those required for NMR protein studies[152].

The initial nanodiscs made use of membrane scaffold proteins; MSP nanodiscs typically use MSP1d1, a helix rich amphipathic protein derived from human apolipoprotein A1. Two proteins encapsulate the lipid bilayer, and the size of the disc is controlled by deletions or extensions on the protein that can yield discs with radii between 6-10 nm[153]. MSP nanodiscs have a small distribution in size, which can be further reduced by the covalent circularisation of the MSP to produce a very homogenous nanodisc preparation[171]. Larger MSP nanodiscs can be made with longer proteins up to 50 nm[171], or larger still using DNA to produce nanodiscs with up to ~100 nm radii[172].

Another class of nanodiscs make use of styrene-maleic acid (SMA) co-polymers as the belt molecule. SMA copolymers were first applied as a means to isolate membrane-bound proteins[161, 173]. Other co-polymers have been developed with specific properties in mind, such as magnetic alignment (SMA-QA)[174], reduction of lipid phase heterogeneity (DIBMA)[175], or chelation of metal ions for paramagnetic relaxation enhancement NMR studies (SMA-EA-DOTA)[176]. SMA nanodiscs usually have a slightly larger size distribution than their MSP counterparts, owing to the polymer preparation – a specific length of polymer is not produced, rather polymers with a distribution in length. However, the preparation of SMA nanodiscs can be done without detergent, and sometimes without purification directly from vesicles, and as such SMA nanodiscs can be considered to be more user-friendly[177].

One of the values of nanodiscs is that they yield a bilayer model that is planar. To achieve planarity (or at least local planarity) using vesicles, one must prepare GUVs. In contrast to

vesicles however, the is a heterogeneity of phase across both SMA and MSP nanodiscs, caused by the disruption of the outermost lipids from the belt molecules[178, 179].

Bicelles are another disc-based lipid system, however in contrast to MSP and SMA discs, bicelles do not use belt molecules, instead making use of surfactants or short tailed lipids. DHPC, a lipid with a zwitterionic PC headgroup and hexayl tails, or the detergent CHAPSO, are commonly used to form bicelles. The surfactant forms a micellular-like belt around the hydrophobic core of the lipid bilayer, and the size of the bicelle is dictated by the ratio of surfactant to lipid, referred to as the q factor[180-182]. Bicelles of a large enough size are known to behave as liquid crystals that can be aligned in magnetic fields, and can be used to extract traditionally solid-state NMR parameters in solution-state NMR[183].

2.4.3 *In Vivo* Models

Another choice that entirely eschews the considerations of simplification is to use live bacteria. There are a growing number of methods that make use of whole bacteria, including the microscopic imaging of bacteria in the presence of AMPs, NMR studies of whole bacteria and AMPs, and MIC testing.

Fluorescence microscopy usually takes advantage of probes that can be taken up by the bacteria, such as GFP (green fluorescent protein), and can be used to produce images of the bacteria, with different probes enabling the imaging of the organism in general, or specific parts of the bacteria[184]. Such techniques have been used to demonstrate that most AMPs do not form pores as the mode of killing in a biological context[185].

Live-cell NMR, in-cell NMR, or whole-cell NMR are applications of NMR to the study of cellular processes and overall fitness. The methods have both solid-state and solution-state

applications and have been used in the study of bacteria[186]. While such methods cannot account for host effects, they offer excellent insight to the mode of action and site of action of the AMP, as well as the opportunity to extract thermodynamic and kinetic parameters of the interaction[187].

3 Results and Discussion

The goals of the work undertaken as part of this thesis were the following:

1. *Development of new methods that can assist in the determination of the mode of action and relevant properties of AMPs to aid in the rational design of new AMPs.*

For this, two methods were developed to assist in understanding specific aspects of the mode of action: WIND-PVPA, an adaption of PVPA, that enables the quantification of ion and water permeability, and a label-free application of MST to determine peptide-lipid binding; these methods are detailed in papers I and II, respectively. Further to this, WIND-PVPA was applied to lulworthinone (paper IV), and to four of the DigiBiotics AMPs that were used in the AMP-MST proof of concept study.

2. *Characterisation of new antimicrobial agents from marine organisms.*

To this end, the structure of two marine natural products were elucidated: lulworthinone, a marine fungal dimeric naphthopyrone, isolated within the DigiBiotics platform, and st-CRP-1, a cysteine rich antimicrobial peptide from a marine ascidian; this research forms the basis of papers III and V, respectively.

4 Modelling AMP mode of action (Paper I-II)

As discussed in the introduction of the models that are used to describe the MOA of AMPs, there are three agreed upon points which are consistent between the main models of membrane disruption (Figure 18):

1. *Binding of AMP to the lipid membrane*
2. *Build up on the lipid membrane*
3. *Leakage across the membrane*

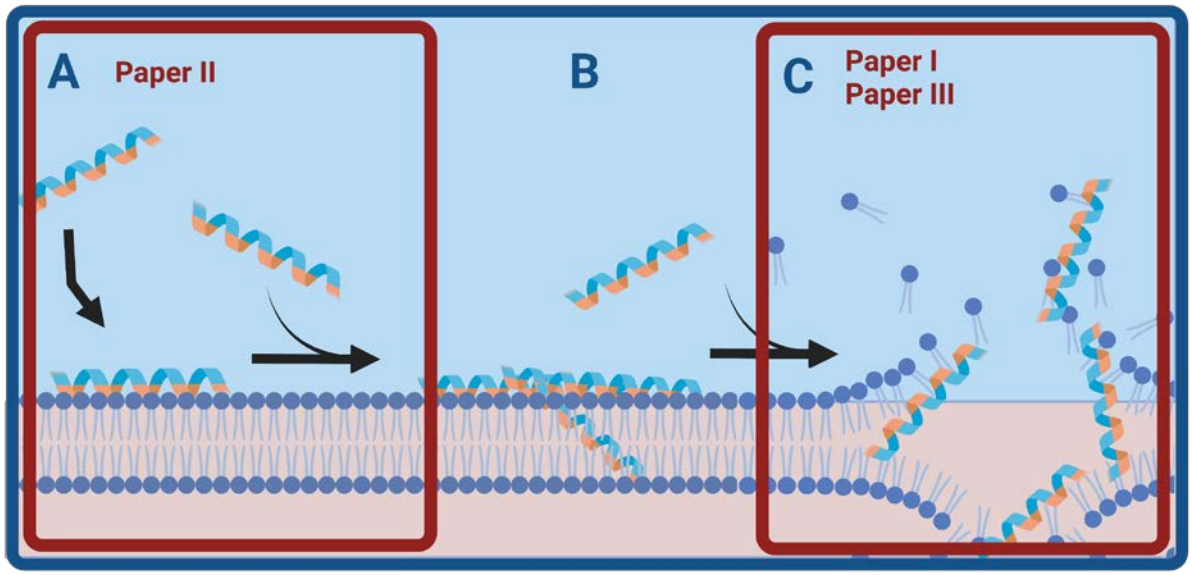

Figure 18:Generalised AMP mode of action highlighting the areas in which this work focuses. A: Initial binding probed in paper II using MST and SPR. C: Disruption of the membrane by assessing leakage using WIND-PVPA.

The main body of the work undertaken in this thesis, and the papers produced, is the development of methods that can quantitatively assess these different aspects of AMP-lipid interactions – specifically points 1 and 3, binding and leakage.

The two methods developed, AMP-MST and WIND-PVPA, share some common features, in that they make use of simplified lipid models – DMPC only for zwitterionic 'host-like' conditions, and a DMPC/DMPG mix as 'bacterial-like' conditions.

4.1 Model design

4.1.1 Lipid selection

The standard lipid composition used for PVPA is a lipid mix known as E80, and is composed of 80% PC lipids with a mixture of fatty acid tails, and 20% of other zwitterionic headgroups, cholesterol and vitamin E that is isolated from egg yolk[188]. This composition is mounted on the cellulose strip initially as two 100 µL additions of 400 nm vesicles that will fill the 600 nm pores of the cellulose, and a final 100 µL addition of 800 nm vesicles on top of the loaded cellulose. The vesicles are immobilised by centrifugation and heating at 50^{o}C. This application of the lipids is typically used to assess uptake of drugs across gastrointestinal barriers, and as such needed to be adjusted to a more bacterial-like model.

To adapt PVPA, firstly, pure DMPC was selected as the inert and zwitterionic species of lipid. No 400 nm vesicles were used to fill the cellulose pores, instead two 100 µL additions of 800 nm vesicles were applied on top of the filter.

The presence of anionic lipids in the bacterial leaflet is key to the selectivity and activity of AMPs as discussed in detail previously. It was therefore imperative that an anionic component was included in both assays. As the WIND-PVPA was developed prior to the MST work, the same lipid compositions were used in paper II to provide consistency. As such, the discussion of the choice of lipid and amount used, will be centred on the applicability towards the PVPA system, and not MST.

4.1.2 Model PG%

One of the first challenges in the adaptation of PVPA to WIND-PVPA was the introduction of vesicles that contained an anionic lipid species, and the loading of the now anionic vesicles onto the anionic cellulose filter. As previously described, the anionic lipid component in

generalised bacterial model membranes can typically account for up to 50% of lipid species, and in bacteria such as *E. coli* approximately 20% of lipid species.

To assess the capacity of the cellulose filter to be loaded with anionic lipids, the electrical resistance and calcein permeability were measured across three lipid compositions using DMPG as the anionic component (50%, 20% and 5% PG), and compared to the DMPC-only composition. The barriers were prepared using the same protocols with the composition of the vesicle stock being the only difference.

Table 1: Summary of results of preliminary tests of the different tested lipid compositions

Composition (DMPC:DMPG)	Calcien P_{app} (10^{-6} cm/s)	Electrical resistance (Ohms x cm^2)
100:0	0.61 ± 0.08	54.23 ± 7.62
95:5	0.49 ± 0.07	53.96 ± 3.16
80:20	1.04 ± 0.12	26.73 ± 7.53
50:50	1.17 ± 0.13	34.16 ± 5.64

Calcein is a good probe for barrier packing due to its hydrophilic nature, and as such, calcein will favour aqueous pathways between the vesicles, rather than moving through the hydrophobic vesicles – through a single bilayer calcein has a P_{app} in the range of 10^{-11} cm/s. The quality criteria for the PVPA barriers typically has calcein P_{app} in the range of 10^{-7} cm/s, and a higher calcein P_{app} indicates poorer packing of vesicles or barrier 'tightness', with more aqueous pathways available. A less tight barrier would also be indicated by a reduced electrical resistance, as ions are able to more freely move across the barrier[145].

The above results showed that a higher proportion of PG results in 'leakier' barriers (Table 1). Visual inspection of the barriers after drying, in preparation for use, showed significant thinning of lipids on the filter, with patches where little lipid appeared to have been immobilised. In contrast, the 5% PG composition yielded satisfactory results in comparison to the DMPC-only PVPA barriers and was therefore selected as the composition for use in the development of

WIND-PVPA. This inability to load vesicles with a higher proportion of anionic lipid species is due to the richly anionic nature of the cellulose filter. The result of this is a negative electrostatic interaction between the anionic lipids and the anionic cellulose, leading to difficulty in the immobilisation of anionic lipids on the filter.

4.2 WIND-PVPA (Paper I)

PVPA is traditionally used to determine the capacity of a drug to permeate across a lipid barrier. With WIND-PVPA, rather than determine the ability of the drug to cross the membrane, the ability of the drug to disrupt the membrane is evaluated. Due to this, the capacity of the AMP to transmit across the barrier is not the primary interest of the assay, so an independent probe was desired.

4.2.1 D_2O

The initial conceptualisation of WIND-PVPA focused on the tracking of water across PVPA barriers. Water was considered to be an ideal probe as in general permeability across the membrane is describing the movement of aqueous components across the hydrophobic bilayer, and by definition would include water. Furthermore, water should be sensitive to small changes in the overall barrier integrity due to its high P_{app} across a lipid bilayer in the range of 10^{-3} cm/s.

To monitor the movement of water, deuterium oxide (D_2O) was chosen. The advantage of using D_2O in combination with NMR is the ability to differentiate between H_2O and D_2O. By having a fixed amount of D_2O in the PVPA donor chamber, and a fixed, lower amount of D_2O in the acceptor chamber, one would be able to monitor an increase in D_2O in the acceptor directly using ^2H NMR.

To maximise the difference between the blank and the positive control (Triton X-100), a range of D_2O:H_2O concentrations were tested, with 80% giving the greatest separation. While 90% or 100% could have been chosen, such concentrations of D_2O would have led to difficulties in

the sample preparation, as concentrated stocks of D_2O-based buffers would have been required. Using 80% D_2O meant that the base buffer stock could be prepared in H_2O, side-stepping the need for larger quantities of D_2O, as well as enabling the use of the same TRIS buffer stock as the base for both the donor and acceptor solutions, all while maintaining a significant portion of the water in the donor chamber as D_2O.

Initial WIND-PVPA experiments did not have any D_2O added to the acceptor solution, i.e. only H_2O was used. The result of this was an inconsistent lock signal for NMR in the samples from earlier time point wells (particularly the 30 second wells), that required manual locking, inhibiting the automated acquisition of data – problematic due to the volume of samples to be run. It was therefore decided to introduce a small volume of D_2O to the acceptor solution (0.5 % v/vol) to allow for the spectrometer lock signal on all samples, enabling the automation of data collection.

4.2.2 Ions

The membrane potential of bacterial cells is vital for many cellular functions, and therefore changes in the permeability of ions that were induced by AMPs was of interest. Furthermore, being able to quantify the ability of AMPs to increase ion permeability across the PVPA barriers may inform the MOA of some AMPs.

The direct detection of a number of ions is possible by NMR through the use of broadband probes - ^{23}Na for example is an NMR active nucleus. However, for many such nuclei the low natural abundance and gyromagnetic ratios mean quantitative analysis can be time consuming or in some cases not feasible, and importantly requires the use of broadband NMR probes.

As direct detection was not possible on the spectrometer to be used, an ion sensitive probe was required - for this purpose ethylenediaminetetraacetic acid (EDTA) was chosen. The disodium salt of EDTA is a hexadentate chelator which can bind dicationic ions in a 1-to-1 stoichiometry. Further to this, when EDTA binds Ca^{2+} or Mg^{2+}, the difference in the size of the ions means there are differences in the conformation of the EDTA-ion complex. These differences in

conformation result in unique chemical shifts for the two complexes[189], which in turn allow for the simultaneous quantification of both Ca^{2+} and Mg^{2+} using ^{1}H NMR (Figure 19).

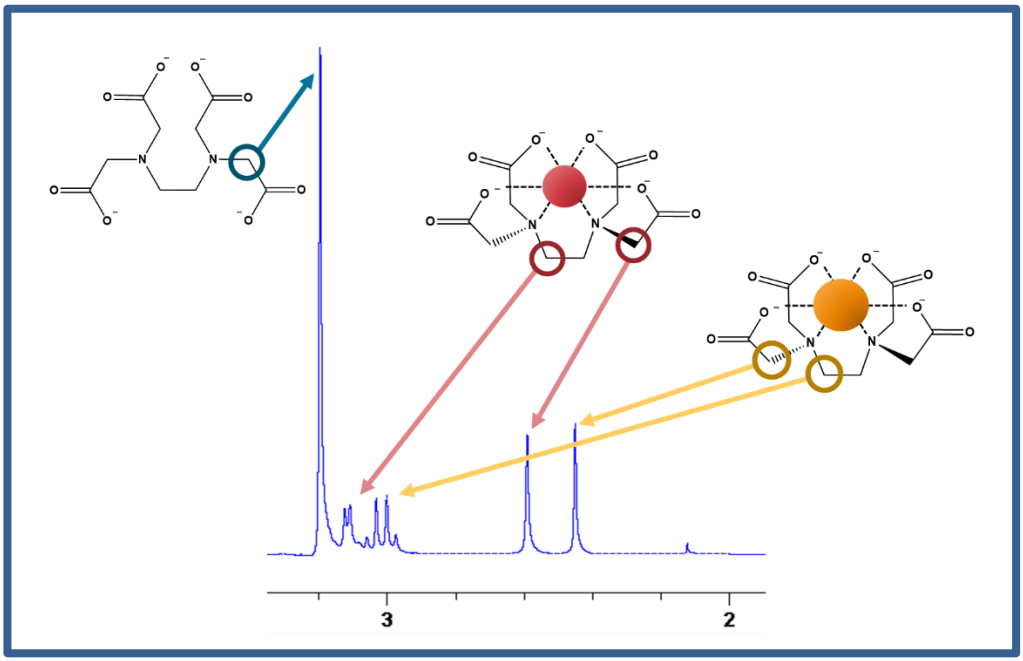

Figure 19: ^{1}H spectrum of Ca^{2+} (yellow) and Mg^{2+} (red) bound EDTA and free EDTA (blue).

To monitor the transmission of ions, the experimental set-up placed 10 mM EDTA in the acceptor chamber, with 100 mM each of $CaCl_2$ and $MgCl_2$ in the donor solution. The high quantity of salt to EDTA ensured that if a small percentage of the ions on the donor-side entered the acceptor, they would be detected while EDTA remained in excess in the acceptor chamber to prevent the competitive binding of EDTA by Ca^{2+} and Mg^{2+} and inhibiting quantification.
One consideration of this experimental setup is the high concentration of salt on the donor compared to the acceptor - 300 mM compared to 120 mM (including counterions of TRIS and EDTA). This difference creates an osmotic pressure towards the donor, making the movement of solutes towards the donor preferable.

The result of the osmotic pressure is that the forward flow (donor to acceptor) must always act against the back flow (acceptor to donor), and that the measured P_{app} will be a result of the average movement of the components, rather than a strict forward only permeability.

4.2.3 Experimental Setup

Two controls are used in the WIND-PVPA experiment: a blank, where no guest molecule is added, and a positive control, Triton X-100 in 2% w/vol. Triton is a detergent, and will solubilise the packed lipid vesicles, readily increasing the apparent permeability of water and ions across the barrier.

The final experimental set-up for WIND-PVPA used the two described controls, along with the guest molecules to be tested, all in triplicate. Each replicate has 12 associated wells which correspond to the time the donor chamber has spent in the acceptor solution. The contents of the donor and acceptor solutions are summarised in Figure 20.

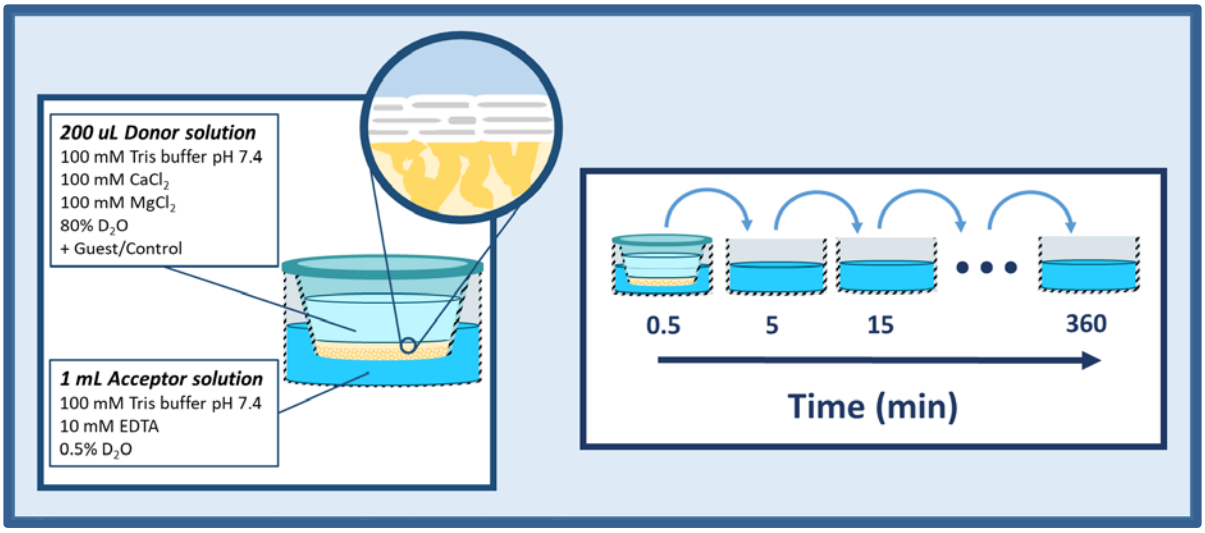

Figure 20: WIND-PVPA experimental overview. Left: Donor and acceptor stock solution contents, and barrier cross-section. Right: Proceedure of moving donor insert from well-to-well.

4.2.4 Peptide:Lipid ratio

In WIND-PVPA, a total of 6 mg of lipid is deposited on a single PVPA barrier giving an approximate 45000 bilayers[1]. The AMP concentration was selected to be 4 mg/mL - equivalent to 0.8 mg added to each PVPA donor chamber.

The overall peptide:lipid (P:L) ratio was typically ~1:10. However, as the PVPA barrier consists of multiple stacked layers, the first layers will be the first available lipids, with the lower layers immediately protected from the AMP and subjecting the first layers to the greatest effect of the AMP– this initial interaction with the first lipid layers can reach P:L of ~15,000:1 per layer.

One of the questions raised over typical leakage assays, such as vesicle leakage assays, is the lack of relevance to MIC testing due to the significantly lower P:L used in such assays. In vesicle leakage assays a typical P:L is 1:100, while in MIC testing the P:L often reaches ratios as great as 1000:1. Therefore, the mechanisms of leakage highlighted by vesicle leakage may not be wholly reflective of the true mechanism that is in effect in MIC assays[25].

While in WIND-PVPA the P:L per layer is higher than MIC testing, the result is that the initial layers of lipid will be exposed to high quantities of AMP that are able to exert a disruptive effect that can increase the transmission of water and ions. In contrast, vesicle leakage is done at a lower P:L ratio, where the results may be indicative of potentially non-biologically relevant modes of action resulting from being underexposed to large quantities of AMP that are present in MIC testing.

[1] This is based on the assumption that no are lipids lost during the immobilization of the lipids, and an even covering of the cellulose filter that is 0.33 cm^2 in area and a DMPC headgroup size of 59.8 $Å^2$ [190].

4.2.5 Results

To show how WIND-PVPA can explore AMP induced changes in barrier integrity, four structurally similar Trp-Arg rich AMPs with a range of activities were selected. These AMPs, along with a blank and triton as a positive control, were run with the two different lipid compositions – pure DMPC and a DMPC/DMPG (5%) mixture – the results of which are summarised in Table 2.

*Table 2: Summary of P_{app} determined for all tested guest molecules in PVPAs with both lipid compositions. * Conducted in the absence of $CaCl_2$ and $MgCl_2$ - No increase observed relative to the blank*

Peptide	MIC (µg/mL)	DMPC (P_{app} x 10^{-6} cm/s)			DMPC/PG (P_{app} x 10^{-6} cm/s)		
	S. Aureus	Ca^{2+}	Mg^{2+}	D_2O	Ca^{2+}	Mg^{2+}	D_2O
KP-76	145	3.5 ± 0.7	4.3 ± 0.8	71 ± 4.9	3.7 ± 0.3	4.0 ± 0.3	94 ± 2.0
AMC-109*	2	-	-	63 ± 0.6	-	-	84 ± 1.2
cWRWRWR	4	3.9 ± 0.9	4.9 ± 1.0	74 ± 4.7	10.2 ± 1.3	10.2 ± 1.3	104 ± 3.9
RAR	-	4.0 ± 0.7	4.9 ± 0.7	78 ± 4.2	3.4 ± 0.1	3.7 ± 0.1	87 ± 0.8
Triton	-	11.3 ± 2.0	12.9 ± 2.5	109 ± 5.3	13.5 ± 1.5	14.5 ± 1.5	132 ± 2.1
Blank	-	3.8 ± 0.9	4.7 ± 1.0	78 ± 5.9	3.5 ± 0.4	4.0 ± 0.4	88 ± 3.1

The results show that using WIND-PVPA, one can demonstrate the impact of general membrane disrupting compounds such as triton, but more importantly that of AMPs. Using WIND-PVPA, one can show the selective influence of AMPs such as WRWRWR, which has no demonstrable effect on the DMPC barrier, but once DMPG is included in the lipid barrier, can exert an effect that is comparable to Triton. Additionally, the effects of a more modestly active AMP such as KP-76 can also be demonstrated, highlighting that WIND-PVPA is not just limited to the most active AMPs.

Interestingly, AMC-109, despite being known to be membrane disruptive and currently in clinical trials as an antimicrobial agent[191], has no measurable effect relative to the blank. It is important to note that AMC-109 was not readily soluble in the high concentration of salt that

is used for the donor solution in the current iteration of WIND-PVPA. However, of note in the *in silico* studies that accompany the experimental method, it was identified that AMC-109 exhibited aggregatory behaviour similar to the hypothesised behaviour described by Bechninger and Lohner for the detergent model of AMP behaviour[111].

With regards to the P_{app}s that are determined by WIND-PVPA, they appear at odds with the known permeabilities of water (~80 $x10^{-6}$ cm/s vs 1 $x10^{-3}$ cm/s) and ions (4 $x10^{-6}$ cm/s vs 1 $x10^{-12}$ cm/s) through a single lipid bilayer, suggesting that water is moving slower than expected, but ions move faster. As such, some considerations of the experimental setup of WIND-PVPA need to be made. The PVPA barrier consists not of a single bilayer, but many thousands of vesicles packed onto one another, with potential aqueous pathways between the vesicles. Therefore, the water must move through these many bilayers, but also through any aqueous pathways that are present. Furthermore, as there is no concentration gradient for water, the P_{app} is determined as changes in the average movement of D_2O from the donor into the acceptor solution, where it must act against the osmotic pressure that favours the movement from the acceptor to the donor.

With regards to the movement of ions, one can consider calcein, which is expected to travel only through the aqueous pathways (as previously noted), and was observed to have a P_{app} of 0.6 $x10^{-6}$ cm/s. In comparison Ca and Mg ions measured a P_{app} of 4-5 $x10^{-6}$ cm/s, i.e. an order of magnitude faster. This would be consistent with a smaller ion being able to move through the same pathways as calcein, as opposed to moving through the thousands of bilayers that make up the PVPA barrier.

It is ultimately difficult to truly discern the actual mechanism by which the water and ions move across the barrier - it is likely a combination of trans-bilayer and aqueous pathways - rather the average transport across the barrier is observed. Despite this, and importantly, one can discern between the effects of disrupting molecules as previously noted; this highlights that, while the understanding of the transport remains imperfect, the mechanism by which the transport occurs is limited by the packed lipid vesicles. This in turn can be disrupted by membrane active compounds such as AMPs and detergents.

4.2.6 WIND-PVPA using E80 lipids

PVPA has been shown to be an accurate model of mammalian drug absorbance when using E80 lipids[147, 192]. It was therefore of interest to use E80 lipids for WIND-PVPA, using the same PVPA barrier preparation as the original PVPA assay (i.e. smaller preparation of liposomes to fill the cellulose pores, and larger liposomes immobilised on top), and the capacity to add 5% DMPG to the E80 lipid composition was tested. For this purpose, the two PVPA barrier preparations that were produced had similar calcein P_{app} in the range of 0.06 x 10^{-6} cm/s – a ten-fold reduction in P_{app} compared to the barriers used in paper I (previously shown in Table 1).

For this application, four AMPs from a library of peptides produced within the DigiBiotics pipeline were chosen. These AMPs were of interest due to their activities and similarity in structure – all are cyclic hexapeptides that contained 3 Trp residues and either 3 Lys or Arg residues that are arranged in a 'clumped' or 'alternating' sequence (the activities and sequences are summarised later in Table 3). The WIND-PVPA was performed in the same fashion as described in paper I and the results of which are summarised in Figure 21

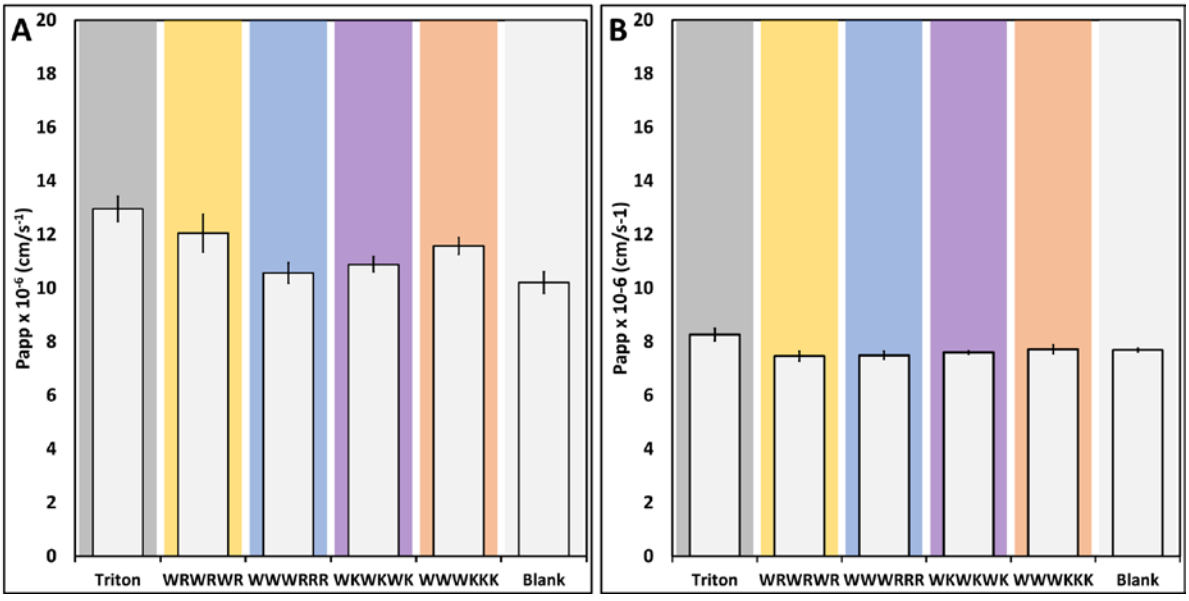

Figure 21: WIND-PVPA D2O results using E80 lipids. A: E80 only. B: E80 with 5% DMPG.

Of note, a lower P_{app} is observed correlating to the 10 fold decrease in calcein P_{app} relative to the WIND-PVPA experiments using the DMPC/DMPG PVPA barriers described in paper I – further demonstrating the dependence of the P_{app} determined on the initial barrier tightness.

There is also a significant reduction in the P_{app} of D_2O for all tested guest molecules, and the blank in the PG-containing composition, indicating that the overall tightness of the barrier is greater. This is ultimately inconsistent with previous findings and as such requires further exploration so as to determine the root cause.

While the zwitterionic E80 results for WRWRWR are inconsistent with paper I (i.e. a significant effect of WRWRWR is observed while in paper I no effect was observed on the zwitterionic DMPC barriers), it must be noted that the E80 lipids have a very different lipid tail composition in comparison to pure DMPC, and that 20% of the headgroups are not PC. In addition, there is also a difference in fatty acid tail composition – E80 fatty acid content is ~25% oleic acid (per manufacturer data sheet) – which will change the phase of the lipids, due to the presence of lower melting point species, to a more disordered phase. As disordered lipid phases are preferable to AMPs[193], this may result in the ability of WRWRWR to interact with and disrupt the integrity of the barrier more readily. Furthermore, as the barriers used here are much tighter (0.06×10^{-6} vs 0.6×10^{-6}), there may be a greater differentiation in effect between the AMPs tested and the blank.

While the E80 lipid composition is suitable WIND-PVPA, particularly as a more representative eukaryotic model than pure DMPC, the limited exploration with including PG suggests that the E80 mixture may not be compatible with the inclusion of anionic lipids.

4.2.7 PVPA Summary

The current WIND-PVPA serves as an introduction to a novel method of quantifying changes in water and ion transmission in the presence of membrane active compounds, and to this end it is successful. As noted, by the introduction of anionic lipid species, WIND-PVPA can demonstrate the selective nature of AMPs, and this effect can be shown for even modestly active species, while inactive AMPs exert no influence on the permeability of ions. Furthermore, as a base platform to build from, there are several areas where the method can be expanded to be a more robust and biologically relevant assay - WIND-PVPA offers an excellent platform for further development.

Developments can be considered in one of two ways: more representative lipid compositions, and more representative ions. Considering the lipids, the mixture of DMPC and DMPG is useful as a simple model to express the importance of anionic lipids, but it is ultimately lacking as a robust and representative model of bacterial membranes, both in terms of head group composition, and lipid-tail composition, but also there is an absence of LPS or LTA that are found in gram-negative and gram-positive bacteria, respectively, amongst other species. Equivalent points can also be raised for pure DMPC being a poorly biologically relevant model of mammalian cell membrane. With regards to the ions used, while Mg^{2+} and Ca^{2+} are important ions in the physiology of cells, they are not as ubiquitous as Na^{+} and K^{+} in the cytoplasm[194].

The quantification of Na^{+} and K^{+} is not feasible with EDTA, however by using kyrptofix-2,2,2 as a chelator instead, it is possible to quantify both Na^{+} and K^{+}, as demonstrated in Figure 22.

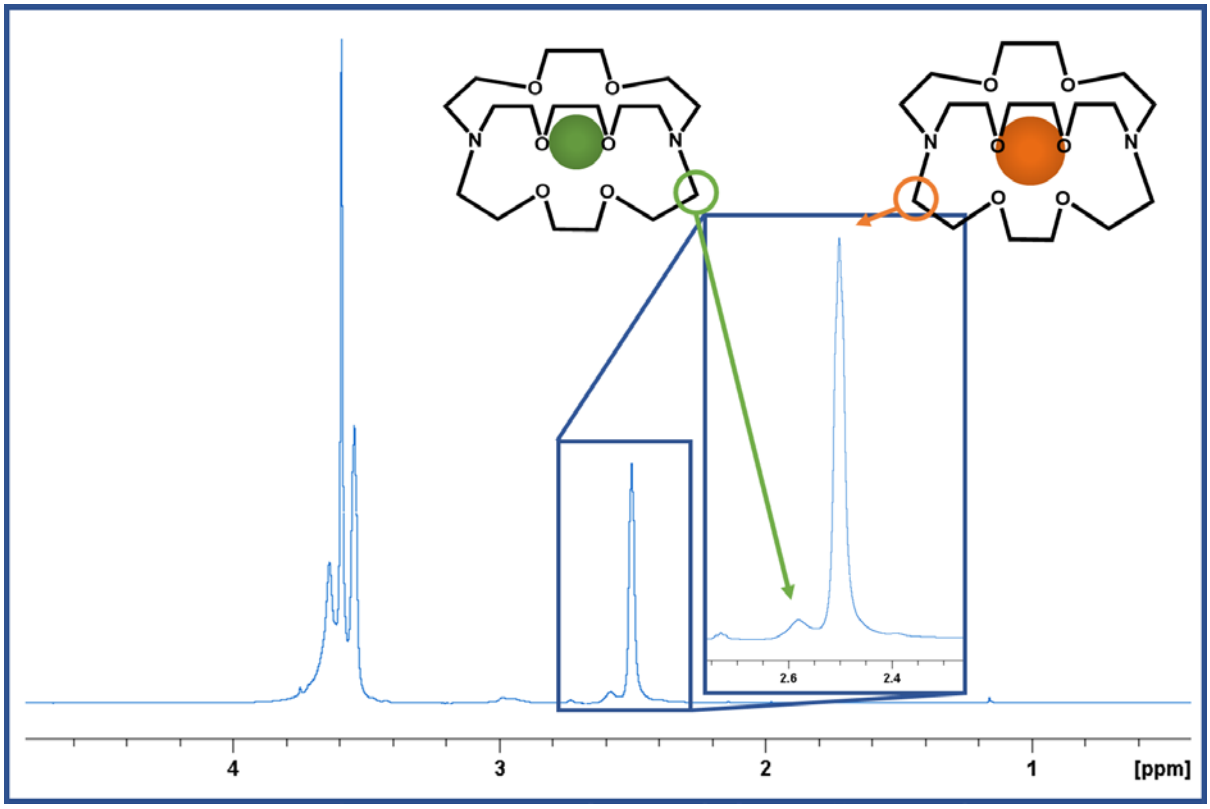

Figure 22: ^{1}H NMR spectra demonstrating the use of kryptofix-2,2,2 as a chelator of Na^{+} (green) and K^{+} (orange) ions.

The results obtained show that while it is possible to simultaneously quantify both Na^{+} and K^{+}, Na^{+} presents a broad peak. This is due to the presence of Na+ as the counter ion to the TRIS

buffer currently used. However, when conducted in the absence of TRIS (and as a result excess Na^+), the Na^+ peak presents as a sharper, more accurately quantifiable peak. While this poses an issue for the simultaneous quantification of Na^+ and K^+ under the current standard WIND-PVPA conditions, the simultaneous measurement of ions likely yields redundant data, as the ions will favour aqueous pathways through the PVPA barrier and are of a similar size. To wit, one ion would suitably describe the pathways for all similar ions. An alternative for further probes that would yield more unique data, would be the use of fluorine containing small molecules such as sugars.

4.3 Binding (Paper II)

Binding was identified as one of the more important aspects of peptide-lipid interactions to be further explored. To this end, MST was identified for its potential applicability to peptide-lipid binding. As previously noted in the introduction to the MST method, MST has been applied to peptide-lipid interactions using labelled AMPs, however in this work the key differentiator is that MST is presented as a label-free method. Further to this, the work is a novel use of SMA-nanodiscs, with the previous method using only vesicles, and is the first demonstration of MST being used to extract the partition coefficient K_P of AMPs.

4.3.1 Label-free

In the procedure described by Yu et al., they investigated the binding of a 13-residue AMP named L-RW, that they covalently attached the fluorescent label FITC to. In the work, they investigated the binding of this label on its own and found that FITC does not interact with lipid vesicles, thus concluding that as FITC on its own does not interact, it will not influence the binding of L-RW[45]. However, despite these assertions, the presence of larger hydrophilic labels such as FITC has been shown to impact the binding properties of molecules to which they are attached[195].

As part of the DigiBiotics platform, the focus was placed on cyclic hexapeptides that are rich in tryptophan and arginine. The presence of Trp in these peptides has an advantage, as not only does the Trp-rich nature of the peptides increase the amphipathic properties of the AMPs, but it also gives the AMPs intrinsic fluorescence that can be exploited for fluorescence-based methods such as MST, without the need for labelling.

The four AMPs selected had been previously used for the assessment of E80 lipids in WIND-PVPA. In addition to these four, a fifth AMP with no observed activity was included, which due to its low activities was expected to have a low binding capacity (Table 3).

Table 3: Summary of the peptides used to assess the use of MST for investigating peptide-lipid interactions. The peptides are accompanied by their activities towards E. coli and S. aureus, as well as a summary of overall charge and number of hydrophobic residues.

Peptide Sequence	MIC (ug/mL)		Overall charge	Hydrophobic residues
	E. Coli	*S. aureus*		
cWWWRRR	8	4	+3	3
cWRWRWR	32	32	+3	3
cWWWKKK	8	32	+3	3
cWKWKWK	64	128	+3	3
cLWwNKr	>250	>250	+2	2

To establish the usability of MST in exploring peptide interactions, the bindings of the chosen peptides were determined for zwitterionic and anionic lipid compositions, using both MST and SPR[1]. The lipid compositions were chosen to match those that had previously been selected for WIND-PVPA: pure DMPC and DMPC:DMPG (5%). Two sets of data were acquired using MST, one set using lipids solubilised as SMA nanodiscs, and a second with the lipids solubilised as vesicles. The further acquisition that was done using SPR was achieved using standard procedures that utilised vesicles.

[1] SPR was used as a more established method to which the evaluated bindings could be compared.

4.3.2 K_D from MST

K_D is a parameter that is readily accessible by MST for the traditional use of the instrument, and the purpose for which it is designed, and as demonstrated in a labelled manner by Yu et al., can be obtained for AMPs[45]. This was therefore the first parameter that was assessed in the label-free method. As per best practices the T-jump region of the MST trace was evaluated to obtain K_D[127] for both vesicles and SMA-nanodiscs – the results of which are summarised in Table 4.

Table 4: Summary of K_D extracted using SPR and MST.

Peptide	SPR K_D (μM)		Vesicle K_D (μM)		SMA K_D (μM)	
	PC	PC/PG	PC	PC/PG	PC	PC/PG
LWwNKr	2548 ± 493	1033 ± 58	670 ± 56	650 ± 123	3.1 ± 0.2	6.0 ± 1.3
WKWKWK	712 ± 27	474 ± 45	282 ± 58	112 ± 29	4.0 ± 0.2	6.0 ± 0.2
WRWRWR	318 ± 62	105 ± 7.0	73 ± 53	24 ± 6.8	1.4 ± 0.2	2.6 ± 0.3
WWWKKK	302 ± 32	112 ± 15	28 ± 2.9	17 ± 13	4.6 ± 2.1	4.3 ± 1.4
WWWRRR	142 ± 35	70 ± 1.2	21 ± 2.8	10 ± 4.6	0.90 ± 0.5	3.0 ± 1.1

In the vesicle MST and SPR derived K_Ds, the results demonstrate the known impact of anionic lipids on binding, with a reduction in K_D when anionic lipids are included. The vesicle based SPR and MST sets of results produce a generally consistent ranking of the AMPs, which bear similarities to the observed MIC results. The AMP with no observed antimicrobial activity, LWwNKr, was shown to have the weakest binding, while the peptides with the greatest activity, WWWRRR, WWWKKK, and WRWRWR, were shown to be the strongest binders; notably, WRWRWR was shown to have the greatest decrease in K_D (approximately threefold reduction) when PG was included. As such, while the absolute value of K_D differs between the vesicle and SPR methods, the relative relationship between the AMPs is generally maintained, and the deviation in absolute value is likely down to differences in experimental differences between the methods – principally, differences in the availability of lipids in solution and those bound

on an SPR chip, and the lipid concentration being varied in MST, versus the AMP concentration being varied in SPR.

The SMA-MST results show a significant deviation from the other two methods, with much lower derived K_Ds and poor differentiation between the AMPs. This is best demonstrated in the case of DMPC/PG nanodiscs where a difference of only ~3 μM is observed between the weakest peptide, LWwNKr (6 μM), and the strongest, WWWRRR (3 μM). The SMA results also further diverge from the other methods, with a modest increase in K_D observed when PG lipids are included, at odds with general expectations. This disagreement cannot be reasonably explained, unless the AMPs are binding to the SMA, as previous uses of nanodiscs to assess the binding of AMPs has shown a clear preference to anionic containing lipid compositions[134, 1]. As such, this warrants further examination of the use of SMA-nanodiscs in MST, and potentially reacquisition of data.

4.3.3 K_P from MST

K_P, as described earlier, is the propensity of a given molecule to favour a lipidic environment over an aqueous one. One of the principal methods through which K_P is determined, is through the changes in fluorescence intensity of a fluorophore as it transitions into a hydrophobic environment. This is often done in the presence of increasing lipid concentration, and as the molecule goes into the lipid environment; the resulting changes in quenching affect the fluorescence intensity from which K_P can be derived, using Equation 7 (repeated below for convenience).

$$I = \frac{I_0 + K_P \gamma_L [Lipid] I_L}{1 + K_P \gamma_L [Lipid]}$$

[1] Importantly, in this study circularised MSP nanodiscs are used, so this does not rule out the possibility of SMA-AMP binding.

MST measures changes in fluorescent intensity to gauge the thermophoretic properties of a complex, and this is generally reported as the MST response (F_{Hot}/F_{Cold}); however, the initial fluorescence intensity of the complex is also reported before the application of the IR laser. Therefore, the ability to extract K_P using the MST reported fluorescence intensity was explored using both SMA-nanodiscs and vesicles.

Table 5: Summary of K_P extracted using SPR and MST.

Peptide	SPR K_P		Vesicle K_P		SMA K_P	
	PC	PC/PG	PC	PC/PG	PC	PC/PG
LWwNKr	278 ± 8	401 ± 19	126 ± 2	188 ± 11	3845 ± 251	2444 ± 150
WKWKWK	531 ± 10	630 ± 33	78 ± 55	396 ± 192	522 ± 45	202 ± 179
WRWRWR	1299 ± 94	3160 ± 146	706 ± 472	1458 ± 785	1667 ± 464	2589 ± 279
WWWKKK	2534 ± 80	5156 ± 341	836 ± 121	1498 ± 211	6207 ± 930	5940 ± 1374
WWWRRR	6649 ± 799	12705 ± 164	3158 ± 1232	3441 ± 749	7367 ± 1671	10351 ± 4304

The extracted initial fluorescence values were normalised on the fluorescence of the AMP in an aqueous environment[1], and plotted against lipid concentration to yield a hyperbolic partition curve that is characteristic of the fluorescent assessment of K_P[123]. This plot was fit to a modified Equation 7 (Equation 8 in paper II) to obtained K_P. K_P could be extracted for all AMPs in the presence of both SMA-nanodiscs and vesicles. These values were then compared to the SPR derived KPs which are summarised in Table 5.

In general, a similar ranking of the AMPs was obtained relative to the more established SPR. In the case of the vesicular MST K_Ps, this ranking was the same with the exception of WRWRWR. This difference was caused by a broad range of K_P that produced a large error. However, with regards to the SMA derived K_Ps, there are several inconsistencies especially for LWwNKr, where it appears to be overestimated relative to the other AMPs and compared to

[1] Measured as the initial fluorescence of the AMP in the absence of lipids.

the vesicle and SPR derived K_Ps. Additionally, a reduced K_P for LWwNKr when PG is introduced was observed when using nanodiscs. Otherwise, the SMA derived K_Ps compared more favourably to those obtained by SPR. However, a general trend of the MST derived K_Ps having larger errors in comparison to the SPR derived K_Ps was observed.

The use of both vesicles and SMA-nanodiscs has drawbacks that make the determination of K_P more error-prone using MST. Vesicles, when in high concentrations, are a cloudy suspension which produces light scattering effects that interfere with the fluorescence measurements. While this is not an issue for the determination of K_D[1], it can influence the determination of K_P. Similar issues are also observed with SMA-discs. While this does not interfere at low lipid concentrations where there is little to no light scattering, and therefore doesn't prevent the extraction of K_P, as the lipid concentration increases, the interference can be a dominant factor and can produce poorly representative fits without the removal of later points.

Solutions for both issues can be considered for further work. With regards to the vesicles, smaller vesicles could be produced, which should result in a diminishing of the cloudy suspension; it is worth noting, though, that this would also present drawbacks, as fusion of the vesicles would occur at a faster rate, reducing the stability of the vesicles that could impact reproducibility, while the increase in curvature stress could influence the binding of the AMPs[120].

4.3.4 SMA vs Vesicles

One of the aims of paper II was to compare the suitability of nanodiscs and vesicles to assess the binding properties of AMPs. Immediately apparent from the obtained bindings and partition coefficients is that the use of SMA discs produced much lower K_Ds for all peptides in the low µM range and greater K_Ps.

[1] The change in the MST response occurs before the cloudiness of the samples is noted and is thus not a significant influence.

This contrasts with the bindings obtained when the lipid compositions are solubilised as vesicles, where a far greater range of K_D is seen, varying from ~700 µM to ~20 µM, a 30-fold difference, for LWwNKr and WWWRRR binding, respectively, to DMPC. This range is more in line with the binding data acquired using SPR, where the range of K_D for DMPC lipids is 2500 µM to 140 µM.

One consideration of nanodiscs is that, although they are more planar in nature than vesicles, they exhibit phase heterogeneity across the disc, as noted previously. The inner lipids of nanodiscs are in a more ordered phase compared to the outer lipids (those that are closest to the belt molecule) that are more disordered due to interference from the styrene moieties in SMA, and the formation of the nanodisc causes a reduction in the melting point of the lipids. As the disordered phase of the outermost lipids is favourable to AMPs, this could be a driving factor behind the preferable interaction and grouping of AMPs in this area of the nanodisc[193]. A further difference between nanodiscs and vesicles is the availability of both sides of the lipid bilayer to AMPs; in vesicles the inner leaflet is protected inside the vesicle, where it is inaccessible without the AMP first moving across the bilayer and into the core of the vesicle - this would allow for a greater area of disordered lipids to be available. The presence of a more favourable phase of lipids could therefore be a factor in a stronger interaction of AMPs to nanodiscs than vesicles that is observed by MST, and could result in weaker peptides having the capacity to more readily bind. This could also be enhanced by the presence of the anionic maleic acid groups that are in the SMA polymer, which will likely have electrostatic interactions with the cationic AMPs – and would likely explain the poor differentiation between the zwitterionic and anionic lipid compositions, and stronger interaction of LWwNKr.

The findings of paper II require further elaboration to further determine the suitability of SMA-nanodiscs. In one instance, the use of different polymers could be explored to remove the acidic moiety. SMAd-A and SMA-QA could be potential alternatives, as the maleic acid is transformed to a malimide[174, 196], however in both cases, the resulting polymers are cationic, and may hamper interactions with the lipids.

4.3.5 MST advantages

MST has several key advantages over many comparable methods, namely the sample required, and speed and ease of use. As a direct comparison to SPR, which takes a day to yield binding data in triplicate (albeit more in depth), as well as considerable time needing to be dedicated to optimisation and chip coverage, K_D and K_P can be determined within an hour using MST. Other methods such as NMR often require labelling of one or more components in the binding, which have been demonstrated with this work to not be necessary with MST.

Furthermore, MST has been demonstrated to be suitable to the single-point screening of libraries of compounds, and has been shown to be automatable, giving additional encouragement to the further development of MST approaches towards evaluating peptide-lipid binding[197, 198]. MST is therefore promising as a fast and sample-efficient method to screen libraries of AMPs for hits/leads, as well as facilitating the possibility of closely assessing the structure activity relationship with binding, as it relates to membrane disruption.

4.3.6 MST concluding remarks

The presented work is a novel demonstration of the capacity of MST to determine the binding of AMPs to lipid models in a label-free manner and highlights the differences in results that one can obtain across different lipid model systems. To this end, it was shown through the use of vesicles that one can extract bindings which correlate well with the more established SPR, and that bindings show a strong correlation with MIC. As such, the combination of the speed of data acquisition using MST and the correlation of binding with activity, and the further use of MST as a screen to give further insight to AMP activity, appears promising. The noted difference between the bindings obtained when using the different models also highlights the need for further study of the applicability of different model membrane systems to the study of peptide-membrane interactions.

The label-free application of MST to peptide-lipid binding is not without limitations. Most importantly, the method relies on the presence of Trp. While to a degree this is not an issue – a majority of AMPs contain at least one Trp residue, as discussed in the introduction – it does

mean that a not insignificant number of AMPs cannot have their lipid bindings examined by this method; furthermore, and just as significant to note, is that any non-peptidic membrane disruptive compounds cannot be examined by this method. This reliance on Trp also means that the AMP must remain at a fixed concentration; therefore, the impact of the increasing concentration of AMP cannot be properly probed using label-free MST, potentially missing any aggregatory behaviour of the AMP that may influence activity and selectivity.

4.4 Combination of MST and WIND-PVPA

A promising aspect of papers I and II is that they evaluate different aspects of AMP membrane disruptive activity as highlighted in Figure 18, and as such they can yield complementary data to one another about how binding can influence disruption, as well as how such properties relate to their antimicrobial activities.

To highlight this, an examination of the E80 WIND-PVPA results of the four cyclic AMPs can be done in combination with the binding data collected in paper II, resulting in some interesting trends. Some caveats must be first noted: the lipids used are not directly comparable (E80 for WIND-PVPA and DMPC/PG for MST), there is an absence of reliable WIND-PVPA anionic lipid results for this set of AMPs, and LWwNKr was not used in the WIND-PVPA study. However, despite these caveats, some interesting trends can be observed.

*Table 6: Summary of results of the peptides studied by both MST and WIND-PVPA, and their activities. KD and KP are taken from the vesicle derived MST values shown in Table 4 and 5. *ΔP_{app} is blank adjusted.*

Peptide	MIC (ug/mL)		K_D (µM)		K_P		ΔP_{app} (cm/s)*	
	E. Coli	*S. aureus*	PC	PC/PG	PC	PC/PG	PC	PC/PG
cWKWKWK	64	128	282 ± 58	112 ± 29	78 ± 55	396 ± 192	0.67 ± 0.5	N/A
cWRWRWR	32	32	73 ± 53	24 ± 7	706 ± 472	1458 ± 785	1.84 ± 0.8	N/A
cWWWKKK	8	32	28 ± 3	17 ± 13	836 ± 121	1498 ± 211	1.36 ± 0.5	N/A
cWWWRRR	8	4	21 ± 3	10 ± 5	3158 ± 1232	3441 ± 749	0.35 ± 0.6	N/A

In the results summarised in Table 6, paper II showed that WWWKKK and WRWRWR are both good binders; it was also demonstrated that they have significant disruptive effect on the E80 PVPA barriers. These two peptides also have reasonable MIC values, one rationale for this is that they possess a membrane lytic MOA, where upon binding they are able to lyse the membrane, resulting in an increase in permeability across the cell wall.

In contrast to this, WWWRRR is identified as being the strongest binder with both the lowest K_D and highest K_P, and is shown to be the most active of the AMPs tested. Despite this, it demonstrated a modest disruptive effect that is within the error of the blank in WIND-PVPA. This poses an important question: is the E80 WIND-PVPA barrier an accurate representation of eukaryotic lipid membranes? If the answer to this is that it is accurate, then one could take this as a demonstration of WWWRRR's inability to disrupt host-like membranes, despite being able to bind well to them. Alternatively, it could be indicative of an overall inability of WWWRRR to disrupt membranes. In such a case, the combination of good activity with strong binding and without a disruptive effect may indicate that WWWRRR has an internal mode of action, and that it binds only to transition into the cell. Unfortunately, it is difficult to delineate between these two cases without complimentary anionic lipid containing WIND-PVPA data. An alternative that would not be identified by WIND-PVPA, is that the mechanism of WWWRRR relies upon membrane bound proteins to exert its effect, such as the structurally similar cWFW, or thanatin and attacin.

Regardless, while this is a limited set of AMPs, it does highlight the possibilities in the combination of WIND-PVPA with MST (or other methods of determining bindings) alongside MIC data to give a greater insight into the mode of action of AMPs, and the potential to distinguish membrane disruptive AMPs and AMPs with other MOAs that may not be clear by using only one of the methods in isolation.

Ultimately, with a broader selection of AMPs with known activities, these methods combined could be further used in concert with derived 3D structures to greater rationalise the conformations of AMPs and their resulting impact on activity; this in turn would make it possible to determine a true structure-activity relationship, rather than a sequence-activity relationship, and help in the rational design of AMPs.

5 Structure Elucidation (Papers III-V)

In the search for new antibiotics (and new pharmaceutical agents in general), natural products are a vital resource that has inspired a host of approved drugs[199]. The discovery therefore of new natural products is an important step in the drug discovery pipeline, not least in terms of antimicrobial agents, where discovery of novel agents has slowed down considerably.

As a result, the structure elucidation of natural products is another important cog in the drug discovery process, whereby the knowledge of the structure of new natural products is needed in the rationalisation of their activity, and for potential diversification towards greater activity.

One of the stated goals of this project is to aid in the structure elucidation of new antimicrobial natural products, and the work presented henceforth describes the elucidation of two natural products with stated antimicrobial activities: lulworthinone and st-CRP-1, in papers III and V, respectively. Additionally, the application of WIND-PVPA towards the determination of the MOA of lulworthinone is described in paper IV.

5.1 Lulworthinone (Papers III-IV)

5.1.1 Structure Elucidation (Paper III)

A marine fungus of the Lulworthiaceae family was isolated from driftwood found in Kongsfjord, Norway. Extracts from the cultures of the fungus were tested for bactericidal activity and identified an active fraction in which the main peak had a HIRES $[M+H]^+$ m/z of 741.22, equivalent to $C_{37}H_{41}O_{14}S$ – lulworthinone.

An initial preparation of lulworthinone was purified by preparative HPLC on a gradient of water and acetonitrile with 0.1% formic acid. While this purification proved difficult resulting from the binding of lulworthinone to the column, it none the less yielded enough lulworthinone for

structure elucidation. The resulting sample of lulworthinone was dissolved in DMSO-d6 for NMR, and determined to be of 80% purity by ^{1}H NMR (Figure 23).

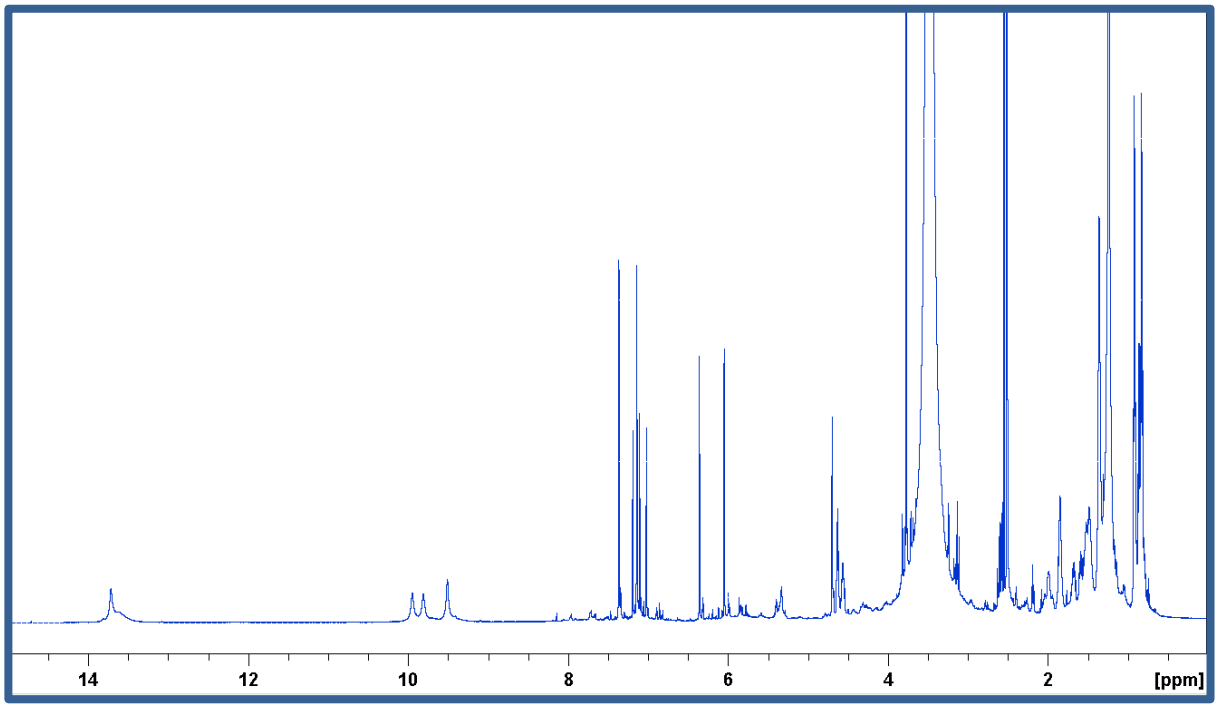

Figure 23: ^{1}H NMR of the initial preparation of lulworthinone.

All 37 carbons could be identified through ^{13}C NMR and showed lulworthinone to have a rich aromatic system with a number of aliphatic signals. Further analysis of the ^{1}H spectrum showed there to be five OH protons, four of which were aromatic, and an abundant aliphatic region. Through HSQC, HMBC and TOCSY, COSY and HMBC experiments, two napthopyrone moieties can be identified along with two five-membered aliphatic chains. These chains could be identified as being connected to the 10 position of the napthopyrones.

The linkage between the napthopyrones was identified by a weak four bond HMBC between the 8 and 5 position of the two fragments. Two of the OH protons could be unambiguously assigned, and two could further be ambiguously assigned to the third position of the napthopyrones based on chemical shift. The deshielded nature of the shift (~14 ppm) suggested the participation in hydrogen bonding, and the C=O at position 2 of the napthopyrone would be an ideal hydrogen bond acceptor. This left an ambiguity in the assignment of the final OH, and the SO_4 group, identified by MS, in the 9’ or 4 position of the second napthopyrone. Due to the absence of NOEs between the protons in this region and the OH, which would be expected if

the OH was attached at this position, it was determined that the SO_4 was in position 9', with the remaining OH at position 4 (Figure 24).

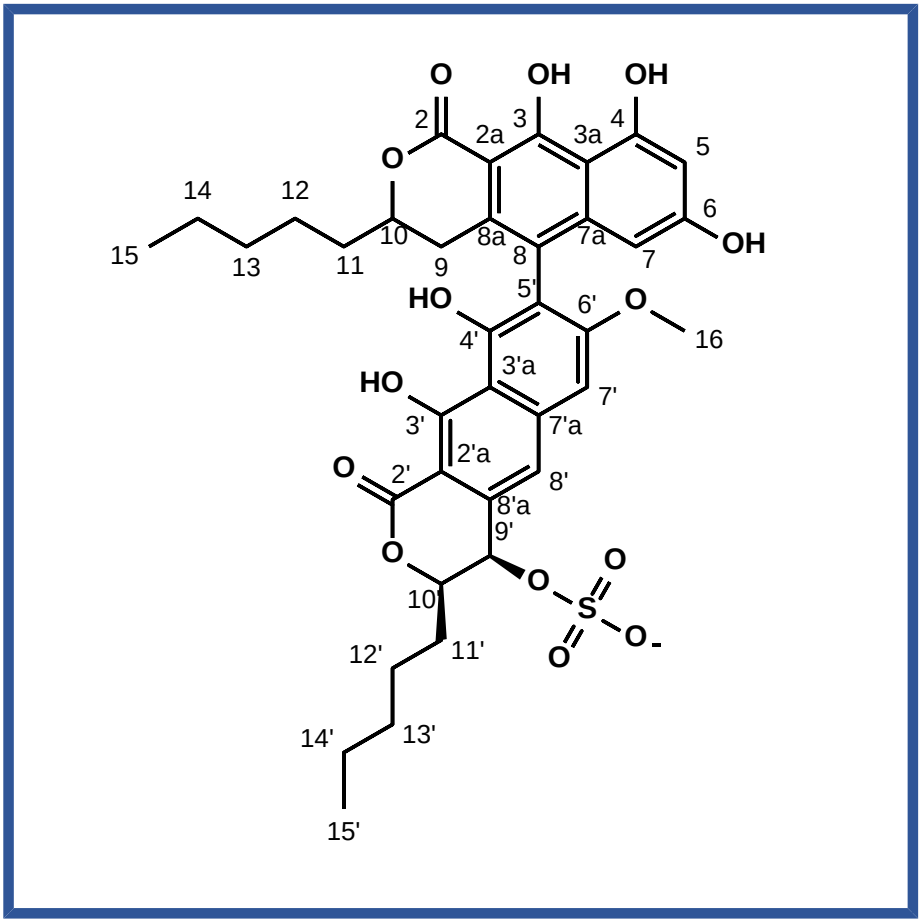

Figure 24:Structure of the first preparation of lulworthinone

Due to the difficulties in the initial isolation of lulworthinone using HPLC, another isolation was prepared using flash chromatography with a water:methanol solvent mix. Lulworthinone was identified in the 100% methanol fraction. Notably, during this preparation lulworthinone was not exposed to any acid.

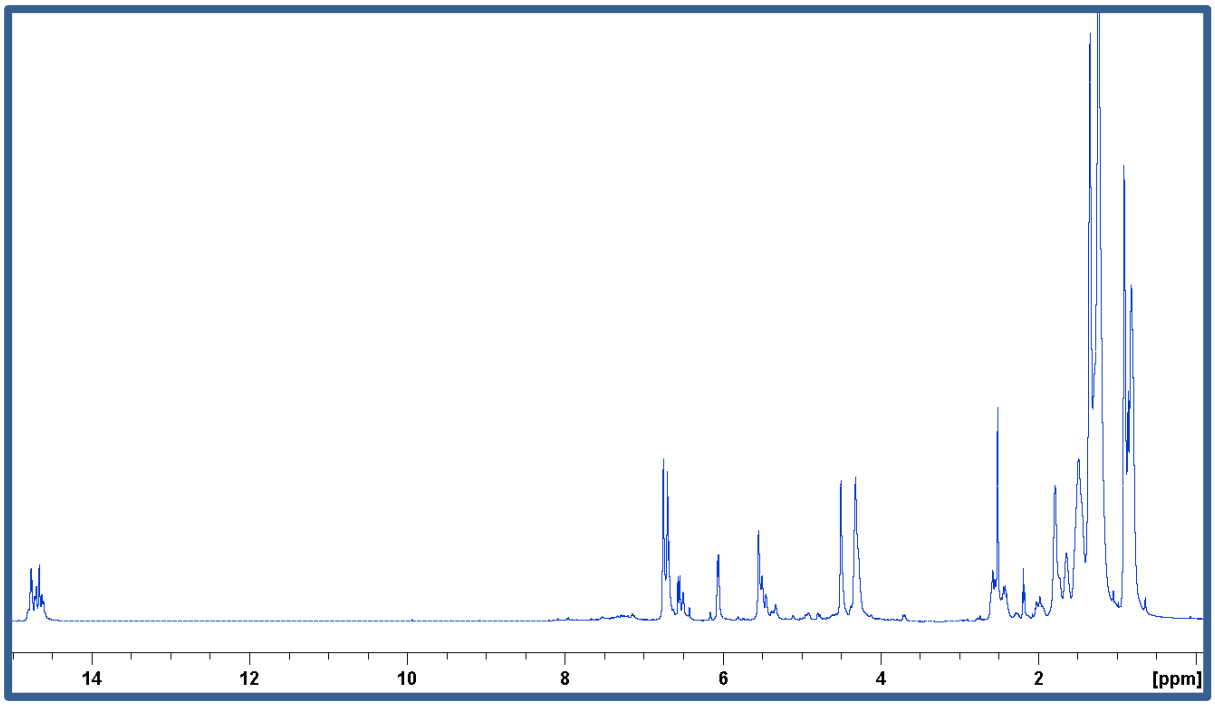

Figure 25: ^{1}H spectrum of the second preparation of lulworthinone.

Initial ^{1}H NMR showed significant deviations between the second preparation and the first (Figure 25). In particular, although the aliphatic region appeared to be unchanged, the napthopyrone protons observed were significantly shifted from the first preparation and appeared to have much broader and heterogenous peak shape – indicative of the formation of aggregates[200]. Furthermore, the OH protons all appeared to be more deshielded in the second preparation, consistent with the participation in hydrogen bonding. Despite these differences, the same structural elements could be identified (two napthopyrones with five membered aliphatic chains), and an overall structure similar to the first preparation could be determined. However, in the new preparation the SO_4 was determined to be in the 6 position (Figure 26).

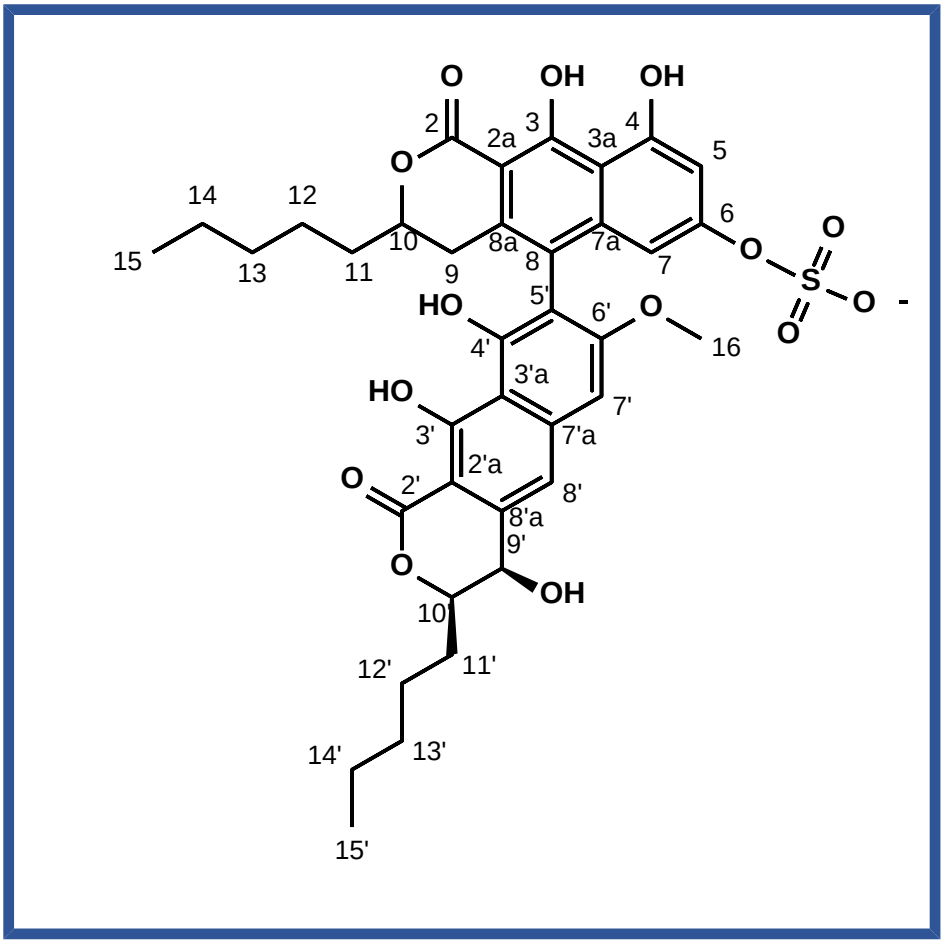

Figure 26: Structure of the second preparation of lulworthinone

To explore the aggregation, and the impact of acidic conditions, the second preparation was exposed to a small amount of HCl and monitored by ^{1}H and HSQC. Upon acidification, a transition to spectra resembling the first preparation was observed; this was particularly evident in the HSQC, when after 24 hours the spectra of the second preparation matched that of the first. Unfortunately, during the acidification process, the OH protons became unobservable, likely due to the increase in proton exchange resulting from the more acidic sample conditions (paper III supp. figure 10).

The conclusion drawn from the acidification test was that the second preparation of lulworthinone was readily able to form aggregates when the SO_4 was in the 6 position. An energy minimisation of a dimer of lulworthinone was done, and provisionally showed that lulworthinone was able to form multiple hydrogen bonds with another molecule of lulworthinone in order to stabilise a dimer. Interestingly, when in its dimeric form, the SO_4

group was positioned in such a way that an SN2 substitution could be possible so as to move the SO_4 from the 6 position of one lulworthinone, to the 9' of another, offering a potential explanation for the different isomers obtained from the acidified and non-acidified conditions.

The second preparation of lulworthinone was tested against multiple gram-positive and gram-negative strains of bacteria, with antibacterial activity identified against reference strains of gram-positive *S. aureus* and *S. agalactiae*, and against clinical strains of *S. aureus*, but no activity against gram-negative bacteria (see paper III table 2).

5.1.2 Further study of Lulworthinone (Paper IV)

The ability of the two forms of lulworthinone to aggregate, the relative activities of the two forms – the non-acidified (**1**) and the acidified form (**2**) - and the respective mode of action of these forms was a focus for the follow up study of lulworthinone. In the initial structure elucidation it was noted that in **1** the spectra showed signs of aggregation (Figure 27).

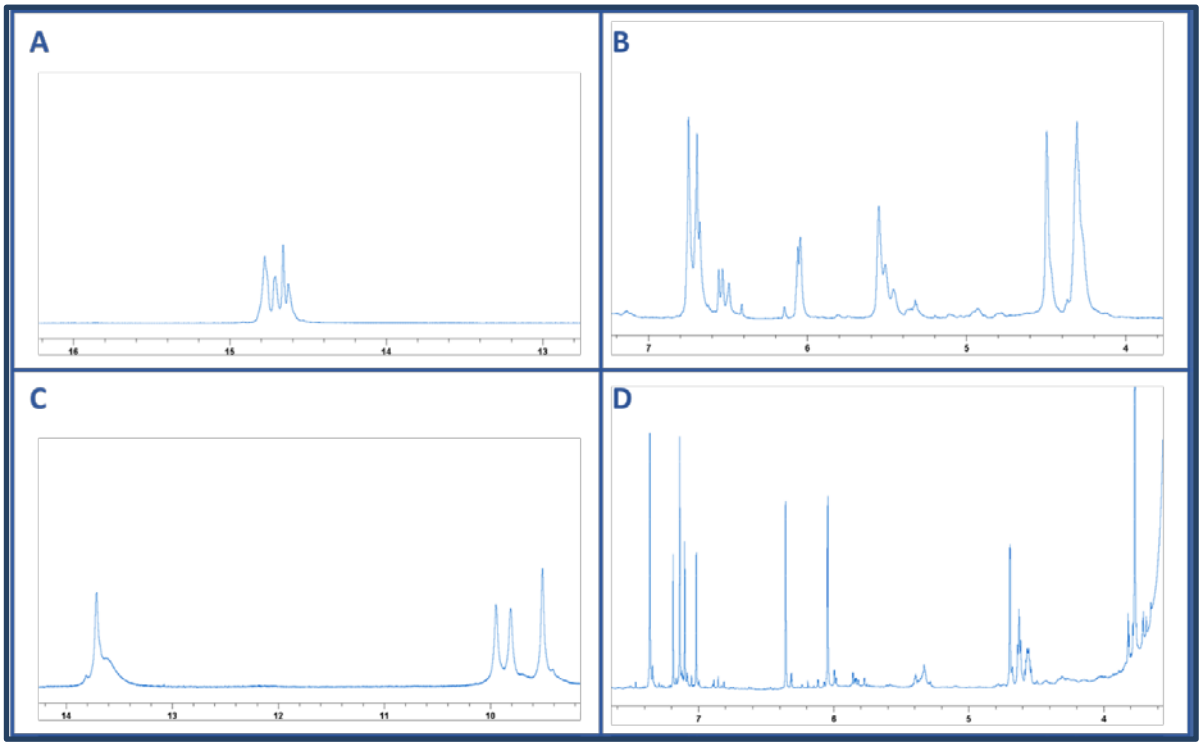

Figure 27: 1H spectra of the preparations of lulworthinone. A: Zoomed on the OH region of the second preparation. B: Highlighting the broader peaks of the aggregating second preparation of lulworthinone. C: Zoomed on the OHs of the first preparation of lulworthinone, highlighting the difference in chemical shift. D: Highlighting the sharper peaks of the non-acyl protons in the first preparation of lulworthinone.

The ^{1}H spectrum of **1** (Fig 27 A and B) demonstrates broader peaks with a few additional peaks attributable to the same proton, likely arising from the different conformations taken up in the aggregate (Fig 27 B). In contrast in **2,** sharp peaks are observed with no additional corresponding peaks from aggregation, suggesting a monomeric form of **2** (Fig 27 D). Further to this, it appears that the OH protons present in **1** are involved in a hydrogen bonding network with all OH significantly deshielded at ~15 ppm (Fig 27 A). In comparison, in **2** only two of the OHs are determined to be involved in hydrogen bonding – likely with the neighbouring carbonyl group (Fig 27 C).

Initial results suggested that **1** was active on bacterial membranes, and DLS results showed that **1** was forming aggregates with a critical aggregation concentration (CAC) of 54 µM, while **2** was not aggregating. To determine the impact of the aggregation and relative activity of the two forms, the K_D and K_P of **1** and **2** were investigated using SPR.

*Table 7: K_P and k_{off} of **1** and **2** towards DMPC, derived using SPR*

Lulworthinone form	K_p ($1x10^3$)	k_{off} s^{-1}
1	44.81 ± 2.47	0.042 ± 0.005
2	0.76 ± 0.04	5.185 ± 1.594

The SPR results highlight the significant differences between the two forms of lulworthinone, with **1** having a significantly higher K_P by two orders of magnitude, suggesting a far greater preference for a membrane environment (Table 7). However, **1** showed complete dissociation without disruption of the lipid bilayer (Paper IV, Supp. Figure S1); this, in combination with the unusually large response units, suggests that in the case of **1**, the bilayer served as a support on which further aggregation could take place, and that the measured K_P is a combination of both lipid binding and aggregation. In contrast **2**, without the possibility of forming such aggregates, has only a modest K_P which is comparable to the SPR derived K_P of LWwNKr from paper II.

The ability of both **1** and **2** to disrupt membranes was investigated with WIND-PVPA; this was especially interesting with regards to the large aggregates of **1** that can form on a lipid surface. For this, WIND-PVPA was conducted using the E80 lipid composition, and similarly to the obtained SPR results, no PG was included. However, no significant effect on ion or water permeability was observable for either **1** or **2**, suggesting that WIND-PVPA is not sensitive to the effects of aggregates forming on top of the barrier, or that such aggregates do not impact the permeability of water or ions in a meaningful way (Figure 28).

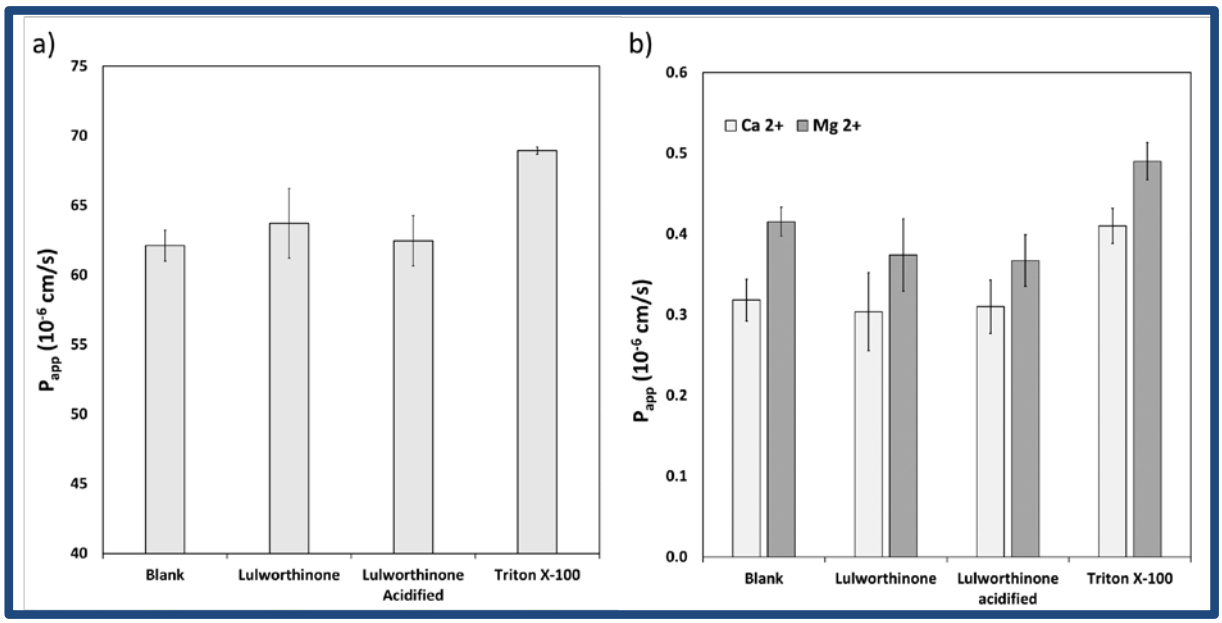

*Figure 28: Lulworthinone WIND-PVPA results. a) D_2O permeability b) Ion permeability. lulworthinone - **1**. lulworthinone acidified – **2**.*

Crucially, in this instance of WIND-PVPA the concentration of both **1** and **2** in the donor is lower than previously used in paper I (4 mg/mL / ~4 mM for paper I vs ~0.1 mg/mL / 100 µM for paper IV). The main reason for this was in order to use concentrations in line with the other assays utilised throughout paper IV. At this concentration a non-significant reduction in the P_{app} of Mg^{2+} is made note of, indicating that at potentially greater concentrations this effect may become significant. It would therefore be prudent to evaluate concentration-dependent effects on WIND-PVPA in a future work, with a focus on the concentration at which membrane-disruptive effects take place – KP-76 and WRWRWR from paper I may be ideal candidates for this as they displayed significantly different disruptive effects that would presumably have different concentrations upon which the disruptive effect of the AMP takes place.

In summary, Paper IV, including the results discussed here showed that for its antibacterial effect **1** relies on its ability to form aggregates – activity of **1** was lost when MIC was performed in the presence of a detergent that would prevent the aggregation of **1**. It concludes that **1** is active on the membrane without disrupting it and that it ultimately prevents cell division by delocalising FtsZ.

Of relevance to the overall work described in this thesis, paper IV is a demonstration of the application of WIND-PVPA alongside binding data to describe the activities of non-peptide membrane active antimicrobial agents with a view to identify the MOA, and how WIND-PVPA can complement existing assays. While in this instance **1** had no observable effect, this helped describe the overall behaviour of the MOA.

5.2 St-CRP-1 (Paper V)

The sea squirt *Synoicum turgens* was collected off the coast of Svalbard, and lyophilised extracts were fractionated by SPE using acetonitrile. One of the fractions was recognised as having antibacterial activity, and two peptides were identified in this fraction and collected – 18 residue St-CRP-1, and 19 residue St-CRP-2. The sequence and disulfide connectivity of St-CRP-1 was determined by MS to be CCDQCYGFCRLVDNCCNS-NH_2 with 1-6/2-4/3-5 disulfide connectivity (St-CRP-2 was not analysed by NMR and will therefore be excluded from this discussion). Enough St-CRP-1 was obtained for structure elucidation by NMR.

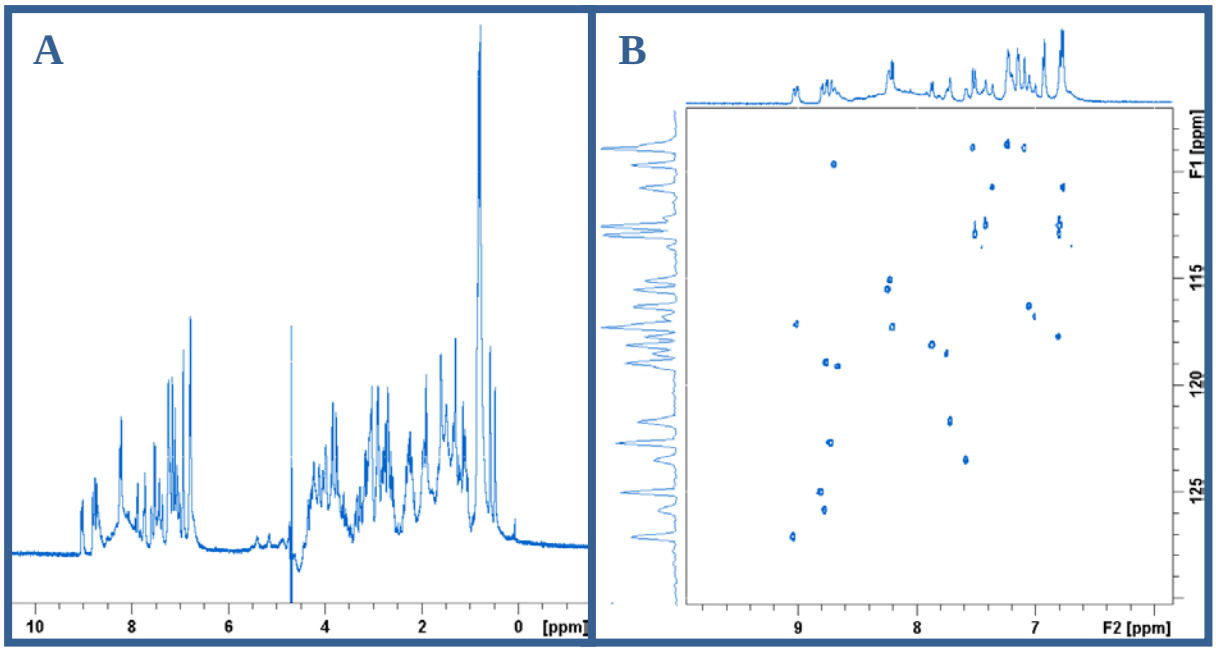

Figure 29: ^{1}H spectrum of St-CRP-1. B: ^{15}N-HSQC spectrum of St-CRP-1

St-CRP-1 was dissolved in H_2O/D_2O 90:10 mix, and initial ^{1}H and ^{15}N-HSQC showed St-CRP-1 to be pure, with minimal impurities (Figure 29A and 29B respectively). A combination of ^{15}N-HSQC, ^{13}C-HSQC, and TOCSY enabled the assignment of all residues, and the sequence was determined by NOESY, which was confirmed by the MS derived sequence.

From the collected NOESY spectra 213 NOEs were extracted and subsequently converted to distance constraints according to NOE intensity. These distances were used as refinement constraints for structure generation, alongside phi and psi torsion angles calculated from ^{13}C chemical shifts using TALOS. The structures were generated using a simulated annealing (SA) algorithm, where the model is 'heated' to a high energy state at 3500 K, and cooled over multiple steps to a minimised energy state at 100 K. The SA is done with the previously defined constraints, and once the minimisation is complete any interatomic distances which disobey the distance constraints are flagged as violations – in such cases the constraints are relaxed or tightened for future refinements. To determine the disulfide connectivity, the first structures were generated and refined with no explicit disulfide bonds. Once the minimised structures yielded no violations, 500 structures were generated in a production run. The S-S interatomic distances of the 10 lowest energy structures were extracted, which revealed a C1-C6/C2-C4/C3-C5 disulfide pattern. Further minimisation was done with the explicit disulfide linkage, before a further 500 structures were generated.

From the production run the 38 structures with an energy of 2 kcal or below were taken. These structures populated one of two conformers: a major conformer with a small helix, and a minor conformer with a knotted loop. The absence of NOEs that would describe this knot structure led to the inclusion of a repulsing constraint between residues Tyr6 and Cys16 for a new production run which eliminated the knot conformer and yielded the final structure ensemble (Figure 30).

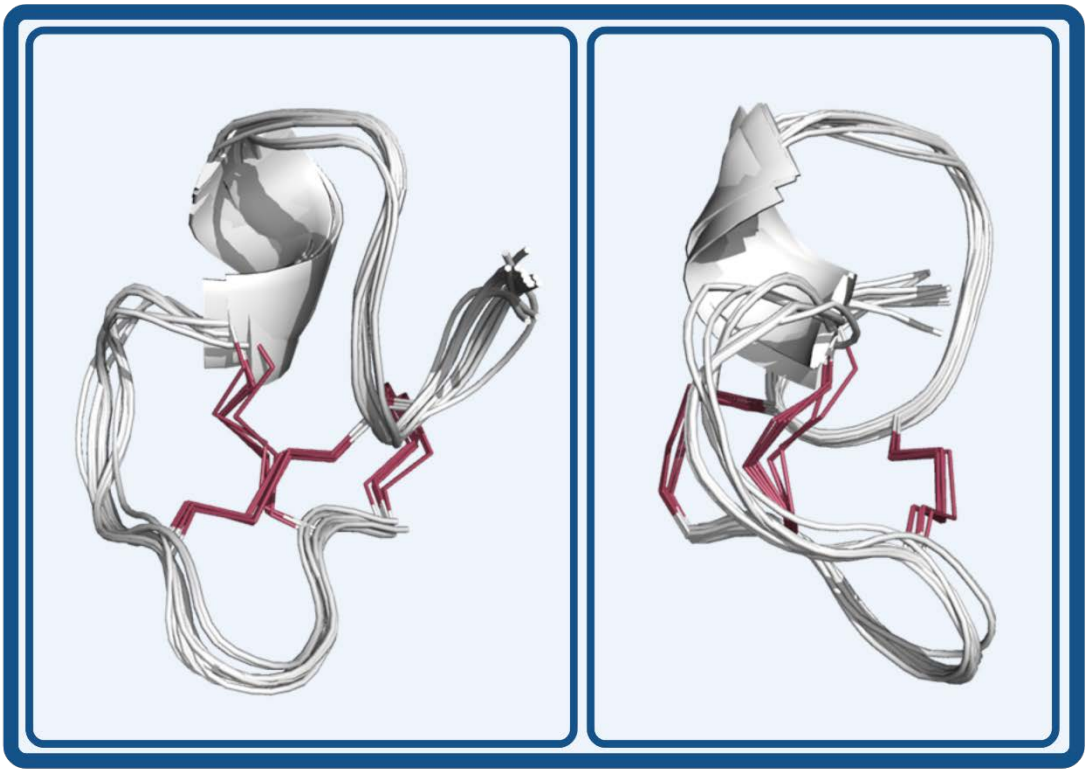

Figure 30: 3D structure of st-CRP-1 generated through SA.

St-CRP-1 demonstrated modest activity against strains of the gram-positive bacteria *C. glutamicum* and *B. subtilis*, however no activity was observed against the gram-positive *S. aureus*, or gram-negative *E. coli* and *P. aeruginosa* in the conditions tested. Furthermore, no toxicity was observed against brine shrimp, or human melanoma or fibroblast cell lines (A2058 and MRC-5 respectively).

Paper V helps to demonstrate the role of AMPs as HDPs, and their prevalence and importance throughout nature, as well as outlining the techniques that are used to elucidate the structures

of peptides. In particular, paper V shows the implementation of SA to generate 3D peptide structures. Such structures can give powerful insight into the behaviours of AMPs and would combine well with both WIND-PVPA and MST to give a robust view of AMP activity. This could be further enhanced by comparisons of an AMP's conformation within and without the membrane, and how structural properties are changed or preserved within the hydrophobic environment – the relationship to binding and membrane disruption of such conformations could yield tremendous insight into the MOA of AMPs.

Unfortunately, not enough material was available for examination by WIND-PVPA; however, the results of this would be of interest, specifically as st-CRP-1 is a cysteine rich peptide. A common characteristic of such AMPs is that they exhibit membrane lytic behaviour that could be demonstrated using WIND-PVPA.

6 Conclusion

The stated aim of the project was to develop new methods and techniques to help determine the mode of action of AMPs, and to assist in the structure elucidation of novel natural products. To these ends five manuscripts were produced, and two DOFIs were submitted. The manuscripts in the main described two *in vitro* methods that can be used to quantify the effects that AMPs have on membrane lipids, and further show the application of one of these methods, WIND-PVPA, to additional AMPs and to lulworthinone, a natural product characterised as influencing membrane potential.

In papers I and IV, WIND-PVPA has been demonstrated as capable of quantifying the disruptive effects of not just AMPs, but also non-peptides, by monitoring changes in the P_{app} of water and ions in a novel adaption of the PVPA method.

Paper II is an original demonstration of how MST can be used to evaluate the binding of AMPs to model membrane systems. With a focus on SMA-nanodiscs and vesicles as membrane models, it helps further the discussion on the relative suitability of these models to evaluate AMP characteristics.

Finally, in papers III and V the structures of two new marine natural product structures are elucidated. This type of work is essential in drug discovery, and the papers show how NMR plays a vital role in its success, while further exploring how to apply different techniques in order to produce relevant structures.

Throughout this thesis it has been outlined, and to a degree demonstrated, how WIND-PVPA and MST can be combined to give a greater understanding of AMP activity alongside more traditional MIC testing. Additionally discussed is how the evaluation of AMP 3D structure could further enhance such techniques, and how this would enable a much greater understanding of AMPs, allowing for the design of novel AMPs with specific MOAs.

Both WIND-PVPA and the application of MST to peptide-lipid interactions are presented as being in their infancy. As such, there is ample scope within these methods to further expand the

work presented here, so as to give more detailed and biologically relevant data and should prove to be a fruitful avenue for further work.

7 References

1. Flemming, S. A. Nobel Lecture: Penicillin. https://www.nobelprize.org/prizes/medicine/1945/fleming/lecture (accessed 30 Dec 2021).
2. Podolsky, S. H., The evolving response to antibiotic resistance (1945–2018). *Palgrave Communications* **2018,** *4* (1), 124.
3. Davies, J., Where Have all the Antibiotics Gone? *Canadian Journal of Infectious Diseases and Medical Microbiology* **2006,** *17*, 707296.
4. Dutescu, I. A., The Antimicrobial Resistance Crisis: How Neoliberalism Helps Microbes Dodge Our Drugs. *International Journal of Health Services* **2020,** *51* (4), 521-530.
5. Manyi-Loh, C.; Mamphweli, S.; Meyer, E.; Okoh, A., Antibiotic Use in Agriculture and Its Consequential Resistance in Environmental Sources: Potential Public Health Implications. *Molecules* **2018,** *23* (4).
6. Chang, Q.; Wang, W.; Regev-Yochay, G.; Lipsitch, M.; Hanage, W. P., Antibiotics in agriculture and the risk to human health: how worried should we be? *Evolutionary Applications* **2015,** *8* (3), 240-247.
7. Byrne, M. K.; Miellet, S.; McGlinn, A.; Fish, J.; Meedya, S.; Reynolds, N.; van Oijen, A. M., The drivers of antibiotic use and misuse: the development and investigation of a theory driven community measure. *BMC Public Health* **2019,** *19* (1), 1425.
8. Prestinaci, F.; Pezzotti, P.; Pantosti, A., Antimicrobial resistance: a global multifaceted phenomenon. *Pathog Glob Health* **2015,** *109* (7), 309-318.
9. O'Neill, J., Antimicrobial resistance: tackling a crisis for the future health and wealth of nations. London: Review on Antimicrobial Resistance; 2014.
10. WHO Antibiotic resistance. https://www.who.int/news-room/fact-sheets/detail/antibiotic-resistance (accessed 30.3.2022).
11. WHO Global Antimicrobial Resistance and Use Surveillance System (GLASS). https://www.who.int/initiatives/glass (accessed 30.3.2022).
12. Oliveira, D. M. P. D.; Forde, B. M.; Kidd, T. J.; Harris, P. N. A.; Schembri, M. A.; Beatson, S. A.; Paterson, D. L.; Walker, M. J., Antimicrobial Resistance in ESKAPE Pathogens. **2020,** *33* (3), e00181-19.
13. Vollmer, W.; Blanot, D.; De Pedro, M. A., Peptidoglycan structure and architecture. *FEMS microbiology reviews* **2008,** *32* (2), 149-167.
14. Epand, R. M.; Epand, R. F., Lipid domains in bacterial membranes and the action of antimicrobial agents. *Biochimica et Biophysica Acta (BBA) - Biomembranes* **2009,** *1788* (1), 289-294.
15. Miller, S. I., Antibiotic Resistance and Regulation of the Gram-Negative Bacterial Outer Membrane Barrier by Host Innate Immune Molecules. *mBio* **2016,** *7* (5), e01541-16.
16. Breijyeh, Z.; Jubeh, B.; Karaman, R., Resistance of Gram-Negative Bacteria to Current Antibacterial Agents and Approaches to Resolve It. *Molecules* **2020,** *25*.
17. Tencza, S. B.; Douglass, J. P.; Creighton, D. J.; Montelaro, R. C.; Mietzner, T. A., Novel antimicrobial peptides derived from human immunodeficiency virus type 1 and other lentivirus transmembrane proteins. *Antimicrobial Agents and Chemotherapy* **1997,** *41* (11), 2394-2398.
18. Hassan, M.; Kjos, M.; Nes, I. F.; Diep, D. B.; Lotfipour, F., Natural antimicrobial peptides from bacteria: characteristics and potential applications to fight against antibiotic resistance. *Journal of Applied Microbiology* **2012,** *113* (4), 723-736.
19. Wiesner, J.; Vilcinskas, A., Antimicrobial peptides: the ancient arm of the human immune system. *Virulence* **2010,** *1* (5), 440-64.
20. Wang, X.; Sun, Y.; Wang, F.; You, L.; Cao, Y.; Tang, R.; Wen, J.; Cui, X., A novel endogenous antimicrobial peptide CAMP211-225 derived from casein in human milk. *Food & Function* **2020,** *11* (3), 2291-2298.
21. van Hoek, M. L.; Prickett, M. D.; Settlage, R. E.; Kang, L.; Michalak, P.; Vliet, K. A.; Bishop, B. M., The Komodo dragon (Varanus komodoensis) genome and identification of innate immunity genes and clusters. *BMC Genomics* **2019,** *20* (1), 684.

22. Hancock, R. E. W., Peptide antibiotics. *The Lancet* **1997,** *349* (9049), 418-422.
23. Arnison, P. G.; Bibb, M. J.; Bierbaum, G.; Bowers, A. A.; Bugni, T. S.; Bulaj, G.; Camarero, J. A.; Campopiano, D. J.; Challis, G. L.; Clardy, J.; Cotter, P. D.; Craik, D. J.; Dawson, M.; Dittmann, E.; Donadio, S.; Dorrestein, P. C.; Entian, K.-D.; Fischbach, M. A.; Garavelli, J. S.; Göransson, U.; Gruber, C. W.; Haft, D. H.; Hemscheidt, T. K.; Hertweck, C.; Hill, C.; Horswill, A. R.; Jaspars, M.; Kelly, W. L.; Klinman, J. P.; Kuipers, O. P.; Link, A. J.; Liu, W.; Marahiel, M. A.; Mitchell, D. A.; Moll, G. N.; Moore, B. S.; Müller, R.; Nair, S. K.; Nes, I. F.; Norris, G. E.; Olivera, B. M.; Onaka, H.; Patchett, M. L.; Piel, J.; Reaney, M. J. T.; Rebuffat, S.; Ross, R. P.; Sahl, H.-G.; Schmidt, E. W.; Selsted, M. E.; Severinov, K.; Shen, B.; Sivonen, K.; Smith, L.; Stein, T.; Süssmuth, R. D.; Tagg, J. R.; Tang, G.-L.; Truman, A. W.; Vederas, J. C.; Walsh, C. T.; Walton, J. D.; Wenzel, S. C.; Willey, J. M.; van der Donk, W. A., Ribosomally synthesized and post-translationally modified peptide natural products: overview and recommendations for a universal nomenclature. *Natural product reports* **2013,** *30* (1), 108-160.
24. Spohn, R.; Daruka, L.; Lázár, V.; Martins, A.; Vidovics, F.; Grézal, G.; Méhi, O.; Kintses, B.; Számel, M.; Jangir, P. K.; Csörgő, B.; Györkei, Á.; Bódi, Z.; Faragó, A.; Bodai, L.; Földesi, I.; Kata, D.; Maróti, G.; Pap, B.; Wirth, R.; Papp, B.; Pál, C., Integrated evolutionary analysis reveals antimicrobial peptides with limited resistance. *Nature Communications* **2019,** *10* (1), 4538.
25. Wimley, W. C., Describing the mechanism of antimicrobial peptide action with the interfacial activity model. *ACS Chem Biol* **2010,** *5* (10), 905-917.
26. Habermann, E., Bee and Wasp Venoms. *Science* **1972,** *177* (4046), 314-322.
27. Tan, S. Y.; Tatsumura, Y., Alexander Fleming (1881-1955): Discoverer of penicillin. *Singapore Med J* **2015,** *56* (7), 366-367.
28. Steiner, H.; Hultmark, D.; Engström, Å.; Bennich, H.; Boman, H. G., Sequence and specificity of two antibacterial proteins involved in insect immunity. *Nature* **1981,** *292* (5820), 246-248.
29. Zasloff, M., Magainins, a class of antimicrobial peptides from Xenopus skin: isolation, characterization of two active forms, and partial cDNA sequence of a precursor. *Proc Natl Acad Sci U S A* **1987,** *84* (15), 5449-53.
30. Ludtke, S. J.; He, K.; Heller, W. T.; Harroun, T. A.; Yang, L.; Huang, H. W., Membrane Pores Induced by Magainin. *Biochemistry* **1996,** *35* (43), 13723-13728.
31. Hristova, K.; Selsted, M. E.; White, S. H., Critical role of lipid composition in membrane permeabilization by rabbit neutrophil defensins. *J Biol Chem* **1997,** *272* (39), 24224-33.
32. Ackermann, M. R.; Gallup, J. M.; Zabner, J.; Evans, R. B.; Brockus, C. W.; Meyerholz, D. K.; Grubor, B.; Brogden, K. A., Differential expression of sheep beta-defensin-1 and -2 and interleukin 8 during acute Mannheimia haemolytica pneumonia. *Microbial Pathogenesis* **2004,** *37* (1), 21-27.
33. Schaal, J. B.; Tran, D.; Tran, P.; Ösapay, G.; Trinh, K.; Roberts, K. D.; Brasky, K. M.; Tongaonkar, P.; Ouellette, A. J.; Selsted, M. E., Rhesus Macaque Theta Defensins Suppress Inflammatory Cytokines and Enhance Survival in Mouse Models of Bacteremic Sepsis. *PLOS ONE* **2012,** *7* (12), e51337.
34. Antcheva, N.; Guida, F.; Tossi, A., Chapter 18 - Defensins. In *Handbook of Biologically Active Peptides (Second Edition)*, Kastin, A. J., Ed. Academic Press: Boston, 2013; pp 101-118.
35. Lacerda, A.; Vasconcelos, É.; PELEGRINI, P.; Grossi-de-Sa, M. F., Antifungal defensins and their role in plant defense. *Frontiers in Microbiology* **2014,** *5* (116).
36. Koehbach, J., Structure-Activity Relationships of Insect Defensins. *Front Chem* **2017,** *5* (45).
37. Sohlenkamp, C.; Geiger, O., Bacterial membrane lipids: diversity in structures and pathways. *FEMS microbiology reviews* **2016,** *40* (1), 133-59.
38. Bogdanov, M.; Pyrshev, K.; Yesylevskyy, S.; Ryabichko, S.; Boiko, V.; Ivanchenko, P.; Kiyamova, R.; Guan, Z.; Ramseyer, C.; Dowhan, W., Phospholipid distribution in the cytoplasmic membrane of Gram-negative bacteria is highly asymmetric, dynamic, and cell shape-dependent. *Science Advances 6* (23), eaaz6333.
39. Kobayashi, T.; Menon, A. K., Transbilayer lipid asymmetry. *Current Biology* **2018,** *28* (8), R386-R391.

40. Bevers, E. M.; Comfurius, P.; Zwaal, R. F. A., Regulatory Mechanisms in Maintenance and Modulation of Transmembrane Lipid Asymmetry: Pathophysiological Implications. *Lupus* **1996,** *5* (5), 480-487.
41. Lad, M. D.; Birembaut, F.; Clifton, L. A.; Frazier, R. A.; Webster, J. R. P.; Green, R. J., Antimicrobial Peptide-Lipid Binding Interactions and Binding Selectivity. *Biophysical Journal* **2007,** *92* (10), 3575-3586.
42. Vorobyov, I.; Allen, T. W., On the role of anionic lipids in charged protein interactions with membranes. *Biochimica et Biophysica Acta (BBA) - Biomembranes* **2011,** *1808* (6), 1673-1683.
43. Schmidt, N. W.; Mishra, A.; Lai, G. H.; Davis, M.; Sanders, L. K.; Tran, D.; Garcia, A.; Tai, K. P.; McCray, P. B.; Ouellette, A. J.; Selsted, M. E.; Wong, G. C. L., Criterion for amino acid composition of defensins and antimicrobial peptides based on geometry of membrane destabilization. *Journal of the American Chemical Society* **2011,** *133* (17), 6720-6727.
44. Schmidt, N. W.; Wong, G. C. L., Antimicrobial peptides and induced membrane curvature: geometry, coordination chemistry, and molecular engineering. *Curr Opin Solid State Mater Sci* **2013,** *17* (4), 151-163.
45. Yu, L.; Fan, Q.; Yue, X.; Mao, Y.; Qu, L., Activity of a novel-designed antimicrobial peptide and its interaction with lipids. **2015,** *21* (4), 274-282.
46. Li, J.; Koh, J.-J.; Liu, S.; Lakshminarayanan, R.; Verma, C. S.; Beuerman, R. W., Membrane Active Antimicrobial Peptides: Translating Mechanistic Insights to Design. *Front Neurosci* **2017,** *11*, 73-73.
47. Scheinpflug, K.; Wenzel, M.; Krylova, O.; Bandow, J. E.; Dathe, M.; Strahl, H., Antimicrobial peptide cWFW kills by combining lipid phase separation with autolysis. *Scientific Reports* **2017,** *7* (1), 44332.
48. Munro, S., Lipid Rafts: Elusive or Illusive? *Cell* **2003,** *115* (4), 377-388.
49. Wadhwani, P.; Epand, R. F.; Heidenreich, N.; Bürck, J.; Ulrich, A. S.; Epand, R. M., Membrane-active peptides and the clustering of anionic lipids. *Biophysical journal* **2012,** *103* (2), 265-274.
50. Matsuzaki, K.; Murase, O.; Fujii, N.; Miyajima, K., An Antimicrobial Peptide, Magainin 2, Induced Rapid Flip-Flop of Phospholipids Coupled with Pore Formation and Peptide Translocation. *Biochemistry* **1996,** *35* (35), 11361-11368.
51. Qian, S.; Heller, W. T., Peptide-Induced Asymmetric Distribution of Charged Lipids in a Vesicle Bilayer Revealed by Small-Angle Neutron Scattering. *The Journal of Physical Chemistry B* **2011,** *115* (32), 9831-9837.
52. Zhang, Q.-Y.; Yan, Z.-B.; Meng, Y.-M.; Hong, X.-Y.; Shao, G.; Ma, J.-J.; Cheng, X.-R.; Liu, J.; Kang, J.; Fu, C.-Y., Antimicrobial peptides: mechanism of action, activity and clinical potential. *Military Medical Research* **2021,** *8* (1), 48.
53. Zhao, Y.; Chen, Z.; Cao, Z.; Li, W.; Wu, Y., Defensins, a novel type of animal toxin-like potassium channel inhibitor. *Toxicon* **2019,** *157*, 101-105.
54. Nelson, N.; Opene, B.; Ernst, R. K.; Schwartz, D. K., Antimicrobial peptide activity is anticorrelated with lipid a leaflet affinity. *PLOS ONE* **2020,** *15* (11), e0242907.
55. Fehlbaum, P.; Bulet, P.; Chernysh, S.; Briand, J. P.; Roussel, J. P.; Letellier, L.; Hetru, C.; Hoffmann, J. A., Structure-activity analysis of thanatin, a 21-residue inducible insect defense peptide with sequence homology to frog skin antimicrobial peptides. *Proc Natl Acad Sci U S A* **1996,** *93* (3), 1221-5.
56. Vetterli, S. U.; Zerbe, K.; Müller, M.; Urfer, M.; Mondal, M.; Wang, S. Y.; Moehle, K.; Zerbe, O.; Vitale, A.; Pessi, G.; Eberl, L.; Wollscheid, B.; Robinson, J. A., Thanatin targets the intermembrane protein complex required for lipopolysaccharide transport in Escherichia coli. *Sci Adv* **2018,** *4* (11), eaau2634.
57. Park, C. B.; Kim, H. S.; Kim, S. C., Mechanism of action of the antimicrobial peptide buforin II: buforin II kills microorganisms by penetrating the cell membrane and inhibiting cellular functions. *Biochem Biophys Res Commun* **1998,** *244* (1), 253-7.
58. Subbalakshmi, C.; Sitaram, N., Mechanism of antimicrobial action of indolicidin. *FEMS Microbiology Letters* **1998,** *160* (1), 91-96.

59. den Blaauwen, T.; Hamoen, L. W.; Levin, P. A., The divisome at 25: the road ahead. *Curr Opin Microbiol* **2017,** *36*, 85-94.
60. Yadavalli, S. S.; Carey, J. N.; Leibman, R. S.; Chen, A. I.; Stern, A. M.; Roggiani, M.; Lippa, A. M.; Goulian, M., Antimicrobial peptides trigger a division block in Escherichia coli through stimulation of a signalling system. *Nature Communications* **2016,** *7* (1), 12340.
61. Di Somma, A.; Avitabile, C.; Cirillo, A.; Moretta, A.; Merlino, A.; Paduano, L.; Duilio, A.; Romanelli, A., The antimicrobial peptide Temporin L impairs E. coli cell division by interacting with FtsZ and the divisome complex. *Biochimica et Biophysica Acta (BBA) - General Subjects* **2020,** *1864* (7), 129606.
62. Mardirossian, M.; Barrière, Q.; Timchenko, T.; Müller, C.; Pacor, S.; Mergaert, P.; Scocchi, M.; Wilson, D. N., Fragments of the Nonlytic Proline-Rich Antimicrobial Peptide Bac5 Kill Escherichia coli Cells by Inhibiting Protein Synthesis. *Antimicrobial Agents and Chemotherapy* **2018,** *62* (8), e00534-18.
63. Le, C.-F.; Fang, C.-M.; Sekaran, S. D., Intracellular Targeting Mechanisms by Antimicrobial Peptides. *Antimicrobial agents and chemotherapy* **2017,** *61* (4), e02340-16.
64. Carlsson, A.; Nyström, T.; de Cock, H.; Bennich, H., Attacin - an insect immune protein - binds LPS and triggers the specific inhibition of bacterial outer-membrane protein synthesis. *Microbiology* **1998,** *144* (8), 2179-2188.
65. Casteels, P.; Ampe, C.; Riviere, L.; Van Damme, J.; Elicone, C.; Fleming, M.; Jacobs, F.; Tempst, P., Isolation and characterization of abaecin, a major antibacterial response peptide in the honeybee (Apis mellifera). *Eur J Biochem* **1990,** *187* (2), 381-6.
66. Bulet, P.; Dimarcq, J. L.; Hetru, C.; Lagueux, M.; Charlet, M.; Hegy, G.; Van Dorsselaer, A.; Hoffmann, J. A., A novel inducible antibacterial peptide of Drosophila carries an O-glycosylated substitution. *J Biol Chem* **1993,** *268* (20), 14893-7.
67. Cociancich, S.; Dupont, A.; Hegy, G.; Lanot, R.; Holder, F.; Hetru, C.; Hoffmann, J. A.; Bulet, P., Novel inducible antibacterial peptides from a hemipteran insect, the sap-sucking bug Pyrrhocoris apterus. *Biochem J* **1994,** *300 (Pt 2)* (Pt 2), 567-75.
68. Knappe, D.; Piantavigna, S.; Hansen, A.; Mechler, A.; Binas, A.; Nolte, O.; Martin, L. L.; Hoffmann, R., Oncocin (VDKPPYLPRPRPPRRIYNR-NH2): a novel antibacterial peptide optimized against gram-negative human pathogens. *J Med Chem* **2010,** *53* (14), 5240-7.
69. Casteels, P.; Ampe, C.; Jacobs, F.; Vaeck, M.; Tempst, P., Apidaecins: antibacterial peptides from honeybees. *The EMBO Journal* **1989,** *8* (8), 2387-2391.
70. Calloni, G.; Chen, T.; Schermann, S. M.; Chang, H. C.; Genevaux, P.; Agostini, F.; Tartaglia, G. G.; Hayer-Hartl, M.; Hartl, F. U., DnaK functions as a central hub in the E. coli chaperone network. *Cell Rep* **2012,** *1* (3), 251-64.
71. Ellis, R. J., The molecular chaperone concept. *Semin Cell Biol* **1990,** *1* (1), 1-9.
72. López-Otín, C.; Bond, J. S., Proteases: multifunctional enzymes in life and disease. *J Biol Chem* **2008,** *283* (45), 30433-30437.
73. Gusman, H.; Grogan, J.; Kagan, H. M.; Troxler, R. F.; Oppenheim, F. G., Salivary histatin 5 is a potent competitive inhibitor of the cysteine proteinase clostripain. *FEBS Lett* **2001,** *489* (1), 97-100.
74. MacKay, B. J.; Denepitiya, L.; Iacono, V. J.; Krost, S. B.; Pollock, J. J., Growth-inhibitory and bactericidal effects of human parotid salivary histidine-rich polypeptides on Streptococcus mutans. *Infect Immun* **1984,** *44* (3), 695-701.
75. Couto, M. A.; Harwig, S. S.; Lehrer, R. I., Selective inhibition of microbial serine proteases by eNAP-2, an antimicrobial peptide from equine neutrophils. *Infect Immun* **1993,** *61* (7), 2991-2994.
76. De Lucca, A. J., Antifungal peptides: potential candidates for the treatment of fungal infections. *Expert Opinion on Investigational Drugs* **2000,** *9* (2), 273-299.
77. Lehrer, R. I.; Ganz, T.; Szklarek, D.; Selsted, M. E., Modulation of the in vitro candidacidal activity of human neutrophil defensins by target cell metabolism and divalent cations. *J Clin Invest* **1988,** *81* (6), 1829-1835.

78. De Lucca, A. J.; Bland, J. M.; Jacks, T. J.; Grimm, C.; Walsh, T. J., Fungicidal and binding properties of the natural peptides cecropin B and dermaseptin. *Medical Mycology* **1998,** *36* (5), 291-298.
79. DeLucca, A. J.; Bland, J. M.; Jacks, T. J.; Grimm, C.; Cleveland, T. E.; Walsh, T. J., Fungicidal activity of cecropin A. *Antimicrobial agents and chemotherapy* **1997,** *41* (2), 481-483.
80. Wang, G.; Li, X.; Wang, Z., APD3: the antimicrobial peptide database as a tool for research and education. *Nucleic Acids Research* **2015,** *44* (D1), D1087-D1093.
81. Reddy, K. V.; Yedery, R. D.; Aranha, C., Antimicrobial peptides: premises and promises. *Int J Antimicrob Agents* **2004,** *24* (6), 536-47.
82. Wachinger, M.; Kleinschmidt, A.; Winder, D.; von Pechmann, N.; Ludvigsen, A.; Neumann, M.; Holle, R.; Salmons, B.; Erfle, V.; Brack-Werner, R., Antimicrobial peptides melittin and cecropin inhibit replication of human immunodeficiency virus 1 by suppressing viral gene expression. *J Gen Virol* **1998,** *79 (Pt 4)*, 731-40.
83. Baxter, A. A.; Lay, F. T.; Poon, I. K. H.; Kvansakul, M.; Hulett, M. D., Tumor cell membrane-targeting cationic antimicrobial peptides: novel insights into mechanisms of action and therapeutic prospects. *Cell Mol Life Sci* **2017,** *74* (20), 3809-3825.
84. Felício, M. R.; Silva, O. N.; Gonçalves, S.; Santos, N. C.; Franco, O. L., Peptides with Dual Antimicrobial and Anticancer Activities. *Front Chem* **2017,** *5*, 5.
85. Yedery, R. D.; Reddy, K. V., Antimicrobial peptides as microbicidal contraceptives: prophecies for prophylactics--a mini review. *Eur J Contracept Reprod Health Care* **2005,** *10* (1), 32-42.
86. Kuroda, K.; Okumura, K.; Isogai, H.; Isogai, E., The Human Cathelicidin Antimicrobial Peptide LL-37 and Mimics are Potential Anticancer Drugs. *Frontiers in Oncology* **2015,** *5* (144).
87. Tanphaichitr, N.; Srakaew, N.; Alonzi, R.; Kiattiburut, W.; Kongmanas, K.; Zhi, R.; Li, W.; Baker, M.; Wang, G.; Hickling, D., Potential Use of Antimicrobial Peptides as Vaginal Spermicides/Microbicides. *Pharmaceuticals (Basel)* **2016,** *9* (1), 13.
88. Zasloff, M., Antimicrobial peptides of multicellular organisms. *Nature* **2002,** *415* (6870), 389-395.
89. Yau, W.-M.; Wimley, W. C.; Gawrisch, K.; White, S. H., The Preference of Tryptophan for Membrane Interfaces. *Biochemistry* **1998,** *37* (42), 14713-14718.
90. Mishra, A. K.; Choi, J.; Moon, E.; Baek, K.-H., Tryptophan-Rich and Proline-Rich Antimicrobial Peptides. *Molecules* **2018,** *23* (4), 815.
91. Travkova, O. G.; Moehwald, H.; Brezesinski, G., The interaction of antimicrobial peptides with membranes. *Advances in Colloid and Interface Science* **2017,** *247*, 521-532.
92. Giangaspero, A.; Sandri, L.; Tossi, A., Amphipathic α helical antimicrobial peptides. . *European Journal of Biochemistry* **2001,** *268* (21), 5589-5600.
93. Abbassi, F.; Lequin, O.; Piesse, C.; Goasdoué, N.; Foulon, T.; Nicolas, P.; Ladram, A., Temporin-SHf, a New Type of Phe-rich and Hydrophobic Ultrashort Antimicrobial Peptide*. *Journal of Biological Chemistry* **2010,** *285* (22), 16880-16892.
94. Aldrich, S. Amino Acids Reference Chart. https://www.sigmaaldrich.com/NO/en/technical-documents/technical-article/protein-biology/protein-structural-analysis/amino-acid-reference-chart (accessed 30.3.2022).
95. Tu, Z.; Young, A.; Murphy, C.; Liang, J. F., The pH sensitivity of histidine-containing lytic peptides. *J Pept Sci* **2009,** *15* (11), 790-795.
96. von Deuster, C. I. E.; Knecht, V., Antimicrobial selectivity based on zwitterionic lipids and underlying balance of interactions. *Biochimica et Biophysica Acta (BBA) - Biomembranes* **2012,** *1818* (9), 2192-2201.
97. Sudheendra, U. S.; Dhople, V.; Datta, A.; Kar, R. K.; Shelburne, C. E.; Bhunia, A.; Ramamoorthy, A., Membrane disruptive antimicrobial activities of human β-defensin-3 analogs. *European Journal of Medicinal Chemistry* **2015,** *91*, 91-99.
98. Gallivan, J. P.; Dougherty, D. A., Cation-π interactions in structural biology. **1999,** *96* (17), 9459-9464.

99. Gallivan, J. P.; Dougherty, D. A., Cation-pi interactions in structural biology. *Proceedings of the National Academy of Sciences of the United States of America* **1999,** *96* (17), 9459-9464.
100. Strøm, M. B.; Haug, B. E.; Skar, M. L.; Stensen, W.; Stiberg, T.; Svendsen, J. S., The Pharmacophore of Short Cationic Antibacterial Peptides. *J. Med. Chem.* **2003,** *46* (9), 1567-1570.
101. Meyer, C. E.; Reusser, F., A polypeptide antibacterial agent isolated fromTrichoderma viride. *Experientia* **1967,** *23* (2), 85-86.
102. Payne, J. W.; Jakes, R.; Hartley, B. S., The primary structure of alamethicin. *Biochem J* **1970,** *117* (4), 757-766.
103. Rinehart, K. L.; Cook, J. C.; Meng, H.; Olson, K. L.; Pandey, R. C., Mass spectrometric determination of molecular formulas for membrane-modifying antibiotics. *Nature* **1977,** *269* (5631), 832-833.
104. Fox, R. O.; Richards, F. M., A voltage-gated ion channel model inferred from the crystal structure of alamethicin at 1.5- resolution. *Nature* **1982,** *300* (5890), 325-330.
105. Wimley, W. C.; Hristova, K., Antimicrobial peptides: successes, challenges and unanswered questions. *The Journal of membrane biology* **2011,** *239* (1-2), 27-34.
106. Leitgeb, B.; Szekeres, A.; Manczinger, L.; Vágvölgyi, C.; Kredics, L., The History of Alamethicin: A Review of the Most Extensively Studied Peptaibol. *Chemistry & Biodiversity* **2007,** *4* (6), 1027-1051.
107. Yang, L.; Harroun, T. A.; Weiss, T. M.; Ding, L.; Huang, H. W., Barrel-Stave Model or Toroidal Model? A Case Study on Melittin Pores. *Biophysical Journal* **2001,** *81* (3), 1475-1485.
108. Jean-François, F.; Elezgaray, J.; Berson, P.; Vacher, P.; Dufourc, E. J., Pore formation induced by an antimicrobial peptide: electrostatic effects. *Biophysical journal* **2008,** *95* (12), 5748-5756.
109. Pouny, Y.; Rapaport, D.; Mor, A.; Nicolas, P.; Shai, Y., Interaction of antimicrobial dermaseptin and its fluorescently labeled analogs with phospholipid membranes. *Biochemistry* **1992,** *31* (49), 12416-12423.
110. Shai, Y., Mechanism of the binding, insertion and destabilization of phospholipid bilayer membranes by α-helical antimicrobial and cell non-selective membrane-lytic peptides. *Biochimica et Biophysica Acta (BBA) - Biomembranes* **1999,** *1462* (1), 55-70.
111. Bechinger, B.; Lohner, K., Detergent-like actions of linear amphipathic cationic antimicrobial peptides. *Biochimica et Biophysica Acta (BBA) - Biomembranes* **2006,** *1758* (9), 1529-1539.
112. Jarmoskaite, I.; AlSadhan, I.; Vaidyanathan, P. P.; Herschlag, D., How to measure and evaluate binding affinities. *eLife* **2020,** *9*, e57264.
113. Lin, J. H.; Sugiyama, Y.; Awazu, S.; Hanano, M., In vitro andin vivo evaluation of the tissue-to-blood partition coefficient for physiological pharmacokinetic models. *Journal of Pharmacokinetics and Biopharmaceutics* **1982,** *10* (6), 637-647.
114. Florindo, C.; Araújo, J. M. M.; Alves, F.; Matos, C.; Ferraz, R.; Prudêncio, C.; Noronha, J. P.; Petrovski, Ž.; Branco, L.; Rebelo, L. P. N.; Marrucho, I. M., Evaluation of solubility and partition properties of ampicillin-based ionic liquids. *International Journal of Pharmaceutics* **2013,** *456* (2), 553-559.
115. Hollmann, A.; Martínez, M.; Noguera, M. E.; Augusto, M. T.; Disalvo, A.; Santos, N. C.; Semorile, L.; Maffía, P. C., Role of amphipathicity and hydrophobicity in the balance between hemolysis and peptide–membrane interactions of three related antimicrobial peptides. *Colloids and Surfaces B: Biointerfaces* **2016,** *141*, 528-536.
116. Mayer, M.; Meyer, B., Group Epitope Mapping by Saturation Transfer Difference NMR To Identify Segments of a Ligand in Direct Contact with a Protein Receptor. *Journal of the American Chemical Society* **2001,** *123* (25), 6108-6117.
117. Huang, R.; Leung, I. K. H., Chapter Fourteen - Protein–Small Molecule Interactions by WaterLOGSY. In *Methods in Enzymology*, Wand, A. J., Ed. Academic Press: 2019; Vol. 615, pp 477-500.
118. Williamson, M. P., Using chemical shift perturbation to characterise ligand binding. *Progress in Nuclear Magnetic Resonance Spectroscopy* **2013,** *73*, 1-16.

119. Lurie, E.; Kaplun, A.; Vassilenko, I.; Dubovskii, P.; Shvets, V., Interaction of N-(2-hydroxybenzyl)-ω-amino carbonic acids, novel amphipathic fatty acid derivatives, with membrane: partition coefficients. *Biochimica et Biophysica Acta (BBA) - Biomembranes* **1995,** *1235* (2), 256-262.
120. Santos, N. C.; Prieto, M.; Castanho, M. A. R. B., Quantifying molecular partition into model systems of biomembranes: an emphasis on optical spectroscopic methods. *Biochimica et Biophysica Acta (BBA) - Biomembranes* **2003,** *1612* (2), 123-135.
121. Kraft Catherine, A.; Garrido Jose, L.; Leiva-Vega, L.; Romero, G., Quantitative Analysis of Protein-Lipid Interactions Using Tryptophan Fluorescence. *Science Signaling* **2009,** *2* (99), pl4-pl4.
122. van de Weert, M.; Stella, L., Fluorescence quenching and ligand binding: A critical discussion of a popular methodology. *Journal of Molecular Structure* **2011,** *998* (1), 144-150.
123. Matos, P. M.; Franquelim, H. G.; Castanho, M. A. R. B.; Santos, N. C., Quantitative assessment of peptide–lipid interactions.: Ubiquitous fluorescence methodologies. *Biochimica et Biophysica Acta (BBA) - Biomembranes* **2010,** *1798* (11), 1999-2012.
124. Stulz, A.; Breitsamer, M.; Winter, G.; Heerklotz, H., Primary and Secondary Binding of Exenatide to Liposomes. *Biophysical journal* **2020,** *118* (3), 600-611.
125. Henriques, S. T.; Castanho, M. A. R. B., Environmental factors that enhance the action of the cell penetrating peptide pep-1: A spectroscopic study using lipidic vesicles. *Biochimica et Biophysica Acta (BBA) - Biomembranes* **2005,** *1669* (2), 75-86.
126. López-Méndez, B.; Baron, B.; Brautigam, C. A.; Jowitt, T. A.; Knauer, S. H.; Uebel, S.; Williams, M. A.; Sedivy, A.; Abian, O.; Abreu, C.; Adamczyk, M.; Bal, W.; Berger, S.; Buell, A. K.; Carolis, C.; Daviter, T.; Fish, A.; Garcia-Alai, M.; Guenther, C.; Hamacek, J.; Holková, J.; Houser, J.; Johnson, C.; Kelly, S.; Leech, A.; Mas, C.; Matulis, D.; McLaughlin, S. H.; Montserret, R.; Nasreddine, R.; Nehmé, R.; Nguyen, Q.; Ortega-Alarcón, D.; Perez, K.; Pirc, K.; Piszczek, G.; Podobnik, M.; Rodrigo, N.; Rokov-Plavec, J.; Schaefer, S.; Sharpe, T.; Southall, J.; Staunton, D.; Tavares, P.; Vanek, O.; Weyand, M.; Wu, D., Reproducibility and accuracy of microscale thermophoresis in the NanoTemper Monolith: a multi laboratory benchmark study. *European Biophysics Journal* **2021,** *50* (3), 411-427.
127. López-Méndez, B.; Uebel, S.; Lundgren, L. P.; Sedivy, A., Microscale Thermophoresis and additional effects measured in NanoTemper Monolith instruments. *European Biophysics Journal* **2021,** *50* (3), 653-660.
128. Abdiche, Y. N.; Myszka, D. G., Probing the mechanism of drug/lipid membrane interactions using Biacore. *Anal Biochem* **2004,** *328* (2), 233-243.
129. Piliarik, M.; Vaisocherová, H.; Homola, J., Surface Plasmon Resonance Biosensing. In *Biosensors and Biodetection*, Rasooly, A.; Herold, K. E., Eds. Humana Press: Totowa, NJ, 2009; pp 65-88.
130. Figueira, T. N.; Freire, J. M.; Cunha-Santos, C.; Heras, M.; Gonçalves, J.; Moscona, A.; Porotto, M.; Salomé Veiga, A.; Castanho, M. A. R. B., Quantitative analysis of molecular partition towards lipid membranes using surface plasmon resonance. *Scientific reports* **2017,** *7*, 45647-45647.
131. Mozsolits, H.; Aguilar, M.-I., Surface plasmon resonance spectroscopy: An emerging tool for the study of peptide–membrane interactions. *Peptide Science* **2002,** *66* (1), 3-18.
132. Feig, A. L., Chapter 19 - Studying RNA–RNA and RNA–Protein Interactions by Isothermal Titration Calorimetry. In *Methods in Enzymology*, Academic Press: 2009; Vol. 468, pp 409-422.
133. Al-Kaddah, S.; Reder-Christ, K.; Klocek, G.; Wiedemann, I.; Brunschweiger, M.; Bendas, G., Analysis of membrane interactions of antibiotic peptides using ITC and biosensor measurements. *Biophysical Chemistry* **2010,** *152* (1), 145-152.
134. Zhang, A. H.; Edwards, I. A.; Mishra, B. P.; Sharma, G.; Healy, M. D.; Elliott, A. G.; Blaskovich, M. A. T.; Cooper, M. A.; Collins, B. M.; Jia, X.; Mobli, M., Elucidating the Lipid Binding Properties of Membrane-Active Peptides Using Cyclised Nanodiscs. *Front Chem* **2019,** *7*, 238-238.
135. Abraham, T.; Lewis, R. N. A. H.; Hodges, R. S.; McElhaney, R. N., Isothermal titration calorimetry studies of the binding of a rationally designed analogue of the antimicrobial peptide gramicidin s to phospholipid bilayer membranes. *Biochemistry* **2005,** *44* (6), 2103-2112.

136. Murphy, J.; Knutson, K.; Hinderliter, A., Chapter 18 - Protein–Lipid Interactions: Role of Membrane Plasticity and Lipid Specificity on Peripheral Protein Interactions. In *Methods in Enzymology*, Academic Press: 2009; Vol. 466, pp 431-453.
137. Heerklotz, H.; Seelig, J., Leakage and lysis of lipid membranes induced by the lipopeptide surfactin. *European Biophysics Journal* **2007,** *36* (4), 305-314.
138. Lundquist, A.; Wessman, P.; Rennie, A. R.; Edwards, K., Melittin-Lipid interaction: A comparative study using liposomes, micelles and bilayer disks. *Biochim. Biophys. Acta-Biomembr.* **2008,** *1778* (10), 2210-2216.
139. Fiedler, S.; Heerklotz, H., Vesicle Leakage Reflects the Target Selectivity of Antimicrobial Lipopeptides from Bacillus subtilis. *Biophysical Journal* **2015,** *109* (10), 2079-2089.
140. Sorochkina, A. I.; Kovalchuk, S. I.; Omarova, E. O.; Sobko, A. A.; Kotova, E. A.; Antonenko, Y. N., Peptide-induced membrane leakage by lysine derivatives of gramicidin A in liposomes, planar bilayers, and erythrocytes. *Biochimica et Biophysica Acta (BBA) - Biomembranes* **2013,** *1828* (11), 2428-2435.
141. Haran, N.; Shporer, M., Study of water permeability through phospholipid vesicle membranes by 17O NMR. *Biochimica et Biophysica Acta (BBA) - Biomembranes* **1976,** *426* (4), 638-646.
142. Tanaka, H.; Matsunaga, K.; Kawazura, H., 23Na and 1H NMR studies on melittin channels activated by tricyclic tranquilizers. *Biophysical journal* **1992,** *63* (2), 569-572.
143. Duval, D.; Riddell, F. G.; Rebuffat, S.; Platzer, N.; Bodo, B., Ionophoric activity of the antibiotic peptaibol trichorzin PA VI: a 23Na- and 35Cl-NMR study. *Biochimica et Biophysica Acta (BBA) - Biomembranes* **1998,** *1372* (2), 370-378.
144. Rathinakumar, R.; Wimley, W. C., Biomolecular Engineering by Combinatorial Design and High-Throughput Screening: Small, Soluble Peptides That Permeabilize Membranes. *Journal of the American Chemical Society* **2008,** *130* (30), 9849-9858.
145. Flaten, G. E.; Dhanikula, A. B.; Luthman, K.; Brandl, M., Drug permeability across a phospholipid vesicle based barrier: A novel approach for studying passive diffusion. *European Journal of Pharmaceutical Sciences* **2006,** *27* (1), 80-90.
146. Naderkhani, E.; Isaksson, J.; Ryzhakov, A.; Flaten, G. E., Development of a Biomimetic Phospholipid Vesicle-based Permeation Assay for the Estimation of Intestinal Drug Permeability. *Journal of Pharmaceutical Sciences* **2014,** *103* (6), 1882-1890.
147. Falavigna, M.; Klitgaard, M.; Brase, C.; Ternullo, S.; Škalko-Basnet, N.; Flaten, G. E., Mucus-PVPA (mucus Phospholipid Vesicle-based Permeation Assay): An artificial permeability tool for drug screening and formulation development. *International Journal of Pharmaceutics* **2018,** *537* (1), 213-222.
148. Salay, L. C.; Procopio, J.; Oliveira, E.; Nakaie, C. R.; Schreier, S., Ion channel-like activity of the antimicrobial peptide tritrpticin in planar lipid bilayers. *FEBS Letters* **2004,** *565* (1-3), 171-175.
149. Makarov, A. A.; Pirrone, G. F.; Shchurik, V.; Regalado, E. L.; Mangion, I., Liposome Artificial Membrane Permeability Assay by MALDI-hydrogen-deuterium exchange mass spectrometry for peptides and small proteins. *Analytica Chimica Acta* **2020,** *1099*, 111-118.
150. Kansy, M.; Senner, F.; Gubernator, K., Physicochemical High Throughput Screening: Parallel Artificial Membrane Permeation Assay in the Description of Passive Absorption Processes. *J. Med. Chem.* **1998,** *41* (7), 1007-1010.
151. Furukawa, A.; Townsend, C. E.; Schwochert, J.; Pye, C. R.; Bednarek, M. A.; Lokey, R. S., Passive Membrane Permeability in Cyclic Peptomer Scaffolds Is Robust to Extensive Variation in Side Chain Functionality and Backbone Geometry. *J. Med. Chem.* **2016,** *59* (20), 9503-9512.
152. Hagn, F.; Nasr, M. L.; Wagner, G., Assembly of phospholipid nanodiscs of controlled size for structural studies of membrane proteins by NMR. *Nat Protoc* **2018,** *13* (1), 79-98.
153. Denisov, I. G.; Grinkova, Y. V.; Lazarides, A. A.; Sligar, S. G., Directed Self-Assembly of Monodisperse Phospholipid Bilayer Nanodiscs with Controlled Size. *Journal of the American Chemical Society* **2004,** *126* (11), 3477-3487.
154. Geiger, O.; López-Lara, I. M.; Sohlenkamp, C., Phosphatidylcholine biosynthesis and function in bacteria. *Biochim Biophys Acta* **2013,** *1831* (3), 503-13.

155. Horne, J. E.; Brockwell, D. J.; Radford, S. E., Role of the lipid bilayer in outer membrane protein folding in Gram-negative bacteria. *Journal of Biological Chemistry* **2020,** *295* (30), 10340-10367.
156. Naudí, A.; Jové, M.; Ayala, V.; Portero-Otin, M.; Barja, G.; Pamplona, R., Membrane lipid unsaturation as physiological adaptation to animal longevity. *Frontiers in Physiology* **2013,** *4*.
157. Dowhan, W., MOLECULAR BASIS FOR MEMBRANE PHOSPHOLIPID DIVERSITY: Why Are There So Many Lipids? *Annual Review of Biochemistry* **1997,** *66* (1), 199-232.
158. May, K. L.; Grabowicz, M., The bacterial outer membrane is an evolving antibiotic barrier. *Proceedings of the National Academy of Sciences* **2018,** *115* (36), 8852.
159. Nielsen, J. E.; Prévost, S. F.; Jenssen, H.; Lund, R., Impact of antimicrobial peptides on E. coli-mimicking lipid model membranes: correlating structural and dynamic effects using scattering methods. *Faraday Discussions* **2021,** *232* (0), 203-217.
160. Hunter, H. N.; Jing, W.; Schibli, D. J.; Trinh, T.; Park, I. Y.; Kim, S. C.; Vogel, H. J., The interactions of antimicrobial peptides derived from lysozyme with model membrane systems. *Biochimica et Biophysica Acta (BBA) - Biomembranes* **2005,** *1668* (2), 175-189.
161. Dörr, J. M.; Koorengevel, M. C.; Schäfer, M.; Prokofyev, A. V.; Scheidelaar, S.; van der Cruijsen, E. A. W.; Dafforn, T. R.; Baldus, M.; Killian, J. A., Detergent-free isolation, characterization, and functional reconstitution of a tetrameric K⁺ channel: The power of native nanodiscs. *Proceedings of the National Academy of Sciences* **2014,** *111* (52), 18607.
162. Nagakubo, T.; Nomura, N.; Toyofuku, M., Cracking Open Bacterial Membrane Vesicles. *Frontiers in Microbiology* **2020,** *10* (3026).
163. Denisov, I. G.; Sligar, S. G., Nanodiscs for structural and functional studies of membrane proteins. *Nature Structural & Molecular Biology* **2016,** *23* (6), 481-486.
164. Ortega, V.; Giorgio, S.; de Paula, E., Liposomal formulations in the pharmacological treatment of leishmaniasis: a review. *Journal of Liposome Research* **2017,** *27* (3), 234-248.
165. Akbarzadeh, A.; Rezaei-Sadabady, R.; Davaran, S.; Joo, S. W.; Zarghami, N.; Hanifehpour, Y.; Samiei, M.; Kouhi, M.; Nejati-Koshki, K., Liposome: classification, preparation, and applications. *Nanoscale Res Lett* **2013,** *8* (1), 102-102.
166. Kreutzberger, M. A.; Tejada, E.; Wang, Y.; Almeida, P. F., GUVs melt like LUVs: the large heat capacity of MLVs is not due to large size or small curvature. *Biophysical journal* **2015,** *108* (11), 2619-2622.
167. Islam, M. Z.; Sharmin, S.; Moniruzzaman, M.; Yamazaki, M., Elementary processes for the entry of cell-penetrating peptides into lipid bilayer vesicles and bacterial cells. *Applied Microbiology and Biotechnology* **2018,** *102* (9), 3879-3892.
168. Domingues, T. M.; Riske, K. A.; Miranda, A., Revealing the Lytic Mechanism of the Antimicrobial Peptide Gomesin by Observing Giant Unilamellar Vesicles. *Langmuir* **2010,** *26* (13), 11077-11084.
169. Bayburt, T. H.; Grinkova, Y. V.; Sligar, S. G., Self-Assembly of Discoidal Phospholipid Bilayer Nanoparticles with Membrane Scaffold Proteins. *Nano Letters* **2002,** *2* (8), 853-856.
170. Serebryany, E.; Zhu, G. A.; Yan, E. C. Y., Artificial membrane-like environments for in vitro studies of purified G-protein coupled receptors. *Biochimica et Biophysica Acta (BBA) - Biomembranes* **2012,** *1818* (2), 225-233.
171. Nasr, M. L.; Baptista, D.; Strauss, M.; Sun, Z.-Y. J.; Grigoriu, S.; Huser, S.; Plückthun, A.; Hagn, F.; Walz, T.; Hogle, J. M.; Wagner, G., Covalently circularized nanodiscs for studying membrane proteins and viral entry. *Nat Methods* **2017,** *14* (1), 49-52.
172. Zhao, Z.; Zhang, M.; Hogle, J. M.; Shih, W. M.; Wagner, G.; Nasr, M. L., DNA-Corralled Nanodiscs for the Structural and Functional Characterization of Membrane Proteins and Viral Entry. *Journal of the American Chemical Society* **2018,** *140* (34), 10639-10643.
173. Jamshad, M.; Grimard, V.; Idini, I.; Knowles, T. J.; Dowle, M. R.; Schofield, N.; Sridhar, P.; Lin, Y.-P.; Finka, R.; Wheatley, M.; Thomas, O. R.; Palmer, R. E.; Overduin, M.; Govaerts, C.; Ruysschaert, J.-M.; Edler, K. J.; Dafforn, T. R., Structural analysis of a nanoparticle containing a lipid bilayer used for detergent-free extraction of membrane proteins. *Nano Res* **2015,** *8* (3), 774-789.

174. Ravula, T.; Hardin, N. Z.; Ramadugu, S. K.; Cox, S. J.; Ramamoorthy, A., Formation of pH-Resistant Monodispersed Polymer-Lipid Nanodiscs. *Angew Chem Int Ed Engl* **2018,** *57* (5), 1342-1345.
175. Oluwole, A. O.; Klingler, J.; Danielczak, B.; Babalola, J. O.; Vargas, C.; Pabst, G.; Keller, S., Formation of Lipid-Bilayer Nanodiscs by Diisobutylene/Maleic Acid (DIBMA) Copolymer. *Langmuir* **2017,** *33* (50), 14378-14388.
176. Hardin, N. Z.; Kocman, V.; Di Mauro, G. M.; Ravula, T.; Ramamoorthy, A., Metal-Chelated Polymer Nanodiscs for NMR Studies. *Angew Chem Int Ed Engl* **2019,** *58* (48), 17246-17250.
177. Ravula, T.; Hardin, N. Z.; Ramamoorthy, A., Polymer nanodiscs: Advantages and limitations. *Chem. Phys. Lipids* **2019,** *219*, 45-49.
178. Stepien, P.; Augustyn, B.; Poojari, C.; Galan, W.; Polit, A.; Vattulainen, I.; Wisnieska-Becker, A.; Rog, T., Complexity of seemingly simple lipid nanodiscs. *Biochimica et Biophysica Acta (BBA) - Biomembranes* **2020,** *1862* (11), 183420.
179. Grethen, A.; Oluwole, A. O.; Danielczak, B.; Vargas, C.; Keller, S., Thermodynamics of nanodisc formation mediated by styrene/maleic acid (2:1) copolymer. *Scientific Reports* **2017,** *7* (1), 11517.
180. Ujwal, R.; Bowie, J. U., Crystallizing membrane proteins using lipidic bicelles. *Methods (San Diego, Calif.)* **2011,** *55* (4), 337-341.
181. Triba, M. N.; Warschawski, D. E.; Devaux, P. F., Reinvestigation by Phosphorus NMR of Lipid Distribution in Bicelles. *Biophysical Journal* **2005,** *88* (3), 1887-1901.
182. Piai, A.; Fu, Q.; Dev, J.; Chou, J. J., Optimal Bicelle q for Solution NMR Studies of Protein Transmembrane Partition(). *Chemistry (Weinheim an der Bergstrasse, Germany)* **2017,** *23* (6), 1361-1367.
183. Sanders, C. R.; Prosser, R. S., Bicelles: a model membrane system for all seasons? *Structure* **1998,** *6* (10), 1227-1234.
184. Zhu, Y.; Mohapatra, S.; Weisshaar, J. C., Rigidification of the Escherichia coli cytoplasm by the human antimicrobial peptide LL-37 revealed by superresolution fluorescence microscopy. *Proceedings of the National Academy of Sciences* **2019,** *116* (3), 1017-1026.
185. Gee, M. L.; Burton, M.; Grevis-James, A.; Hossain, M. A.; McArthur, S.; Palombo, E. A.; Wade, J. D.; Clayton, A. H. A., Imaging the action of antimicrobial peptides on living bacterial cells. *Scientific Reports* **2013,** *3* (1), 1557.
186. Sugiki, T.; Yamaguchi, Y.; Fujiwara, T.; Inouye, M.; Ito, Y.; Kojima, C., In-cell NMR as a sensitive tool to monitor physiological condition of Escherichia coli. *Scientific Reports* **2020,** *10* (1), 2466.
187. Pandit, G.; Biswas, K.; Ghosh, S.; Debnath, S.; Bidkar, A. P.; Satpati, P.; Bhunia, A.; Chatterjee, S., Rationally designed antimicrobial peptides: Insight into the mechanism of eleven residue peptides against microbial infections. *Biochimica et Biophysica Acta (BBA) - Biomembranes* **2020,** *1862* (4), 183177.
188. Li, J.; Wang, X.; Zhang, T.; Wang, C.; Huang, Z.; Luo, X.; Deng, Y., A review on phospholipids and their main applications in drug delivery systems. *Asian Journal of Pharmaceutical Sciences* **2015,** *10* (2), 81-98.
189. Somashekar, B. S.; Ijare, O. B.; Nagana Gowda, G. A.; Ramesh, V.; Gupta, S.; Khetrapal, C. L., Simple pulse-acquire NMR methods for the quantitative analysis of calcium, magnesium and sodium in human serum. *Spectrochimica Acta Part A: Molecular and Biomolecular Spectroscopy* **2006,** *65* (2), 254-260.
190. Kučerka, N.; Nieh, M.-P.; Katsaras, J., Fluid phase lipid areas and bilayer thicknesses of commonly used phosphatidylcholines as a function of temperature. *Biochimica et Biophysica Acta (BBA) - Biomembranes* **2011,** *1808* (11), 2761-2771.
191. Laulund, A. S.; Schwartz, F. A.; Christophersen, L.; Høiby, N.; Svendsen, J. S. M.; Stensen, W.; Thomsen, K.; Cavanagh, J. P.; Moser, C., Lactoferricin inspired peptide AMC-109 augments the effect of ciprofloxacin against Pseudomonas aeruginosa biofilm in chronic murine wounds. *Journal of Global Antimicrobial Resistance* **2021**.

192. Falavigna, M.; Klitgaard, M.; Berthelsen, R.; Müllertz, A.; Flaten, G. E., Predicting Oral Absorption of fenofibrate in Lipid-Based Drug Delivery Systems by Combining In Vitro Lipolysis with the Mucus-PVPA Permeability Model. *Journal of Pharmaceutical Sciences* **2021,** *110* (1), 208-216.
193. Su, J.; Marrink, S. J.; Melo, M. N., Localization Preference of Antimicrobial Peptides on Liquid-Disordered Membrane Domains. *Frontiers in Cell and Developmental Biology* **2020,** *8*.
194. Kay, A. R., How Cells Can Control Their Size by Pumping Ions. *Frontiers in Cell and Developmental Biology* **2017,** *5*.
195. Hedegaard, S. F.; Derbas, M. S.; Lind, T. K.; Kasimova, M. R.; Christensen, M. V.; Michaelsen, M. H.; Campbell, R. A.; Jorgensen, L.; Franzyk, H.; Cárdenas, M.; Nielsen, H. M., Fluorophore labeling of a cell-penetrating peptide significantly alters the mode and degree of biomembrane interaction. *Scientific Reports* **2018,** *8* (1), 6327.
196. Ravula, T.; Hardin, N. Z.; Ramadugu, S. K.; Ramamoorthy, A., pH Tunable and Divalent Metal Ion Tolerant Polymer Lipid Nanodiscs. *Langmuir* **2017,** *33* (40), 10655-10662.
197. Linke, P.; Amaning, K.; Maschberger, M.; Vallee, F.; Steier, V.; Baaske, P.; Duhr, S.; Breitsprecher, D.; Rak, A., An Automated Microscale Thermophoresis Screening Approach for Fragment-Based Lead Discovery. *J Biomol Screen* **2016,** *21* (4), 414-21.
198. Zhou, X.; Pan, Y.; Wang, Y.; Wang, B.; Yan, Y.; Qu, Y.; Ke, X., Tanshinones induce tumor cell apoptosis via directly targeting FHIT. *Scientific Reports* **2021,** *11* (1), 12217.
199. Patridge, E.; Gareiss, P.; Kinch, M. S.; Hoyer, D., An analysis of FDA-approved drugs: natural products and their derivatives. *Drug Discovery Today* **2016,** *21* (2), 204-207.
200. Ganesh, A. N.; Donders, E. N.; Shoichet, B. K.; Shoichet, M. S., Colloidal aggregation: From screening nuisance to formulation nuance. *Nano Today* **2018,** *19*, 188-200.

PAPER I

BBA - Biomembranes 1864 (2022) 183911

Contents lists available at ScienceDirect

BBA - Biomembranes

journal homepage: www.elsevier.com/locate/bbamem

WIND-PVPA: Water/Ion NMR Detected PVPA to assess lipid barrier integrity *in vitro* through quantification of passive water- and ion transport

Philip Rainsford [a,1], B. Ravdna Sarre [a,1], Margherita Falavigna [b], Bjørn Olav Brandsdal [a], Gøril Eide Flaten [b], Martin Jakubec [a,1], Johan Isaksson [a,*,1]

[a] Dept. Chemisty, UiT the Arctic University of Norway, 9037 Tromsø, Norway
[b] Dept. Pharmacy, UiT the Arctic University of Norway, 9037 Tromsø, Norway

ARTICLE INFO

Keywords:
Nuclear magnetic resonance
PVPA
Permeability assay
Water permeability
Salt permeability
Antimicrobial peptides
Lipid vesicles

ABSTRACT

Water/Ion NMR Detected – Phospholipid Vesicle Permeability Assay (WIND-PVPA), is presented as a novel, straightforward and automatable method to assess lipid barrier integrity *in vitro*. The apparent permeability constants of water- and ions across the PVPA barriers are determined in a one-pot experiment under the influence of membrane-active guest molecules. NMR spectroscopy is used to quantify the water directly (D_2O) and the ions indirectly (complexed with EDTA) as a function of time. WIND-PVPA is demonstrated using four anti-microbial peptides, to show that membrane active molecules can be differentiated by their disruptive influence on the PVPA system. The results obtained are compared with explicit molecular dynamics simulations of lipid bilayers, AMPs, water and salt, where the motions of all individual water molecules relative to the lipid bilayer are monitored over the course of the simulations, allowing the calculation of theoretical apparent permeability constants of the corresponding single bilayer systems.

Proof-of-principle is presented that WIND-PVPA can be used to evaluate the lipid barrier destabilizing effect of active guest molecules by measuring changes in passive water- and ion permeabilities upon exposure. The method is highly flexible in terms of barrier composition, choice of probes and membrane active compounds.

1. Introduction

The escalation of multi-resistant bacteria, in combination with the low success rate of the discovery of new classes of antibiotics during the last decades, presents a dire threat to human health globally [1]. The need for new classes of antibiotics, as well as other treatment strategies, is ever increasing. On this background, the bacterial membrane has attracted increased attention as a drug target for several reasons. Firstly, there is limited development of resistance against antimicrobials that target the bacterial cell membrane [2]. Secondly, direct targeting of the cell membrane is a promising strategy to perturb non-growing, dormant infections and biofilms, where drugs targeting the bacterial metabolism are inefficient [3]. Thirdly, the development of many drug discovery hits with novel antimicrobial activities are discontinued due to inadequate permeability into the target bacteria, especially in the case of gram-negative bacteria, and thus targeting bacterial membrane permeability has emerged as a novel strategy in drug discovery [4].

One class of molecules with the capacity to directly target the cell membrane is antimicrobial peptides (AMPs). AMPs are a ubiquitous part of the innate immune defence in all living organisms, and they have been widely studied [5], with more than 3000 natural AMPs reported and characterized [6]. However, most natural AMPs are neither sufficiently potent, nor have suitable ADMET properties (absorption, distribution, mechanism, excretion, and toxicity) to be viable as commercial antibiotics for systemic (oral) administration. Over the last few decades, extensive effort has been put in to explore the potential of synthetic optimized AMPs to be developed into more realistic drug candidates.

One challenge in the rational design of AMPs is that drug discovery tools are traditionally not developed to deal with large, flexible molecules that target an amorphous target like a cell surface and act through diverse and poorly defined mechanisms. There is a lack of an in-depth understanding of AMP modes of action (MOA) and how to best optimize their activity since their MOA are diverse and often involve various types of self-aggregation on the bacterial membrane, needing to reach a

* Corresponding author.
E-mail address: johan.isaksson@uit.no (J. Isaksson).
[1] Shared authorship

https://doi.org/10.1016/j.bbamem.2022.183911
Received 22 December 2021; Received in revised form 23 February 2022; Accepted 5 March 2022
Available online 22 March 2022

local critical threshold concentration before efficacy is achieved [7]. The structural and physicochemical interplay between peptides and lipid bilayers needs to be characterized in order to determine the MOA of AMPs and optimize the activity of AMPs and other membrane-active compounds. An interesting interfacial activity model has been proposed with some success in unifying how the MOA of AMPs can be expressed [8]. The reviewed results therein identify that pore-forming peptides are exceedingly rare, and instead the overwhelming majority of AMPs does not form discrete pores in membranes, not even transiently, but instead causes bilayer leakage by a general disruption of membrane integrity. It is also noted that high peptide to lipid ratios used in vesicle-based leakage assays are prone to induce vesicle fusion, which in turn cause the release of the vesicle contents [8].

Hydration in general plays a vital role in lipid bilayer structure and function, for example, defining the stability of lipid vesicles in solution and controlling the permeability of small molecules across lipid bilayers [9]. Small uncharged molecules, including water, passively cross lipid bilayers with relative ease, which is necessary to maintain osmotic equilibrium while restricting the free diffusion of ions and large biomolecules. The topic is under some debate, but data suggests that the two dominating models can be used to describe water permeability – the solubility-diffusion model [10], and the transient pore formation model, the latter being more successful for describing the permeability of charged solutes [11]. In the rate-limiting diffusion step through the hydrophobic core of the bilayer, the diffusion is limited by available space, and hence the rate of diffusion is coupled to the order and motion of the lipid core, as solvated water and lipid molecules are dynamically linked to each other [12]. On a similar note, the rate of transient pore formation is expected to be higher in thinner and less ordered lipid phases. There is thus a link between lipid perturbation and increased permeability in both models [13].

Small cationic synthetic AMPs are known to associate near the lipid surface and both cause disorder in the lipid packing and pull down water molecules deeper towards the core of the lipid bilayer [14–15]. It is known that lipid bilayer hydration is associated with changes in lipid bilayer properties like increased permeability, increased area per lipid and reduced electric membrane potential. Small synthetic AMPs typically kill bacteria *via* what is traditionally described as a carpet model where peptides associate to-, and aggregate on, the membrane surface, where they give rise to a large imbalance in charge and surface tension between the outer and inner leaflet, eventually leading to a collapse of the membrane integrity [16]. Also, at concentrations lower than the critical concentration, the AMPs leads to membrane thinning, surface tension, clustering of anionic lipids and membrane deformation, all being physicochemical properties associated with increased permeability, loss of membrane potential and subsequent lysis [17]. It is also commonly observed that small synthetic AMPs exert an inhibitory effect on bacterial growth before they reach the critical Minimal Inhibitory Concentration (MIC) of fast membrane disruption. These observations, together with the role of membrane hydration and the bacterial membrane potential in permeability has sparked an interest in developing a simple assay to measure how the integrity of lipid bilayers is influenced by various AMPs or other guest molecules by quantifying the passive transport of ions and water across barriers composed of lipid bilayers.

As an alternative approach to vesicle leakage or vesicle swelling, we have explored the possibilities of measuring permeabilities across barriers constructed by immobilized phospholipid bilayer vesicle films on a solid membrane support. For this purpose, we have adapted an *in vitro* Phospholipid Vesicle-based Permeation Assay (PVPA) that was previously developed in our institute as an *in vitro* permeability model for passive drug transport through human biological barriers like intestine-, skin- and mucus membranes [18–21]. PVPA barriers are composed of a membrane filter support upon which liposomes with different size distributions and compositions are immobilized through cycles of centrifugation and freeze-thawing [18]. The resulting barriers are thus composed of layers of tightly packed vesicles on top of cellulose filter. Such barriers can be used to monitor the permeation of drugs from a donor to an acceptor compartment, which is subsequently quantified spectroscopically.

In the current study we have explored the possibility of using a modified version of the PVPA method, the Water/Ion NMR Detected-PVPA (WIND-PVPA), as a robust and straightforward way to measure to what extent guest molecules affect the membrane permeabilities of different entities, like ions, water molecules or other molecules of interest. The method was developed to study water and ion mobility over bacterial membranes in the context of bacterial membrane potential, but the method could be tailored to different contexts by studying the permeability of different molecules across different barriers.

2. Results and discussion

2.1. The PVPA model system

The PVPA model is an *in vitro* permeability model that is compatible with a wide array of molecular environments and barrier compositions (Fig. 1) [20–22]. In order to prove the principle of using the PVPA to probe for membrane disruptive activity of active AMPs, a model system composed by DMPC and DMPG was chosen. This composition has previously been successfully applied for the selection of active AMPs from combinatorial libraries [23]. In order to assess the effect of the surface charge of the lipid bilayers, the experiments were repeated in both pure DMPC (from here on referred to as **PC**) and 95% DMPC, 5% DMPG (*w/w*) (from here on referred to as **PC/PG**).

Ion and water transition across the barriers was monitored by solution NMR. A set amount of D_2O (80% *v/v*) was introduced into the donor chamber, while the acceptor chamber contained only 0.5% D_2O (for lock). Water transmission was subsequently quantified directly by ^2H NMR. In order to monitor ion transfer across the barrier, free EDTA was included in the acceptor chamber as a reporter molecule, while salts (100 mM $CaCl_2$ and 100 mM $MgCl_2$) were added to the donor chamber and the emerging proton resonances of the EDTA-Ca^{2+} and EDTA-Mg^{2+} complexes in the acceptor chamber were quantified using ^1H NMR. Transitioned ions form strong complexes with EDTA, which gives rise to unique and stable non-overlapping proton signals for the ion complexes, which can be used to identify and quantify the ion complexes individually [24]. This allows for parallel monitoring of both Mg^{2+} and Ca^{2+} in a single pot experiment provided there is unbound EDTA in excess (Fig. S1 in the SI). The cumulative amounts quantified from the integration of the ^1H and ^2H resonances in the acceptor solutions were plotted *versus* time to visualize the permeability profiles, and the apparent permeability constants (P_{app}) were calculated according to Eq. (1) (See Materials and methods).

The potential to use the PVPA to measure changes in permeability as a function of exposure to various guest molecules has been evaluated using four synthetic peptides (compounds **1–4**) and TritonX-100 (**5**) as a positive control for membrane disruption (Fig. 2). KP-76 (**1**), AMC-109 (**2**) and cyclic hexapeptide cWRWRWR (**3**) are established synthetic AMPs with known MIC values (inserted table in Fig. 2) that have been selected for their different activities despite their chemical similarity [25–26]. From this set, AMC-109 (formerly LTX-109) is an AMP with a MOA that targets the bacterial cell wall. AMC-109 is currently in phase IIA trials for treatment of topical infections [27]. Due to poor solubility of AMC-109 in the donor buffer, owing to the high concentration of salts, only D_2O transmission data was acquired for AMC-109 [25–26]. The RAR peptide was selected for its chemical similarity to both KP-76 and AMC-109, while it is neither interacting with lipid bilayers nor possessing any antimicrobial effect because of its lack of hydrophobic bulk (unpublished results). Triton (2% *w/v*), used as positive control, is known to effectively lyse cell membranes and to be efficient at solubilizing PC lipids [28]. In the PVPA, Triton is observed to increase the water permeability across both **PC** and **PC/PG** barriers by approximately 50% [28].

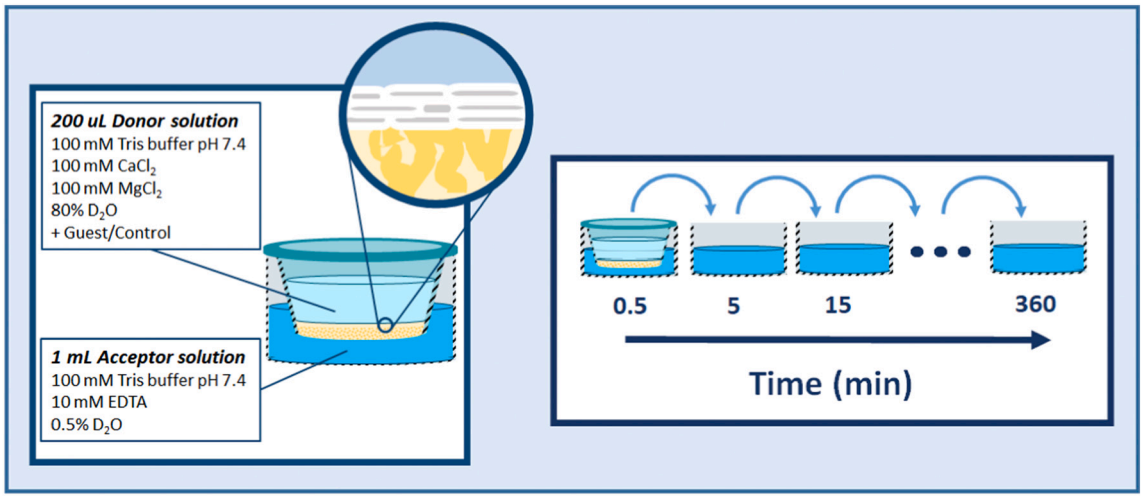

Fig. 1. Experimental setup of the PVPA model in which phospholipid vesicles are packed on top of a porous cellulose support strip that is attached to a plastic insert. The insert houses the donor solution which contains the guest molecule and is placed in a well of acceptor solution for increasing intervals of time.

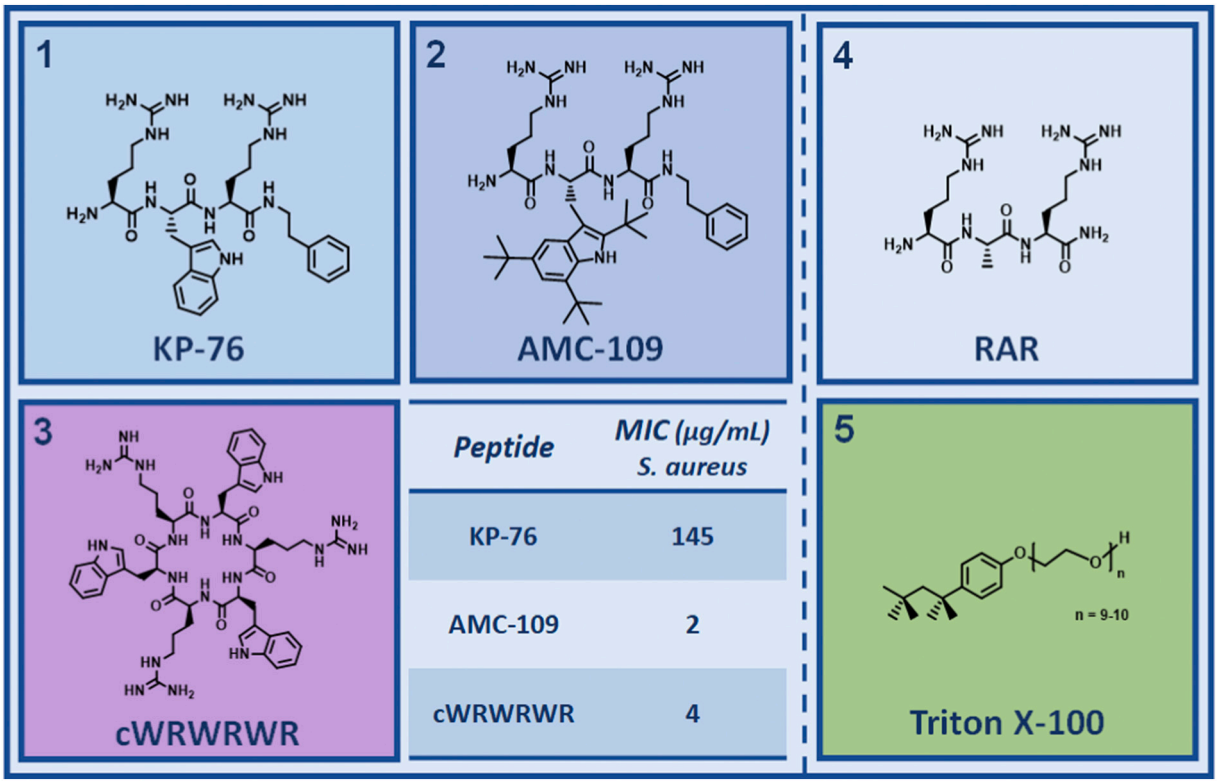

Fig. 2. Chemical structures of compounds (1) **KP-76** (RWR-NHPh) [26], (2) **AMC-109** (RTBtR-NHPh) [29], (3) **cWRWRWR**, (4) **RAR** and (5) **TritonX-100**. Minimum inhibitory concentration (MIC) for *S. aureus* strain ATCC 25923.

In order to show that the PVPA model can be used to evaluate the lipid bilayer integrity in response to external factors, the D_2O transmission across the barriers was quantified under different salt concentrations, lipid compositions, and in the presence of different AMPs.

2.2. Salt influence

The permeability of water and solutes across any semi-permeable barrier is known to be affected by several factors, *i.e.* the osmotic pressure, hydrostatic pressure difference and concentration differences of the solute in question – as described by the Kedem-Katchalsky equations [30–31]. In the PVPA experimental setup, the addition of salt on one side of the barrier gives rise to a net osmotic pressure on the semi-permeable barrier. This will drive water molecules against the salt gradient, since water crosses lipid bilayers more easily than ions. The ions also exert a concentration driven flux from the donor to the acceptor chamber, which is expected to also affect the water flux in the system. Salt is furthermore known to potentially affect the ordering and structure of the lipid bilayers themselves [32–33]. Therefore, the basic influence of the salt concentration on D_2O transmission across the **PC/PG** barriers in the PVPA setup was first controlled by a series of blank experiments with increasing equimolar concentrations of $MgCl_2$ and $CaCl_2$ (Fig. S1 in the

Supporting information).

As expected, the measured rate of D_2O transmission decreased with increasing total salt concentration, as more water is retained on the donor side through osmotic pressure. The combined effect of salt presence on the system is hard to predict accurately for different systems, and Fig. S1 illustrates the importance of running blanks using identical lipid and salt concentrations, as well as other potential additives like for example DMSO as a solubility enhancer. There are no indications that the method does not tolerate salt concentrations up to 200 mM, thus allowing the acquisition of water and salt permeability data in a one-pot experiment if the appropriate blank is used.

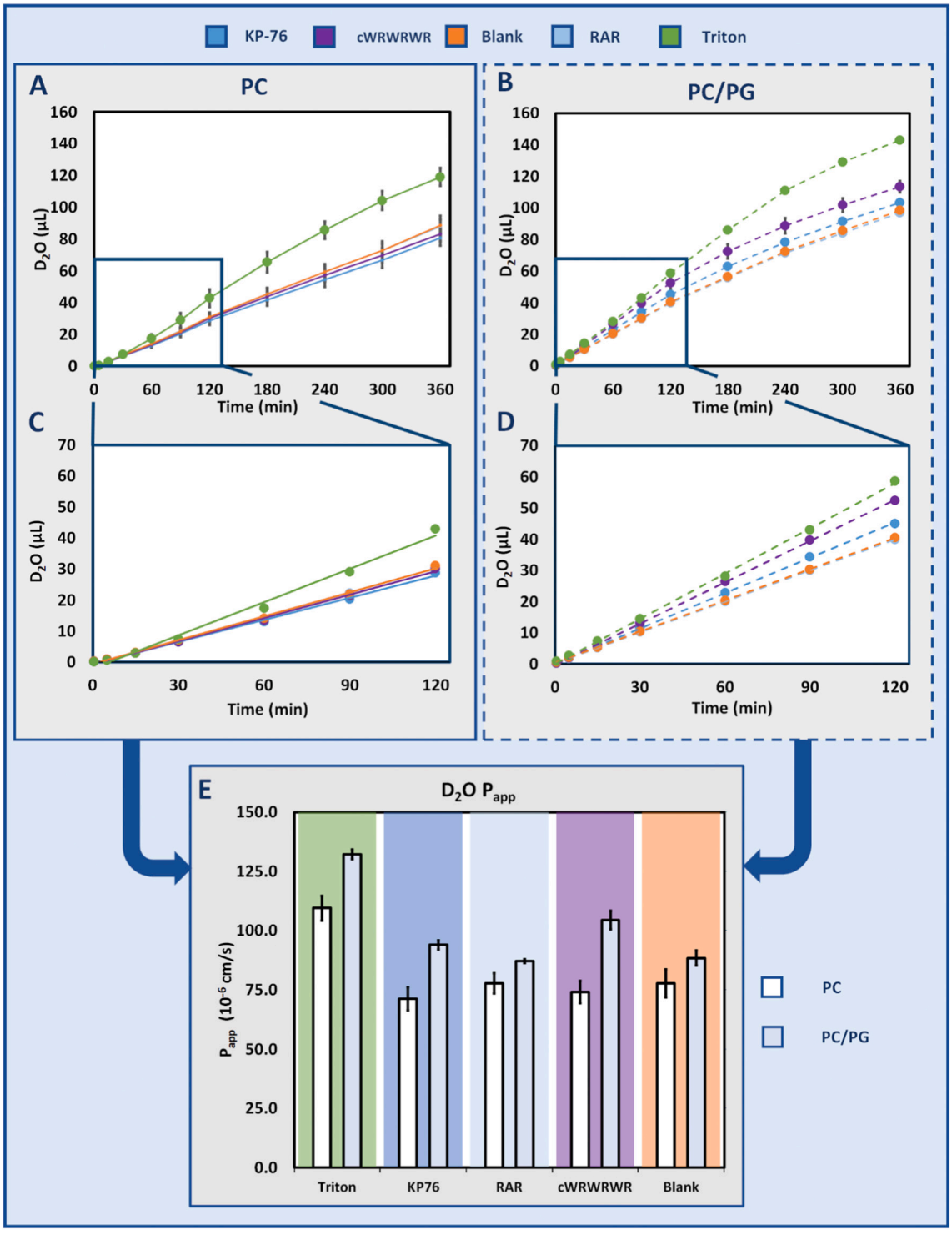

Fig. 3. Summary of the changes in the water permeability in the presence of antimicrobial peptides (**KP-76** and **cWRWRWR**,), negative control (**RAR**), positive control (**Triton**), or in the absence of any guest molecules (**blank**). The cumulative volume of D_2O transmitted across **PC** barriers was plotted against the 6 h experiment time acquired across (a) uncharged **PC** barriers and charged (b) **PC/PG** barriers. The respective initial slopes are expanded in (c) and (d). The apparent permeability constants (P_{app}) calculated from the initial slopes are summarised in (e). Error bars represent the standard deviation of the three replicates.

2.3. Water transmission

The permeability of water was tested for two lipid compositions – the **PC** and the **PC/PG**. In the **PC** barriers, the tested peptides showed little to no effect on the water transmission compared to the blank, with only Triton significantly increasing the permeability of water (Fig. 3 A, C). The abundance of negatively charged lipids on the surface of bacteria and cancer cells is known to be a selectivity factor for many antimicrobial/anticancer peptides, and the observed lack of membrane destabilization could potentially be attributed to the lack of any negative net charge on the lipid barrier surface. It is worth noting that this observation alone would not rule out other causes, like for example the overall quality of the lipid packing, or vesicle fusion on the membrane support being more efficient in the absence of charge.

There was a consistent trend that the baseline transmission of D_2O across the barrier is increased when PG was present. This increase is observable in all tested samples, most evidently by the blank and the control peptide. Comparison of the controls showed an ~15% increase in water transmission for Triton and the blank with the introduction of DMPG.

Interestingly, significant additional reductions in barrier integrity were observed for the active peptides with the introduction of a negatively charged component to the barriers. The addition of 5% PG lipids allows favourable electrostatic interactions between the positively charged peptides and the negatively charged lipids, which was reflected in the AMPs significantly reducing the integrity of the lipid barrier in the assay (Fig. 3 B, D). The cyclic cWRWRWR (**3**) increased the P_{app} of water from 74 to 104 $\times$ 10^{-6} cms^{-1} (~40%) across the **PC/PG** barrier compared to the **PC** barrier, which was close to the P_{app} increase caused by Triton treatment. Similarly, the presence of charged lipids enabled also the moderately active peptide, KP-76 (**1**), to increase the permeability across the barrier from 71 to 94 $\times$ 10^{-6} cms^{-1} (~30%). The negative control peptide, RAR (**4**), had no observable effect on the P_{app} of D_2O across neither the **PC** nor the **PC/PG** barriers compared to the control.

AMC-109 (**2**) was not soluble in the salt concentration used in the one-pot experiment, thus only the water permeability was assessed in the absence of salt across **PC** barriers (Fig. 4). Even though the peptide possesses a low MIC value of 2 μg/ml, there is no detectable effect on the water permeability under these experimental conditions. This will be further discussed together with the computer simulation results below.

2.4. Ion transmission

Ion transmission was monitored by ^1H NMR using EDTA as a reporter molecule. EDTA has a strong affinity for divalent ions and forms stable complexes with unique chemical shifts with both Mg^{2+} and Ca^{2+}. Comparison of Ca^{2+} and Mg^{2+} P_{app} (Fig. 5) shows that the P_{app} and total transmission for Mg^{2+} was consistently higher than for Ca^{2+}. This observation was in line with the expectation that the smaller size of the Mg^{2+} ions would allow them to more easily cross the barrier. It is noteworthy that there is a lag-phase before permeated ions can be detected that is not present for water. However, overall the ion permeability reflects the same pattern as for the water permeability above. In pure **PC** barriers there is no observed increase of permeability upon treatment with KP-76 (**1**), AMC-109 (**3**) and RAR (**4**), while in the **PC/PG** barriers there is an increase in ion leakage reflecting the ranking of the MIC values of the peptides; the most active compound, cWRWRWR (**3**), showed the largest increase in ion permeability. While the relative changes in the P_{app} of ions are consistent with the respective D_2O transmissions, there are some significant deviations.

The ion permeability did not change significantly upon the introduction of charged lipids as was the case for water permeability (compare Figs. 3e and 5e). This suggested that the overall increase in water permeability observed for the **PC/PG** barriers over the **PC** barriers was not just a potential effect of imperfect lipid packing onto the cellulose support caused by anionic repulsion. This was also supported by both barriers having near identical electric resistance and calcein permeability (Supp Table S1).

With respect to the effect of peptide exposure, a stronger relative impact on ion transmission is observed for cWRWRWR (**3**) in **PC/PG** barriers compared to the respective D_2O transmissions. The ion P_{app} is increased two-fold in the presence of charge, while only a 40% increase is observed for D_2O. This behavior is not observed for KP-76 (**1**), where there is no observed increase in salt permeability. This difference in response indicates that there is difference in how KP-76 (**1**) and cWRWRWR (**3**) interact with the lipid barriers, and particularly in how cWRWRWR (**3**) facilitates ion transport across the barrier.

The full time resolved permeability curve further reveals differences in behavior of the different guest molecules. The initial transmission rate of ions is higher for cWRWRWR (**3**) than that of Triton (**5**), but over time the rate in the presence of Triton (**5**) steadily increases to the point that it overtakes the permeabilizing effect of cWRWRWR (**3**) after 240 min

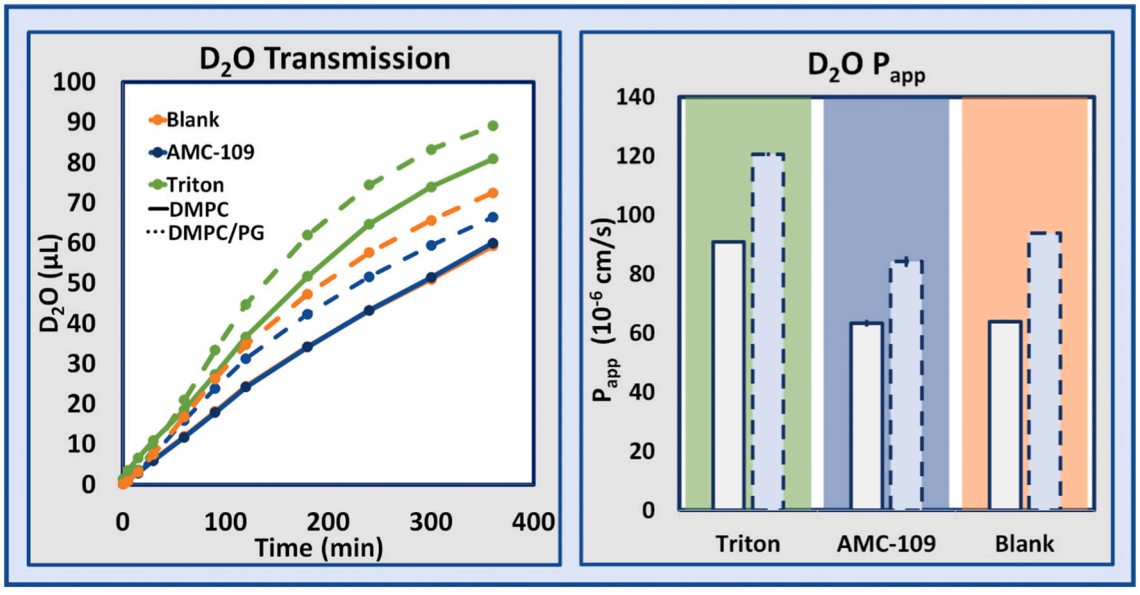

Fig. 4. Water permeability of AMC-109 (**2**) across PC barriers in no salt conditions. Left – The cumulative volume of D_2O transmitted across **PC** (solid lines) and **PC/PG** (dashed lines) barriers. Right - The apparent permeability constant (P_{app}) calculated from the initial slopes.

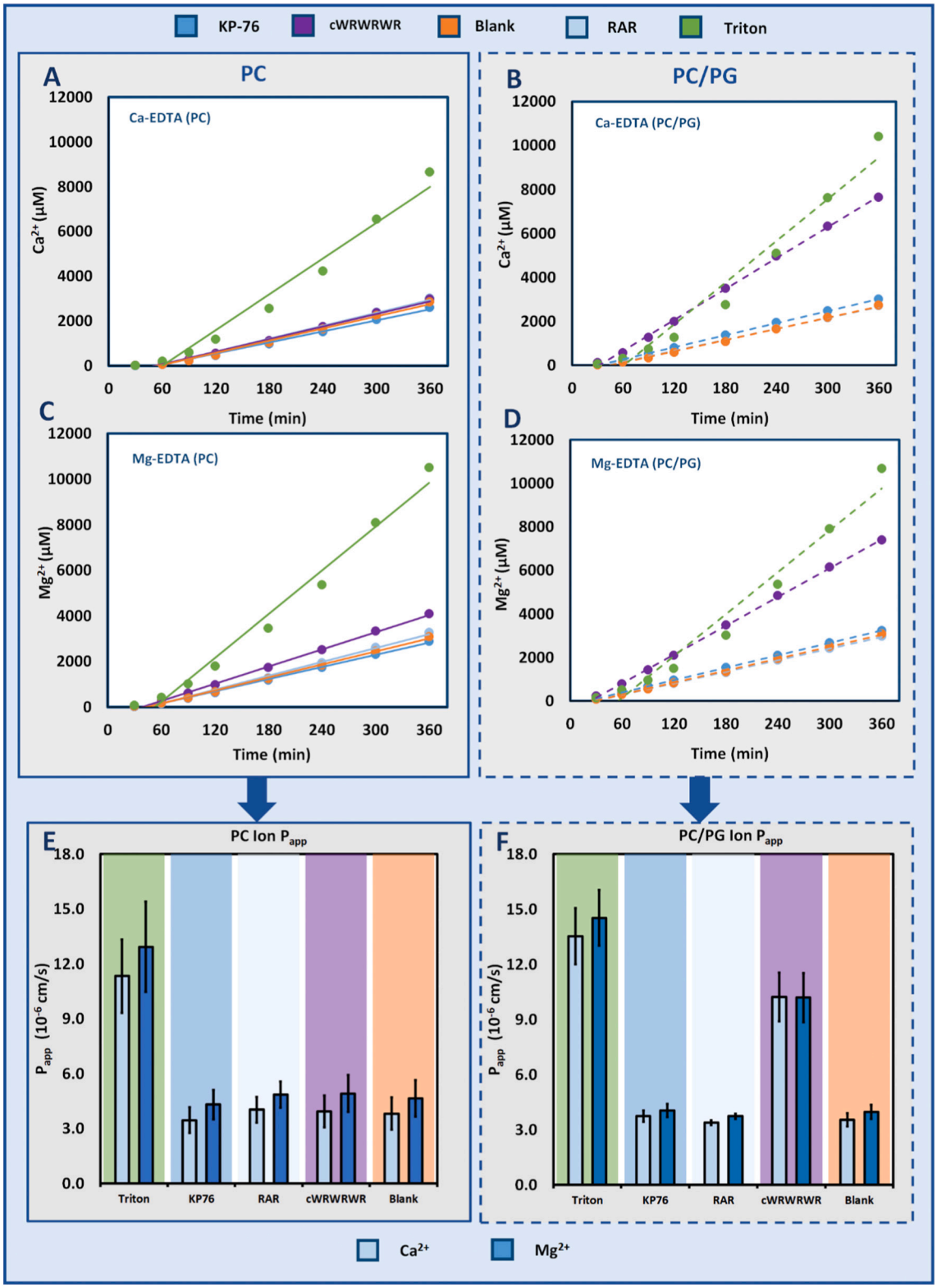

Fig. 5. The observed changes in the permeability of Ca^{2+} and Mg^{2+} in presence of antimicrobial peptides - KP-76 (**1**), cWRWRWR (**3**), controls RAR (**4**), Triton (**5**), and blank, across both **PC** and **PC/PG** barriers. The top graphs show the cumulative concentration of Ca^{2+} transmitted across (a) **PC** and (b) **PC/PG** barriers during the 2 first hours of the experiment. The middle panels show the corresponding plots for Mg^{2+} across (c) **PC** and (d) **PC/PG** barriers. The solid line presents the linear fit of the seven data points in this period. The bottom panel summarizes the calculated P_{app} of Ca^{2+} and Mg^{2+} across the (e) **PC** and (f) **PC/PG** barriers. Error bars represent the standard deviation of three replicates.

(Supp Fig. S2). The accelerating effect on the P_{app} by Triton (**5**) exposure suggests that Triton (**5**), unlike the AMPs, exerts a continuous dissolving effect on the lipids that make up the barriers.

Based on the permeability measurements alone it is difficult to make any detailed conclusions about how the different lipid compositions and AMP interactions affect the water- and ion permeabilities. To increase our understanding of the studied systems we have therefore complemented the permeability experiments with a computer simulation setup to that allows the quantification of membrane hydration, water permeability, lipid disorder and bilayer thickness in the presence of AMPs.

2.5. Molecular modelling

Explicit atom calculations of biomembranes are computationally demanding, hence two of the peptides, KP-76 (**1**) and AMC-109 (**2**), were selected for detailed computer simulations. Data analysis protocols were setup to analyse the effect of the antimicrobial peptides on the lipid bilayer integrity, and to explore the behavior of the water in the presence and absence of AMPs. The simulations were setup using explicit lipid molecules in the two lipid compositions used in the assay – 100% DMPC (**PC**) and 95% DMPC/5% DMPG (**PC/PG**). Simulations were then performed in the presence of 0, 4 or 8 peptide molecules per 336 lipid molecules, in triplicates with different seeds over a total of 600 ns. The analysis was started after 5 ns of simulation to ensure the system was in an equilibrated state throughout the trajectory.

To track water molecules crossing the bilayer, a script was written to select all water molecules that during the simulation entered the hydrophobic core of the bilayer (see experimental section for details). The selected waters were then recorded throughout the trajectory to distinguish between molecules crossing and exiting the bilayer at the opposite side (Fig. 6b) from the ones merely entering and returning to the bulk water on the side they came from (Fig. 6a).

First, the two lipid compositions were simulated without any guest peptides to establish the baseline passive water permeability in the two models. Analysis of the water molecules revealed that over the course of 195 ns, 30 ± 6 and 36 ± 7 water molecules crossed the bilayer for **PC** and **PC/PG** respectively. There were no major events observed for the lipid bilayer on the studied time scale, but water molecules were instead passively diffusing through, distributed over the whole trajectory. The simulation time is expected to be too short to observe events like transient pore formation taking place with any probability, but long enough to allow the observation of water molecules crossing through passive diffusion (see Fig. 6b for a representative trajectory in pure lipids and Supplementary for all analysed trajectories).

The observed simulated rates correspond to a theoretical permeability constant of 2.2 ± 0.4 and 2.6 ± 0.5 × 10^{-3} cm/s for the two lipid compositions respectively.

Bilayers of the two lipid compositions were then challenged with exposure to 4- or 8 AMP molecules, corresponding to 1:84 and 1:42 peptide:lipid ratio respectively. That places the concentration in a range below the MIC values that report rapid killing of bacteria through membrane-cataclysmic events. The effects on the lipid bilayer order and thickness, as well as the water permeability, were examined for signs of general destabilization that could explain bacteriostatic effects below the MIC of rapid cell disruption.

With respect to the two lipid compositions used, the overall result was that the number of water molecules penetrating the bilayers was similar (Fig. 7a). Experiment suggests that water penetrates the **PC/PG** barriers slightly more efficiently than the pure PC barriers, and this is also the weak trend observed in the simulations, though the sampling was insufficient to identify any statistically significant differences in permeability (Fig. 7b).

The statistically significant observation that could be made from the water counts was that the presence of 8 molecules of KP-76 (**1**) increased the number of water molecules that successfully penetrated deep into the bilayer (Fig. 7a). However, it was qualitatively observed that peptides penetrating down into the bilayer often pulled water molecules with them, increasing the overall hydration of the hydrophobic core. In order to visualize the total hydration of the bilayer core, the time each water molecule spent in the $-5 < Z < 5$ range was integrated over each trajectory (Fig. 7c). The hydration plot displayed a clear trend that more

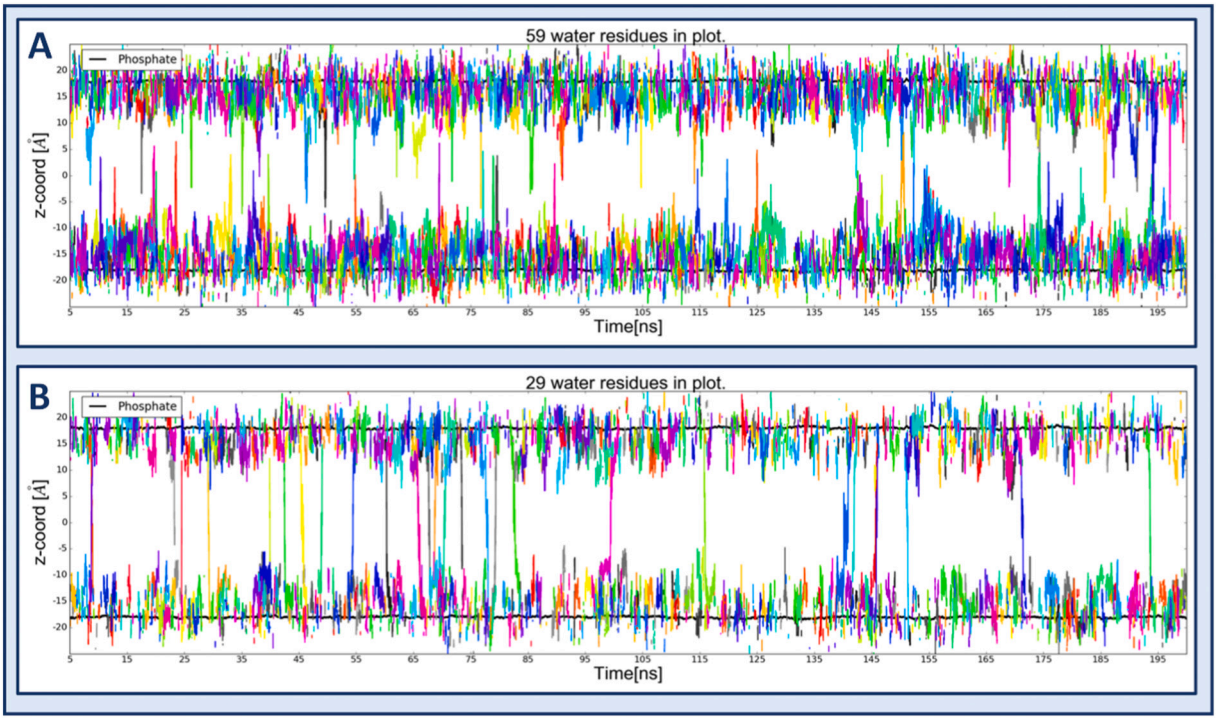

Fig. 6. Representative plot of selected water molecules that either enter the hydrophobic core and return to the bulk water of the same side (a) or that cross the bilayer and exit on the opposite side (b). Each color represents one unique water molecule.

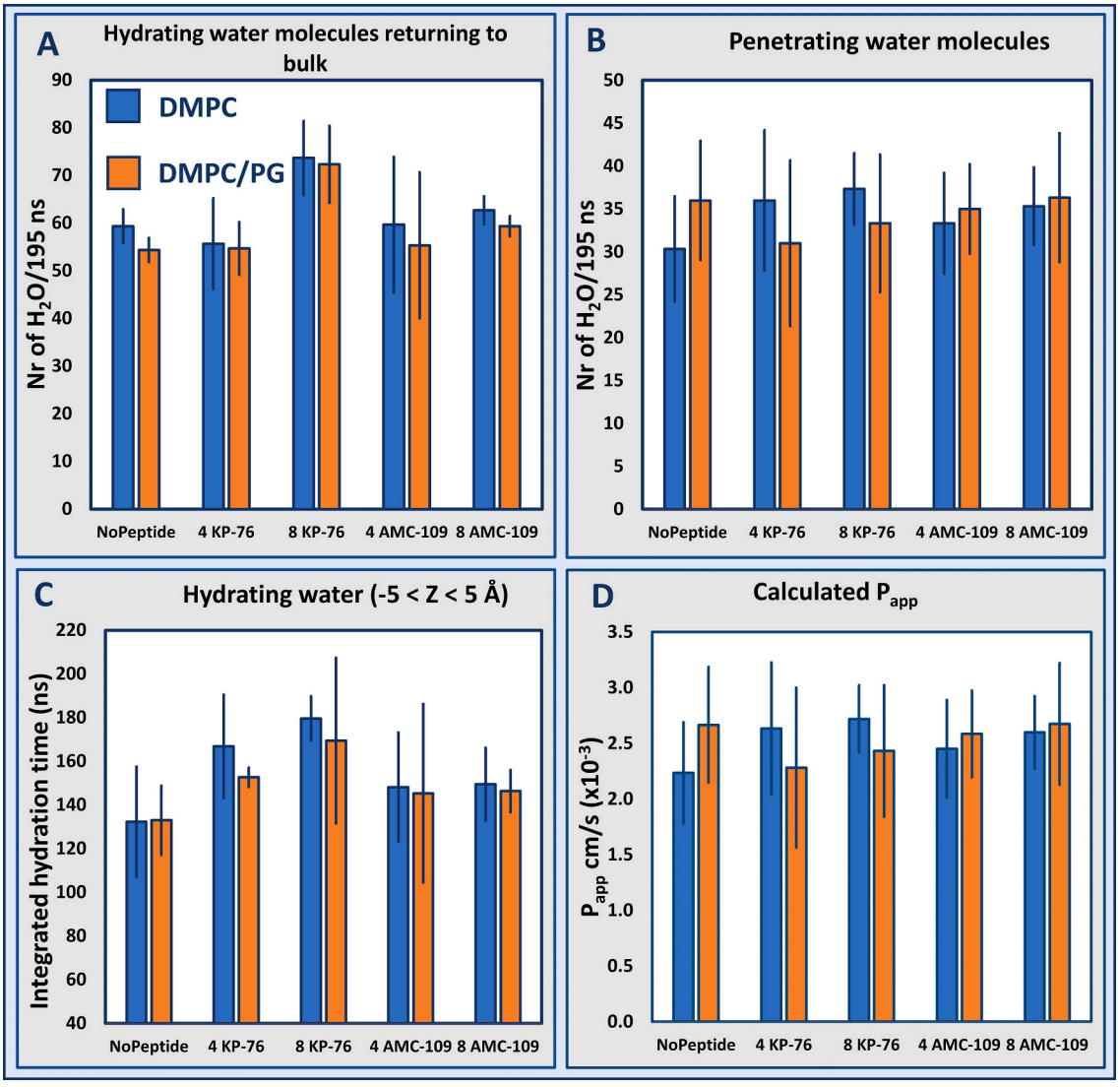

Fig. 7. Diagram showing the raw number of water molecules that enter the lipid bilayer during the simulations and then either (a) return to the bulk water or (b) cross the bilayer. In (c) the time of all water molecules spent within 5 Å of the middle if the bilayer is integrated to represent the overall hydration of the hydrophobic core. For completeness, (d) shows the simulated P_{app} calculated from the permeation counts in (b). Simulations have been performed in using either **PC** (blue) or **PC/PG** (orange), and in the presence of 4 or 8 KP-76 (**1**) or AMC-109 (**2**) (formerly LTX-109) respectively. (For interpretation of the references to color in this figure legend, the reader is referred to the web version of this article.)

water resides longer in the bilayer when more KP-76 (**1**) is added to the simulations - this is true in both compositions. Thus, while these simulations were not sufficiently long and did not include a sufficiently high peptide:lipid ratio to reproduce a statistically significant increase in the permeating water molecules count, they could show that the water molecules that entered the bilayer stayed there for a longer time, and therefore the total water content in the lipid bilayer over time increased significantly.

AMC-109 (**2**) did not cause any increase in water permeability or hydration in the simulations, which is in agreement with the lack of effect observed in the WIND-PVPA, despite AMC-109 (**2**) being a potent AMP able to disrupt bacterial cell walls at critical peptide:lipid ratios. Inspection of the simulations quickly revealed that AMC-109 (**2**) was prone to self-aggregate instead of penetrating into the lipid bilayer, explaining the lack of observable effect (Fig. 8) *versus* lipid compositions with a low charge density. This had the effect that for the majority of the time, AMC-109 (**2**) had no contact surface with the lipid bilayer, and hence did not significantly reduce the bilayer integrity.

3. Conclusion

The effect of three antimicrobial compounds on the permeability of zwitterionic lipid barriers has been compared in the presence- (**PC/PG**), and absence (**PC**), of negative charge for three anti-microbial peptides: KP-76 (**1**), AMC-109 (**2**) and cWRWRWR (**3**). KP-76 (**1**) has a modest MIC value, whereas AMC-109 (**2**) and cWRWRWR (**3**) both possess potent anti-microbial activities, reflected by MIC values of 2 μg/ml and 4 μg/ml against *S. aureus* respectively (Table 1).

Interestingly, none of the peptides had any statistically significant effect on the barrier integrity in the absence of negatively charged lipids, but as soon as a small fraction of charge was introduced (5% PG) a destabilizing effect of the peptide interactions began to emerge. KP-76 (**1**), cWRWRWR (**3**), and RAR (**4**) followed the expected trend according to their respective activities, where the modestly active KP-76 (**1**) results in a small but statistically significant increase in water permeability across the barrier with 5% positive charge (**PC/PG**), while the more potent cyclic peptide had a pronounced effect on the permeability, and especially on the ion permeability which saw a twofold increase in permeability compared to the blank. These observations are in line with

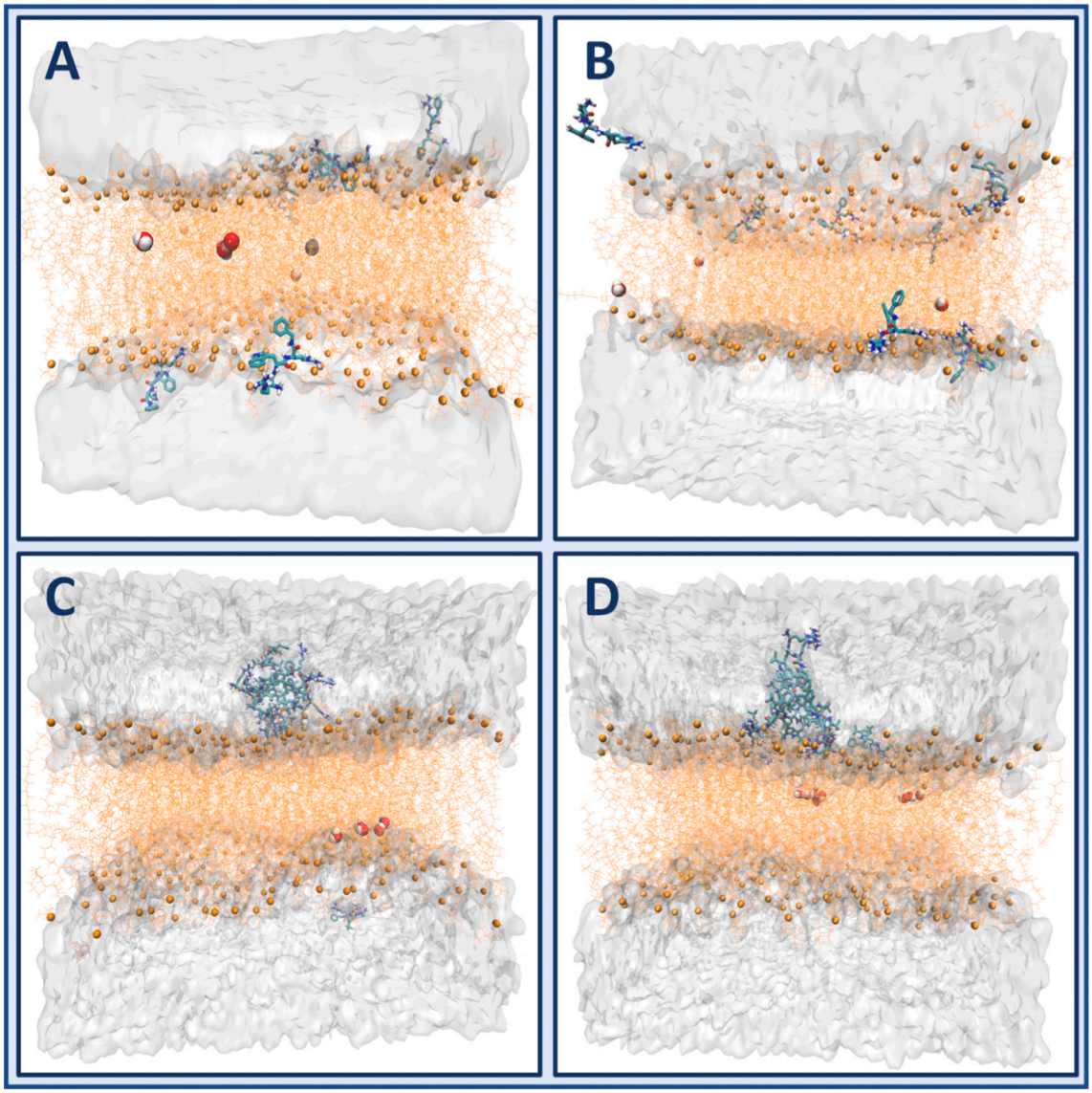

Fig. 8. Representative snapshots of the simulation of 8 molecules of KP-76 (**1**) in (a) **PC** and (b) **PC/PG** bilayers, compared to 8 molecules of AMC-109 (**2**) in (c) **PC** and (d) **PC/PG** bilayers. AMC-109 (**2**) displayed a clear tendency to self-aggregate and to stay in these aggregates during the simulation time.

this class of peptides displaying a selectivity for negatively charged surfaces of bacterial- and cancer cells over the neutral surface of healthy eukaryotic cells [34–35].

The most active peptide, AMC-109 (**2**), did however behave unexpectedly in the assay, not displaying any effect on the permeability of neither the **PC** nor the **PC/PG** barriers. The computer simulations provided a plausible explanation as to why AMC-109 (**2**) did not damage the integrity of the barriers, as AMC-109 (**2**) was prone to spontaneously self-aggregate and form stable micelle-like structures in the simulations. This could potentially serve as a reservoir for peptide molecules and contribute to a more pronounced threshold concentration and selectivity towards bacterial cells with a high negative charge density. This behavior of AMC-109 (**2**) is being thoroughly investigated elsewhere (personal communication Wouter H. Roos). This highlights the importance of supporting experiment with simulations or orthogonal methods. Together these results give us a glimpse of the mode of action of this class of antimicrobials, where solubility, local concentrations and peptide to lipid ratios are central to the anti-microbial effect.

The proposed WIND-PVPA method has some characteristics that need to be recognized. The barriers are not a single bilayer, but rather a stack of packed unilamellar vesicles. As such, the *absolute* values of the apparent permeabilities through the barriers (10^{-6} cm/s range for water) are expected to be significantly different from the *absolute* permeabilities through single bilayers (10^{-3} cm/s range for water) [36] as the barriers are several orders of magnitude thicker than a monolayer. Therefore, the WIND-PVPA should be used to assess the relative response to membrane disrupting- or dissolving stress. There are also indications of that PVPA barriers inherently can have microscopic hydrophilic pathways contributing to the total permeation. In the original PVPA, the barrier leakiness is assessed by measuring the calcein permeability – a large polar molecule with low permeability. The quality criterium for "tight" barriers is that the calcein permeability is $<10^{-7}$, whereas the native calcein permeability across a single bilayer is expected to be in the 10^{-11} range from literature reported liposome leakage [37]. Therefore, it is not possible to determine the actual mechanisms behind permeabilities that are lower than 10^{-7}, which is the case for both calcein and sodium ions.

The concentrations used in the assay were 4 mg/ml, which is high with respect to the MIC values of these peptides. However, at the same time the peptide:lipid ratio was approximately 1:10, which is in a range that will normally induce destabilization of vesicles, but is low with the respect to the peptide:lipid ratio used in MIC assays, which can be as

Table 1
Summary of P_{app} determined for all tested guest molecules in PVPAs with both lipid compositions.

	MIC (μg/mL)	DMPC (P_{app} x 10^{-6} cm/s)			DMPC/PG (P_{app} x 10^{-6} cm/s)		
	S. Aureus	Ca^{2+}	Mg^{2+}	D_2O	Ca^{2+}	Mg^{2+}	D_2O
KP-76	145	3.5 ± 0.7	4.3 ± 0.8	71 ± 4.9	3.7 ± 0.3	4.0 ± 0.3	94 ± 2.0
AMC-109[a]	2	–	–	63 ± 0.6	–	–	84 ± 1.2
cWRWRWR	4	3.9 ± 0.9	4.9 ± 1.0	74 ± 4.7	10.2 ± 1.3	10.2 ± 1.3	104 ± 3.9
RAR	–	4.0 ± 0.7	4.9 ± 0.7	78 ± 4.2	3.4 ± 0.1	3.7 ± 0.1	87 ± 0.8
Triton	–	11.3 ± 2.0	12.9 ± 2.5	109 ± 5.3	13.5 ± 1.5	14.5 ± 1.5	132 ± 2.1
Blank	–	3.8 ± 0.9	4.7 ± 1.0	78 ± 5.9	3.5 ± 0.4	4.0 ± 0.4	88 ± 3.1

[a] Conducted in the absence of $CaCl_2$ and $MgCl_2$ - No increase observed relative to the blank.

much as 1000:1 due to the low cell density in the assay [8]. It is also expected that the outermost bilayers will experience higher local concentrations of guest molecules than the deeper layers will, and hence could potentially experience cataclysmic events if the guest molecule has disruptive properties. The batch consistency also needs to be considered. It's important to routinely probe the zeta potential and calcein permeability of every new batch (see Methods). If these factors are under control, WIND-PVPA offers a unique method to monitor *changes* in membrane permeability that is straightforward to setup, can be tailored to different scientific questions and can potentially be scaled up and automated for screening.

We herein show the proof of principle that the WIND-PVPA method can be used to assess the influence of AMPs and other membrane active molecules on the integrity of lipid-based barriers. WIND-PVPA as a method is easy to use and is very flexible in its application. The barriers themselves can be designed to mimic any microbial- or physiological barrier by using different lipid compositions, lipid- or cell wall isolations. The experiment can also be modified to monitor different entities, for example other salt/reporter pairs, size markers, biomarkers or isotopes. The core experiment can thus be tailored to provide data on different scientific questions, including integrity, permeability, selectivity and mode-of-action. The core methodology is currently being developed in multiple directions outside the scope of this work.

4. Materials and methods

All common chemicals are of analytical purity and supplied by Merck KGaA, Darmstadt, Germany. All the lipid samples had been supplied by Avanti Lipids (Alabaster, Alabama, US).

4.1. Preparation of PVPA barriers

PVPA barriers were prepared following a modified method from Flaten et al., (2006) [18]. Briefly, DMPC (**PC**) or DMPC:DMPG (5% DMPG, *w*/w) (**PC/PG**) liposomes were prepared *via* the thin film hydration technique, and the PVPA barriers were prepared by depositing either **PC** or **PC/PG** liposomes on top of nitrocellulose membrane filters (pore size 650 nm) and by immobilizing them by cycles of heating at 50 °C. The liposomes utilized for the preparation of the PVPA barriers were manually extruded through 800 nm filters prior to their addition on top of the membrane filters. To prepare for further use, the PVPA barriers were thawed at 50° C for 45 min, or until dry. Integrity of barriers was tested by calcein permeability assay and electrical resistance (Supp Table S1).

4.2. WIND-PVPA

The WIND-PVPA experiment consists of a donor and receiver chamber separated by a lipid barrier. The experiment has been done in 24 well plates, which served as a series of receiver chambers. The donor chamber is part of the barrier and can be moved freely from well to well. After the addition of the sample solution to the donor chamber, the barrier was moved from well to well in series of time points – 0.5, 5, 15, 30, 60, 90, 120, 180, 240, 300, 360 min and one overnight sample. The donor chamber contained 200 μl of 100 mM Tris buffer pH 7.4, 100 mM $CaCl_2$, 100 mM $MgCl_2$, the tested peptide (4 mg/ml) or Triton (2% *w/v*) in 80% D_2O (Merck KGaA, Darmstadt, Germany) and 20% MiliQ water. The receiver chamber contained 1 ml of 100 mM Tris buffer pH 7,4 and 10 mM EDTA in 0.5% D_2O and 99.5% MilliQ water. Afterwards, both donor and acceptor solutions were transferred to 5 mm short NMR tube for NMR measurement. The transition experiment was completed at 20 °C (controlled room temperature). Due to poor solubility in the presence of the salts, the AMC-109 (**2**) WIND-PVPA used a 10 mM Tris buffer pH 7.4 without salts in the donor chamber, nor EDTA in the acceptor chamber – all other aspects of the experimental setup remained the same.

The apparent permeability coefficient (P_{app}) was calculated for water and both Mg^{2+} and Ca^{2+} ions from Eq. (1) derived from Fick's law:

$$P_{app}\left(\frac{cm}{s}\right) = \frac{dQ}{dt} * \frac{1}{A * C_d} \quad (1)$$

where dQ/dt is transition speed of D_2O (μl/min) or ions (μmol/min), A is surface area of PVPA barriers (cm^2) and C_d is volume of water (μl) or concentration of ions (μM) in donor compartment.

4.3. NMR acquisition

NMR spectra were acquired on a Bruker Avance III HD spectrometer operating at 600 MHz, equipped with an inverse TCl cryo probe. All NMR spectra were acquired at 298 K using 5 mm tubes using standard pulse programs for acquisition in Topspin 3.5pl7 (Bruker BioSpin, Germany). Spectra were processed automatically using TopSpin 4.0.8 (Bruker, Germany) and Matlab R2020b with Signal processing and Bioinformatics toolbox (USA, MA, Natick). The processing scripts are available at https://github.com/MarJakubec/TopSpin-Matlab-Processing.

The integrals of the D_2O peaks were adjusted *via* subtraction of the baseline level of D_2O present in the acceptor solution. The cumulative adjusted integrals were converted to volume using a calibration curve and plotted against time. The slope of the line consisting of the points that made up the first 2 h for each series was calculated and plotted. The same process was repeated for EDTA using the peaks between 2.42 - 2.48 ppm, and 2.56–2.61 ppm respectively for Ca^{2+} and Mg^{2+} to yield the concentration of each ion.

4.4. Computational details

The AMPs, KP-76 (**1**) and AMC-109 (**2**) (formerly LTX-109) were used in the molecular dynamics (MD) simulations [25–26]. The molecular models of the synthetic AMPs were built with Maestro (Schrödinger Release 2021–4: Maestro, Schrödinger, LLC, New York, NY, 2021). The topology and parameters where generated using the automatic CGenFF program ParamChem [38] The resulting atomic charges were compared to charges of similar residues in the CHARMM36 All-Hydrogen Topology File for Proteins as well as the general CGenFF topology File [39]. Two lipid bilayers were built using the CHARMM-

GUI membrane builder [40]. One consisting of 336 DMPC lipids (**PC**), the other having 319 DMPC lipids and 17 DMPG lipids to give a 95% DMPC/5% DMPG bilayer (**PC/PG**). Both bilayer systems have an ion concentration of 100 mM $MgCl_2$ and 100 mM $CaCl_2$. The **PC/PG** bilayer has an additional 17 sodium counter-ions due to the negative charge of DMPG lipids. The lipid bilayers were calibrated for 30 ns. Further, VMD [41] was used to prepare 4 systems for each of the calibrated **PC**- and **PC/PG** bilayer, containing 4 and 8 molecules of KP-76 (**1**) and AMC-109 (**2**) respectively. For systems with AMPs, Cl^- was added as counter-ions to the positively charged AMPs. Water molecules within the hydrophobic region of the lipid bilayer were removed. The same procedure was applied to the **PC** and **PC/PG** bilayer systems not containing AMPs, which were used for further simulations. Three parallels of each system were then simulated for 200 ns. The NAMD software package [42] was used for the MD simulations, which were performed under periodic boundary conditions in the NpT ensemble. The CHARMM36 All-Hydrogen Lipid Parameters [43] were used for the lipids. Water was modelled using the TIP3P model and the geometry of the water molecules was constrained using the SHAKE algorithm (36). A target pressure of 1 atm [44] was obtained using the Langevin piston method (34), with an oscillation period of 100 fs and damping time scale of 50 fs. Langevin dynamics was used to control the temperature at the physiological temperature 310 K, with a damping coefficient of 1 ps^{-1} [45]. The Particle Mesh Ewald (PME) method was applied for long-range electrostatic forces [46]. Further, the bonded forces were evaluated every 1 fs, short-range none-bonded forces every 2 fs, and long-range electrostatics every 4 fs. A smooth cut-off was used between 8 and 10 Å.

4.5. Data analysis

The simulated systems had the lipid bilayer oriented in the xy-plane with the z-axis perpendicular to the membrane surface. Before analysis, the frames of the trajectory were placed with the membrane centre of mass at x-, y- and z = 0.

Permeability of water and ions as well as the saturation of the membrane models was examined. The z-coordinates of water oxygens or ions within a given distance of the lipid bilayer hydrophobic core were extracted every frame (5 ps steps) of the 200 ns MD simulation trajectory. The resulting water molecules or ions were considered further if they were present 2 frames or more. The z-coordinates of a given water molecule or ion were then tracked to see if the residue would permeate the lipid bilayer or return to the bulk water from where it entered. In addition to counting the number of water molecules that cross the centre of the bilayer, the overall time which water molecules spent within 5 Å of the bilayer centre was accounted for. Further, water molecules which crossed the centre of the lipid bilayer were examined to see if during the simulation they were within 8 Å of the peptides simultaneously to the selected hydrophobic core. The z-coordinates were extracted every frame the water residues were in both the selections.

The apparent permeability constants from the simulations were calculated according to Eq. (2).

$$P_{app} = \frac{r}{2c_w} \tag{2}$$

where r is the number of water molecules crossing the membrane divided by the length of the simulations and the area of the lipid bilayer cross-section, and c_w is the number of water molecules in the simulations divided by volume of the water [47]. The average volume of the water in the simulated buffer was determined by separately simulating a box containing 100 mM $CaCl_2$, 100 mM $MgCl_2$ in water only for 1.5 ns under identical simulation conditions.

In addition to permeability and saturation two more parameters were evaluated. First, the ordering of nonpolar hydrocarbon chains in the lipid bilayer characterized by the lipid order parameters, S_{CH}, given by Eq. (3).

$$S_{CH} = \frac{3}{2}\langle cos^2\theta \rangle - \frac{1}{2} \tag{3}$$

where θ is the angle between the CH bond (carbon-hydrogen bond) to the bilayer surface normal [48]. The angular brackets donate the time average. Second, density profiles were calculated using the VMD Density Profile Tool [49]. The program calculates a one-dimensional projection of selected atomic densities (atoms/Å3). The selected groups of molecules or atoms were water molecules within 3 Å of the lipid bilayer, phosphates in the lipid head groups and AMPs in systems with peptides present. The calculations were done with a 1 Å resolution and projected onto the z-axis of the system. For systems without AMPs present the S_{CH} were calculated as an average for all lipids. In systems with AMPs present there were two selections. First, every lipid residue which had a contact point within 3 Å of a peptide. Second, the lipid residues which do not appear in the first selection. For systems without peptides, the average S_{CH} of three parallel simulations were calculated and compared to the individual systems and parallel runs with peptides present. Both lipid order parameters and density profiles were calculated as an average over the last 195 ns of the simulation. Also, both parameters were calculated every 0.1 ns.

Abbreviations

NMR	Nuclear Magnetic Resonance
PVPA	Phospholipid Vesicle Permeability Assay
DMPC	1,2-dimyristoyl-sn-glycero-3-phosphocholine
DMPG	1,2-Dimyristoyl-sn-glycero-3-phospho-rac-(1-glycerol)
MOA	Mode of action
AMP	Antimicrobial Peptides
MIC	Minimal Inhibitory Concentration

CRediT authorship contribution statement

PR, MJ and JI designed and planned the project. PR and MJ established NMR procedures under the supervision of JI. MF prepared PVPA barriers under the supervision of GF. Modelling was done by RS under the supervision of JI and BOB. Figures were prepared by PR and RS. Original draft was written by PR, MJ, RS and JI. Funding for this project was acquired by JI. All authors interpreted data and commented on the final version of the manuscript.

Declaration of competing interest

The authors declare that they have no known competing financial interests or personal relationships that could have appeared to influence the work reported in this paper.

Acknowledgements

This project received funding from the DigiBiotics project of the Research Council of Norway (project ID 269425), the AntiBioSpec project of UiT the Arctic University of Norway (Cristin ID 20161326). The publication charges for this article have been funded by a grant from the publication fund of UiT the Arctic University of Norway. The simulations were performed on resources provided by UNINETT Sigma2 - the National Infrastructure for High Performance Computing and Data Storage in Norway, project nr. NN9888K.

Appendix A. Supplementary data

Supplementary data to this article can be found online at https://doi.org/10.1016/j.bbamem.2022.183911.

References

[1] O.collab <collab>World Health, Antimicrobial Resistance: Global Report on Surveillance, World Health Organization, Geneva, 2014.
[2] A.K. Marr, W.J. Gooderham, R.E. Hancock, Antibacterial peptides for therapeutic use: obstacles and realistic outlook, Curr. Opin. Pharmacol. 6 (5) (2006) 468–472.
[3] J.G. Hurdle, A.J. O'Neill, I. Chopra, R.E. Lee, Targeting bacterial membrane function: an underexploited mechanism for treating persistent infections, Nat. Rev. Microbiol. 9 (1) (2011) 62–75.
[4] J.D. Prajapati, U. Kleinekathöfer, M. Winterhalter, How to enter a bacterium: bacterial porins and the permeation of antibiotics, Chem. Rev. 121 (9) (2021) 5158–5192.
[5] M. Zasloff, Antimicrobial peptides of multicellular organisms, Nature 415 (6870) (2002) 389–395.
[6] J.M. Ageitos, A. Sánchez-Pérez, P. Calo-Mata, T.G. Villa, Antimicrobial peptides (AMPs): ancient compounds that represent novel weapons in the fight against bacteria, Biochem. Pharmacol. 133 (2017) 117–138.
[7] A. Hollmann, M. Martinez, P. Maturana, L.C. Semorile, P.C. Maffia, Antimicrobial peptides: interaction with model and biological membranes and synergism with chemical antibiotics, Front. Chem. 6 (2018) 204.
[8] W.C. Wimley, Describing the mechanism of antimicrobial peptide action with the interfacial activity model, ACS Chem. Biol. 5 (10) (2010) 905–917.
[9] E. Disalvo, Membrane Hydration: The Role of Water in the Structure and Function of Biological Membranes vol. 71, 2015.
[10] Q. Al-Awqati, One hundred years of membrane permeability: does Overton still rule? Nat. Cell Biol. 1 (8) (1999) E201–E202.
[11] S. Paula, A.G. Volkov, A.N. Van Hoek, T.H. Haines, D.W. Deamer, Permeation of protons, potassium ions, and small polar molecules through phospholipid bilayers as a function of membrane thickness, Biophys. J. 70 (1) (1996) 339–348.
[12] R. Kausik, S. Han, Dynamics and state of lipid bilayer-internal water unraveled with solution state 1H dynamic nuclear polarization, Phys. Chem. Chem. Phys. 13 (17) (2011) 7732–7746.
[13] D. Huster, A.J. Jin, K. Arnold, K. Gawrisch, Water permeability of polyunsaturated lipid membranes measured by 17O NMR, Biophys. J. 73 (2) (1997) 855–864.
[14] Y. Shai, Mode of action of membrane active antimicrobial peptides, Pept. Sci. 66 (4) (2002) 236–248.
[15] Y. Shai, Mechanism of membrane permeation and pore formation by antimicrobial peptides, in: Protein-Lipid Interactions, 2005, pp. 187–217.
[16] E. Gazit, I.R. Miller, P.C. Biggin, M.S. Sansom, Y. Shai, Structure and orientation of the mammalian antibacterial peptide cecropin P1 within phospholipid membranes, J. Mol. Biol. 258 (5) (1996) 860–870.
[17] J. Li, J.-J. Koh, S. Liu, R. Lakshminarayanan, C.S. Verma, R.W. Beuerman, Membrane active antimicrobial peptides: translating mechanistic insights to design, Front. Neurosci. 11 (73) (2017).
[18] G.E. Flaten, A.B. Dhanikula, K. Luthman, M. Brandl, Drug permeability across a phospholipid vesicle based barrier: a novel approach for studying passive diffusion, Eur. J. Pharm. Sci. 27 (1) (2006) 80–90.
[19] A. Engesland, M. Skar, T. Hansen, N. Škalko-basnet, G.E. Flaten, New applications of phospholipid vesicle-based permeation assay: permeation model mimicking skin barrier, J. Pharm. Sci. 102 (5) (2013) 1588–1600.
[20] M. Falavigna, M. Klitgaard, C. Brase, S. Ternullo, N. Škalko-Basnet, G.E. Flaten, Mucus-PVPA (mucus phospholipid vesicle-based permeation assay): an artificial permeability tool for drug screening and formulation development, Int. J. Pharm. 537 (1–2) (2018) 213–222.
[21] M. Falavigna, M. Pattacini, R. Wibel, F. Sonvico, N. Škalko-Basnet, G.E. Flaten, The vaginal-PVPA: a vaginal mucosa-mimicking in vitro permeation tool for evaluation of mucoadhesive formulations, Pharmaceutics 12 (6) (2020) 568.
[22] M. Falavigna, M. Klitgaard, E. Steene, G.E. Flaten, Mimicking regional and fasted/fed state conditions in the intestine with the mucus-PVPA in vitro model: the impact of pH and simulated intestinal fluids on drug permeability, Eur. J. Pharm. Sci. 132 (2019) 44–54.
[23] R. Rathinakumar, W.C. Wimley, High-throughput discovery of broad-spectrum peptide antibiotics, FASEB J. 24 (9) (2010) 3232–3238.
[24] A. Mónico, E. Martínez-Senra, F.J. Cañada, S. Zorrilla, D. Pérez-Sala, Drawbacks of dialysis procedures for removal of EDTA, PLOS ONE 12 (1) (2017), e0169843.
[25] B.E. Haug, W. Stensen, M. Kalaaji, Ø. Rekdal, J.S. Svendsen, Synthetic antimicrobial peptidomimetics with therapeutic potential, J. Med. Chem. 51 (14) (2008) 4306–4314.
[26] J. Svenson, W. Stensen, B.O. Brandsdal, B.E. Haug, J. Monrad, J.S. Svendsen, Antimicrobial peptides with stability toward tryptic degradation, Biochemistry 47 (12) (2008) 3777–3788.
[27] J. Håkansson, J.P. Cavanagh, W. Stensen, B. Mortensen, J.-S. Svendsen, J. Svenson, In vitro and in vivo antibacterial properties of peptide AMC-109 impregnated wound dressings and gels, J. Antibiot. 74 (5) (2021) 337–345.
[28] A.D.C. França, T.P. Sudbrack, N.L. Archilha, R. Itri, K.A. Riske, Effects caused by triton X-100 on lipid bilayers of different composition, Biophys. J. 102 (2012).
[29] J. Isaksson, B.O. Brandsdal, M. Engqvist, G.E. Flaten, J.S.M. Svendsen, W. Stensen, A synthetic antimicrobial peptidomimetic (LTX 109): stereochemical impact on membrane disruption, J. Med. Chem. 54 (16) (2011) 5786–5795.
[30] A. Slezak, B. Turczynski, Modification of the Kedem-Katchalsky equations, Biophys. Chem. 24 (2) (1986) 173–178.
[31] O. Kedem, A. Katchalsky, Thermodynamic analysis of the permeability of biological membranes to non-electrolytes, Biochim. Biophys. Acta 27 (1958) 229–246.
[32] R. Koynova, M. Caffrey, Phases and phase transitions of the phosphatidylcholines, Biochim. Biophys. Acta Rev. Biomembr. 1376 (1) (1998) 91–145.
[33] M.M.A.E. Claessens, B.F. van Oort, F.A.M. Leermakers, F.A. Hoekstra, M.A. Cohen Stuart, Charged lipid vesicles: effects of salts on bending rigidity, stability, and size, Biophys. J. 87 (6) (2004) 3882–3893.
[34] H.-T. Chou, H.-W. Wen, T.-Y. Kuo, C.-C. Lin, W.-J. Chen, Interaction of cationic antimicrobial peptides with phospholipid vesicles and their antibacterial activity, Peptides 31 (10) (2010) 1811–1820.
[35] M.-A. Sani, F. Separovic, How membrane-active peptides get into lipid membranes, Acc. Chem. Res. 49 (6) (2016) 1130–1138.
[36] J.C. Mathai, S. Tristram-Nagle, J.F. Nagle, M.L. Zeidel, Structural determinants of water permeability through the lipid membrane, J. Gen. Physiol. 131 (1) (2008) 69–76.
[37] B. Maherani, E. Arab-Tehrany, A. Kheirolomoom, D. Geny, M. Linder, Calcein release behavior from liposomal bilayer; influence of physicochemical/mechanical/structural properties of lipids, Biochimie 95 (11) (2013) 2018–2033.
[38] K. Vanommeslaeghe, E. Hatcher, C. Acharya, S. Kundu, S. Zhong, J. Shim, E. Darian, O. Guvench, P. Lopes, I. Vorobyov, A.D. Mackerell Jr., CHARMM general force field: A force field for drug-like molecules compatible with the CHARMM all-atom additive biological force fields, J. Comput. Chem. 31 (4) (2010) 671–690.
[39] R.B. Best, X. Zhu, J. Shim, P.E.M. Lopes, J. Mittal, M. Feig, A.D. MacKerell, Optimization of the additive CHARMM all-atom protein force field targeting improved sampling of the backbone ϕ, ψ and side-chain $\chi1$ and $\chi2$ dihedral angles, J. Chem. Theory Comput. 8 (9) (2012) 3257–3273.
[40] S. Jo, J.B. Lim, J.B. Klauda, W. Im, CHARMM-GUI membrane builder for mixed bilayers and its application to yeast membranes, Biophys. J. 97 (1) (2009) 50–58.
[41] W. Humphrey, A. Dalke, K. Schulten, VMD: visual molecular dynamics, J. Mol. Graph. 14 (1) (1996), 33-8, 27-8.
[42] J.C. Phillips, R. Braun, W. Wang, J. Gumbart, E. Tajkhorshid, E. Villa, C. Chipot, R. D. Skeel, L. Kalé, K. Schulten, Scalable molecular dynamics with NAMD, J. Comput. Chem. 26 (16) (2005) 1781–1802.
[43] J.B. Klauda, R.M. Venable, J.A. Freites, J.W. O'Connor, D.J. Tobias, C. Mondragon-Ramirez, I. Vorobyov, A.D. MacKerell, R.W. Pastor, Update of the CHARMM all-atom additive force field for lipids: validation on six lipid types, J. Phys. Chem. B 114 (23) (2010) 7830–7843.
[44] S.E. Feller, Y. Zhang, R.W. Pastor, B.R. Brooks, Constant pressure molecular dynamics simulation: the Langevin piston method, J. Chem. Phys. 103 (11) (1995) 4613–4621.
[45] U. Essmann, L. Perera, M.L. Berkowitz, T. Darden, H. Lee, L.G. Pedersen, A smooth particle mesh Ewald method, J. Chem. Phys. 103 (19) (1995) 8577–8593.
[46] J.-P. Ryckaert, G. Ciccotti, H.J.C. Berendsen, Numerical integration of the cartesian equations of motion of a system with constraints: molecular dynamics of n-alkanes, J. Comput. Phys. 23 (3) (1977) 327–341.
[47] R.M. Venable, A. Krämer, R.W. Pastor, Molecular dynamics simulations of membrane permeability, Chem. Rev. 119 (9) (2019) 5954–5997.
[48] L.S. Vermeer, B.L. de Groot, V. Réat, A. Milon, J. Czaplicki, Acyl chain order parameter profiles in phospholipid bilayers: computation from molecular dynamics simulations and comparison with 2H NMR experiments, Eur. Biophys. J. 36 (8) (2007) 919–931.
[49] T. Giorgino, Computing 1-D atomic densities in macromolecular simulations: the density profile tool for VMD, Comput. Phys. Commun. 185 (1) (2014) 317–322.

SUPPORTING INFORMATION*

WIND-PVPA: Water/Ion NMR Detected PVPA to assess lipid barrier integrity *in vitro* through quantification of passive water- and ion transport

Philip Rainsford,[a‡] *B. Ravdna Sarre,*[a‡] *Margherita Falavigna,*[b] *Gøril E. Flaten,*[b] *Martin Jakubec,*[a‡] *Johan Isaksson*[a‡*]

[a] Dept. Chemistry, UiT the Arctic University of Norway, 9037 Tromsø, Norway, [b] Dept. Pharmacy, UiT the Arctic University of Norway, 9037 Tromsø, Norway, [‡]Shared authorship

- This document is truncated to include only experimental supplementary information. Further supplementary information is available in the full document available at: https://doi.org/10.1016/j.bbamem.2022.183911

1 Table of Contents

2 Supplementary figures for experimental part

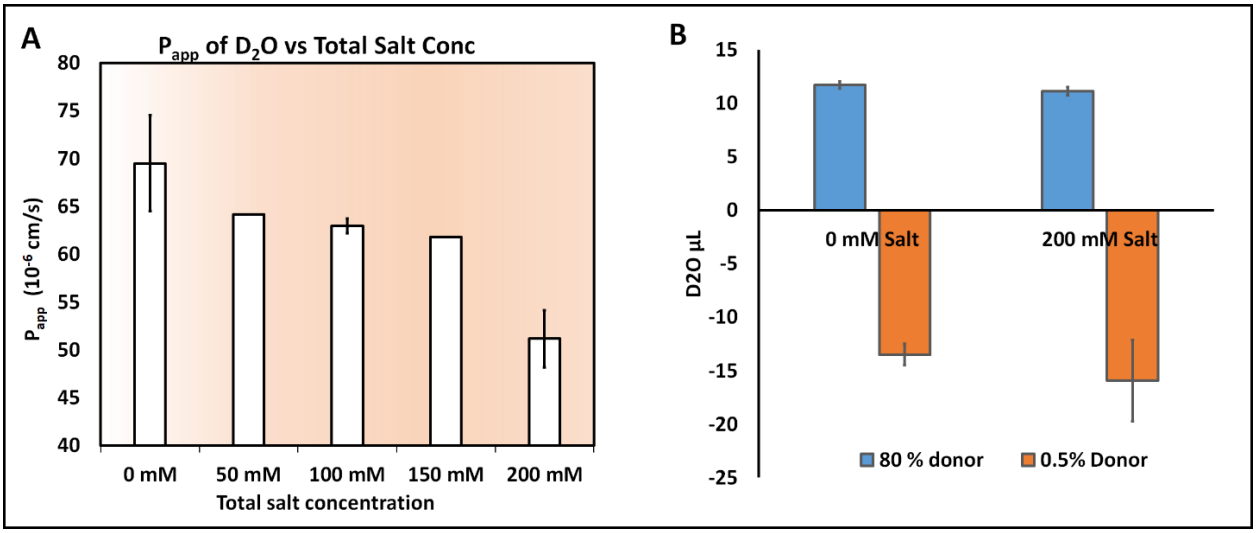

Figure 1. A) The P_{app} of D_2O across DMPC/DMPG (5%) barriers as a function of total salt concentration in the donor chamber - total salt represents the sum of equimolar quantities of $CaCl_2$ and $MgCl_2$. The end point (200 mM) represents the experimental conditions used. B) The backflow of water was probed after 30 minutes as a function of the amount of salt in the donor chamber.

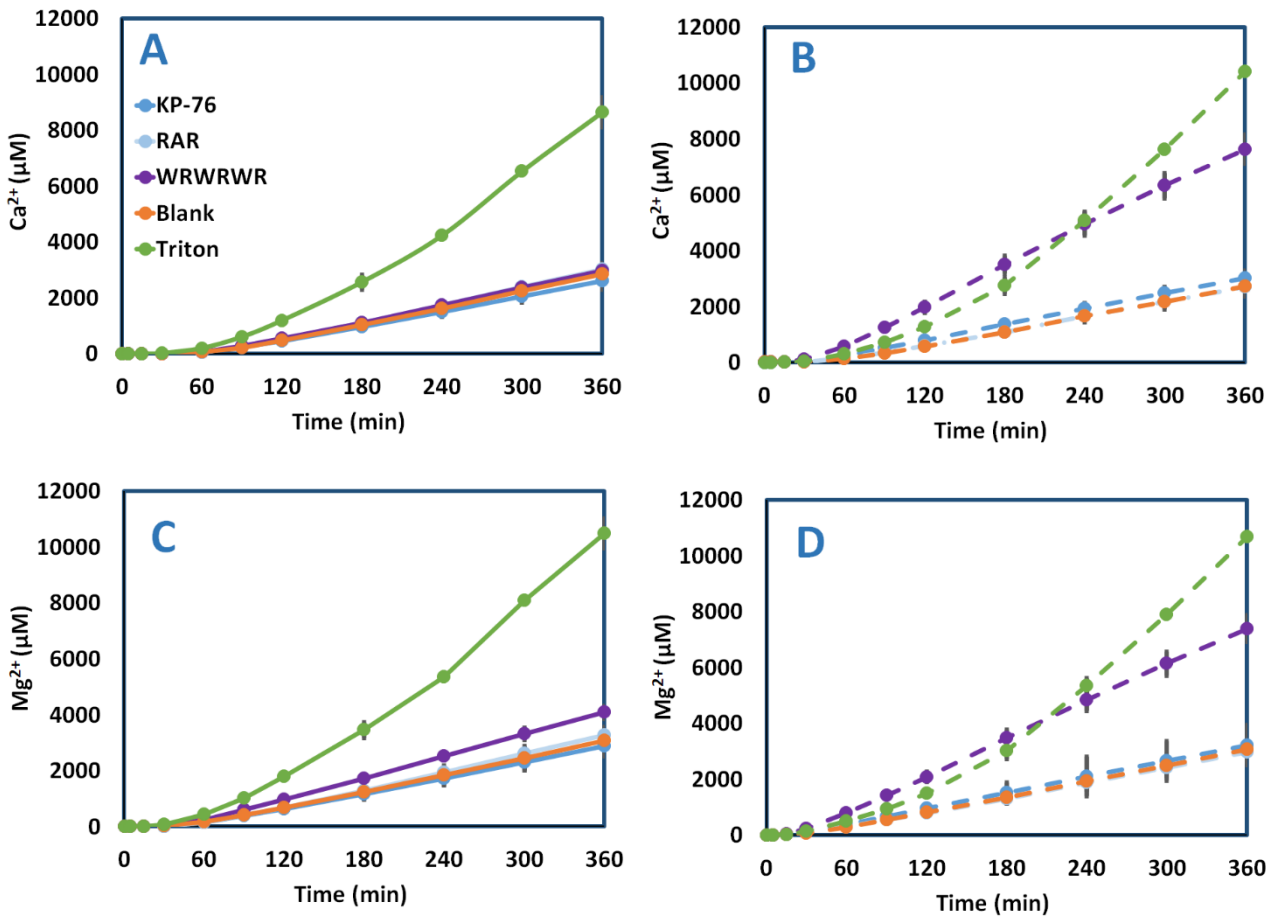

Figure 2: Full expansion of ion WIND-PVPA experiments. Left: DMPC. Right: DMPC/DMPG. Top: Ca^{2+}. Bottom: Mg^{2+}.

Table 1: Calcein permeability and electrical resistance of PVPA barriers (n=4).

Papp (10-6 cm/s)	Mean	SD
DMPC	0.61	0.08
DMPC: DMPG (PG 5%)	0.49	0.07

El. Res. (Ohms*cm2)	Mean	SD
DMPC	54.23	7.62
DMPC: DMPG (PG 5%)	53.96	3.16

PAPER II

Application of label free microscale thermophoresis: Measurement of antimicrobial peptide affinity (K_D) and partitioning (K_P) to lipid vesicles and SMA-nanodiscs

Philip Rainsford[a], Martin Jakubec[a], Mitchell Silk[a], Richard Engh[a], Johan Isaksson[a]

[a] Department of Chemistry, Faculty of Science and Technology, UiT the Arctic University of Norway, 9019 Tromsø, Norway

Abstract

Antimicrobial peptides (AMPs) are of great interest of as a new form of antibacterial agent, due to the reduced capacity of resistance bacteria have towards them. This reduced capacity is in part due to AMPs targeting the bacterial membrane. The initial binding of AMPs to the membranes is a universal step, regardless of which mode-of-action model best describes the interaction of the AMP, and parameters related to binding such as K_P and K_D are universally applicable.

Herein, we demonstrate the use of microscale thermophoresis (MST) to reliably extract K_D and K_P in a quick and label-free manner using the intrinsic tryptophan as fluorophore, with minimal sample requirements. MST is demonstrated with both small unilamellar vesicles (SUVs) and SMA-nanodiscs, and compared to the corresponding lipid interactions measured by SPR. It is shown that SUVs are best suited for the extraction of K_D and K_P, while SMA-nanodiscs appear to be less ideal due to lipid phase heterogeneity, and potential interference from AMP-SMA interactions. It is also shown that the tested AMPs show a significant reduction in K_D when 5% anionic lipids are added to the lipid composition in the membrane models, highlighting their preference towards anionic bacterial membranes. The extracted K_D and K_P correlate well with the bactericidal activity of the tested AMPs. In summary, MST is shown to be a promising method for fast and low threshold investigation of parameters that describe peptide-lipid interactions, allowing straightforward identification of whether a compound of interest is membrane active or not, as well as the internal ranking of their affinities.

Introduction

Antimicrobial peptides (AMPs) have attracted attention as a potential answer for antimicrobial resistance development as the discovery of new antibiotics classes slowed down to a halt.[1] AMPs are a class of short peptides, usually composed of 12-50 amino acids. They are the indispensable components of innate immune defence and can be found in bacteria, plants, insects, fish, birds and other animals.[2-5] Currently, sequences for more than 20 000 AMPs with antimicrobial properties are published in various depositories,[6-10] which makes them an ideal pool of potential therapeutic candidates. Compared to traditional antibiotics, the antimicrobial mode of action of the majority of the AMPs seems to be either tuned to target the integrity of membrane bilayer specifically or to have multiple targets and combinations of modes of action. Membrane active AMPs are of particular interest as there is a reduced capacity for resistance development against membrane-active compounds due to the required effort for the organism to change the characteristics of the cell membrane.[11, 12] In addition, the membrane is one of the barriers which AMP needs to cross to interact with potential intracellular targets.

The net charge of AMPs is an essential factor in early interaction with the negatively charged bacterial membrane.[13] Most AMPs are cationic peptides with a favourable initial electrostatic interaction to the net negatively charged bilayer arising from negatively charged phosphatidylglycerols and cardiolipins.

The initial interaction provides the basis for a translocation of lipophilic groups into the bilayer causing a disturbance of lipid packing in the bilayer. Membrane-targeting AMPs can vary significantly in length and sequence, with no motif specific to membrane targeting.[14] Tryptophan-arginine (Trp-Arg) rich peptides are particularly potent compared to other charge carrying residues (like Lys and His) and other lipophilic residues like (Phe, Val, Leu and Ile).[15] Cationic Arg provides initial membrane binding and the indole moiety interacts favourably with the interface between the aqueous environment and the lipid membrane, forming hydrogen bonds with the carbonyl group of the lipid tail.[16]

The AMPs affinity towards lipid vesicles can be expressed as a binding event, with the dissociation constant – K_D. The interaction can also be expressed as a biphasic environment, where the AMP interaction with lipids is viewed as partitioning between two phases – expressed as partitioning constant K_P. The K_D and K_P for lipid interactions are useful screening descriptors for compounds targeting the bacterial membrane. However, the currently used methods to assess lipid affinity are using either large quantities of samples (NMR), require labelling (florescence), are time-consuming or need to be tuned for each individual compound (SPR).

Herein we propose Microscale Thermophoresis (MST) as viable method for quick screening of AMPs affinities towards lipid bilayers. MST consumes a minimal amount of sample and time and can utilize the intrinsic fluorescence of aromatic moieties, like tryptophan.

MST is a simple but powerful tool, based on the directed movement of molecules in a temperature gradient, that enables the user to probe both the local environment and the thermophoretic properties of the formed complex - to which a fluorophore label is attached.[17] The relative changes in fluorescence intensity over different points in time is measured while being irradiated by an IR laser. The method is sensitive to changes in fold, shape, solvation shell, charge, or overall size of the ligand-bound complex. These changes affect the local environment of a fluorophore through changes in dynamic and static quenching, as well as the thermophoretic properties of the complex. These changes can be used to monitor binding affinities and/or phase partitioning.

MST is primarily used to assess biomolecular interactions the binding of ligands to various substrates[17] and polymerisation.[18] The lipid model systems used in this work - vesicles and nanodiscs - have been utilised in MST, but only as a method to solubilise membrane bound proteins in a native-like conformation for further study.[19, 20] MST has previously been used to assess AMP-lipid interactions by Yu et al. to assess the binding of a FITC-labelled AMP.[21]

In this work, we demonstrate that MST can also be used to characterize peptide interactions to the lipids of small unilamellar vesicles (SUVs) and nanodiscs, in a label-free experiment using the intrinsic fluorescence of tryptophan.

Materials and Methods

Materials

Lipids were purchased from Avanti Polar Lipids via Sigma Aldrich (Merck KGaA, Darmstadt, Germany) MST consumables from Matricks AS (Oslo, Norway). SPR consumables were purchased from Cytiva Europe – Norge (Tyristrand,Norway). All other materials were purchased from Sigma Aldrich in analytical purity, unless otherwise stated. Peptides were prepared in house.

Peptide Synthesis

Linear peptide synthesis: 2-chlorotrityl chloride resin (0.15 mmol, 1.0 meq, 150 mg) was swelled in DCM (5 mL) for 30 min. The resin was drained and treated with a solution of Fmoc-

amino acid (0.3 mmol) and diisopropylethylamine (1.8 mmol, 313 μL) in DCM (5 mL). The resin mixture was left overnight under gentle agitation at room temp. The resin mixture was drained, treated with MeOH (3 x 5 mL) to cap unreacted sites and dried with diethyl ether (3 x 5 mL). The linear peptides were prepared using an automated solid-phase peptide synthesizer (Biotage Initiator+ Microwave System with Robot Sixty). The pre-loaded 2-chlorotrityl chloride resin was first swelled in DMF (20 min, 70°C). Fmoc deprotections involved treatment of the resin with 20% piperidine/DMF (4.5 mL, 3 min) once at room temp. followed by a second treatment at 70°C by microwave reactor. Amino acid couplings involved treatment of the resin with 4 eq. of Fmoc-amino acid (0.5 M in DMF), 4 eq. of HOBt (0.5 M in DMF), 4 eq. of HBTU (0.6 M in DMF) and 8 eq. of DIEA (2M in NMP) for 5 min at 75°C by microwave reactor for all Fmoc-amino acids except Fmoc-Arg(Pbf)-OH, which was coupled for 60 min at room temp. After each Fmoc deprotection and amino acid coupling, the resin was washed with DMF (4 x 4.5 mL x 45 sec). After preparation of the resin-bound side-chain protected linear peptide, a final Fmoc deprotection and wash was preformed and the resin dried (3 x 5 mL MeOH, 3 x 5 mL Et_2O). The resin-bound peptide was treated with 20% 1,1,1,3,3,3-Hexafluoro-2-propanol in DCM (2 x 5 mL x 15 min), followed by rinsing of the resin with DCM (5 mL). The filtrates were combined and concentrated under reduced pressure to yield the side-chain protected linear peptide.

Head-to-tail cyclisation and deprotection: The linear peptide (approx. 0.15 mmol) and diisopropylethylamine (0.9 mmol, 157 μL) were dissolved in DMF (10 mL) and added to a solution of PyBOP (0.45 mmol, 234 mg) in DMF (100 mL) under light stirring at room temp. After 1-2 h (monitored for completion by mass spectrometry), the mixture was concentrated by reduced pressure and treated with a solution of TFA/triisopropylsilane/water (4 mL, 95%, 2.5%, 2.5%) then left to stand for 3 h. The mixture was concentrated under N_2 gas flow followed by precipitation with ice-cold diethyl ether (15 mL). The precipitate was collected by filtration, washed with diethyl ether (15 mL), dissolved in 50% acetonitrile/water and lyophilized to yield the crude, cyclic, side-chain deprotected peptide.

Purification: Peptides were purified by preparative reverse-phase HPLC (Waters 600 instrument with Waters 2487 Dual Absorbance detector) with a SunFire Prep. C18 OBD column (10 μm, 19 x 150 mm) using linear gradients of 0.1% TFA/water (buffer A) and 0.1% TFA/acetonitrile (buffer B) with a flow rate of 10 mL/min unless otherwise stated.

Analysis: Crude and final cyclic peptide products were analyzed by FT-MS (Thermo Scientific LTQ Orbitrap XL instrument) and by analytical reverse-phase HPLC (Waters 2795 Alliance HT system with Waters 2996 PDA Detector), using an Ascentis C18 column (3 μm, 3 x 100 mm) and solvents of 0.1% TFA/water (buffer A) and 0.1% TFA/acetonitrile (buffer B) with a linear gradient of 0-60% buffer B over 15 min and a flow rate of 0.5 mL/min.

Vesicle Preparation

DMPC and DMPC with 5% DMPG vesicles were prepared by solubilising a known weight of lipid in chloroform with small amount of methanol to help dissolve charged lipid head group of PG. The chloroform stock was placed on a rotavapor until a dry lipid film was obtained which was then further dried for additional 3 h. The lipid film was then solubilised in a 10 mM TRIS buffer (pH 7.6) containing 100 mM NaCl to yield a 20 mM lipid stock, that was milky in appearance.

To produce the working vesicle stock, 1 mL of vesicle stock was extruded 20 times through a 0.1 µm filter using an Avanti Lipids mini-extruder. Vesicle size was confirmed by using Malvern Zetasizer Nano ZS (Malvern Panalytical Ltd, Malvern, United Kingdom). 200 µL vesicle sample measured in 40 µL microcuvettes revealed vesicle diameters to be 144 ± 44 nm (DMPC) and 140 ± 48 nm (DMPC/PG).

Nanodiscs

The DMPC, and DMPC with 5% DMPG 21 mM vesicle stocks were used for the nanodisc preparation. The stocks were combined with an 8% SMA stock solution to yield a final SMA concentration of 1%. The combined SMA and lipid mixture Incubated at room temperature overnight and purified by SEC. Fractions containing SMA discs were concentrated using centrifugation filters. Total lipid concentration was determined by ^{31}P NMR. Size determination revealed nanodisc sizes to be 10.1 nm (DMPC) and 10.3 nm (DMPC/PG).

SPR

The SPR experiments were performed using a T200 Biacore instrument (GE Healthcare, Oslo, Norway) at room temperature. L1 chip was covered with extruded DMPC liposomes (1 mM in 10 mM HEPES buffer pH 7.4 with 100 mM NaCl) using flowrate 2 µl.min^{-1} for 2400 seconds. Chip coverage was tested by injection of 0.1 mg.ml^{-1} for 1 minute at 30 µl.min^{-1}, change of < 400 RU indicated sufficient coverage.

Increasing concentration of tested peptides (peptides **1, 2, 3** and **4**-from 4 to 128 µM; peptide **5 –** from 24 to 768 µM) were injected over immobilized vesicles with flowrate 15 µl.min^{-1} for 200 s and with 400 s dissociation phase. Surface of liposomes was stabilized after each injection by three subsequent injections of 10 mM NaOH at 30 µl.min^{-1} for 30 second each. Between experiments, the chip surface was cleaned by 20 mM CHAPS, 40 mM octyl-β-D-glucopyranoside and 30% ethanol, each solution was injected for 1 min at 30 µl.min^{-1} . The control flow cell was treated same way, excepted only HEPES buffer was injected. The results were processed using in-laboratory MATLAB scripts (MATLAB R2020a; scripts are available at https://github.com/MarJakubec). K_D was obtained from steady state analysis using intensities from 190-second dissociation time, using Eq (1)

$$R_{eq} = \frac{c\,R_{max}}{K_D + c} + R_{off} \quad (1)$$

Where R_{eq} = response at steady state equilibrium, c = concentration of peptides, R_{max} = maximum response and R_{off} – response offset.

K_P was obtained from same steady state affinity values by using method presented by Figuera *et al.* (2017), Eq (2).[22]

$$\frac{RU_S}{RU_L} = \frac{\gamma_L K_P \frac{M_S}{M_L}[S]_W}{1 + \sigma\gamma_L K_P [S]_W} \quad (2)$$

Where RU_S and RU_L are relative responses of solute (peptides) and lipids, respectively, γ_L is the molar volume of the lipids, M_S and M_L are the molecular mass of solute and lipid respectively and $[S]_W$ is the concentration of solute in water. K_P and σ are obtained from fit with σ being lipid to solute ratio.

For k_{off} evaluation we have used formalism of Figuera et al (2017)[22] for linearization of dissociation process, where we have identified the contribution from two different populations In dissociation response. k_{off} was then obtained by Eg (3) and average by Eq (4).

$$S_L(t) = \alpha e^{-k_{off,\alpha}t} + \beta e^{-k_{off,\beta}t} + S_{L,r} \quad (3)$$

$$k_{off} = \frac{\alpha k_{off,\alpha} + \beta k_{off,\beta}}{\alpha + \beta} \quad (4)$$

Where S_L is respectively linearized ratio of solute and lipid, α and β are individual populations and $S_{L,r}$ is retained solute fraction.

MST experimental procedure

All MST measurements were conducted on a NanoTemper Monolith NT.Labelfree, using Monolith NT. Labelfree standard treated zero background capillaries.

A dilution series of vesicles were prepared from 3 mM to 100 nM lipid concentrations, comprising of 15 discrete samples, and an additional zero lipid sample totalling 16 lipid concentrations. Final MST samples were prepared by combination of 25 µL lipid solution and 25 µL 5 µM peptide solution (Table 1 in the Supporting Information).

MST was conducted with excitation power set to 15%, with high MST power. Laser on times of 3 sec pre-laser, 30 seconds on time were used with 3 seconds after heating. F_{Hot} was taken from the T-jump period after 1.5 seconds, and 25 seconds for the thermophoresis evaluation, and F_{Cold} taken in the second prior to IR laser activation. For the evaluation of K_P, the initial fluorescence was taken as reported during the period before the application of the laser. The MST response and initial fluorescence were extracted directly as a text file for further processing in MATLAB.

MST data processing

The dissociation coefficient K_D describes the equilibrium between the rate constants k_{on} and k_{off}.[23]

$$K_D = \frac{k_{on}}{k_{off}} \quad (5)$$

In a typical binding experiment that yields a sigmoidal curve, the Hill / Sigmoid-E_{Max} equation can be fitted to yield K_D.[24]

$$y = y_0 + \frac{E_{Max}\,[Lipid]^n}{{K_D}^n + [Lipid]^n} \quad (6)$$

Where y is the MST response, y_0 is the MST response of the AMP only, n is the hill coefficient that describes the steepness of the binding slope, and E_{Max} represents the maximal effect of the tested substrate.[24]

The removal of outlying MST response points was necessary, where erroneous points were identified by poor MST trace shape or higher than expected initial fluorescence that was absent in the other replicates or subsequent points - no further treatment of data was necessary.

The partition coefficient K_p defines the preference of a solute for an aqueous or lipidic environment, with a K_p resulting in a greater preference for the lipidic environment.

$$K_P = \frac{S[Lipid]}{S[Aqueous]} \tag{7}$$

The K_p of a molecule can be determined experimentally by observing changes in fluorescent intensity in the presence of an increasing concentration of lipid, and fitting to equation 8.[25]

$$\frac{I}{I_{aq}} = \frac{1 + (K_p \ V_m \ [Lipid] \ \frac{I_L}{I_{aq}})}{1 + (K_p \ V_m \ [Lipid])} \tag{8}$$

In equation 8 the fluorescence intensity of the AMP (I) is normalised on the fluorescence intensity of the AMP in an aqueous environment (I_{aq}), V_m is the molar volume of the lipids and I_L is the fluorescence intensity of the AMP in the lipidic environment. For V_m, the average molar volume of the lipid composition is used. In the case of the DMPC only environments it is taken as the V_m of DMPC (1.023 nm^3), and in the DMPC-DMPG mixture it is the weighted average relative to the composition used ($V_{m\ DMPG}$ =0.997 nm^3).[26]

Results and Discussion

As a proof of principle, the interactions between five cyclic hexamer antimicrobial peptides and two lipid systems (vesicles and nanodiscs) were analysed by MST and SPR (Figure 1). AMPs **1** - **4** were selected based on previously established pharmacophore of alternating versus clumped distribution of charged and hydrophobic moieties.[27-31] AMPs **1-4** have confirmed antimicrobial activity (Table 1) and are a combination of alternating and clumped tryptophan residues with either arginine or lysine residues. AMP **5** was included as a negative control as it is inactive against the tested bacterial strains (Table 1). The association of these peptides with either pure DMPC or a mixture of 95% DMPC and 5% PG bilayers were assessed.

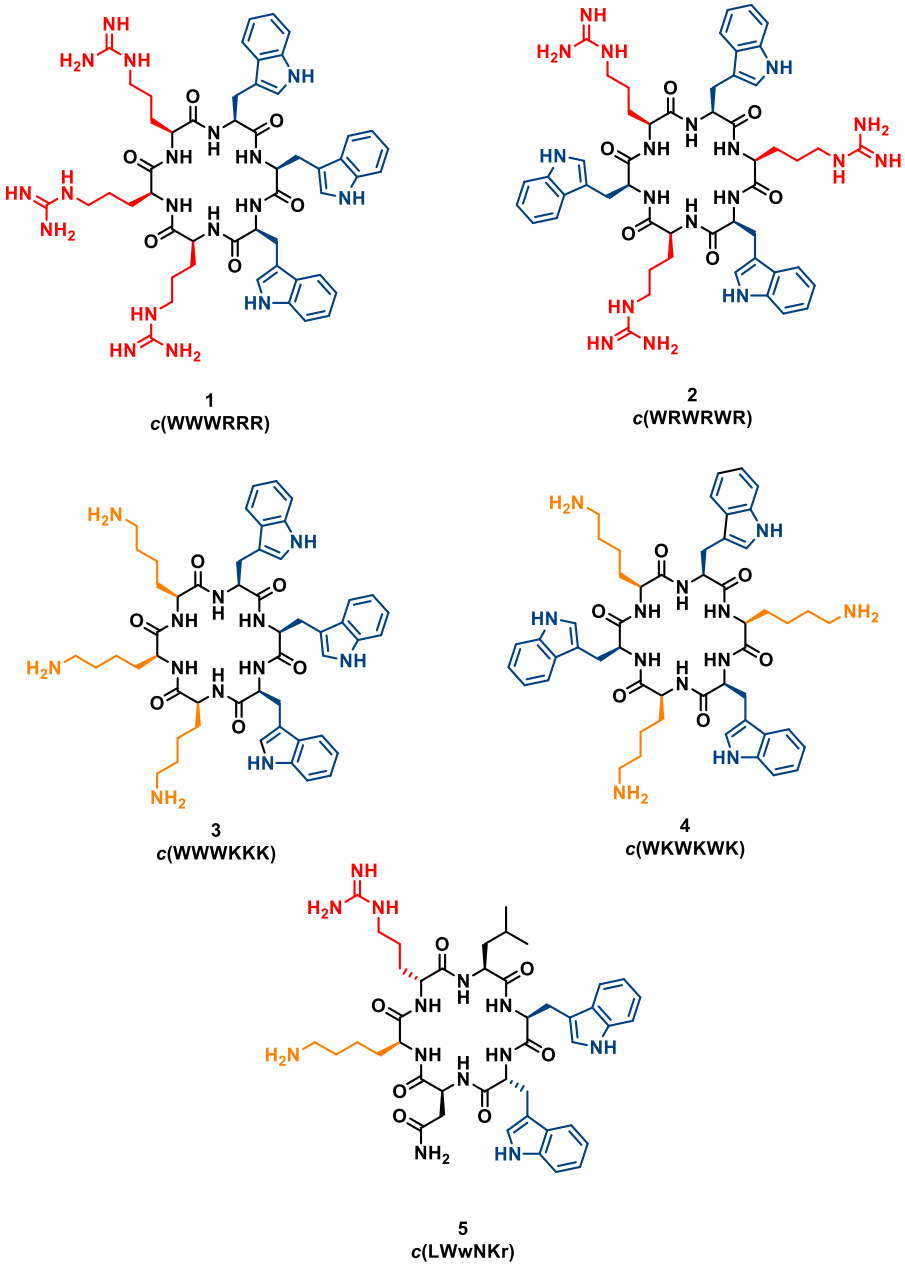

Figure 1: Structures of the five AMPs Coloured red/orange - Arg/Lys, blue – Trp.

Table 1: Summary of the cyclic hexapeptides

#	Peptide Sequence	MIC, *E. Coli* (µg/ml)	MIC, *S. aureus* (µg/ml)	Overall Charge	Hydrophobic AA
1	**WWWRRR**	8	4	+3	3
2	**WRWRWR**	32	32	+3	3
3	**WWWKKK**	8	32	+3	3
4	**WKWKWK**	64	128	+3	3

5	**LWwNKr**	>250	>250	+2	2

MST Response profiles for K_D

The extracted MST responses from the T-jump were plotted against the $\log_{10}$ of the total lipid concentration (nM) (Figure 2). K_D for each response profile was extracted according to equation 6.

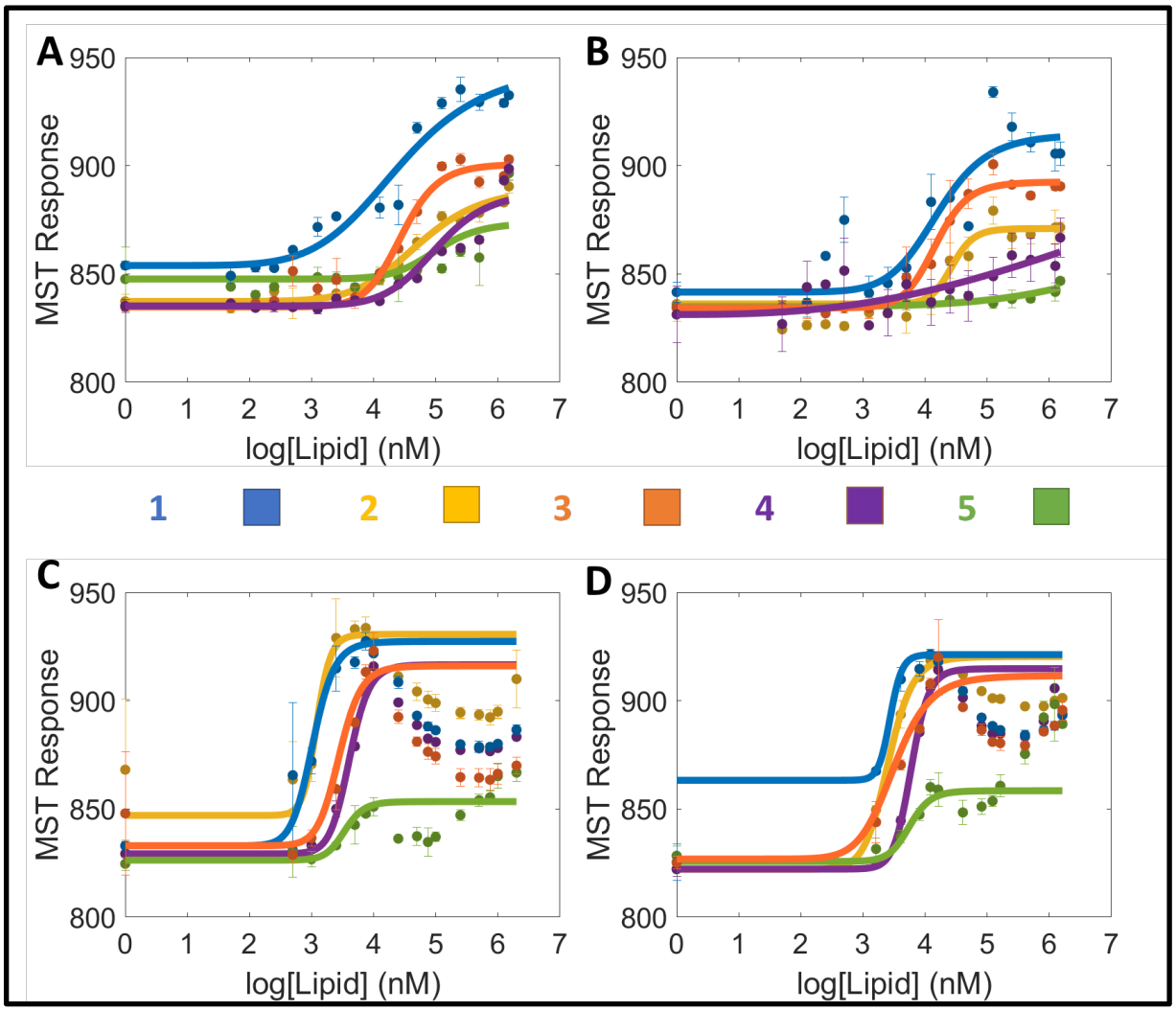

Figure 2: MST response against lipid concentration and K_D fits of 1-5 in different lipid compositions and preparations. The upper panels show 100 µm vesicles consisting of (A) 100% DMPC or (B) 95% DMPC/5% DMPG) while the lower panels show SMA-nanodiscs consisting of (C) 100% DMPC or (D) 95% DMPC/5% DMPG

The dose-response profile of MST against lipid concentration is expected to follow a sigmoidal curve if the interaction is well described by a two-state model, and this was observed when vesicles were used as lipid system (Figures 2A and 2B). In the cases of AMPs **5** and **4**, the sigmoidal curve shape was not fully sampled in vesicles due to the weaker binding shifting the curve outside of the sampling window. The K_D of the peptides could readily be extracted and ranked by their lipid affinities according to **1**>**3**>**2**>**4**>**5** in PC and **1**>**3**=**2**>**4**>**5** in PC/PG. All fitted K_D values are summarised in Table 3.

For the SMA-nanodiscs (Figures 2C and 2D), an additional secondary change was observed at increasing lipid concentrations beyond the maximum MST response of the initial interaction. The secondary response decreased until a steady-state was reached. This pattern has been previously observed for the MST thermophoresis response in the case of higher stoichiometric binding where additional interacting ligands gave rise to a new species of the complex.[17]

The exact nature of the secondary response was not further investigated within the scope of this work, but a plausible explanation could be that increasing numbers of interacting peptides accumulate on the discs, interacting heterogeneously with the different phase moieties within the disc as the disc gets gradually saturated. Thus, the interaction is ongoing over a much larger concentration span than the initial sigmoidal fit would indicate in Figures 2C and 2D, making traditional analysis severely under-estimate the K_D. Therefore, the fitted line should be considered more of a navigational aid in these plots than an actual determination of the true K_D of the interaction. The fitted values are nevertheless presented in Table 3 for completeness. The physical interpretation of the primary sigmoid could very well represent the collapse of the nanodisc rather than the initial binding of a small number of lipids to a big excess of AMPs.

A final increase in response is also observed for the very highest lipid concentrations, however this is likely caused by light scattering interference arising from high lipid concentration since this was observed also for the inactive peptide (**5**) and turbidity is starting to become apparent at the highest lipid concentrations.

Surface Plasmon Resonance (SPR) characterization

The interactions between lipids and AMPs **1-5** were investigated by SPR, using the same two lipid compositions as in the MST measurements (Figure 4) as a benchmark. Vesicles were immobilized on an L1 chip and increasing concentration of AMPs were injected over them. Binding constants, K_D and K_P, were both extracted from steady state after 180s of flow and are listed in Tables 3 and 4. The dissociation rates, k_{off}, were calculated from the dissociation step, using the methodology presented by Figueira *et al.*[32] and are listed in Table 2.

*Table 2: Summary of k_{off} of AMPs **1-5** evaluated by SPR.*

Peptide	K_{off} DMPC (s^{-1})	K_{off} DMPC/PG (s^{-1})
1	0.22 ± 0.02	0.19 ± 0.01
2	0.87 ± 0.19	0.48 ± 0.05
3	0.48 ± 0.07	0.32 ± 0.05
4	0.90 ± 0.24	1.32 ± 0.05
5	1.76 ± 0.12	1.75 ± 0.16

SPR showed that **1** was overall strongest binding compound, followed by **3, 2, 4** and lastly **5**. This trend was also preserved when anionic lipids were present, however the overall affinity of all compounds was increased. The k_{off} also closely resembled this trend with the most active **1** having the slowest dissociation. The overall conclusion from SPR points towards increased affinities of clumped peptides over alternating ones towards both zwitterionic and ionic lipid bilayers.

Thermophoresis profiles

While the current best practice for MST binding measurements is to analyse the T-jump region of the MST trace[33], the steady-state thermophoresis region still yields useful information regarding sample stability[34]. This was of particular interest due as the diffusion-mediated response could potentially reveal any instabilities of the respective lipid model systems when exposed to high concentrations of AMPs. The thermophoresis response of the measured fluorophore, which is a part of the AMPs, is expected to directly reflect the binding equilibrium between the bound and free states. The thermophoresis response is dictated by the diffusion of the complex over the measurement window of 25 seconds, and thus reflects changes in slow processes, in contrast to the T-jump response which immediately responds to changes in the microenvironment of the fluorophore. Thermophoresis is evaluated as the MST response when F_{Hot} is selected around 25 seconds (Figure 4).

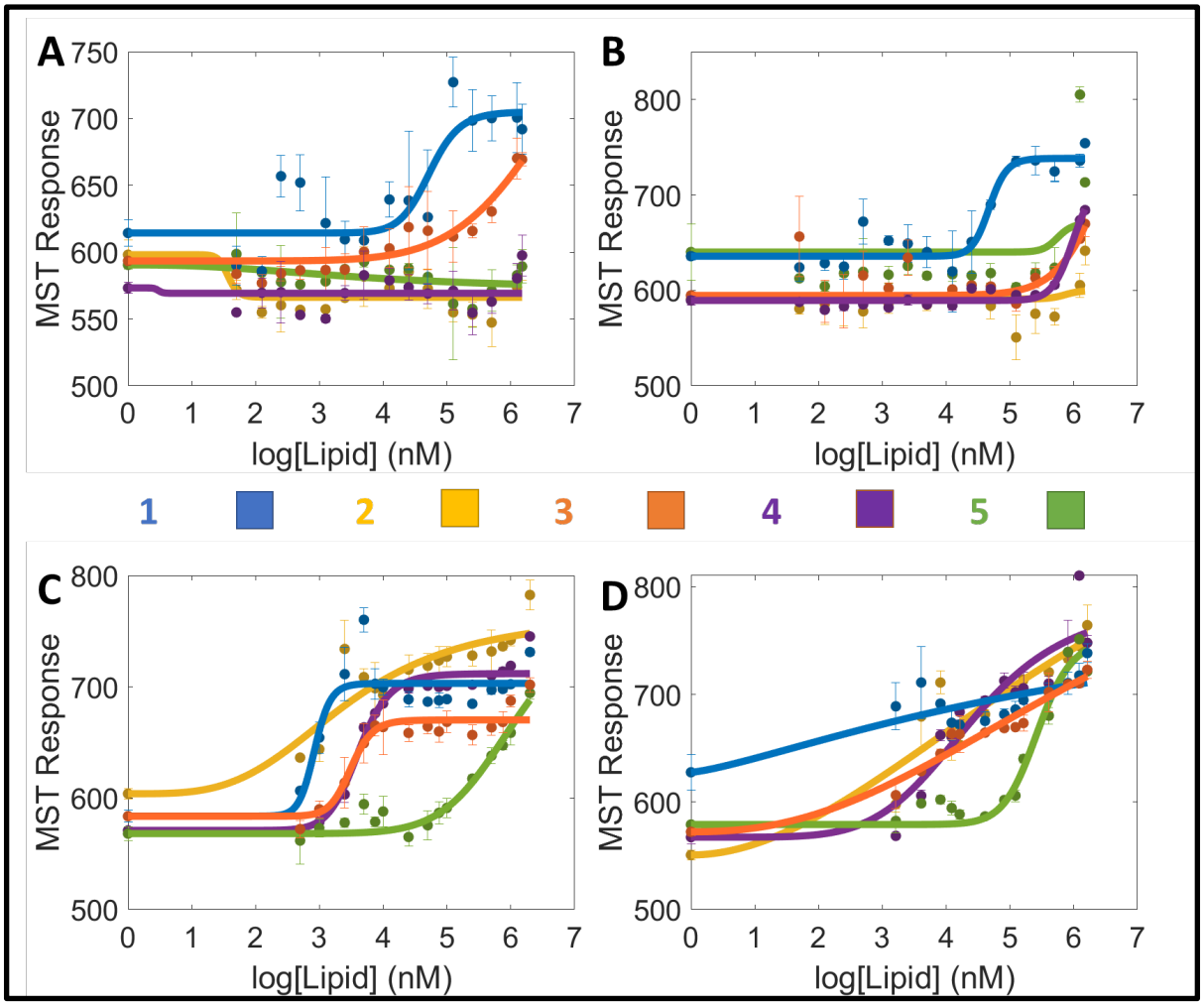

Figure 3: MST thermophoresis response against lipid concentration fits of 1-5 in different lipid compositions and preparations. The upper panels show 100 µm vesicles consisting of (A) 100% DMPC or (B) 95% DMPC/5% DMPG) while the lower panels show SMA-nanodiscs consisting of (C) 100% DMPC or (D) 95% DMPC/5% DMPG.

In the case of the vesicles, such a change in response was only observed for **1** and **2** in DMPC lipids, and for **1**, **2** and **3** when PG lipids are present. They produced a measurable thermophoresis response, possibly because their k_{off} rates were slow enough to have their diffusion rate correlated to that of the

lipid vehicles throughout the detection window. This would be in agreement with the relative k_{off} determined by SPR, where **1** and **2** have a slow k_{off}, and **3** has a similarly slow rate in the presence of PG lipids (Table 2). Overall, the thermophoresis profiles provide less information than the T-jump profiles for AMP-lipid vesicles interactions.

In contrast, the SMA-nanodiscs showed a more pronounced sigmoidal thermophoresis response, particularly in the instance of DMPC nanodiscs (Figures 3C and 3D). This could be the result of a stronger interaction, and slower k_{off} rates for AMP/SMA-discs, but it could also reflect the disassembly of the nanodisc at high peptide:lipid ratios. *Note: The SMA-disc series is insufficiently sampled and this experiment will be repeated before submission*.

Disassociation constant K_D

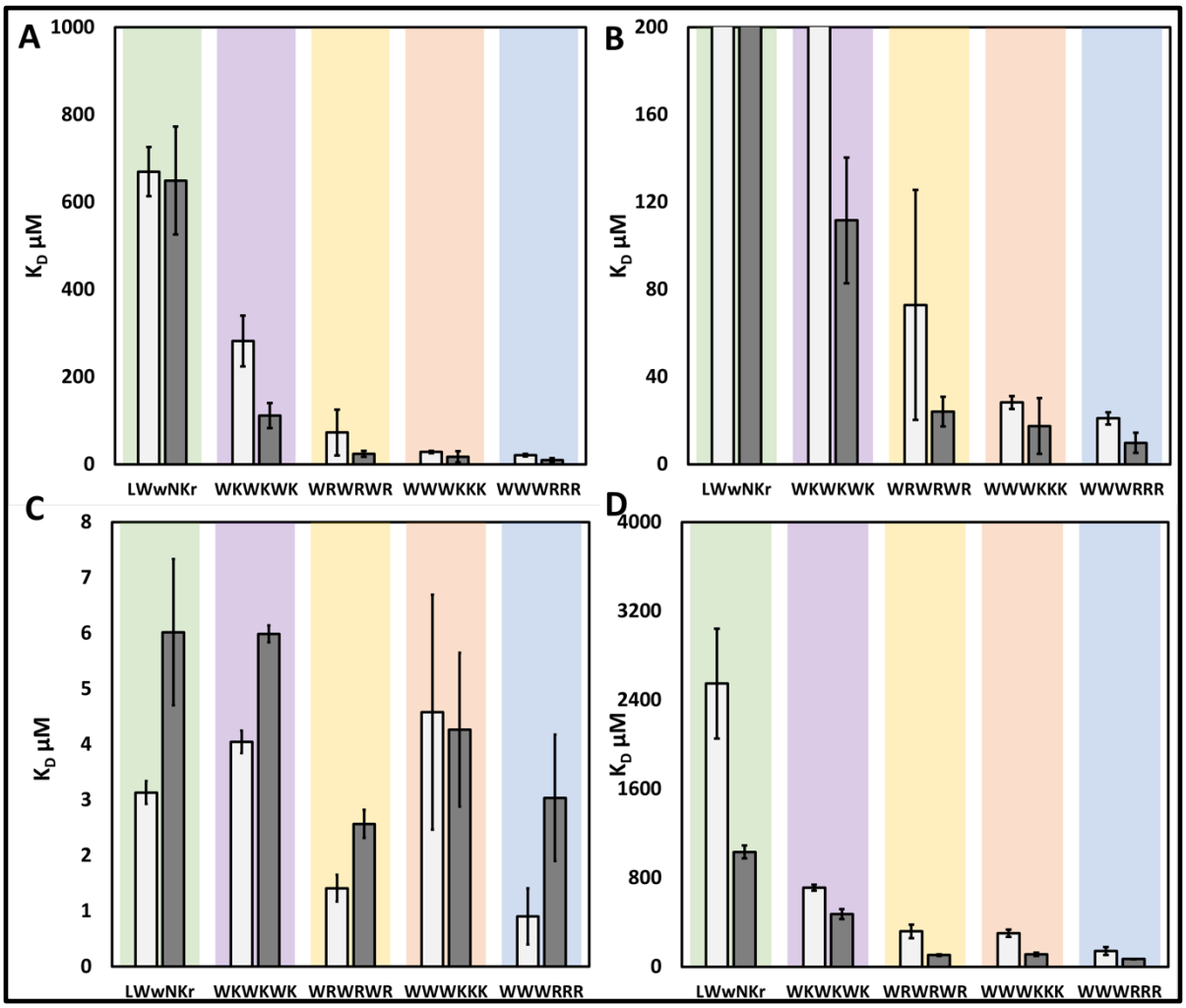

Figure 4: K_Ds determined by MST and SPR to DMPC (light grey) and DMPC/PG (dark grey). A: K_D determined using MST and 100 um vesicles (zoomed B) C: K_D determined using MST and SMA nanodiscs D: KD determined using SPR and Vesicles (extruded through 100 nm filter).

Table 3:Summary of K_D determined using SPR and MST (T-jump).

#	SPR K_D (µM)		MST Vesicle K_D (µM)		MST SMA K_D (µM)	
	PC	PC/PG	PC	PC/PG	PC	PC/PG
1	142 ± 35	70 ± 1.2	21 ± 2.8	10 ± 4.6	0.90 ± 0.5	3.0 ± 1.1
2	318 ± 62	105 ± 7.0	73 ± 53	24 ± 6.8	1.4 ± 0.2	2.6 ± 0.3
3	302 ± 32	112 ± 15	28 ± 2.9	17 ± 13	4.6 ± 2.1	4.3 ± 1.4
4	712 ± 27	474 ± 45	282 ± 58	112 ± 29	4.0 ± 0.2	6.0 ± 0.2
5	2548 ± 493	1033 ± 58	670 ± 56	650 ± 123	3.1 ± 0.2	6.0 ± 1.3

Comparison of the MST vesicle derived and SPR derived K_D showed that the absolute K_D obtained by MST are were systematically offset by an approximate factor 5. However, the relative values showed a great deal of similarity between the MST and SPR K_D, resulting in the same stratification of the peptides. The inactive peptide **5** had a considerably higher K_D compared to **1-4**. A larger separation between the bindings of **1-4** was also observed with the clumped sequence peptides **1** and **3** having significantly stronger binding than **4**. In both instances the impact of the presence of PG lipids in the vesicles has on binding is clear, with an almost universal decrease in K_D for all peptides by a factor of 2. This highlights how cationic AMPs such as the ones tested can exert selectivity towards bacterial membranes where anionic lipids are present on the outer membrane, and the role such anionicity has in this selectivity.

Comparison of the two sets of MST derived K_D shows a large difference between the vesicles and SMA-nanodisc lipid systems. The apparent line fits for the SMA discs result in overestimated binding due to the secondary response not being included in the line fit. This yields all peptides **1-5** having K_D of 6 µM or lower in Table 3. Visually, the strongest binders also produce the earliest and strongest MST response, but the full line shape was not sufficiently sampled to allow successful ranking of the AMPs from the SMA-nanodisc experiment. Importantly, the apparent K_D may not describe the actual interaction but rather the physical event occurring at the highest peptide:lipid ratios, which is possibly the disassembly of the nanodisc caused by peptide overload.

On a general note, it is important to keep the relative size of the lipid systems used in mind. Vesicles produced had a diameter of ~140 nm and would consist of approximately 200,000 lipids (with a molecular weight of ~140 MDa), in comparison the nanodiscs that contain approximately 900 lipids (lipid weight of ~600 kDa[1]) (Table 4). The AMPs used have molecular weights between 884 Da and 1027 Da, therefore when multiple AMPs are able to bind to a disc, the resulting change in weight, size and shape of the nanodisc will be larger, than with a vesicle.

*Table 4: Comparison of estimated vesicle and nanodisc sizes. *surface area of both sides of the bilayer. ** assuming 100% DMPC composition.*

Model	Vesicle	SMA-nanodisc
Radius (nm)	72	10
Surface area (nm2)*	120000	530

[1] Weight excludes SMA polymer due to the uncertainty of the amount of SMA per disc.

Total number of lipids**	200000	900
Approx. weight**	140 MDa	600 kDa[1]

Another important consideration is the fraction of the lipids in the different methods that are available to the AMPs. In nanodiscs both sides are exposed to the AMPs, while for vesicles only the outer leaflet of the vesicle is exposed. In SPR, an unknown fraction of the immobilised lipids are available for interactions, depending on the degree of fusion occurring on the surface of the chip.

Furthermore, the heterogeneity of the lipid phases in the nanodiscs is a factor that will potentially affect the interactions. The lipids solubilised in SMA-nanodiscs are less tightly packed than those in solubilised in vesicles and have a reduced melting point[35]. The inner-most lipids of nanodiscs are in a more ordered phase,[36] while the outer most lipids, those closest to the SMA-belt, are more perturbed by the styrene groups of SMA.[35] AMPs are known to favour lipids that are in a more disordered phase, and therefore one would expect the AMPs to interact more easily with the disordered region, and give rise to heterogeneous interactions and distributions within the nanodiscs.[37] Vesicles in contrast, have a uniformity of phase (at 25°C this is near the T_m of DMPC and in the liquid-ordered phase).[26]

The extracted MST-nanodisc K_D are in the same range that have been previously extracted using MSP-nanodiscs and ITC where Zhang et al.[38] observed binding to anionic lipid nanodiscs in the range of 1-2 µM. Using fluorescent based approaches and vesicles, Christiaens et al. found that the peptides had a broad range of bindings from 350 µM towards PC vesicles, down to low µM-nM bindings to anionic rich vesicles[39]. Such results show that AMPs can bind in the low µM range to both vesicles and nanodiscs when anionic lipids are present, though the binding of the AMPs should be much weaker towards zwitterionic membrane models. It should be noted, that while the reduction in K_D observed for **1-5** is not as large as described in the above works when anionic lipids are introduced, the amount of anionic component introduced (5%) is low in comparison. Zhang et al. and Christiaens et al. make use of up to 20% anionic lipid compositions. In this context it is worth noting that the SMA polymer itself carries negative charges that may be responsible for accommodating the initial interaction with cationic AMPs, and for diluting the expected effect of adding 5% charged lipids.

The previously noted difference between the SPR and MST K_Ds could be explained by the experimental differences between the two methods, specifically that the AMP concentration is fixed in MST while varied in SPR. Hence, the MST method could be considered as the binding of the lipids to the AMP, rather than the AMP binding to the lipids. This is important because at the lowest lipid concentrations being exposed to a constant high peptide concentration, it is highly questionable if either vesicles or nanodiscs can exist in their original assembly, but we rather have to assume that they at some point get disassembled by the vast excess of membrane active peptides and that this process is a part of the measurable response. Further, by keeping the AMP concentration fixed in MST the possibility to explore concentration dependent effects of the AMPs, such as aggregation, is lost. Other instances of experimental method differences that may result in differences in binding could be fewer easily accessible lipids in SPR a result of them being bound to the SPR chip, where the chip-facing side of the vesicle is less accessible (though still accessible), and the AMP stock flowing across the vesicles may result in a weaker observable binding. The two methods produce bindings that are consistent relative to one another with regards to the ranking of the AMPs and the relative differences between the determined K_D, and the fact that the real lipid concentration that is available for binding may be significantly different from the total lipid concentration in the methods which is the one being plotted could explain at least some of the variation in the absolute K_D.

Fluorescence intensity and K_P

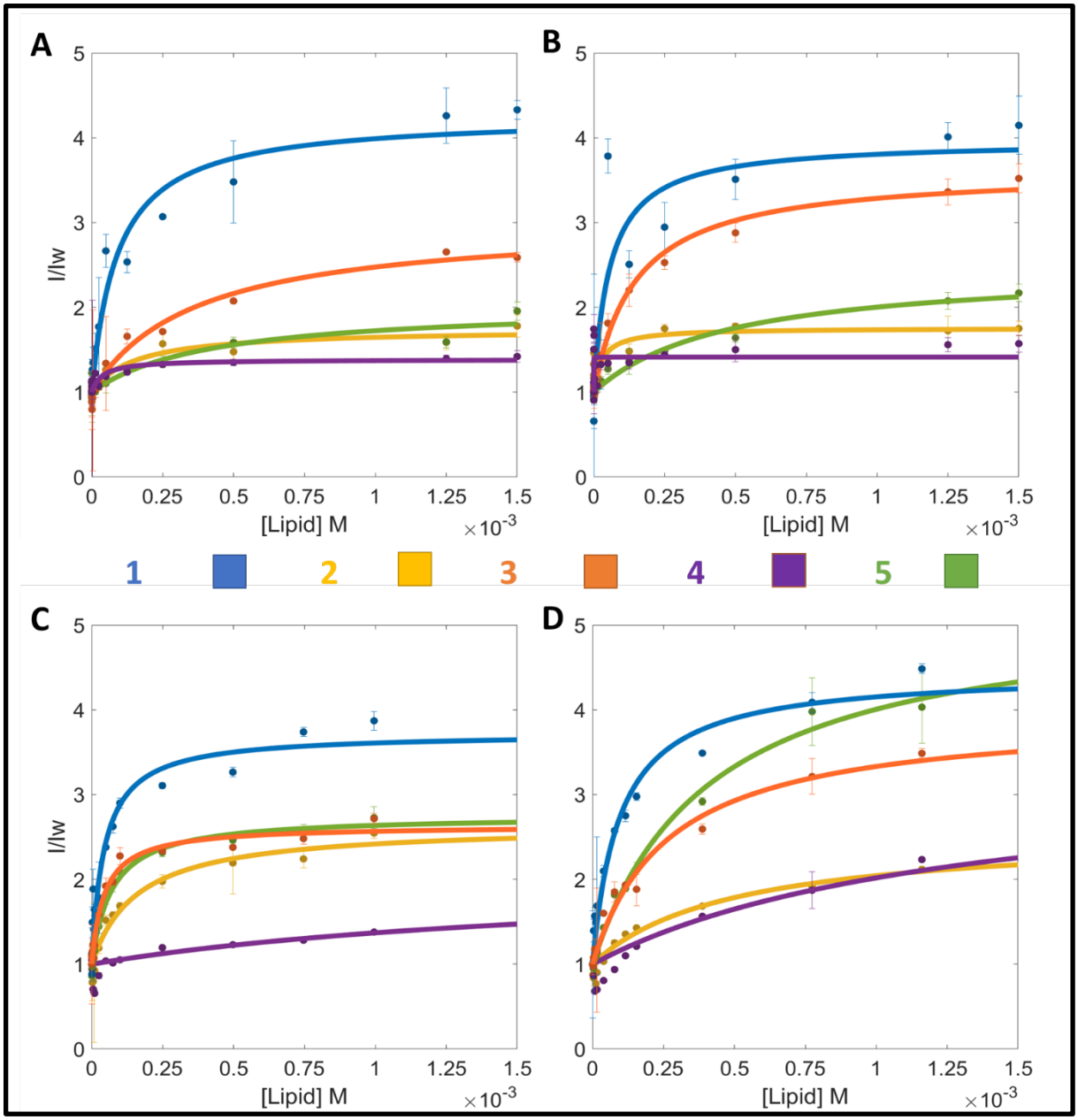

Figure 5: Initial fluorescence and K_P fits of 1-5 in different lipid compositions and preparations. The upper panels show 100 µm vesicles consisting of (A) 100% DMPC or (B) 95% DMPC/5% DMPG) while the lower panels show SMA-nanodiscs consisting of (C) 100% DMPC or (D) 95% DMPC/5% DMPG.

The fluorescence intensities from both SMA-nanodisc and vesicle MST derived data were treated identically. The intensities were normalized on the intensity in pure aqueous solution and plotted against the lipid concentration. The plots produced a characteristic hyperbolic partition curve which could be fit to equation 8[25]. The fitting readily yielded K_P in all instances (Figure 5), which are summarised in Table 5. In brief, the determined K_P follows the K_D trend that **1**>**3**~**2**>**4**>**5** in both vesicles and SMA-nanodiscs for both lipid compositions. The exception is that the negative control peptide, **5**, displays a partition coefficient in nanodiscs that is in the same range as the active peptide **3**, but not in vesicles, and its increased relative K_P is clearly observable in Figure 5. This could again be an indication of that the SMA polymer belt interacts with cationic peptides and interferes with the results.

In both SMA and vesicle datasets there was interference from light scattering effects that lead to an increase in fluorescence intensity at the highest lipid concentrations. The final lipid concentration of ~2 mM was thus removed from the fluorescence fit. The extracted KPs from MST are shown in Figure 6, and all results are summarised in Table 5.

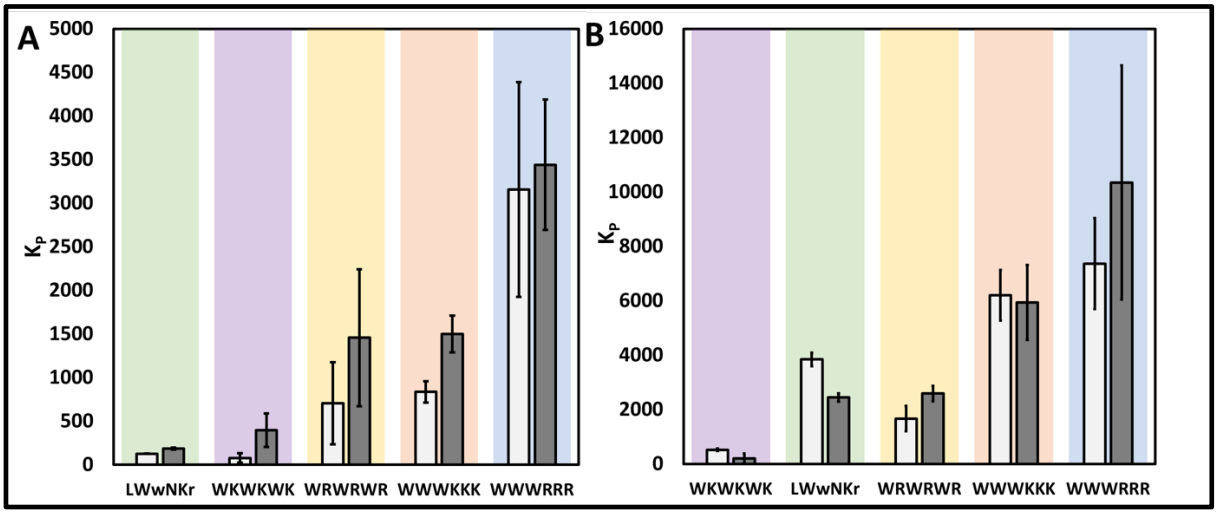

Figure 6: K_Ps determined by MST to DMPC (light grey) and DMPC/PG (dark grey). A: K_P determined using MST and 100 um vesicles B: K_P determined using MST and SMA-nanodiscs.

Table 5: Summary of K_P determined using SPR and MST

Peptide	SPR K_P		Vesicle K_P		SMA K_P	
	PC	PC/PG	PC	PC/PG	PC	PC/PG
1	6649 ± 799	12705 ± 164	3158 ± 1232	3441 ± 749	7367 ± 1671	10351 ± 4304
2	1299 ± 94	3160 ± 146	706 ± 472	1458 ± 785	1667 ± 464	2589 ± 279
3	2534 ± 80	5156 ± 341	836 ± 121	1498 ± 211	6207 ± 930	5940 ± 1374
4	531 ± 10	630 ± 33	78 ± 55	396 ± 192	522 ± 45	202 ± 179
5	278 ± 8	401 ± 19	126 ± 2	188 ± 11	3845 ± 251	2444 ± 150

The absolute K_P determined using MST-nanodiscs is generally comparable to the SPR determined K_Ps, particularly in the case of the PG containing nanodiscs. However, there are some exceptions. Firstly, **5** has a much higher than expected K_P relative to its activity as previously noted, especially in comparison to the vesicle MST and SPR values, where it is the peptide with the lowest K_P, alongside **2**. Furthermore, in the instance of **3, 4**, and **5**, a higher K_P is observed for PC only, which is again in contrast to the SPR and vesicle-based MST (Figure 6B). The general trend for the observed K_P followed the same ranking obtained by SPR, and a similar relationship between the K_Ps – **5** and **4** have much lower K_Ps compared to **2-3** that are similar, and **1** having the largest K_P. The presence of PG has less of an impact on the weaker binding peptide **5**, while for the more stronger binding peptides, the presence of PG has a much greater impact, approximately doubling the K_P – the main outlier in this trend is **1**, where the MST derived K_Ps do not significantly differ in both average and as a result of the error. The vesicle derived MST K_Ps are lower overall compared to the SMA derived values, however, this is to be expected given the stronger binding that was observed to the nanodiscs. A further potential cause of the

difference between the vesicle and SPR K_P (outside of previously discussed differences between SPR and MST) may be due to MST measuring the fluorescence intensity at a fixed wavelength. As a result, any blueshift in wavelength that can be associated with Trp being in a more hydrophobic environment cannot be properly observed, and as such may lead to an underestimation of K_P when using MST[40]. Despite this, and as noted, the relative K_P extracted using vesicles and MST correlates well with those extracted by SPR, showing that MST can be applied in this fashion.

Conclusions

We have shown that it is possible to extract both K_D and K_P of AMPs towards models of zwitterionic and anionic lipid bilayers by using MST on the intrinsic fluorescence of tryptophan. While the extraction of the binding parameters is challenging due to potential interference from light scattering effects and lipid system disassembly events at the extreme high- and low lipid concentrations respectively, the method produces reliable results. The measured K_D and K_P of **1-5** correlate well with both of their respective bactericidal activities (as shown by MIC values) and with the ranking of binding obtained using SPR. We have successfully shown that MST can be used with various lipid particles (SUV and nanodiscs) giving a quick and label-free method for studying membrane activities. However, the SMA-nanodiscs negatively charged polymer belt shows signs of not being a suitable nanodisc system for interaction studies with cationic AMPs, and other nanodisc assemblies should probably be considered for this application.

Author Contributions

Conceptualisation: PR. Peptide synthesis and purification: MS. Nanodisc and vesicle preparation, and MST: PR. Vesicle preparation and SPR: MJ. Data analysis: PR and MJ. Original draft: PR. Visualisation: PR. Writing and editing: PR, MJ, MS, JI. Supervision: RE and JI. All authors reviewed and approved final version.

References

1. Mahlapuu, M.; Hakansson, J.; Ringstad, L.; Bjorn, C., Antimicrobial Peptides: An Emerging Category of Therapeutic Agents. *Front Cell Infect Microbiol* **2016,** *6*, 194.
2. Le, C.-F.; Fang, C.-M.; Sekaran, S. D., Intracellular Targeting Mechanisms by Antimicrobial Peptides. *Antimicrob Agents Chemother* **2017,** *61* (4), e02340-16.
3. Wang, G., Human antimicrobial peptides and proteins. *Pharmaceuticals (Basel)* **2014,** *7* (5), 545-594.
4. Huan, Y.; Kong, Q.; Mou, H.; Yi, H., Antimicrobial Peptides: Classification, Design, Application and Research Progress in Multiple Fields. *Frontiers in Microbiology* **2020,** *11* (2559).
5. Kumar, P.; Kizhakkedathu, J. N.; Straus, S. K., Antimicrobial Peptides: Diversity, Mechanism of Action and Strategies to Improve the Activity and Biocompatibility In Vivo. *Biomolecules* **2018,** *8* (1), 4.
6. Shi, G.; Kang, X.; Dong, F.; Liu, Y.; Zhu, N.; Hu, Y.; Xu, H.; Lao, X.; Zheng, H., DRAMP 3.0: an enhanced comprehensive data repository of antimicrobial peptides. *Nucleic Acids Res* **2022,** *50* (D1), D488-D496.

7. Wang, G.; Li, X.; Wang, Z., APD3: the antimicrobial peptide database as a tool for research and education. *Nucleic Acids Res* **2016,** *44* (D1), D1087-93.
8. Waghu, F. H.; Idicula-Thomas, S., Collection of antimicrobial peptides database and its derivatives: Applications and beyond. *Protein Sci* **2020,** *29* (1), 36-42.
9. Pirtskhalava, M.; Amstrong, A. A.; Grigolava, M.; Chubinidze, M.; Alimbarashvili, E.; Vishnepolsky, B.; Gabrielian, A.; Rosenthal, A.; Hurt, D. E.; Tartakovsky, M., DBAASP v3: database of antimicrobial/cytotoxic activity and structure of peptides as a resource for development of new therapeutics. *Nucleic Acids Res* **2021,** *49* (D1), D288-D297.
10. Piotto, S. P.; Sessa, L.; Concilio, S.; Iannelli, P., YADAMP: yet another database of antimicrobial peptides. *Int J Antimicrob Agents* **2012,** *39* (4), 346-51.
11. Hancock, R. E. W.; Sahl, H.-G., Antimicrobial and host-defense peptides as new anti-infective therapeutic strategies. *Nature Biotechnology* **2006,** *24* (12), 1551-1557.
12. Hancock, R. E. W., Peptide antibiotics. *The Lancet* **1997,** *349* (9049), 418-422.
13. Wang, C. K.; Shih, L. Y.; Chang, K. Y., Large-Scale Analysis of Antimicrobial Activities in Relation to Amphipathicity and Charge Reveals Novel Characterization of Antimicrobial Peptides. *Molecules* **2017,** *22* (11).
14. Lei, J.; Sun, L.; Huang, S.; Zhu, C.; Li, P.; He, J.; Mackey, V.; Coy, D. H.; He, Q., The antimicrobial peptides and their potential clinical applications. *Am J Transl Res* **2019,** *11* (7), 3919-3931.
15. Strøm, M. B.; Haug, B. E.; Skar, M. L.; Stensen, W.; Stiberg, T.; Svendsen, J. S., The Pharmacophore of Short Cationic Antibacterial Peptides. *J. Med. Chem.* **2003,** *46* (9), 1567-1570.
16. Rice, A.; Wereszczynski, J., Probing the disparate effects of arginine and lysine residues on antimicrobial peptide/bilayer association. *Biochimica et Biophysica Acta (BBA) - Biomembranes* **2017,** *1859* (10), 1941-1950.
17. Jerabek-Willemsen, M.; André, T.; Wanner, R.; Roth, H. M.; Duhr, S.; Baaske, P.; Breitsprecher, D., MicroScale Thermophoresis: Interaction analysis and beyond. *Journal of Molecular Structure* **2014,** *1077*, 101-113.
18. Topf, A.; Franz, P.; Tsiavaliaris, G., MicroScale Thermophoresis (MST) for studying actin polymerization kinetics. *BioTechniques* **2017,** *63* (4), 187-190.
19. Jerabek-Willemsen, M.; Wienken, C. J.; Braun, D.; Baaske, P.; Duhr, S., Molecular Interaction Studies Using Microscale Thermophoresis. *ASSAY and Drug Development Technologies* **2011,** *9* (4), 342-353.
20. Bartoschik, T.; Galinec, S.; Kleusch, C.; Walkiewicz, K.; Breitsprecher, D.; Weigert, S.; Muller, Y. A.; You, C.; Piehler, J.; Vercruysse, T.; Daelemans, D.; Tschammer, N., Near-native, site-specific and purification-free protein labeling for quantitative protein interaction analysis by MicroScale Thermophoresis. *Scientific Reports* **2018,** *8* (1), 4977.
21. Yu, L.; Fan, Q.; Yue, X.; Mao, Y.; Qu, L., Activity of a novel-designed antimicrobial peptide and its interaction with lipids. **2015,** *21* (4), 274-282.
22. Figueira, T. N.; Freire, J. M.; Cunha-Santos, C.; Heras, M.; Gonçalves, J.; Moscona, A.; Porotto, M.; Salomé Veiga, A.; Castanho, M. A. R. B., Quantitative analysis of molecular partition towards lipid membranes using surface plasmon resonance. *Scientific Reports* **2017,** *7* (1), 45647.
23. Jarmoskaite, I.; AlSadhan, I.; Vaidyanathan, P. P.; Herschlag, D., How to measure and evaluate binding affinities. *eLife* **2020,** *9*, e57264.
24. Salahudeen, M. S.; Nishtala, P. S., An overview of pharmacodynamic modelling, ligand-binding approach and its application in clinical practice. *Saudi Pharm J* **2017,** *25* (2), 165-175.
25. Matos, P. M.; Franquelim, H. G.; Castanho, M. A. R. B.; Santos, N. C., Quantitative assessment of peptide–lipid interactions.: Ubiquitous fluorescence methodologies. *Biochimica et Biophysica Acta (BBA) - Biomembranes* **2010,** *1798* (11), 1999-2012.
26. Marsh, D., *Handbook of lipid bilayers*. 2nd ed. ed.; CRC Press: Boca Raton, Fla, 2013.
27. Speck, S.; Courtiol, A.; Junkes, C.; Dathe, M.; Müller, K.; Schulze, M., Cationic Synthetic Peptides: Assessment of Their Antimicrobial Potency in Liquid Preserved Boar Semen. *PLOS ONE* **2014,** *9* (8), e105949.

28. Finger, S.; Kerth, A.; Dathe, M.; Blume, A., The efficacy of trivalent cyclic hexapeptides to induce lipid clustering in PG/PE membranes correlates with their antimicrobial activity. *Biochimica et Biophysica Acta (BBA) - Biomembranes* **2015,** *1848* (11, Part A), 2998-3006.
29. Lau, Q. Y.; Ng, F. M.; Cheong, J. W. D.; Yap, Y. Y. A.; Tan, Y. Y. F.; Jureen, R.; Hill, J.; Chia, C. S. B., Discovery of an ultra-short linear antibacterial tetrapeptide with anti-MRSA activity from a structure–activity relationship study. *European Journal of Medicinal Chemistry* **2015,** *105*, 138-144.
30. Gopal, R.; Kim, Y. J.; Seo, C. H.; Hahm, K.-S.; Park, Y., Reversed sequence enhances antimicrobial activity of a synthetic peptide. *Journal of Peptide Science* **2011,** *17* (5), 329-334.
31. Gopal, R.; Na, H.; Seo, C. H.; Park, Y., Antifungal Activity of (KW)n or (RW)n Peptide against Fusarium solani and Fusarium oxysporum. *International Journal of Molecular Sciences* **2012,** *13* (11).
32. Figueira, T. N.; Freire, J. M.; Cunha-Santos, C.; Heras, M.; Gonçalves, J.; Moscona, A.; Porotto, M.; Salomé Veiga, A.; Castanho, M. A. R. B., Quantitative analysis of molecular partition towards lipid membranes using surface plasmon resonance. *Scientific reports* **2017,** *7*, 45647-45647.
33. López-Méndez, B.; Baron, B.; Brautigam, C. A.; Jowitt, T. A.; Knauer, S. H.; Uebel, S.; Williams, M. A.; Sedivy, A.; Abian, O.; Abreu, C.; Adamczyk, M.; Bal, W.; Berger, S.; Buell, A. K.; Carolis, C.; Daviter, T.; Fish, A.; Garcia-Alai, M.; Guenther, C.; Hamacek, J.; Holková, J.; Houser, J.; Johnson, C.; Kelly, S.; Leech, A.; Mas, C.; Matulis, D.; McLaughlin, S. H.; Montserret, R.; Nasreddine, R.; Nehmé, R.; Nguyen, Q.; Ortega-Alarcón, D.; Perez, K.; Pirc, K.; Piszczek, G.; Podobnik, M.; Rodrigo, N.; Rokov-Plavec, J.; Schaefer, S.; Sharpe, T.; Southall, J.; Staunton, D.; Tavares, P.; Vanek, O.; Weyand, M.; Wu, D., Reproducibility and accuracy of microscale thermophoresis in the NanoTemper Monolith: a multi laboratory benchmark study. *European Biophysics Journal* **2021,** *50* (3), 411-427.
34. López-Méndez, B.; Uebel, S.; Lundgren, L. P.; Sedivy, A., Microscale Thermophoresis and additional effects measured in NanoTemper Monolith instruments. *European Biophysics Journal* **2021,** *50* (3), 653-660.
35. Grethen, A.; Oluwole, A. O.; Danielczak, B.; Vargas, C.; Keller, S., Thermodynamics of nanodisc formation mediated by styrene/maleic acid (2:1) copolymer. *Scientific Reports* **2017,** *7* (1), 11517.
36. Stepien, P.; Augustyn, B.; Poojari, C.; Galan, W.; Polit, A.; Vattulainen, I.; Wisnieska-Becker, A.; Rog, T., Complexity of seemingly simple lipid nanodiscs. *Biochimica et Biophysica Acta (BBA) - Biomembranes* **2020,** *1862* (11), 183420.
37. Su, J.; Marrink, S. J.; Melo, M. N., Localization Preference of Antimicrobial Peptides on Liquid-Disordered Membrane Domains. *Frontiers in Cell and Developmental Biology* **2020,** *8*.
38. Zhang, A. H.; Edwards, I. A.; Mishra, B. P.; Sharma, G.; Healy, M. D.; Elliott, A. G.; Blaskovich, M. A. T.; Cooper, M. A.; Collins, B. M.; Jia, X.; Mobli, M., Elucidating the Lipid Binding Properties of Membrane-Active Peptides Using Cyclised Nanodiscs. *Frontiers in Chemistry* **2019,** *7*.
39. Christiaens, B.; Symoens, S.; Vanderheyden, S.; Engelborghs, Y.; Joliot, A.; Prochiantz, A.; Vandekerckhove, J.; Rosseneu, M.; Vanloo, B., Tryptophan fluorescence study of the interaction of penetratin peptides with model membranes. *European Journal of Biochemistry* **2002,** *269* (12), 2918-2926.
40. Santos, N. C.; Prieto, M.; Castanho, M. A. R. B., Quantifying molecular partition into model systems of biomembranes: an emphasis on optical spectroscopic methods. *Biochimica et Biophysica Acta (BBA) - Biomembranes* **2003,** *1612* (2), 123-135.

Supplemental materials: Novel application of label free MST: Measurement of AMP affinity (K_D) and partitioning (K_P) to lipid vesicles and SMA-nanodiscs

Philip Rainsford, Martin Jakubec, Mitchell Silk, Richard Engh, Johan Isaksson

Supp. 1

Cyclic Peptide Purification and characterisation:

1; *Cyclo*(WWWRRR). *Linear precursor:* H_2N-Arg(Pbf)-Arg(Pbf)-Arg(Pbf)-Trp(Boc)-Trp(Boc)-Trp(Boc)-OH. *Cyclic: cyclo*(Trp-Trp-Trp-Arg-Arg-Arg). Purification gradient: 15-75% buffer B over 60 min, t_R = 18 min (33% buffer B). Yield: 46.7 mg (30.0% relative to linear precursor) as a white solid. ESI-FTMS $[M + H]^+$ calculated: 1027.5419, found: 1027.5473, $[M + 2H]^{2+}$ calculated: 514.2785, found: 514.2770, $[M + 3H]^{3+}$ calculated: 343.1882, found: 343.1872.

2; *Cyclo*(WRWRWR). *Linear precursor:* H_2N-Arg(Pbf)-Trp(Boc)-Arg(Pbf)-Trp(Boc)-Arg(Pbf)-Trp(Boc)-OH. *Cyclic: cyclo*(Trp-Arg-Trp-Arg-Trp-Arg). Purification gradient: 5-65% buffer B over 60 min, t_R = 25 min (30% buffer B). Yield: 26.9 mg (22.6% relative to linear precursor) as a white solid. ESI-FTMS $[M + 2H]_{2+}$ calculated: 514.2785, found: 514.2779, $[M + 3H]_{3+}$ calculated: 343.1882, found: 343.1883.

3; *Cyclo*(WWWKKK). *Linear precursor:* H_2N-Lys(Boc)-Lys(Boc)-Lys(Boc)-Trp(Boc)-Trp(Boc)-Trp(Boc)-OH. *Cyclic: cyclo*(Trp-Trp-Trp-Lys-Lys-Lys). Purification gradient: 10-70% buffer B over 60 min, t_R = 22 min (32% buffer B). Yield: 49.5 mg (39.0% relative to linear precursor) as a white solid. ESI-FTMS $[M + H]_+$ calculated: 943.5307, found: 943.5354, $[M + Na]_+$ calculated: 965.5126, found: 965.5159, $[M + 2H]_{2+}$ calculated: 472.2693, found: 472.2702.

4; *Cyclo*(WWWKKK). *Linear precursor:* H_2N-Trp(Boc)-Lys(Boc)-Trp(Boc)-Lys(Boc)-Trp(Boc)-Lys(Boc)-OH. *Cyclic: cyclo*(Trp-Lys-Trp-Lys-Trp-Lys). Purification gradient: 5-65% buffer B over 60 min, t_R = 21 min (26% buffer B). Yield: 40.7 mg (41.8% relative to linear precursor) as a white solid. ESI-FTMS $[M + H]_+$ calculated: 943.5307, found: 943.5308, calculated: 472.2693, found: 472.2689.

5; *Cyclo*(LWwNKr). *Linear precursor:* H_2N-Trp(Boc)-D-Trp(Boc)-Asn(Trt)-Lys(Boc)-D-Arg(Pbf)-Leu-OH. *Cyclic: cyclo*(Leu-Trp-D-Trp-Asn-Lys-D-Arg). Purification gradient: 10-70% buffer B over 60 min, 6 mL/min, t_R = 23 min (33% buffer B). Yield: 35.1 mg (44.9% relative to linear

precursor) as a white solid. ESI-FTMS $[M + H]^+$ calculated: 884.4895, found: 884.4895, $[M + 2H]^{2+}$ calculated: 442.7487, found: 442.7483.

MST Sample	Final lipid concentration (nM)	Final AMP concentration (nM)
1	1500000	2500
2	1250000	2500
3	500000	2500
4	250000	2500
5	125000	2500
6	50000	2500
7	25000	2500
8	12500	2500
9	5000	2500
10	2500	2500
11	1250	2500
12	500	2500
13	250	2500
14	125	2500
15	50	2500
16	0	2500

Supp. Table 1: Table of lipid and peptide concentrations for MST

PAPER III

frontiers in Microbiology

ORIGINAL RESEARCH
published: 01 October 2021
doi: 10.3389/fmicb.2021.730740

Lulworthinone, a New Dimeric Naphthopyrone From a Marine Fungus in the Family Lulworthiaceae With Antibacterial Activity Against Clinical Methicillin-Resistant *Staphylococcus aureus* Isolates

Marte Jenssen[1], Philip Rainsford[2], Eric Juskewitz[3], Jeanette H. Andersen[1], Espen H. Hansen[1], Johan Isaksson[2], Teppo Rämä[1] and Kine Ø. Hansen[1]*

[1] Marbio, The Norwegian College of Fishery Science, Faculty of Biosciences, Fisheries and Economics, UiT the Arctic University of Norway, Tromsø, Norway, [2] Department of Chemistry, Faculty of Science and Technology, UiT the Arctic University of Norway, Tromsø, Norway, [3] Research Group for Host Microbe Interactions, Department of Medical Biology, Faculty of Health Sciences, UiT the Arctic University of Norway, Tromsø, Norway

OPEN ACCESS

Edited by:
Carolina Elena Girometta, University of Pavia, Italy

Reviewed by:
Susan Semple, University of South Australia, Australia
Adelaide Almeida, University of Aveiro, Portugal

***Correspondence:**
Marte Jenssen
marte.jenssen@uit.no

Specialty section:
This article was submitted to Microbiotechnology, a section of the journal Frontiers in Microbiology

Received: *25 June 2021*
Accepted: *06 September 2021*
Published: *01 October 2021*

Citation:
Jenssen M, Rainsford P, Juskewitz E, Andersen JH, Hansen EH, Isaksson J, Rämä T and Hansen KØ (2021) Lulworthinone, a New Dimeric Naphthopyrone From a Marine Fungus in the Family Lulworthiaceae With Antibacterial Activity Against Clinical Methicillin-Resistant Staphylococcus aureus Isolates. Front. Microbiol. 12:730740. doi: 10.3389/fmicb.2021.730740

The emergence of drug-resistant bacteria is increasing rapidly in all parts of the world, and the need for new antibiotics is urgent. In our continuous search for new antimicrobial molecules from under-investigated Arctic marine microorganisms, a marine fungus belonging to the family Lulworthiaceae (Lulworthiales, Sordariomycetes, and Ascomycota) was studied. The fungus was isolated from driftwood, cultivated in liquid medium, and studied for its potential for producing antibacterial compounds. Through bioactivity-guided isolation, a novel sulfated biarylic naphtho-α-pyrone dimer was isolated, and its structure was elucidated by spectroscopic methods, including 1D and 2D NMR and HRMS. The compound, named lulworthinone (**1**), showed antibacterial activity against reference strains of *Staphylococcus aureus* and *Streptococcus agalactiae*, as well as several clinical MRSA isolates with MICs in the 1.56–6.25 μg/ml range. The compound also had antiproliferative activity against human melanoma, hepatocellular carcinoma, and non-malignant lung fibroblast cell lines, with IC_{50} values of 15.5, 27, and 32 μg/ml, respectively. Inhibition of bacterial biofilm formation was observed, but no eradication of established biofilm could be detected. No antifungal activity was observed against *Candida albicans*. During the isolation of **1**, the compound was observed to convert into a structural isomer, **2**, under acidic conditions. As **1** and **2** have high structural similarity, NMR data acquired for **2** were used to aid in the structure elucidation of **1**. To the best of our knowledge, lulworthinone (**1**) represents the first new bioactive secondary metabolite isolated from the marine fungal order Lulworthiales.

Keywords: antibacterial, marine fungi *sensu stricto*, Lulworthiales, lulworthinone, MRSA, natural product, mycology, natural product artifact

INTRODUCTION

Antimicrobial resistance is quickly developing as a worldwide threat, causing problems not only in the general community but also in healthcare facilities. Infections caused by methicillin-resistant *Staphylococcus aureus* (MRSA) has become a worldwide health menace (WHO, 2014). There is an urgent need to develop new antibiotics to fight these resistant microbes. The fungal kingdom has historically played an important role in the discovery and development of antibiotics and other drugs against non-infective diseases (Demain, 2014). The penicillins and cephalosporins are examples of important antibiotics isolated from fungi (Demain, 2014), from the genera *Penicillium* and *Sarocladium* (one syn. *Cephalosporium*), respectively. In marine natural product discovery, the genera *Aspergillus* and *Penicillium* have proven to be the most prolific producers of new compounds with biological activities (Imhoff, 2016). As the focus of marine natural product discovery has been on mold fungi belonging to the few genera mentioned above, the strictly marine clades of fungi remain understudied (Overy et al., 2014).

One of the understudied marine clades include the fungal order Lulworthiales from which no secondary metabolites have been reported since the discovery of the type genus and species, *Lulworthia fucicola*, in the beginning of the twentieth century (Sutherland, 1915). The order Lulworthiales was established in 2000 to accommodate the new family Lulworthiaceae in the class Sordariomycetes (Kohlmeyer et al., 2000). More recently, a new subclass, Lulworthiomycetidae, was described containing the orders Lulworthiales and Koralionastetales (Maharachchikumbura et al., 2015). Lulworthiaceae is the sole family in the Lulworthiales order, and Lulworthiaceae spp. are regarded as strictly marine species, which include the following genera: *Cumulospora*, *Halazoon*, *Hydea*, *Kohlmeyerella*, *Lulwoana*, *Lulworthia*, *Lindra*, *Matsusporium*, and *Moleospora* (Poli et al., 2020). Recently, a novel genus was introduced to the Lulworthiaceae, *Paralulworthia*, with two new species described, *Paralulworthia gigaspora* and *Paralulworthia posidoniae* (Poli et al., 2020). Hyde et al. (2020) also included the following genera in the family: *Haloguignardia*, *Lolwoidea*, *Moromyces*, *Orbimyces*, *Rostrupiella*, and *Sammeyersia*.

Fungi in the family Lulworthiaceae have been isolated from a variety of substrates and environments. Some examples include corals (Góes-Neto et al., 2020), plants located in salt marches (Calado et al., 2019), seagrass (Poli et al., 2020), Portuguese marinas (Azevedo et al., 2017), sandy beaches of the Cozumel island in Mexico (Velez et al., 2015), brown seaweed (Zuccaro et al., 2008), and driftwood (Rämä et al., 2014). The distribution of Lulworthiales fungi in marine habitats has been studied throughout the history of marine mycology (Johnson, 1958; Kohlmeyer et al., 2000; Koch et al., 2007; Rämä et al., 2014; Azevedo et al., 2017; Góes-Neto et al., 2020), but the biosynthetic potential of these fungi has not been investigated, most likely due to the special knowledge required for their isolation (Overy et al., 2019) and low growth rates.

In this paper, we report the isolation of a new antibacterial compound, lulworthinone (**1**), from a liquid culture of a marine fungus belonging to Lulworthiaceae (isolate 067bN1.2). We elucidate the structure of **1** and study its bioactivity against prokaryotic and eukaryotic cells with focus on antibacterial activity against clinical MRSA isolates. Compound **1** represents the first secondary metabolite reported from this order of fungi, and to the best of our knowledge, the first biarylic dimeric naphtho-α-pyrone substituted with a sulfate group. Initially, the compound was isolated using preparative HPLC under acidic conditions. As this procedure caused significant wear and tear to the equipment, the isolation was switched to flash chromatography under neutral conditions. When comparing spectroscopic data from the two samples, one isolated at neutral and one at acidic conditions, structural differences were observed. It was later determined that **1** concerts into the artifact **2** under acidic conditions.

MATERIALS AND METHODS

Biological Material and Phylogenetic Analysis of Isolate 067bN1.2

The marine fungus 067bN1.2 was isolated from a dead pine (*Pinus* sp.) collected in the splash zone in Kongsfjord, Berlevåg Norway in 2010. The isolate grew from a small wooden cube plated onto agar medium (specified below) during a campaign to study wood-inhabiting fungi of 50 intertidal and sea-floor logs along the Northern Norwegian coast, where Lulworthiales was one of the five most frequent orders isolated (Rämä et al., 2014). The fungus was subcultured and DNA sequenced, and the fungus was phylogenetically placed in the Lulworthiales order (isolate TR498 represents 067bN1.2 in Rämä et al., 2014). At the time of the publication (2014), the closest match from Blast, based on a 5.8S/large ribosomal subunit (LSU) dataset, was *Lulworthia medusa* (LSU sequence: AF195637). The following primer pairs were used for the internal transcribed spacer (ITS), LSU and small ribosomal subunit (SSU) sequencing, respectively: ITS5-ITS4 (White et al., 1990), LR0R-LR5 (Vilgalys and Hester, 1990; Rehner and Samuels, 1994), and NS1-NS4 (White et al., 1990). The ITS, LSU, and SSU sequences are deposited in GenBank under the following accessions: MW377595, MW375591, and MW375590. The mycelium of the fungus was preserved on pieces of agar in 20% glycerol solution at −80°C.

To identify the isolate 067bN1.2 growing as an asexual morph in culture and determine its systematic position within the order Lulworthiales, a phylogenetic analysis was run using a dataset consisting of nrSSU, nrITS, and nrLSU sequences. The reference sequences included in the analyses were sampled based on recent phylogenetic studies focusing on Lulworthiales (Azevedo et al., 2017; Poli et al., 2020) and retrieved from Genbank (**Supplementary Table 1**). Sequences for each gene were aligned individually using the E-INS-I and G-INS-I algorithms of MAFFT v7.388 (Katoh et al., 2002; Katoh and Standley, 2013) in Geneious Prime v.11.0.4 followed by manual adjustment. The concatenated dataset consisting of SSU, 5.8S, and LSU sequences and having a length of 2,270 nt was run through PartitionFinder v2.1.1 (Lanfear et al., 2017) to test for best-fit partitioning schemes and evolutionary models with the following settings: models MrBayes, linked branch lengths, greedy search, and AIC

and BIC model selection (Lanfear et al., 2012). This suggested three partitions with varying models: symmetrical model with equal base frequencies and gamma distributed rate variation among sites without (SYM+G) and with (SYM+I+G) invariable sites and general time reversible model with variable base frequencies and gamma distributed rate variation among sites (GTR+G). A phylogenetic analysis was set up applying suggested models using Parallel-MPI MrBayes v3.2.7a with beagle, and was run for 5,000,000 generations or until average standard deviation of split frequencies was below 0.0009 with sampling each of the 2,500 generations (Ronquist et al., 2012). In addition, RAxML in Geneious v10.2.3 was run with the same partitions under GTRCAT and GTRGAMMA using rapid-bootstrapping algorithm with 2,000 replicates with search for best scoring ML tree (Stamatakis, 2006). The resulting MrBayes tree was similar to the RAxML tree, excluding some of the basal nodes within Lulworthiaceae shown as polytomies in the MrBayes tree.

Fungal Cultivation and Extraction

For the purpose of this study, the fungal isolate was plated from glycerol stock and grown on nutrient-poor malt agar with sea salts [4 g/L malt extract (Moss Malt Extrakt, Jensen & Co AS), 40 g/L sea salts (S9883, Sigma-Aldrich), 15 g/L agar (A1296, Sigma-Aldrich) and Milli-Q® H_2O] until the growth covered the entire agar plate (approximately 40 days). Milli-Q® H_2O was produced with the in-house Milli-Q® system. One-half of the agar plate covered in mycelium was used to inoculate each liquid culture, in malt medium with added sea salts (4 g/L malt extract, 40 g/L sea salts). Two cultures of 200 ml were inoculated and incubated for 107 days at static conditions and 13°C. Before the addition of resin for extraction, mycelium was taken from the culture for inoculation of another round of cultures. The second cultivation contained four cultures with 250 ml of malt extract medium supplemented with sea salts and cultivated under the same conditions for 83 days. The total culture volume used for the extraction of **1** was 1.4 L. The cultures were extracted using Diaion HP-20 resin (13607, Supelco) and methanol (20864, HPLC grade, VWR) as described previously (Kristoffersen et al., 2018; Schneider et al., 2020). The extract was dried in a rotary evaporator at 40°C under reduced pressure and stored at −20°C.

Dereplication

As part of our ongoing search for antimicrobial compounds, extracts of marine microorganisms are fractioned into six fractions using flash chromatography, as previously described (Schneider et al., 2020). When we investigated the antibacterial potential of fractions produced from several understudied marine fungi, one fraction from isolate 067bN1.2 piqued our interest due to its antibacterial activity. In the active fraction, **1** was the dominating peak. The monoisotopic mass, calculated elemental composition and fragmentation pattern of **1** was determined using UHPLC-ESI-HRMS. UHPLC-ESI-HRMS was performed with positive ionization mode, using an Acquity I-class UPLC with an Acquity UPLC C18 column (1.7 μm, 2.1 mm × 100 mm), coupled to a PDA detector and a Vion IMS QToF (all from Waters). Compounds were eluted with a gradient over 12 min, from 10 to 90% acetonitrile (LiChrosolv, 1.00029, Supelco) with 0.1% formic acid (Sigma-Aldrich) in Milli-Q H_2O and a flow rate of 0.45 ml/min. Waters UNIFI 1.9.4 Scientific Information System was used to process and analyze the data. Elemental compositions of compounds in the samples were used to search relevant databases, such as Chemspider, in order to identify known compounds. Since the calculated elemental composition gave no hits in database searches, **1** was nominated for isolation.

Isolation of 1

Initial attempts to isolate **1** was performed using mass guided preparative HPLC. This strategy proved difficult due to extensive binding of the compound to an Atlantis Prep C18 (10 μM, 10 × 250 mm) (Waters) column, leading to inefficient isolation and column contamination. The preparative system and mobile phases used were as previously described (Schneider et al., 2020). The resulting sample (referred to as compound **2**) was later used to assist in structure elucidation of compound **1**.

To avoid wear and tear of the preparative HPLC system, attempts were made to isolate **1** using flash chromatography. The dried extract was dissolved in 90% methanol, and 2 g of Diaion HP-20SS (13615, Supelco) was added before removing the solvent under reduced pressure. Flash columns were prepared as previously described (Kristoffersen et al., 2018). The column was equilibrated using 5% methanol, before the dried extract-Diaion HP-20SS mixture was applied to the top of the column (maximum 2 g of extract per round). The fractionation was performed on a Biotage SP4™ system (Biotage) with a flow rate of 12 ml/min and a stepwise gradient from 5 to 100% methanol over 32 min. The following stepwise elution method was used: methanol:water (5:95, 25:75, 50:50, 75:25, 6 min per step, resulting in 12 fractions) followed by methanol (100% over 12 min, resulting in six fractions). The MeOH fractions were analyzed using UHPLC-ESI-HRMS. In the second fraction eluting at 100% MeOH, **1** was the dominating peak and was submitted for NMR and bioactivity analysis. The sample of **1** was therefore produced by pooling the second fraction eluting at 100% MeOH from multiple rounds of flash fractionation and drying the resulting volume under reduced pressure.

Structure Elucidation of 1

The structure of **1** was established by 1D and 2D NMR experiments. NMR spectra were acquired in DMSO-d_6 and methanol-d_3 on a Bruker Avance III HD spectrometer operating at 600 MHz for protons, equipped with an inverse TCI probe cryogenically enhanced for ^{1}H, ^{13}C, and ^{2}H. All NMR spectra were acquired at 298 K, in 3-mm solvent matched Shigemi tubes using standard pulse programs for proton, carbon, HSQC, HMBC, HMQC (J = 4–5 Hz), COSY, NOESY, ROESY and 1,1-ADEQUATE experiments with gradient selection and adiabatic versions where applicable. ^{1}H/^{13}C chemical shifts were referenced to the residual solvent peak (δ_H = 2.50 PPM, δ_C = 39.52 PPM for DMSO). All data were acquired and processed using Topspin 3.5pl7 (Bruker Biospin) including the structure elucidation module CMC-se v. 2.5.1. ^{13}C prediction was done using Mestrelabs MestReNova software version 14.2.0-26256 with the Modgraph NMRPredict Desktop. Optical rotation

data were obtained using an AA-10R automatic polarimeter (Optical Activity LTD).

Lulworthinone (**1**): green colored film. $[\alpha]^{20}_{D}$ -120 ± 0.02 (*c* 0.2 DMSO). ^{1}H and ^{13}C NMR spectroscopic data, **Supplementary Table 3**. HRESIMS *m/z* 741.2204 $[M+H]^{+}$ (calculated for $C_{37}H_{41}O_{14}S$, 741.2217).

Minimal Inhibitory Concentration Determination Against Reference Bacteria

The Minimal Inhibitory Concentration (MIC) of **1** against a panel of Gram-positive and Gram-negative reference bacteria was determined by broth microdilution, at final concentrations 0.2–100 μg/ml (twofold dilution series). The experiments were performed with three technical replicates. The panel of reference bacteria consisted of the following strains: *S. aureus* (ATCC 25923), MRSA (ATCC 33591), *Escherichia coli* (ATCC 25922), *Pseudomonas aeruginosa* (ATCC 27853), *Enterococcus faecalis* (ATCC 29212), and *Streptococcus agalactiae* (ATCC 12386), all strains from LGC Standards (Teddington). Briefly, the bacteria were inoculated from freeze stock onto blood agar plates (University Hospital of North Norway) and transferred to liquid medium for overnight incubation at 37°C. *S. aureus*, *E. coli*, and *P. aeruginosa* were grown in Brain Heart Infusion medium (BHI, 53286, Sigma-Aldrich), and *E. faecalis* and *S. agalactiae* were grown in Difco™ Mueller Hinton medium (MH, 275730, BD Biosciences). After overnight incubation in the respective media, the bacteria were brought to exponential growth by addition of fresh media, and incubated to reach a turbidity of 0.5 McFarland standard. The bacteria were diluted in their respective media 1:1,000 prior to addition. Subsequently, the bacteria were added to 96-well microtiter plates at 50 μl/well. A mixture of 50 μl of autoclaved Milli-Q® H_2O and 50 μl fresh autoclaved media was used as negative control, and 50 μl of autoclaved Milli-Q® H_2O was added to 50 μl of bacteria suspension as growth control. The compound was diluted in DMSO and autoclaved Milli-Q® H_2O (highest concentration of DMSO in the assay was 0.5%), and 50 μl was added to the bacterial suspension. Final volume in the wells was 100 μl. The plates were incubated overnight at 37°C. After incubation, growth was measured by absorbance at 600 nm with 1420 Multilabel Counter VICTOR^{3}™ (Perkin Elmer). Assay controls with gentamicin in a dilution series are routinely run, as well as routine counting of CFUs for each bacterium. For the strains where the compound displayed activity, the MIC was determined with three biological replicates each containing three technical replicates (n = 9). The lowest concentration of **1** that completely inhibited the growth of the bacteria was determined as the MIC.

To investigate if **1** had a bacteriocidal or bacteriostatic effect on *S. aureus* and *S. agalactiae*, the compound was inoculated together with the bacteria, as described above, and after overnight incubation, the inoculum was plated onto agar and incubated overnight at 37°C. The experiment was done with 12.5 and 25 μg/ml concentrations of **1** in triplicate, with two biological replicates (n = 6). Inspired by Zheng et al. (2007), we tested **1**, together with reserpine (broad spectrum efflux pump inhibitor) against the Gram-negative reference strains *E. coli* and *P. aeruginosa*. The assay was conducted as described above, with reserpine (L03506, Thermo Fisher Scientific) added to a final concentration of 20 μg/ml.

Minimal Inhibitory Concentration Determination Against Clinical Bacterial Isolates

Initial testing of **1** was conducted against a panel containing clinically relevant antibiotic-resistant bacteria: Gram-positive MRSA, vancomycin-resistant *Enterococcus faecium* (VRE), and Gram-negative bacteria resistant to extended-spectrum beta-lactamases as well as carbapenemases (ESBL-Carba) (detailed information about the clinical isolates can be found in **Supplementary Table 2**). The initial testing was conducted at one concentration, 100 μg/ml.

The final antibacterial testing of **1** was executed using the five clinical MRSA isolates and the VRE isolates (**Supplementary Table 2**). The isolates were tested by broth microdilution according to the Clinical Laboratory Standard Institute (CLSI) (2012) method MO7-A9. In brief, **1** was solubilized with 100% DMSO and diluted with autoclaved Milli-Q® H_2O to prepare a 200 μg/ml working solution. The final DMSO concentration did not exceed 1% to exclude any artificial influence on the assay. The bacterial inoculum was prepared to contain 1×10^{6} CFU/ml in cationic-adjusted BBL™ Mueller-Hinton II broth (BD). The inoculum was mixed in a 1:1 ratio with the working solution of **1** (twofold dilutions, ranging from 0.2 to 100 μg/ml) for a final amount of 5×10^{5} CFU/ml in each well of a 96-well round-bottom polypropylene plate (Greiner Bio-One GmbH). Growth control (without compound) and sterility control (without bacteria) were included for each strain. Each strain was tested in three independent biological replicates with four technical replicates on consecutive days. As quality assurance for the assay, the protocol was also performed with *E. coli* ATCC 25922 using Gentamicin (Merck Life Science) as a reference antibiotic. The 96-well plates were incubated at 37°C for 24 h without shaking. The MIC values were defined as the lowest concentration of **1** resulting in no visual bacterial growth, determined by visual inspection and 600 nm absorbance measurements with CLARIOstar plate reader (BMG LABTECH).

Inhibition of Biofilm Production and Eradication of Established Biofilm

Inhibition of biofilm production by **1** of *Staphylococcus epidermidis* (ATCC 35984, LGC Standards) was determined at final concentrations 0.2–100 μg/ml (twofold dilution series). Briefly, the bacteria were inoculated from freeze stock onto blood agar plates (University Hospital of North Norway) and transferred to tryptic soy broth (TSB, 22092, Sigma-Aldrich) for overnight incubation at 37°C. The overnight cultures were subsequently diluted 1:100 in fresh TSB with 1% glucose and added to 96-well microtiter plates, 50 μl/well. Positive control was *S. epidermidis* in fresh media with glucose, and negative control was a non-biofilm producing *Staphylococcus haemolyticus* (clinical isolate 8-7A, University Hospital of North Norway) in

fresh media with glucose. The compound was diluted in DMSO and autoclaved Milli-Q® H_2O (highest concentration of DMSO in the assay was 0.5%), and 50 μl was added to the bacterial suspension. Final volume in the wells was 100 μl. The plates were incubated at 37°C overnight. Growth inhibition of the bacterium was determined by visual inspection of the plates prior to further treatment. The bacterial suspension was poured out and the biofilm was fixated by heat, before adding 70 μl of 0.1% crystal violet solution (V5265, Sigma-Aldrich) and staining for 5 min. The crystal violet solution was removed and the wells were washed with water before the plates were dried by heat. The bound crystal violet was dissolved in 70 μl of 70% ethanol, and the presence of violet color, indicating biofilm formation, was measured at 600 nm absorbance using a 1420 Multilabel Counter VICTOR^{3TM} reader. Percent biofilm formation was calculated using the equation below. The data were visualized using GraphPad Prism 8.4.2, and the built-in ROUT method was used to detect and remove outliers from the dataset (Q = 1%).

$$\text{Percent (\%) biofilm formation} = \frac{(\text{absorbance treated wells} - \text{absorbance negative control})}{(\text{absorbance positive control} - \text{absorbance negative control})} \times 100 \quad (1)$$

To determine whether **1** could eradicate biofilm established by *S. epidermidis*, a modified biofilm inhibition assay protocol was performed. Here, the bacteria were grown overnight in a microtiter plate to allow the biofilm to be established prior to the addition of **1**. After addition of **1**, the plates are incubated overnight. Following this, the biofilm was fixated and colored and results were read as stated above. The experiment was conducted once with three technical replicates with concentrations of 0.2–100 μg/ml (twofold dilution series).

Determination of Antiproliferative Activity Toward Human Cell Lines

The antiproliferative activities of **1** was evaluated against the melanoma cell line A2058 (ATCC, CRL-11147^{TM}), the hepatocellular carcinoma cell line HepG2 (ATCC, HB-8065^{TM}), and the non-malignant lung fibroblast cell line MRC5 (ATCC, CCL-171^{TM}) in a MTS *in vitro* cell proliferation assay. The compound was tested in concentrations from 6.3 to 100 μg/ml against all cell lines, with three biological replicates each containing three technical replicates (n = 9). A2058 was cultured and assayed in Dulbecco's Modified Eagle's Medium (D-MEM, D6171, Sigma-Aldrich). HepG2 was cultured and assayed in MEM Earle's (F0325, Biochrom) supplemented with 5 ml of non-essential amino acids (K0293, Biochrom) and 1 mM sodium pyruvate (L0473, Biochrom). MRC5 was cultured and assayed in MEM Eagle (M7278, Sigma-Aldrich) supplemented with 5 ml of non-essential amino acids, 1 mM sodium pyruvate, and 0.15% (w/v) sodium bicarbonate (L1713, Biochrom). In addition, all media were supplemented with 10% fetal bovine serum (FBS, S1810, Biowest), 10 μg/ml gentamicin (A2712, Biochrom), and 5 ml of glutamine stable (200 mM per 500 ml medium, X0551, Biowest). Briefly, the cells were seeded in 96-well microtiter plates (Nunclon Delta Surface, VWR) at 2,000 cells/well for A2058, 4,000 cells/well for MRC5, and 20,000 cells/well for HepG2. After incubation for 24 h in 5% CO_2 at 37°C, the media was replaced and compound was added, generating a total volume of 100 μl/well. A2058 and MRC5 were incubated for 72 h before assaying, and HepG2 for 24 h. Subsequently, 10 μl of CellTiter 96 AQueous One Solution Reagent (G358B, Promega) was added to each well and the plates were incubated for 1 h at 37°C. Following this, the absorbance was measured at 485 nm with a DTX 880 multimode detector (Beckman Coulter). Negative controls were cells assayed with their respective cell media, and positive controls were cells treated with 10% DMSO (D4540, Sigma-Aldrich). Percent cell survival was calculated using the equation below. The data were visualized using GraphPad Prism 8.4.2 and IC_{50} was calculated. The built-in ROUT method was used to detect and remove outliers from the dataset (Q = 1%).

$$\text{Percent (\%) cell survival} : \frac{(\text{absorbance treated wells} - \text{absorbance positive control})}{(\text{absorbance negative control} - \text{absorbance positive control})} \times 100 \quad (2)$$

Minimal Inhibitory Concentration Determination Against *Candida albicans*

The MIC of **1** was determined by broth microdilution against *C. albicans* (ATCC 90028, LGC Standards), at final concentrations of 0.2–100 μg/ml (twofold dilution series). The experiment was performed as one biological replicate, with three technical replicates (n = 3). Briefly, the fungus was inoculated from freeze stock onto potato dextrose agar [24 g/L potato dextrose broth (P6685, Sigma-Aldrich), 15 g/L agar (A1296, Sigma-Aldrich)] and incubated overnight at 37°C. From the overnight culture, five to eight colonies were transferred to 5 ml of sterile 0.9% NaCl, before the cell density was adjusted to 1–5 × 10^6 cells/ml by adding 0.9% NaCl. The cell density was evaluated with 0.5 McFarland standard (Remel 0.5 McFarland Equivalence Turbidity Standard, 10026732, Thermo Fisher Scientific). The fungal suspension was further diluted 1:50, and then 1:20 (1–5 × 10^3 CFU/ml) in RPMI medium (R7755, Sigma-Aldrich) with 0.165 mol/L MOPS (M3183, Sigma-Aldrich) and 10.25 ml of L-glutamine. The compound was added to the microtiter plate together with the fungal suspension (1:1), to a final volume of 200 μl. The final concentration of fungal cells was 0.5–2.5 × 10^3 CFU/ml. Absorbance in the wells was measured with 1420 Multilabel Counter VICTOR^{3TM} right after addition of compound, after 24 h and after 48 h. The plates were incubated at 37°C. Amphotericin B was used as negative control at final concentration 8 μg/ml. Growth control contained fungal suspension and autoclaved Milli-Q® H_2O.

RESULTS

Systematic Placement of the Fungal Isolate 067bN1.2

Due to lack of distinct morphological characters of the cultured asexual morph and closely related reference sequences

in GenBank, the fungus is identified to family level, as Lulworthiaceae sp., for the purpose of this study. A phylogenetic study was carried out with 28 taxa (including outgroups and isolate 067bN1.2), all representing different species, as shown in **Figure 1**. The combined dataset of 5.8S, SSU, and LSU had an aligned length of 2,270 characters, and phylogenetic inference was estimated using both Maximum Likelihood and Bayesian Inference criteria. The isolate producing **1**, 067bN1.2, was placed on its own branch within the Lulworthiaceae, forming a sister clade to the clade including *Halazoon fuscus*, *Lulworthia medusa*, *Lulworthia* cf. *purpurea* and *Halazoon melhae*. Sequences of *Koralionastes ellipticus* were included to exclude the possibility that the isolate 067bN1.2 is part of the family Koralionastetaceae. *Koralionastes ellipticus* was placed outside of Lulworthiaceae.

Isolation and Structure Elucidation

Compound **1** was selected for isolation due to its antibacterial activity in an initial screen of fractions from several understudied marine fungi. Compound **1** was the dominating peak in the active fraction from fungal isolate 067bN1.2 Lulworthiaceae sp., and subsequently the fungus was re-cultivated, cultures were extracted, and the compound was isolated using RP flash chromatography. The extraction of 1.4 L of fungal culture yielded 1,017.2 mg of extract.

Initially, attempts were made to isolate the compound using preparative HPLC. This strategy had several drawbacks, including unfavorable behavior of the compound in the preparative column. This resulted in the compound eluting over several minutes (band broadening) and carryover. A batch of the compound was, however, retrieved using this strategy, resulting in a compound later determined to be a structural isomer and artifact of compound **1** (referred to as **2** throughout this article), produced due to the acidic conditions in the mobile phase. The structures of **1** and **2** can be seen in **Figure 2**.

Flash chromatography was better suited for the isolation of **1**. This isolation strategy yielded 63.8 mg of **1**, corresponding to a yield of ∼45 mg/L culture medium. Compound **1** was obtained as a green colored substance. The molecular formula was calculated to be $C_{37}H_{40}O_{14}S$ by UHPLC-ESI-HRMS (*m/z* 741.2204 $[M+H]^+$) (calculated as $C_{37}H_{41}O_{14}S$, 741.2217), suggesting 18 degrees of unsaturation. The low-energy collision mass spectrum of **1** can be seen in **Supplementary Figure 2**. MS signals of a neutral loss of 80 Da (ESI+) was observed, indicating the presence of a sulfate group in the structure. The UV absorption maxima were 224, 260, and 373 nm, which corresponded well with the previously published dinapinones (Kawaguchi et al., 2013). The UV-vis spectrum for **1** can be seen in **Supplementary Figure 3**. The IR spectrum of **1** displayed absorption bands for sulfoxide (S=O, 1,002 cm^{-1}), aromatic alkene (C=C, 1542 and 1,618 cm^{-1}), carbonyl (C=O, 1,645 cm^{-1}), alkane (C-H, 2,857 cm^{-1}), aromatic alkene (C-H, 2926 cm^{-1}), and hydroxyl (C-OH, 3455 cm^{-1}) bonds. After isolation, the structure of **1** (**Figure 2**) was elucidated by 1D and 2D NMR experiments (**Supplementary Figures 4–16**).

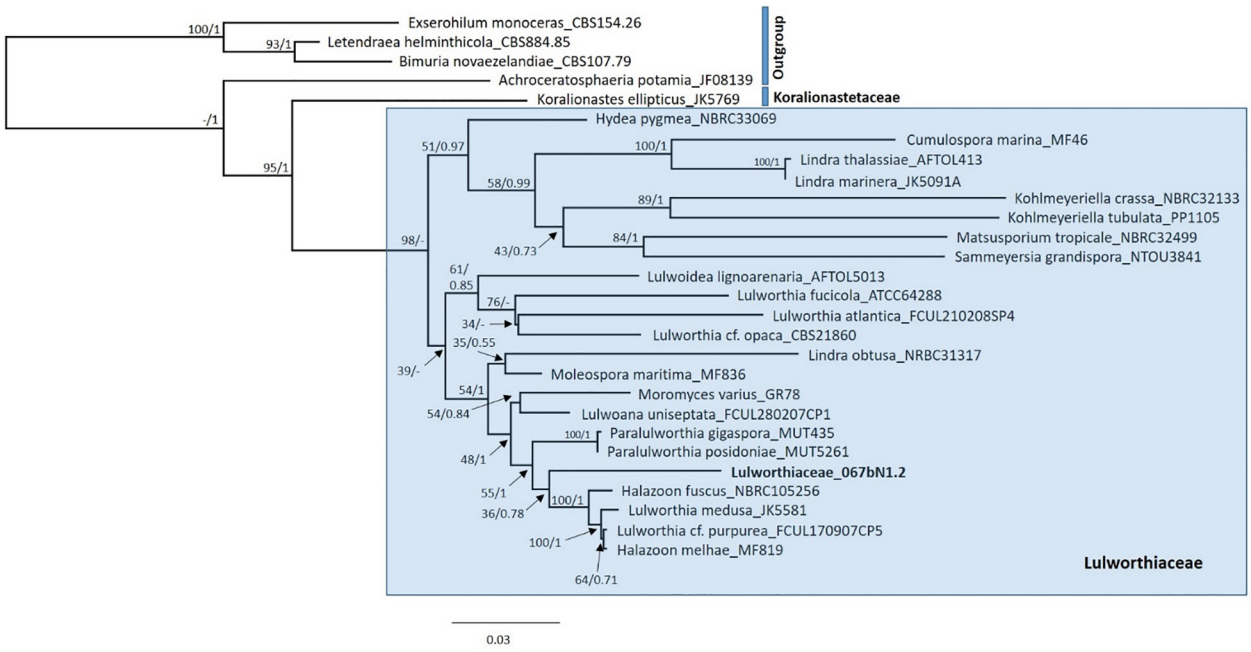

FIGURE 1 | Maximum Likelihood tree (RAxML) from the combined analysis of 5.8S, SSU, and LSU from isolates of Lulworthiaceae. One isolate from Koralionastetaceae was included, and four strains as outgroups. Node support is given as Bootstrap support values at the nodes, and posterior probabilities are included where the branching was alike (BS/PP). The isolate under investigation, Lulwortihaceae_067bN1.2, is highlighted in bold. Due to topological similarity only the ML tree is shown here containing both Bayesian posterior probabilities and Bootstrap support values. Bayesian Inference tree can be found in **Supplementary Figure 1**. – indicates that the node is missing in the Bayesian analysis. No support value is given to the node separating the outgroup taxa from the ingroup in ML analysis.

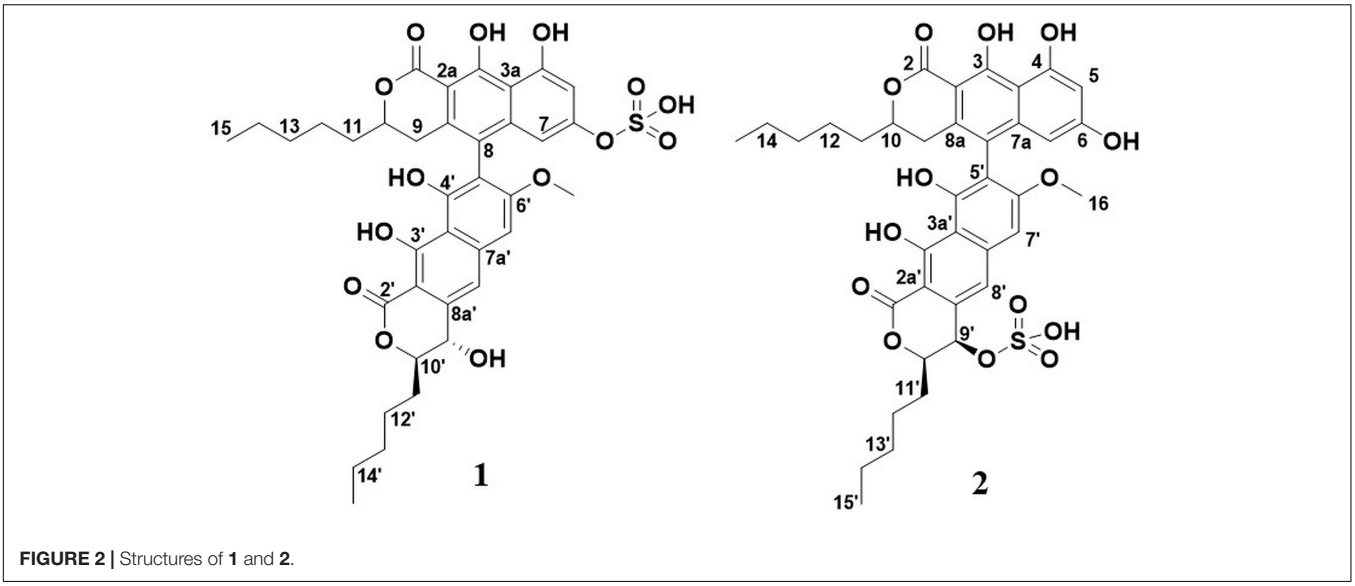

FIGURE 2 | Structures of **1** and **2**.

Initial structure elucidation was made on the sample isolated by preparative HPLC with formic acid present in the mobile phases (compound **2**). The established molecular formula suggested a highly conjugated system. The purity of **2** was estimated to be ∼80% from a quantitative proton spectrum with respect to non-solvent impurities (**Supplementary Figure 4**). Four singlet protons were identified in the aromatic region, along with three O-CH signals at ∼4.5 ppm with complex couplings along with a methoxy singlet at 3.77 ppm. Furthermore, five hydroxyl protons were identified; three between 9.5 and 10.0 ppm, and two between 13.5 and 14.0 ppm. The deshielded nature of the latter sets them apart from the other hydroxyls and suggests they may be involved in an angled intramolecular hydrogen bond, which is commonly seen for keto-enol pair configurations such as this. All 37 carbons could be identified by 1D ^{13}C NMR (**Supplementary Figure 5**), which showed **2** to contain a large number of aromatic quaternary carbons, two ester-like carbonyls, along with 10 peaks in the aliphatic region (**Table 1**).

HSQC, HMBC, and 1,1-ADEQUATE spectra (**Supplementary Figures 6, 7**) allowed the identification of two substituted napthopyrone-like moieties, as well as two five-membered aliphatic chains (denoted *C15-C11* and *C15'-C11'*, respectively), which were fully assigned using a combination of HSQC-TOCSY, TOCSY, COSY, and HMBC (**Figure 3**i). The aliphatic chains were determined to be attached at the *C10* position of the napthopyrone-like moieties by tracing the spin system into *H9* and *H9'*, respectively, and supported by multiple long-range ^{1}H-^{13}C correlations. The *C2* and *C2'* carbonyls could be directly assigned from long-range couplings from the *10*/*10'* position, but the hydroxyl carrying carbons in positions *3/3'* and *4/4'* could only be assigned through weak $^{4}J_{CH}$ correlations from the aromatic protons (**Figure 3**iii).

The *OH-4* and *OH-6* could be assigned based on NOE correlations between *OH-6* and both *H5* and *H7*, while *OH-4* only displayed correlations with *H5*. The *OH-3* and *OH-3'* are predicted to have more deshielded chemical shifts due to their proximity to the carbonyl moiety and a probable intramolecular hydrogen bond—however, it was not possible to individually distinguish *OH3* and *OH-3'* due to the absence of any correlations in NOESY, ROESY, and HMBC spectra. Thus, four fragments could initially be elucidated (**Figure 3**i). A weak $^{4}J_{C8H7'}$ correlation could be detected, linking fragment ***A*** to fragment ***B*** (**Figure 3**i) at the *C8* and *C5'* positions, respectively, and thus the only remaining ambiguity is the position of the -SO^{3-} group vis-à-vis the remaining -OH in the 9' or 4' positions. The absence of NOEs and COSY correlations between *OH-4'* and *H9'* suggests that it is positioned at *C4'* with the sulfate positioned at *C9'* (**Figure 3**ii). The $^{3}J_{HH}$ coupling constant between *H9'* and *H10'* was measured to be 2.0 Hz from line shape fitting the splitting of H9', indicating that these protons are at a significantly offset dihedral angle to one another—thus suggesting a relative R/S or S/R configuration of 9' and 10'. ^{13}C prediction was consistent with the structure of **2** (**Supplementary Figure 9**), with a mean error of 2.79 ppm between the observed and predicted ^{13}C shifts.

A second isolation where no acidic conditions were used, yielding **1**, was also examined. ^{1}H NMR revealed significantly perturbed chemical shifts as well as line broadening and heterogeneity throughout the spectra (**Supplementary Figure 11**). Multiple resonances in the carbon spectrum (**Supplementary Figures 12, 13**), especially for two resonances in the carbonyl area (presumably C3 and C3'), are heterogenous, reflecting the nuclei existing in several stable, but slightly different micro environments. The same observation is made in the proton spectrum (**Supplementary Figure 11**) for H9', OMe-6', H5, H7, 4'-OH, and 4-OH. A major difference was observed in the non-acidic preparation (**1**), compared to **2**, the presence of a 9'-OH. At ∼15 ppm, two heterogeneous OH protons were observed, deshielded by approximately 1 ppm compared to the OH-3's in the original sample preparation, while the three hydroxyls at ∼10 ppm could no longer be detected (**Supplementary Figures 8–13**). Thus, the detectable aromatic hydroxyl groups, identified as OH-4' and OH-4,

TABLE 1 | Summary of chemical shift and correlations for **2** (DMSO-d_6).

Position	δ^{13}C, type	δ^{1}H, splitting (Hz)	COSY	HMBC (^{1}H → ^{13}C)
2	171.6, C	–	–	–
2'	171.0, C	–	–	–
2a'	99.4, C	–	–	–
2a	99.2, C	–	–	–
3	162.5, C	–	–	–
3'	161.5, C	–	–	–
3a'	108.6, C	–	–	–
3a	107.5, C	–	–	–
4	159.0, C	–	–	–
4'	154.9, C	–	–	–
5'	111.7, C	–	–	–
5	102.1, CH	6.35, s	–	3, 3a, 4, 6, 7
6	161.2, C	–	–	–
6'	160.7, C	–	–	–
7a	140.6, C	–	–	–
7a'	140.1, C	–	–	–
7	100.7, CH	6.04, s	–	3, 3a, 5, 6, 8
7'	99.7, CH	7.14, s	–	3', 3a', 4', 5', 6', 8, 8'
8a'	137.4, C	–	–	–
8a	132.9, C	–	–	–
8	118.7, C	–	–	–
8'	117.5, CH	7.36, s	–	2', 3a', 4', 6', 7'a, 7', 9'
9'	65.3, CH	4.69, d (J = 2.0)	–	2a', 8', 8a', 10', 11'
9	31.0, CH2	2.59, m	10	2a, 7a, 8, 8a, 10, 11
10'	83.2, CH	4.62, ddd (J = 7.9, 6.0, 2.0)	11'	2', 8a', 9', 11', 12'
10	79.4, CH	4.56, dddd (J = 9.6, 7.4, 5.5, 4.1)	9, 11	2, 8a, 12
11	34.2, CH2	1.59, dd (J = 16.7, 9.5) 1.68, dd (J = 16.5, 4.0)	10, 12	10, 12
11'	30.0, CH2	1.85, m	10', 12'	9', 10', 12', 13'
12'	24.7, CH2	1.48, 1.52, m	11', 13'	11', 13', 14'
12	24.5, CH2	1.27, 1.36, m	11, 13	11, 13, 14
13'	31.3, CH2	1.23, m	12', 14'	11', 12', 14', 15'
13	31.6, CH2	1.36, m	12, 14	11, 12, 14, 15
14'	22.5, CH2	1.36, m	13', 15'	12', 13', 15'
14	22.4, CH2	1.24, m	15	12, 13, 15
15'	14.4, CH3	0.92, m	14'	13', 14'
15	14.3, CH3	0.82, m	14	13, 14
16	56.5, O-CH3	3.77, s	–	6'
OH3*	–	13.71, s		
OH3*	–	13.62, s		
OH4	–	9.80, s		
OH4'	–	9.51, s		
OH6	–	9.94, s		

**Ambiguous assignment.*

appeared to be involved in (stronger) hydrogen bonding, while three aromatic hydroxyls, the remaining OH-6, OH-3' and OH-3, were unaccounted for. At the same time, the majority of all other nuclei in the molecule are shielded by approximately 0.5 ppm. Together, these observations suggest that the neutral pH preparation resulted in a different molecule, **1**, that formed loose aggregates in DMSO and methanol, stabilized by both hydrogen bonding (deshielding) and stacking (shielding) interactions. Overall, worse spectral quality resulted in that the C2 and C3 from **2** could not be individually assigned in **1**, although they must correspond to the two chemical shifts of 169.4 and 173 ppm by the logic of elimination. A number of the carbons show heterogenic peaks (notably the presumed C3 and C3'), most likely as the result of through space proximity to the sulfate group and sensitivity to its different possible conformation (details in section "Discussion").

The identity of **1** was established to be identical to **2** with the only difference being that the sulfate group was attached to C6 instead of C9', supported by the loss of the OH correlating with H5 and H7, and the appearance of an OH

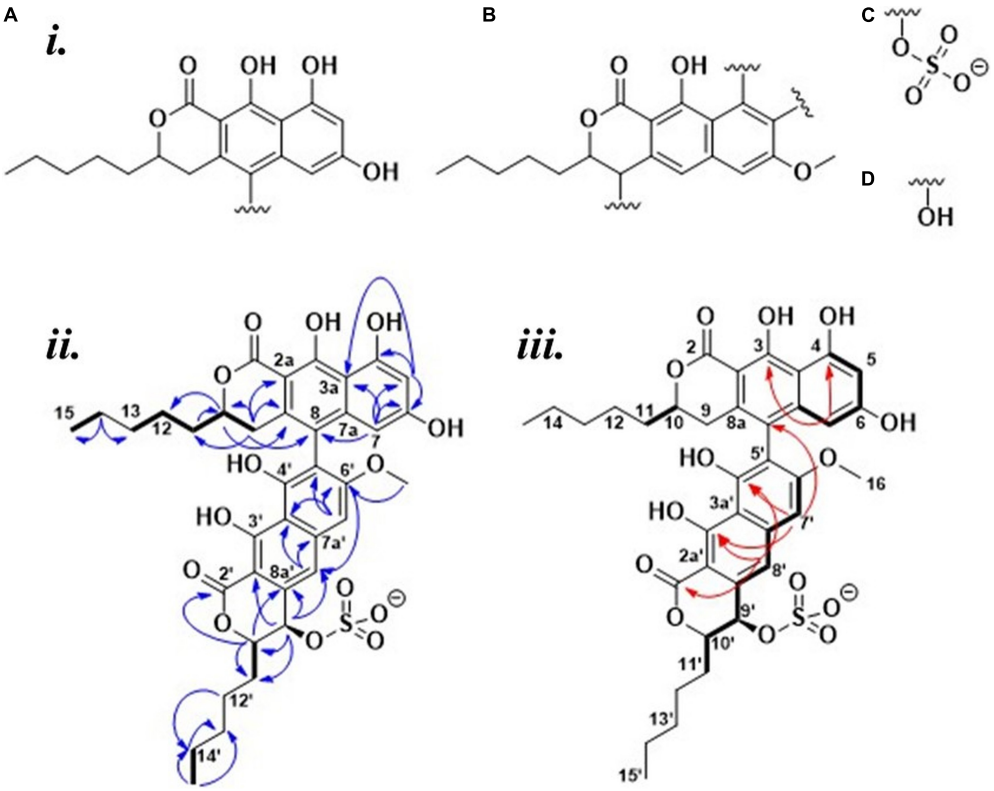

FIGURE 3 | (*i*) Fragments identified for **2**: **(A,B)** The napthopyrone-like moieties; **(C)** a sulfate group; **(D)** a spare hydroxyl group. (*ii*) Elucidated structure of **2**: Bold bonds = COSY, blue arrows = HMBC, and (*iii*) red arrows = weak $^{4}J_{CH}$ correlations, Bold bonds = 1,1-ADEQUATE.

correlating with H9' through a $^{3}J_{HH}$. There is furthermore a heterogeneity and chemical shift perturbation hotspot (vis-à-vis **2**) around the C6 position to support the assignment of a C6 sulfate. All chemical shifts and correlations are summarized in **Supplementary Table 3**. The data do not unambiguously prove whether the 3-OH's are deprotonated or if the signal is lost due to rapid exchange, but the fact that the OH-9' is observable under the same conditions is an indicium for the OH-3's to be deprotonated in **1**. No plausible resonance structures to explain the deprotonation and deshielding that does not involve the oxidation, and thus change in mass, have been found.

The non-aggregated **2** could be scavenged by lowering the pH of **1** with the addition of hydrochloric acid, upon which ^{1}H and HSQC spectra of the two samples of **2** show a great resemblance (**Supplementary Figure 10**). The molecular formula of **2** and **1** as well as the scavenged **2** were identical in the two preparations, as no change in mass was observed by high-resolution mass spectrometry.

Antibacterial Activity Against Reference and Clinical Strains

Compound **1** was tested against six reference bacteria (four Gram-positive and two Gram-negative strains). The compound was active against two of the Gram-positive reference strains, *S. aureus* and *S. agalactiae*, with MIC values of 6.25 and 12.5 μg/ml, respectively. No activity was observed against the Gram-negative strains, *E. coli* and *P. aeruginosa*, or the Gram-positive *E. faecalis* or MRSA strain (**Supplementary Table 4**). As bacterial resistance toward available antibiotics is the main challenge in future treatment of pathogenic diseases, **1** was tested against a panel of drug-resistant clinical strains (**Supplementary Table 2**). The panel included five MRSA and six VRE strains. Compound **1** was also tested in a pre-screen against four Gram-negative clinical bacterial strains: *E. coli*, *Klebsiella pneumoniae*, *Acinetobacter baumanii*, and *P. aeruginosa* (all ESBL-Carba). No activity was detected against the Gram-negative bacteria (**Supplementary Table 4**). Compound **1** showed activity against the MRSA strains with MICs in the 1.56–6.25 μg/ml (2.12–8.44 μM) range, see **Table 2**. The activity of the compound was significantly less profound against the VRE strains (MIC = 50 μg/ml or higher) (**Supplementary Table 4**).

To investigate if **1** has bacteriostatic or bacteriocidal effects on the two reference strains *S. aureus* and *S. agalactiae*, both were incubated with the compound at 12.5 and 25 μg/ml overnight and subsequently plated onto agar. For *S. aureus*, there was no growth on the plates after overnight incubation, indicating a bacteriocidal effect of **1**. For *S. agalactiae*, one of the parallels at 12.5 μg/ml (MIC of **1** against this bacterium) displayed growth on the agar plate, which was expected as visual growth could also be seen in the microtiter plate for this parallel. The remaining five parallels at this concentration, and the concentration above,

had no growth in the microtiter plates, or on agar after overnight incubation. This strongly indicates that **1** also has bacteriocidal effect on *S. agalactiae*. Compound **1** was also tested together with the efflux pump inhibitor reserpine to see if the lack of activity toward Gram-negative strains was caused by efflux of **1**, but no activity was obtained.

Inhibition of Biofilm Production and Eradication of Established Biofilm

The ability of **1** to inhibit biofilm production by *S. epidermidis* and to remove established *S. epidermidis* biofilm was assessed. In the biofilm inhibition assay, the biofilm production was completely inhibited (below 5% biofilm formation) down to 12.5 μg/ml (**Figure 4**). Clear inhibition of the bacterial growth could also be observed to 25 μg/ml by visual inspection of plates before fixation of biofilm, raising the question if the biofilm inhibition is mainly caused by growth inhibition of the bacterium. To further evaluate the potential biofilm activity, removal of established biofilm was assessed. There was no activity of **1** at concentrations up to 100 μg/ml against the established biofilm, further supporting the hypothesis that the biofilm inhibition is mainly due to growth inhibition of the bacterium.

TABLE 2 | Minimal inhibitory concentrations (MICs) of **1** against reference strains and clinical isolates.

Strain type	Strain	MIC in μg/ml
Clinical strains	*S. aureus* N315	1.56
	S. aureus 85/2082	3.13
	S. aureus NCTC 10442	3.13
	S. aureus WIS [WBG8318]	6.25
	S. aureus IHT 99040	3.13
Reference strains	*S. aureus* ATCC® 25923	6.25
	S. agalactiae ATCC® 12386	12.5

The median MIC values are reported (n = 12 for clinical isolates, n = 9 for reference strains).

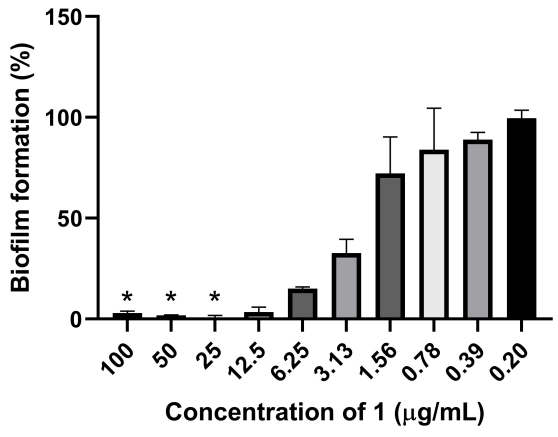

FIGURE 4 | Inhibition of bacterial biofilm formation by **1** against the biofilm producing *S. epidermidis*. *The bacterial growth was completely inhibited at compound concentrations down to 25 μg/ml.

Antiproliferative Activity Against Human Cells and Antifungal Activity

The antiproliferative activities of **1** was assessed against human melanoma cells (A2058), human non-malignant lung fibroblasts (MRC5), and human hepatocellular carcinoma cells (HepG2), in a concentration range of 6.25–100 μg/ml. The non-malignant cell line was included as a test for general toxicity, while the other cell line was included to assess possible anti-cancer activities. Antiproliferative activity was observed against all cell lines, with IC_{50} values of 15.5, 32, and 27 μg/ml against A2058, MRC5, and HepG2, respectively (**Table 3**). Compound **1** was also assayed for antifungal activity against *C. albicans* at concentrations up to 100 μg/ml, and no activity was seen.

DISCUSSION

In this study, we describe the discovery, isolation, and characterization of the new secondary metabolite lulworthinone (**1**). This novel antibacterial compound was isolated from an extract of a slow-growing marine fungus of the family Lulworthiaceae. To the best of our knowledge, this is the first reported secondary metabolite isolated from this fungal family and the order Lulworthiales. Since the isolate did not branch close to the *Lulworthia* type species, *L. fucicola* (in the *Lulworthia sensu stricto* clade) and there was a lack of support at many nodes of the phylogenetic tree, we restrained from identifying the isolate 067bN1.2 to genus and determine its identity to family level only.

A fraction of the Lulworthiaceae sp. extract was nominated for chemical investigation as it was active in an initial antibacterial screen. The content of the active Lulworthiaceae sp. fraction was dominated by **1**, whose calculated elemental composition gave no hits in database searches, indicating that the compound suspected to be responsible for the observed antibacterial activity, was novel. In the attempt to utilize preparative HPLC to isolate this compound, **2** was generated during the procedure (acidic mobile phase). As compounds **1** and **2** have the same mass, HRMS analysis did not detect the change in the positioning of the sulfate group, and the sample from the preparative HPLC isolation was characterized using NMR, believing it was **1**. As preparative HPLC was deemed inconvenient for compound isolation, flash chromatography (neutral mobile phase) was utilized to isolate sufficient amounts of **1** to conduct a thorough characterization of the compound's bioactivity. This method allows larger amounts of sample to be processed per run, but generally is less effective in separating compounds of interest from sample impurities, compared to preparative HPLC isolation. However, due to the high concentration of **1** in the extract, **1** was successfully isolated using this method. The resulting sample was submitted

TABLE 3 | Antiproliferative activity (IC_{50}) of **1** against human cell lines (*n* = 9).

Cell type	IC_{50} in μg/ml
A2058, melanoma	15.5 ± 0.6
MRC5, normal lung fibroblasts	32 ± 1
HepG2, hepatocellular carcinoma	27 ± 1

to NMR analysis to confirm its structure. The samples from both isolations were confirmed to be novel biarylic dimeric naphtho-α-pyrones substituted with a sulfate group. However, NMR analysis revealed that the sulfate group was located on different positions in the two compounds. The rearrangement was hypothesized to be catalyzed by the acidic nature of the HPLC mobile phase. This hypothesis was confirmed by subjecting **1** to acidic conditions (**Supplementary Figure 10**). The resulting sample was analyzed using NMR, confirming that **1** had indeed converted into **2**. As **2** was proven to be an artifact of **1**, all bioactivity testing was conducted using **1** isolated under neutral conditions.

The propensity of **1** to interact with itself to form higher-ordered structures, while **2** did not, offered some insight into their structural behavior in solution. In particular, the sulfate in the 6-position appeared to facilitate oligomeric aggregation, and a simple 3D model allows some speculation as to why this could be (**Figure 5**). The ground state of the naphthopyrone does not have the ability to form complementary "base pairs" with itself through hydrogen bonds between the carbonyls and hydroxyls. However, when the sulfate is in the 6-position, it can reach the C3 double OH "mismatch" in the three-dimensional structure and potentially stabilize the hydroxyls either by 4-coordnating a water molecule or a Na^+ ion together with deprotonated 3'-hydroxyls, or by directly hydrogen bonding to the protonated hydroxyls. This would provide a feasible rationale for the propensity for aggregation of **1** but not of **2**. The structural dimer model also provides a plausible explanation as to why the sulfate group would specifically and irreversibly migrate to C9' under acidic conditions even though the C9' is expected to be a less likely position for the sulfate than any other phenol position. The sulfate is in an oligomeric state involving this kind of "base pairing" positioned to be intermolecularly attacked by the OH-9' of the paired molecule, which is not possible in the monomeric state. Lowered pH is expected to ensure protonated sulfate, which would make it more susceptible for an electrophilic attack from OH-9'. If oligomeric states are indeed stabilized by the coordination of water or sodium, then lowered pH and the protonation of the 3- and 3'-oxygens would further destabilize the oligomer, which together with the lack of stabilization from the position 6 sulfate would make both the association and the reaction irreversible and trap the sulfate in the 9' position of monomeric **2** with lowered ability to self-aggregate.

Lulworthia spp. fungi have spores with end chambers containing mucus, which helps in spore attachment to surfaces (Jones, 1994). It has been observed that in liquid culture of the isolate 067bN1.2, the fungus forms a gel-like mucus, having the ability to adhere to the bottom of the culture flasks. No spores are formed in culture, and it remains unclear whether the mucus formed under cultivation of 067bN1.2 has chemical resemblance

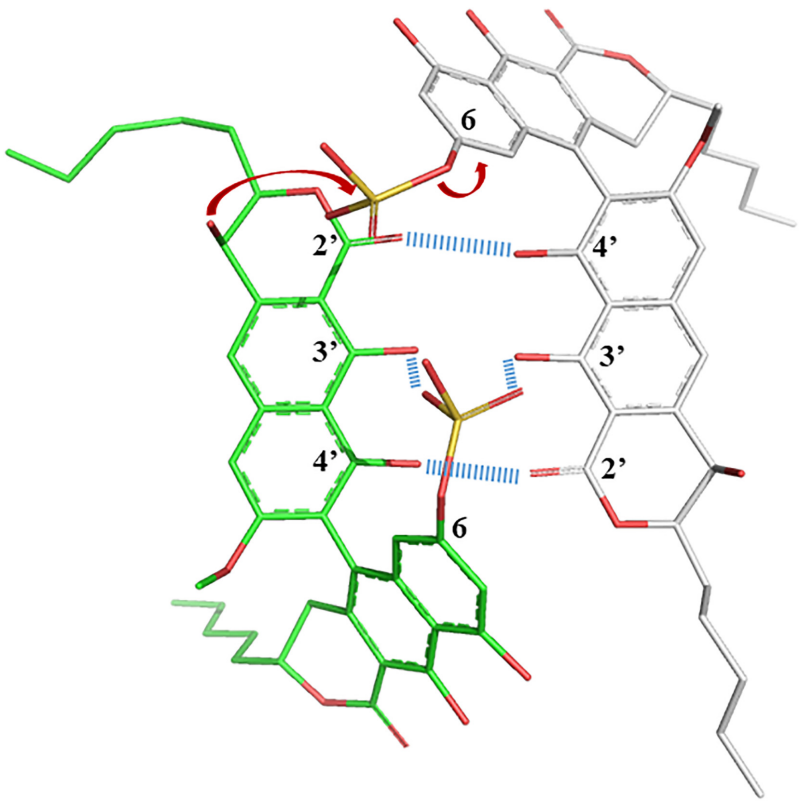

FIGURE 5 | Crude sculpted and minimized structural model of **1** displaying the sulfate potential role in stabilizing oligomerization, as well as the possibility to intermolecularly react specifically at the C-9' position to form **2** under acidic conditions.

to the mucus in end chambers of *Lulworthia* spp. spores, as it has not yet been characterized. The sheathing of mucoid by *L. medusa* has been reported in a publication from 1973, where the fungus was found and isolated from a piece of submerged pine and cultivated in bottles in media supplemented with artificial seawater (Davidson, 1973). Also in the current study, the fungus was found to adhere to the culture flask during cultivation in artificial seawater media. Davidson hypothesizes around the physiological and ecological implications of the mucoid, important in cation binding and transport, for the adhesion of other microorganisms, avoiding desiccation in intertidal regions or for the production of a matrix to concentrate exoenzymes (Davidson, 1973). Compound **1** is isolated in high yields from the fungal culture, but the ecological role of naphthopyrone-type compounds is largely unclear. The antibacterial activity of **1**, however, could indicate a protective role against pathogenic attacks, but the compound may have other types of bioactivities as well. It has been speculated that similar compounds (bis-naphthopyrones) from filamentous ascomycetes were produced to protect the fungus from predators (Xu et al., 2019). The study found that several animal predators, like woodlice, preferred feeding on fungi that had disrupted aurofusarin synthesis, and also that predation stimulated the production of aurofusarin in several *Fusarium* species (Xu et al., 2019). We have also observed marine mites feeding on fruitbody contents of Lulworthiales fungi. It is thus possible that in the natural habitat of these fungi, the naphthopyrones are produced as a means of protection.

Compound **1** was found to be a dimeric biarylic naphtho-α-pyrone substituted with a sulfate group. The naphthopyrone moiety is recurring in nature, as monomers, dimers, and trimers, and has been found from several natural sources, like plants and filamentous fungi. Naphthopyrones have also previously been isolated from organisms from the marine environment (Li et al., 2016). Compounds from this class have shown different bioactivities, among these the inhibition of triacylglycerol synthesis (Kawaguchi et al., 2013), inhibition of enzymatic activity (Zheng et al., 2007), protection against animal predators (Xu et al., 2019), antimalarial activities (Isaka et al., 2010), and antiproliferative activities (Isaka et al., 2010; Li et al., 2016). Several of these compounds have displayed antibacterial activities against Gram-positive bacteria (Suzuki et al., 1992; Wang et al., 2003; Zheng et al., 2007; Boudesocque-Delaye et al., 2015; Rivera-Chavez et al., 2019). Lu et al. (2014) defined three groups of bis-naphtho-γ-pyrones based on the diaryl bond connection between the monomers, the chaetochromin-, asperpyrone-, and nigerone-type bis-naphtho-γ-pyrones. Based on this categorization, **1** would be categorized as an asperpyrone-type bis-naphtho-α-pyrone, due to the relative placement of the oxygen atoms in the pyrone moieties. Compound **1** is substituted with a sulfate group. One of the most abundant elements in seawater is sulfur, and many sulfated compounds have been isolated from marine organisms, mostly from marine invertebrates, but also from microorganisms (Kornprobst et al., 1998; Francisca et al., 2018). Compound **1** represents, however, the first report of a dimeric naphtho-α-pyrone substituted with a sulfate group.

In the current study, **1** was broadly assessed for potential bioactivities: antibacterial activities against bacterial reference strains and clinical strains, antiproliferative activities toward a selection of human cell lines, both malignant and non-malignant, anti-fungal activity, inhibition of bacterial biofilm formation, and the eradication of established bacterial biofilm. Intriguingly, **1** showed activity against multidrug-resistant MRSA strains with MICs between 1.56 and 6.25 μg/ml (2.12–8.44 μM). In comparison, a natural product originally isolated from *Clitophilus scyphoides* (organism name at time of isolation: *Pleurotus mutilus*, Basidiomycota) pleuromutilin showed MICs in a similar range against selected reference strains (e.g., MIC = 0.66 μM against *S. aureus*, MIC = 2.64 μM against *K. pneumoniae*, and MIC = 21.13 μM against *B. subtilis*) while having significantly higher MIC values against other reference strains (e.g., MIC ≥ 100 μM against *P. aeruginosa*) (Kavanagh et al., 1951). An optimized analog of pleuromutilin, lefamulin (Xenleta®), was approved as an antibiotic drug by the US Food and Drug Administration in 2019. The herein reported MIC values thus place **1** in an activity segment, which makes it an interesting candidate for further development toward becoming a marketed antibiotic drug. In comparison to other antibacterial napthopyrones, **1** falls within the same MIC range with regard to activity toward Gram-positive bacteria. Two heterodimers, isolated from the tubers of *Pyrenacantha kaurabassana*, showed antibacterial activity against different strains of *S. aureus* with MICs in the range of 2.7–89.9 μM (Boudesocque-Delaye et al., 2015). In a recent paper from 2019, mycopyranone, a new binaphthopyranone, was isolated from the fermentation broth of *Phialemoniopsis*. The compound showed antibacterial activity against both *S. aureus* and a MRSA strain, with MICs of ≤8.7 μM against both strains (Rivera-Chavez et al., 2019). Possibly the most known naphthopyrone, viriditoxin showed MICs in the 4–8 μg/ml range against different *Staphylococcus* isolates (Wang et al., 2003).

Furthermore, the lack of activity against the Gram-negative reference and clinical strains shows the selectivity of **1** against Gram-positive bacteria. Yet, no activity or weak activity was observed against the clinical VRE isolates and the reference strain of *E. faecalis*, indicating that the activity is selective toward groups of Gram-positives, in this case *S. aureus* and *S. agalactiae*. Surprisingly, no activity was observed against the reference MRSA strain, and the reason behind this is not clear. No activity was observed for the combination of **1** and the efflux pump inhibitor reserpine, indicating that the lack of susceptibility by Gram-negatives is caused by another mechanism. In the antiproliferative activity assay, the most potent activity of **1** was observed against the melanoma cells (IC_{50} = 15.5 μg/ml). Against the non-malignant lung fibroblasts, which were included as a test for general toxicity, the compound had an IC_{50} of 32 μg/ml, which is more than five times higher than the highest MIC value against the multidrug-resistant MRSA. The concentrations where **1** did not display any toxic effect on the cells (∼100% cell survival) were 20, 12.5, and 15 μg/ml for MRC5, A2058, and HepG2, respectively. This indicates that there is little overlap between the concentration where **1** has antibacterial activity and the concentration where toxicity occurs against the human cells.

This observed difference is a good starting point when entering structure optimization, as it indicates that production of non-toxic variants of **1** can be obtained.

We isolated 45 mg/L of **1** when the Lulworthiaceae sp. fungus was grown in liquid media supplemented with sea salts. This shows that slow-growing marine fungi *sensu stricto* can produce high yields of novel compounds for chemical characterization and screening for biological activities. Compound **1** was found to be a novel sulfated dimeric naphthopyrone, and showed potent growth inhibition of multidrug-resistant MRSA with MICs down to 1.56 μg/ml, which is much lower than the IC_{50} detected against the non-malignant cell line (32 μg/ml). This study demonstrates that the family Lulworthiaceae and order Lulworthiales have biosynthetic potential to produce bioactive secondary metabolites and supports the view of Overy et al. (2014) that marine fungi *sensu stricto* should be studied for natural product discovery, despite their slow growth (Overy et al., 2014). Our study highlights the potential role of marine fungi *sensu stricto* in tackling the worldwide AMR crisis.

DATA AVAILABILITY STATEMENT

The datasets presented in this study can be found in online repositories. The names of the repository/repositories and accession number(s) can be found in the article/ **Supplementary Material**.

AUTHOR CONTRIBUTIONS

MJ was responsible for conducting experiments, data analysis, and writing and revising the draft manuscript. PR and JI were responsible for the NMR analysis of the compound and the writing related to this. EJ conducted the antibacterial testing against the clinical bacterial isolates and wrote this section in the "Materials and Methods," and contributed to the writing of the MIC results. KH assisted in writing and revision of the manuscript and contributed to the experiment design. TR did the initial isolation of the fungus and the phylogenetic analysis, contributed to the experiment design by selecting this fungus for the study, and revised the manuscript. JA and EH contributed to the conceptualization of the work, supervised the work, and revised the manuscript. All authors reviewed and approved the final manuscript.

FUNDING

This project received funding from the DigiBiotics project of the Research Council of Norway (project ID 269425), the AntiBioSpec project of UiT the Arctic University of Norway (Cristin ID 20161326), and the Centre for New Antibacterial Strategies at UiT the Arctic University of Norway (TR). The publication charges for this article have been funded by the publication fund of UiT the Arctic University of Norway.

ACKNOWLEDGMENTS

We would like to acknowledge the technical support by Kirsti Helland and Marte Albrigtsen by execution of the bioactivity assays, the contribution of Chun Li in the work with the sequencing of the genetic elements of the isolate, and Ole Christian Hagestad with his assistance in the phylogenetic analysis. We thank the Advanced Microscopy Core Facility (AMCF) of the UiT the Arctic University of Norway for the access to their devices. We would also like to acknowledge the Norwegian National Advisory Unit on Detection of Antimicrobial Resistance (K-res), University Hospital of North Norway for the VREs.

SUPPLEMENTARY MATERIAL

The Supplementary Material for this article can be found online at: https://www.frontiersin.org/articles/10.3389/fmicb.2021.730740/full#supplementary-material

REFERENCES

Azevedo, E., Barata, M., Marques, M. I., and Caeiro, M. F. (2017). Lulworthia atlantica: a new species supported by molecular phylogeny and morphological analysis. *Mycologia* 109, 287–295. doi: 10.1080/00275514.2017.1302255

Boudesocque-Delaye, L., Agostinho, D., Bodet, C., Thery-Kone, I., Allouchi, H., Gueiffier, A., et al. (2015). Antibacterial polyketide heterodimers from Pyrenacantha kaurabassana Tubers. *J. Nat. Prod.* 78, 597–603. doi: 10.1021/np5003252

Calado, M. D. L., Carvalho, L., Barata, M., and Pang, K.-L. (2019). Potential roles of marine fungi in the decomposition process of standing stems and leaves of Spartina maritima. *Mycologia* 111, 371–383. doi: 10.1080/00275514.2019.1571380

Clinical Laboratory Standard Institute (CLSI) (2012). Clinical and laboratory standards institute methods for dilution antimicrobial susceptibility tests for bacteria that grow aerobicallyapproved standard. *J. Infect. Chemother.* 18, 816–826.

Davidson, D. E. (1973). Mucoid sheath of Lulworthia medusa. *Trans. Brit.Mycol. Soc.* 60, 577–579. doi: 10.1016/S0007-1536(73)80042-7

Demain, A. L. (2014). "Valuable secondary metabolites from fungi," in *Biosynthesis and Molecular Genetics of Fungal Secondary Metabolites*, eds J. F. Martín, S. Zeilinger, and C. García-Estrada (Springer).

Francisca, C., Marta, C.-D.-S., Emília, S., Madalena, P., and Anake, K. (2018). Sulfation pathways: sources and biological activities of marine sulfated steroids. *J. Mol. Endocrinol.* 61, T211–T231. doi: 10.1530/JME-17-0252

Góes-Neto, A., Marcelino, V. R., Verbruggen, H., da Silva, F. F., and Badotti, F. (2020). Biodiversity of endolithic fungi in coral skeletons and other reef substrates revealed with 18S rDNA metabarcoding. *Coral. Reefs* 39, 229–238. doi: 10.1007/s00338-019-01880-y

Hyde, K. D., Norphanphoun, C., Maharachchikumbura, S. S. N., Bhat, D. J., Jones, E. B. G., Bundhun, D., et al. (2020). Refined families of sordariomycetes. *Mycosphere* 11:1059. doi: 10.5943/mycosphere/11/1/7

Imhoff, J. F. (2016). Natural products from marine fungistill an underrepresented resource. *Mar. Drugs* 14, 1–19. doi: 10.3390/md14010019

Isaka, M., Yangchum, A., Rachtawee, P., Komwijit, S., and Lutthisungneon, A. (2010). Hopane-type triterpenes and binaphthopyrones from the scale insect pathogenic fungus Aschersonia paraphysata BCC 11964. *J. Nat. Prod.* 73, 688–692. doi: 10.1021/np1000363

Johnson, T. W. (1958). Marine fungi. IV. *Lulworthia* and *Ceriosporopsis*. *Mycologia* 50, 151–163. doi: 10.2307/3756191

Jones, E. B. G. (1994). Fungal adhesion. *Mycol. Res.* 98, 961–981. doi: 10.1016/S0953-7562(09)80421-8

Katoh, K., and Standley, D. M. (2013). MAFFT multiple sequence alignment software version 7: improvements in performance and usability. *Mol. Biol. Evol.* 30, 772–780. doi: 10.1093/molbev/mst010

Katoh, K., Misawa, K., Kuma, K., and Miyata, T. (2002). MAFFT: a novel method for rapid multiple sequence alignment based on fast Fourier transform. *Nucleic Acids Res.* 30, 3059–3066. doi: 10.1093/nar/gkf436

Kavanagh, F., Hervey, A., and Robbins, W. J. (1951). Antibiotic substances from *Basidiomycetes*: VIII. Pleurotus Multilus (Fr.) Sacc. and Pleurotus Passeckerianus Pilat. *Proc. Natl. Acad. Sci. U.S.A.* 37, 570–574. doi: 10.1073/pnas.37.9.570

Kawaguchi, M., Uchida, R., Ohte, S., Miyachi, N., Kobayashi, K., Sato, N., et al. (2013). New dinapinone derivatives, potent inhibitors of triacylglycerol synthesis in mammalian cells, produced by *Talaromyces pinophilus* FKI-3864. *J. Antibiot.* 66, 179–189. doi: 10.1038/ja.2012.127

Koch, J., Pang, K.-L., and Jones, E. B. G. (2007). Rostrupiella danica gen. et sp. nov., a Lulworthia-like marine lignicolous species from Denmark and the USA. *Bot. Mar.* 50, 294–301. doi: 10.1515/BOT.2007.034

Kohlmeyer, J., Spatafora, J. W., and Volkmann-Kohlmeyer, B. (2000). Lulworthiales, a new order of marine Ascomycota. *Mycologia* 92, 453–458. doi: 10.2307/3761504

Kornprobst, J.-M., Sallenave, C., and Barnathan, G. (1998). Sulfated compounds from marine organisms. *Comput. Biochem. Physiol.* 119, 1–51. doi: 10.1016/S0305-0491(97)00168-5

Kristoffersen, V., Rämä, T., Isaksson, J., Andersen, J. H., Gerwick, W. H., Hansen, E., et al. (2018). Characterization of rhamnolipids produced by an Arctic marine bacterium from the *Pseudomonas* fluorescence Group. *Mar. Drugs* 16:163. doi: 10.3390/md16050163

Lanfear, R., Calcott, B., Ho, S. Y. W., and Guindon, S. (2012). PartitionFinder: combined selection of partitioning schemes and substitution models for phylogenetic analyses. *Mol. Biol. Evol.* 29, 1695–1701. doi: 10.1093/molbev/mss020

Lanfear, R., Frandsen, P. B., Wright, A. M., Senfeld, T., and Calcott, B. (2017). PartitionFinder 2: new methods for selecting partitioned models of evolution for molecular and morphological phylogenetic analyses. *Mol. Biol. Evol.* 34, 772–773. doi: 10.1093/molbev/msw260

Li, D.-H., Han, T., Guan, L.-P., Bai, J., Zhao, N., Li, Z.-L., et al. (2016). New naphthopyrones from marine-derived fungus *Aspergillus niger* 2HL-M-8 and their in vitro antiproliferative activity. *Nat. Prod. Res.* 30, 1116–1122. doi: 10.1080/14786419.2015.1043553

Lu, S., Tian, J., Sun, W., Meng, J., Wang, X., Fu, X., et al. (2014). Bis-naphtho-γ-pyrones from fungi and their bioactivities. *Molecules* 19, 7169–7188. doi: 10.3390/molecules19067169

Maharachchikumbura, S. S. N., Hyde, K. D., Jones, E. B. G., McKenzie, E. H. C., Huang, S.-K., Abdel-Wahab, M. A., et al. (2015). Towards a natural classification and backbone tree for Sordariomycetes. *Fungal. Divers.* 72:301. doi: 10.1007/s13225-015-0331-z

Overy, D. P., Bayman, P., Kerr, R. G., and Bills, G. F. (2014). An assessment of natural product discovery from marine (sensu strictu) and marine-derived fungi. *Mycology* 5, 145–167. doi: 10.1080/21501203.2014.931308

Overy, D. P., Rämä, T., Oosterhuis, R., Walker, A. K., and Pang, K.-L. (2019). The neglected marine fungi, sensu stricto, and their isolation for natural products' discovery. *Mar. Drugs* 17, 1–20. doi: 10.3390/md17010042

Poli, A., Bovio, E., Ranieri, L., Varese, G. C., and Prigione, V. (2020). Fungal diversity in the Neptune forest: Comparison of the mycobiota of *Posidonia oceanica, Flabellia petiolata*, and *Padina pavonica*. *Front. Microbiol.* 11:933. doi: 10.3389/fmicb.2020.00933

Rämä, T., Nordén, J., Davey, M. L., Mathiassen, G. H., Spatafora, J. W., and Kauserud, H. (2014). Fungi ahoy! Diversity on marine wooden substrata in the high North. *Fungal. Ecol.* 8, 46–58. doi: 10.1016/j.funeco.2013.12.002

Rehner, S. A., and Samuels, G. J. (1994). Taxonomy and phylogeny of *Gliocladium* analysed from nuclear large subunit ribosomal DNA sequences. *Mycol. Res.* 98, 625–634. doi: 10.1016/S0953-7562(09)80409-7

Rivera-Chavez, J., Caesar, L., Garcia-Salazar, J. J., Raja, H. A., Cech, N. B., Pearce, C. J., et al. (2019). Mycopyranone: a 8,8'-binaphthopyranone with potent anti-MRSA activity from the fungus *Phialemoniopsis* sp. *Tetrahedron Lett.* 60, 594–597. doi: 10.1016/j.tetlet.2019.01.029

Ronquist, F., Teslenko, M., van der Mark, P., Ayres, D. L., Darling, A., Höhna, S., et al. (2012). MrBayes 3.2: efficient Bayesian phylogenetic inference and model choice across a large model space. *Syst. Biol.* 61, 539–542. doi: 10.1093/sysbio/sys029

Schneider, Y., Jenssen, M., Isaksson, J., Hansen, K. Ø, Andersen, J. H., and Hansen, E. H. (2020). Bioactivity of serratiochelin A, a siderophore isolated from a co-culture of Serratia sp. and Shewanella sp. *Microorganisms* 8, 1–17. doi: 10.3390/microorganisms8071042

Stamatakis, A. (2006). RAxML-VI-HPC: maximum likelihood-based phylogenetic analyses with thousands of taxa and mixed models. *Bioinformatics* 22, 2688–2690. doi: 10.1093/bioinformatics/btl446

Sutherland, G. K. (1915). Additional notes on marine Pyrenomycetes. *New Phytol.* 14, 183–193. doi: 10.1111/j.1469-8137.1915.tb07185.x

Suzuki, K., Nozawa, K., Nakajima, S., Udagawa, S., and Kawai, K. (1992). Isolation and structures of antibacterial binaphtho-α-pyrones, talaroderxines A and B, from Talaromyces derxii. *Chem. Pharm. Bull.* 40, 1116–1119. doi: 10.1248/cpb.40.1116

Velez, P., González, M. C., Cifuentes, J., Rosique-Gil, E., and Hanlin, R. T. (2015). Diversity of sand inhabiting marine ascomycetes in some tourist beaches on Cozumel Island, Mexico. *Mycoscience* 56, 136–140. doi: 10.1016/j.myc.2014.04.007

Vilgalys, R., and Hester, M. (1990). Rapid genetic identification and mapping of enzymatically amplified ribosomal DNA from several Cryptococcus species. *J. Bacteriol.* 172, 4238–4246. doi: 10.1128/jb.172.8.4238-4246.1990

Wang, J., Galgoci, A., Kodali, S., Herath, K. B., Jayasuriya, H., Dorso, K., et al. (2003). Discovery of a small molecule that inhibits cell division by blocking FtsZ, a novel therapeutic target of antibiotics. *J. Biol. Chem.* 278, 44424–44428. doi: 10.1074/jbc.M307625200

White, T. J., Bruns, T., Lee, S., and Taylor, J. (1990). "Amplification and direct sequencing of fungal ribosoman RNA genes for phylogenetics," in *PCR ProtocolsA Guide to Methods and Applications*, eds M. A. Innis, D. H. Gelfand, J. J. Sninsky, and T. J. White (San Diego: Academic Press).

WHO (2014). *Antimicrobial ResistanceGlobal Report on Surveillance*. Available online at: http://www.who.int/drugresistance/documents/surveillancereport/en/. (accessed February 26, 2018).

Xu, Y., Vinas, M., Alsarrag, A., Su, L., Pfohl, K., Rohlfs, M., et al. (2019). Bis-naphthopyrone pigments protect filamentous ascomycetes from a wide range of predators. *Nat. Commun.* 10, 1–12. doi: 10.1038/s41467-019-11377-5

Zheng, C. J., Sohn, M.-J., Lee, S., Hong, Y.-S., Kwak, J.-H., and Kim, W.-G. (2007). Cephalochromin, a FabI-directed antibacterial of microbial origin. *Biochem. Biophys. Res. Commun.* 362, 1107–1112. doi: 10.1016/j.bbrc.2007.08.144

Zuccaro, A., Schoch, C. L., Spatafora, J. W., Kohlmeyer, J., Draeger, S., and Mitchell, J. I. (2008). Detection and identification of fungi intimately associated with the brown seaweed Fucus serratus. *Appl. Environ. Microbiol.* 74, 931–941. doi: 10.1128/AEM.01158-07

Conflict of Interest: The authors declare that the research was conducted in the absence of any commercial or financial relationships that could be construed as a potential conflict of interest.

Publisher's Note: All claims expressed in this article are solely those of the authors and do not necessarily represent those of their affiliated organizations, or those of the publisher, the editors and the reviewers. Any product that may be evaluated in this article, or claim that may be made by its manufacturer, is not guaranteed or endorsed by the publisher.

Supplementary Material

Table of Content

Supplementary Figure 15:HMQC optimized for 4 Hz $^{n}J_{CH}$ displays some of the important $^{4}J_{CH}$ for assignment.

Supplementary Figure 16: NOESY (600 ms mixing time) of **1**.

Supplementary Table 1: Dataset of nrITS, nrLSU and nrSSU used for phylogenetic analysis of 067bN1.2. All sequences were acquired from Genbank.

Species	**Strain**	**Source**	**nrITS**	**nrLSU**	**nrSSU**
Achroceratosphaeria potamia	JF 08139	Submerged wood of *Platanus* sp.	-	GQ996538	GQ996541
Bimuria novae-zelandiae	CBS 107.79	Soil	-	AY016356	AY016338
Cumulospora marina	MF46	Submerged wood	-	GU252135	GU252136
Cumulospora varia	GR78	Submerged wood	-	EU848578	EU848593
Halazoon fuscus	NBRC 105256	Driftwood	-	GU252147	GU252148
Halazoon melhae	MF819	Drift stems of *Phragmites australis*	-	GU252143	GU252144
Hydea pygmea	NBRC 33069	Driftwood	-	GU252133	GU252134
Kohlmeyeriella crassa	NBRC 32133	Sea foam	LC146741	LC146742	AY879005
Kohlmeyeriella tubulata	PP115	Marine environment	-	AF491265	AY878998
Koralionastes ellipticus	JF08139	Coral rocks with sponges	-	EU863585	EU863581
Letendraea helminthicola	CBS 884.85	Yerba mate	EU715680	AY016362	AY016345
Lindra marinera	JK 5091A	Marine environment	-	AY878958	AY879000
Lindra obtusa	NBRC 31317	Sea foam	LC146744	AY878960	AY879002
Lindra thalassiae	AFTOL 413	Marine environment	DQ491508	DQ470947	DQ470994
Lulworthia atlantica	FCUL210208 SP4	Sea water	KT347205	JN886843	KT347193
Lulworthia cf. *opaca*	CBS 21860	Driftwood in seawater	-	AY878961	AY879003
Lulworthia cf. *purpurea*	FCUL170907 CP5	Sea water	KT347219	JN886824	KT347201
Lulworthia fucicola	ATCC 64288	Intertidal wood	-	AY878965	AY879007

Lulworthia grandispora	NTOU3841	Driftwood	-	KY026048	KY026044
Lulworthia lignoarenaria	AFTOL 5013	Marine environment	-	FJ176903	FJ176848
Lulworthia medusa	JK 5581	Spartina	-	AF195637	AF195636
Lulworthiaceae	067bN1.2	Driftwood	MW377595	MW375591	MW375590
Matsusporium tropicale	NBRC 32499	Submerged wood	-	GU252141	GU252142
Moleospora maritima	MF836	Drift stems of *Phragmites australis*	-	GU252137	GU252138
Paralulworthia gigaspora	MUT 435	*P. oceanica* – rhizomes	MN649242	MN649250	MN649246
Paralulworthia posidoniae	MUT 5261	*P. oceanica* – rhizomes	MN649245	MN649253	MN649249
Setosphaeria monoceras	CBS 154.26	n.d.	DQ337380	AY016368	DQ238603
Zalerion maritima	FCUL280207 CP1	Sea water	KT347216	JN886806	KT347203

Supplementary Table 2: Information regarding the clinical isolates used for antibacterial activity testing of **1**.

Clinical isolate	**Antibiotic Resistance Mechanism**	**Reference**	**Source (gifted/bought)**
S. aureus N315	MRSA	Ito et al. (1999). Cloning and nucleotide sequence determination of the entire mec DNA of pre-methicillin-resistant *Staphylococcus aureus* N315. *Antimicrob. Agents Chemother*,*43*, 1449-1458. doi: 10.1128/AAC.43.6.1449	T. Ito, Juntendo University, Tokyo (Japan)
S. aureus 85/2082		Suzuki et al. (1993). Distribution of mec Regulator Genes in Methicillin-Resistant *Staphylococcus* Clinical Strains. *Antimicrob. Agents Chemother.*,*37*, 1219-1226. doi: 0066-4804/93/061219-08$02.00/0	T. Ito, Juntendo University, Tokyo (Japan)
S. aureus NCTC 10442		Ito et al. (2001).Structural comparison of three types of staphylococcal cassette chromosome mec integrated in the chromosome in methicillin-resistant *Staphylococcus aureus*. *Antimicrob. Agents Chemother*,*45*, 1323-1336. doi: 10.1128/AAC.45.5.1323-1336.2001.	NCTC
S. aureus WIS [WBG8318]		Ito et al. (2004).Novel Type V Staphylococcal Cassette Chromosome mec Driven by a Novel Cassette Chromosome Recombinase, ccrC. *Antimicrob. Agents. Chemother.*,*48*, 2637–2651. doi: 10.1128/AAC.48.7.2637-2651.2004	K. Hiramatsu, Juntendo University, Tokyo, (Japan)
S. aureus IHT 99040		Salmenlinna, S., Lyytikäinen, O., & Vuopio-Varkila, J. (2002).Community-Acquired Methicillin-Resistant *Staphylococcus aureus*, Finland.*Emerging infectious diseases*, *8*, 602–607.doi: 10.3201/eid0806.010313	Saara Salmenlinna (IHT, Helsinki, Finland)
E. faecium 50673722	VRE	Sivertsen A, Janice J, Pedersen T,Wagner TM, Hegstad J, Hegstad	K-res [a]

		K. 2018. Theenterococcus cassette chromosome, agenomic variation enabler in enterococci.*mSphere*, 3, 1-13. doi:10.1128/mSphere.00402-18	
*E. faecium*50901530		-	K-res [a]
*E. faecium*K36-18		-	K-res [a]
*E. faecium*50758899		-	K-res [a]
*E. faecium*TUH50-22		-	K-res [a]
*E. faecium*1-H-4		-	K-res [a]
E. coli 50676002	ESBL-Carba	-	K-res [a]
K. pneumoniae K47-25		-	K-res [a]
A. baumanii K47-42		-	K-res [a]
P. aeruginosa K34-7		-	K-res [a]
E.coli ATCC 25922	-	ATCC	ATCC

[a] 2006-2015 The Norwegian National Advisory Unit on Detection of Antimicrobial Resistance (K-res), University Hospital of North Norway – UNN.

Supplementary Table 3: Summary of chemical shift and correlations for **1**(DMSO-d_6).

Position	δ^{13}C, type	δ^{1}H, splitting (Hz)	COSY	HMBC (^{1}H → ^{13}C)
2	170.0*,C	-	-	-
2'	169.7, C	-	-	-
2a'	98.3, C	-	-	-
2a	98.0, C	-	-	-
3	173.8*, C	-	-	-
3'	173.8, C	-	-	-
3a'	112.2, C	-	-	-
3a	113.0, C	-	-	-
4	162.0, C	-	-	-
4'	160.3, C	-	-	-
5'	108.7, C	-	-	-
5	101.8, CH	6.55, h	-	3a, 4, 6, 7
6	155.3, C	-	-	-
6'	160.0, C	-	-	-
7a	138.2, C	-	-	-
7a'	139.3, C	-	-	-
7	104.6, CH	6.05, h	-	3a, 5, 6, 8
7'	96.6, CH	6.69, h	-	3',3a', 5', 6', 8'
8a'	139.2, C	-	-	-
8a	133.3, C	-	-	-
8	113.2, C	-	-	-
8'	110.9, CH	6.74, h	-	2',2a',3',3a',7a',7',8a',9'
9'	65.7, CH	4.69, h	OH9'	2a', 8', 8a', 10'
9	31.7, CH2	2.40/2.57, m	10	8, 8a, 10
10'	80.3, CH	4.62, m	11'	8a', 9', 11', 12'
10	77.2, CH	4.56, m	9	8a, 12
11	33.7, CH2	1.52, m 1.64, m	12	10
11'	29.5, CH2	1.78, m	10', 12'	10'
12'	24.2, CH2	1.27/1.34, m	11',13'	11',13',14'
12	24.3, CH2	1.47, m	11, 13	11,13,14
13'	31.2, CH2	1.34, m	12'	14',15'
13	30.9, CH2	1.21, m	12	14,15
14'	22.1, CH2	1.34, m	15'	13',15'
14	22.0, CH2	1.23, m	15	13,15
15'	14.0, CH3	0.90, t (J=6.5)	14'	13',14'
15	13.9, CH3	0.81, h	14	13,14
16	55.4, O-CH3	3.77, h	-	6'
OH3*	-	-, s		
OH3*	-	-, s		
OH4	-	14.74, h		4,3a,5
OH4'	-	14.65, h		4',3a',5
OH9'	-	5.51, h	9'	

*Ambiguous assignment

Supplementary Table 4: Results for the MIC determination of **1** against clinical isolates and reference strains (MIC of 50 µg/ml or higher/above highest tested concentration).

Strain type	**Strain**	**MIC in µg/ml**
Clinical isolates	*E. faecium* 50673722	>100
	E. faecium 50901530	>100
	E. faecium K36-18	100
	E. faecium 50758899	>100
	E. faecium TUH50-22	100
	E. faecium 1-H-4	50
	E. coli 50676002	>100
	K. pneumoniae K47-25	>100
	A. baumanii K47-42	>100
	P. aeruginosa K34-7	>100
Reference strains	*Enterococcus faecalis* ATCC® 29212	>100
	Methicillin resistant *S. aureus* ATCC® 33591	>100
	Escherichia coli ATCC® 25922	>100
	Pseudomonas aeruginosa ATCC® 27853	>100

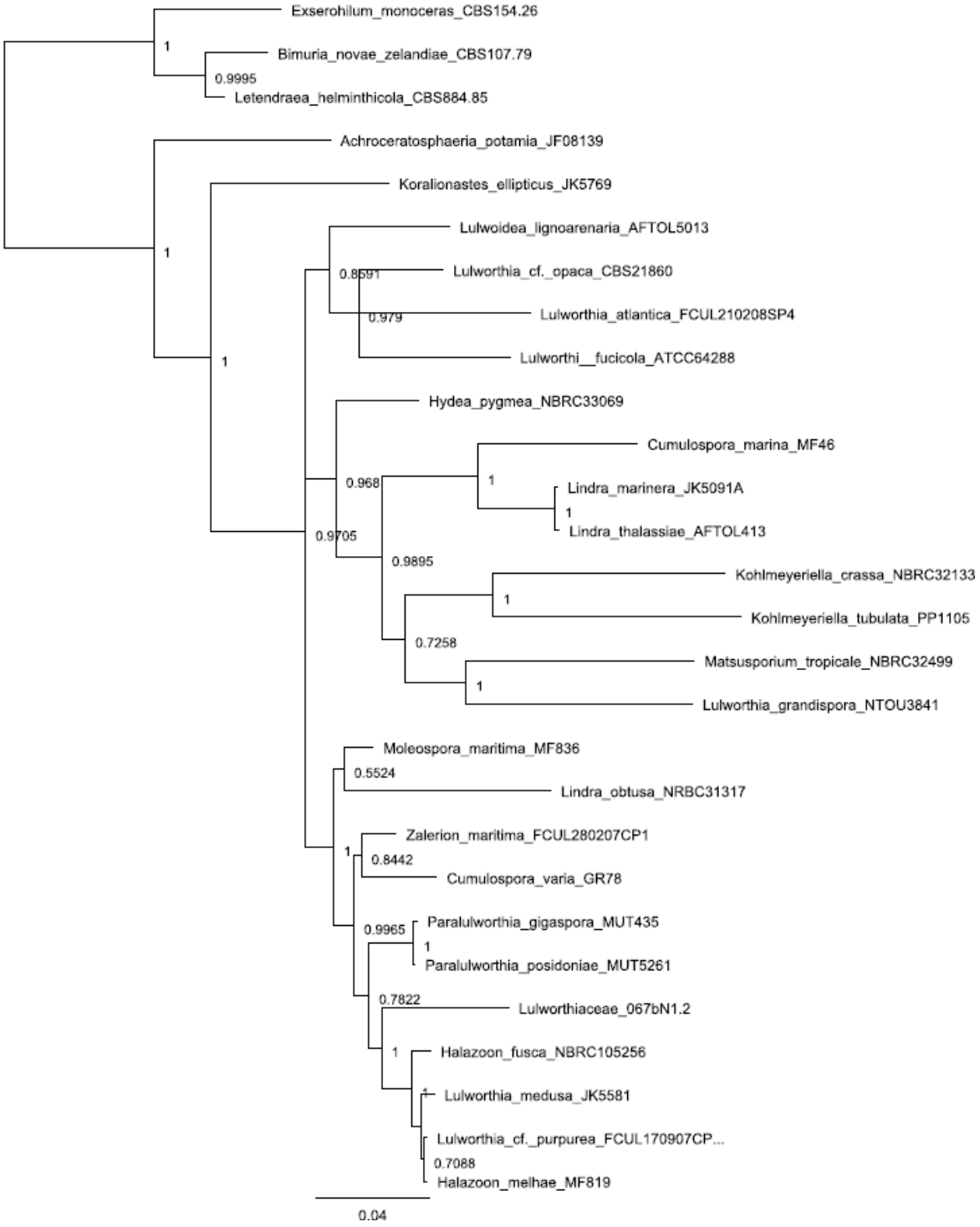

Supplementary Figure 1: MrBayes tree from the 5.8S, SSU and LSU analysis, showing the placement of 067bN1.2 within the family Lulworthiaceae. Node support given as posterior probabilites. *Exserophilum monoceras, Letendraea helminthicola, Bimufia novae-zelandiae* and *Achroceratosphaeria potamia* were included as outgroups taxa. *Koralionastes ellipticus* was included as a member of the family Koralionastetaceae. The remaining sequences are all part of Lulworthiaceae.

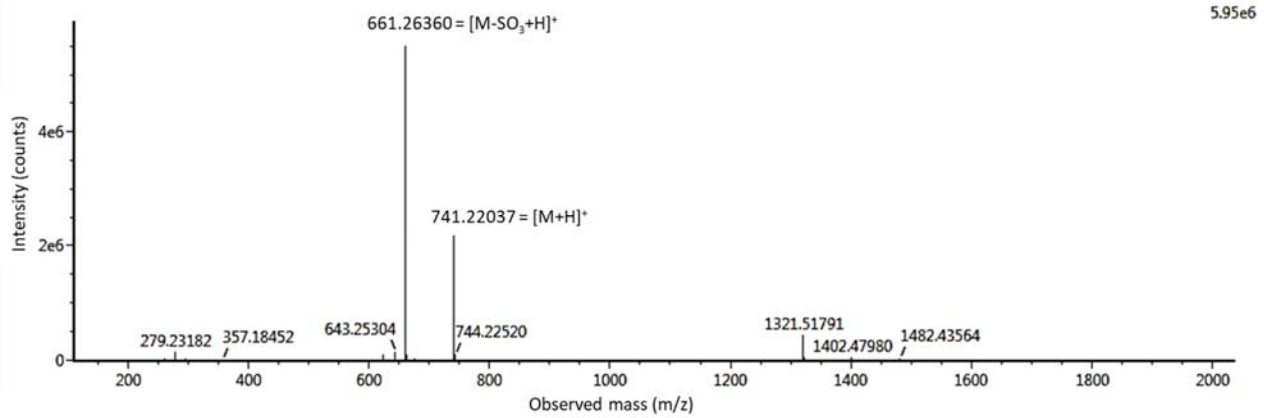

Supplementary Figure 2: Low-collision energy mass spectrum of lulworthinone (**1**) in ESI+.

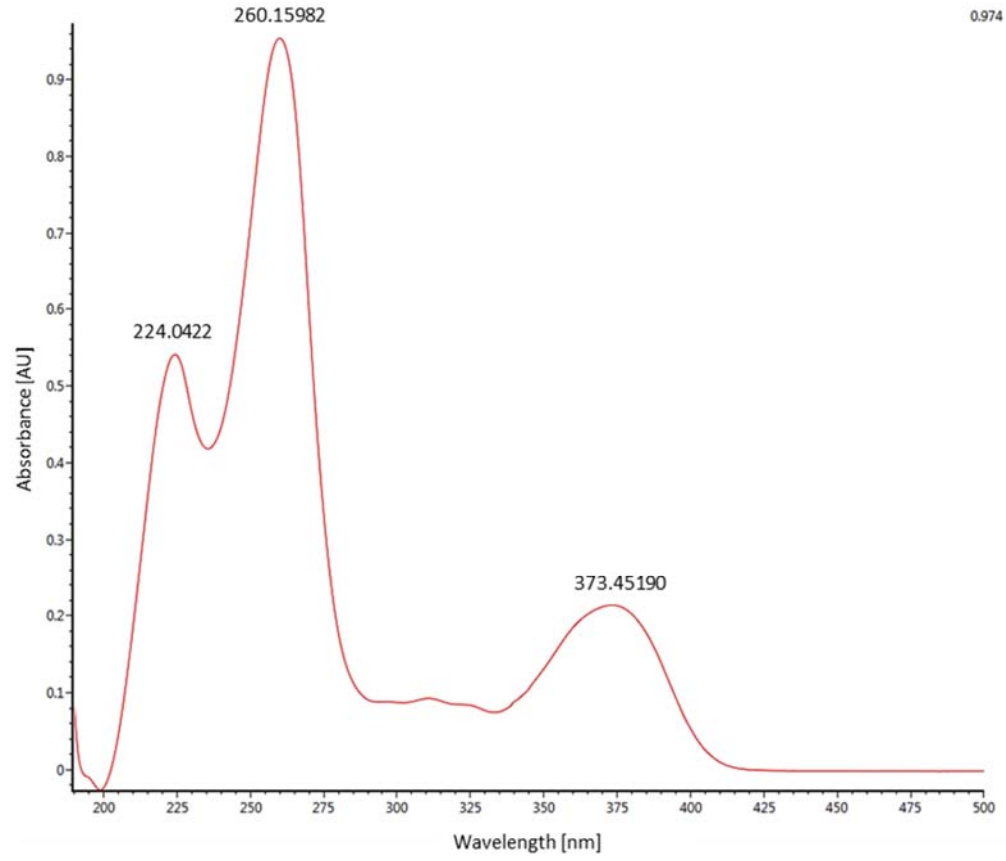

Supplementary Figure 3:UV-Vis spectrum of lulworthinone (**1**).

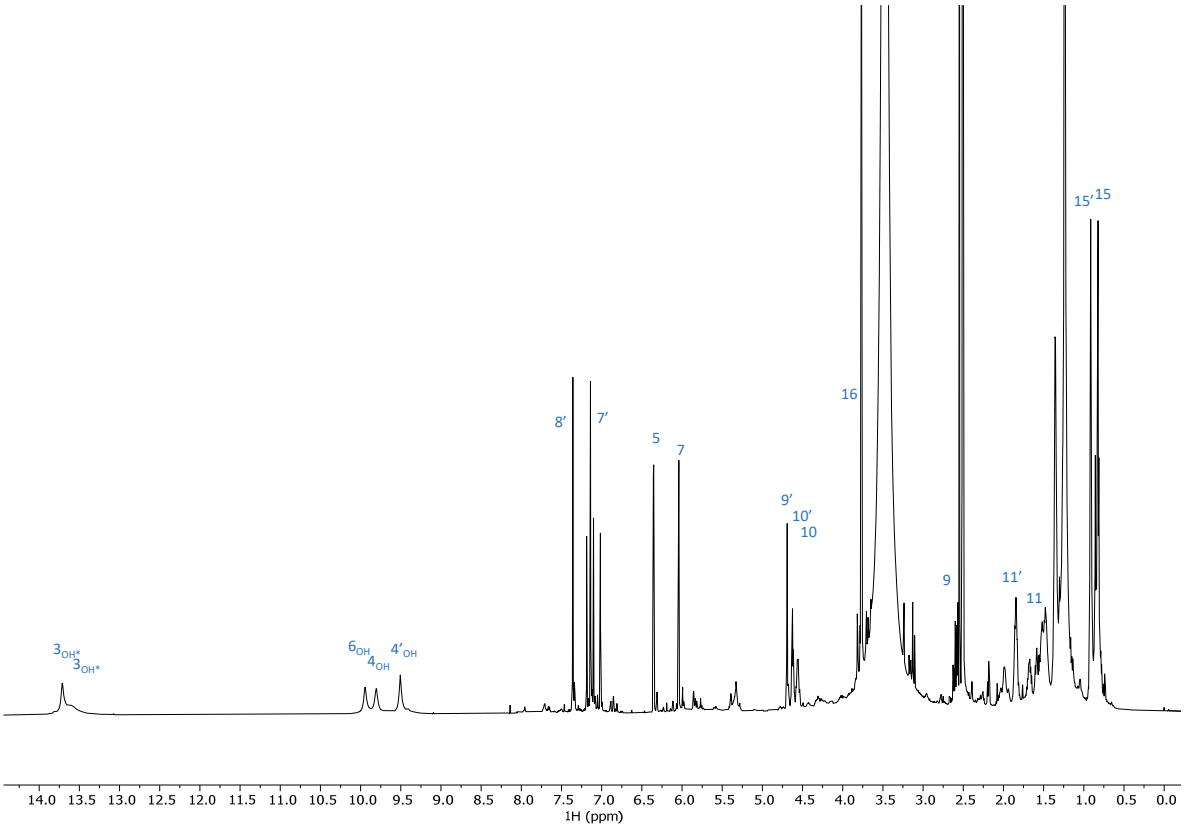

Supplementary Figure 4: 1D proton spectrum of **2**.

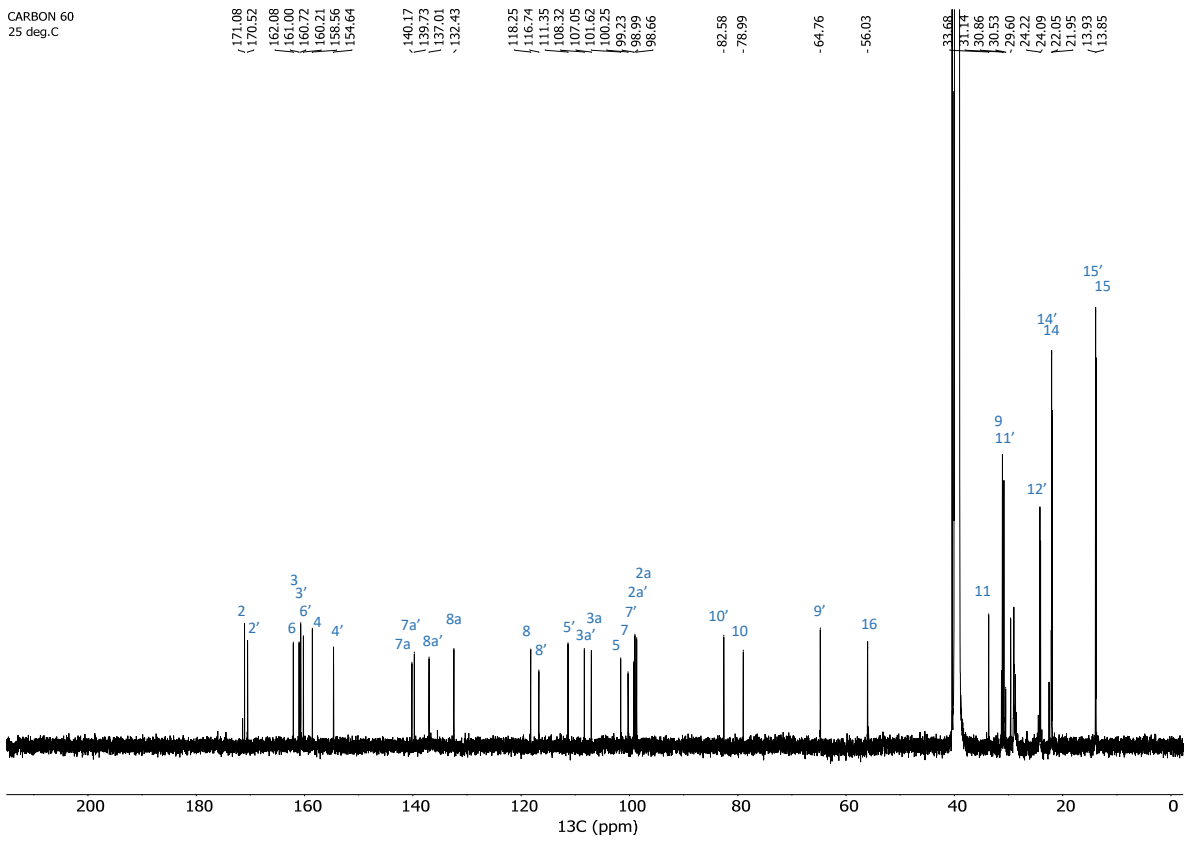

Supplementary Figure 5: 1D carbon spectrum of **2**.

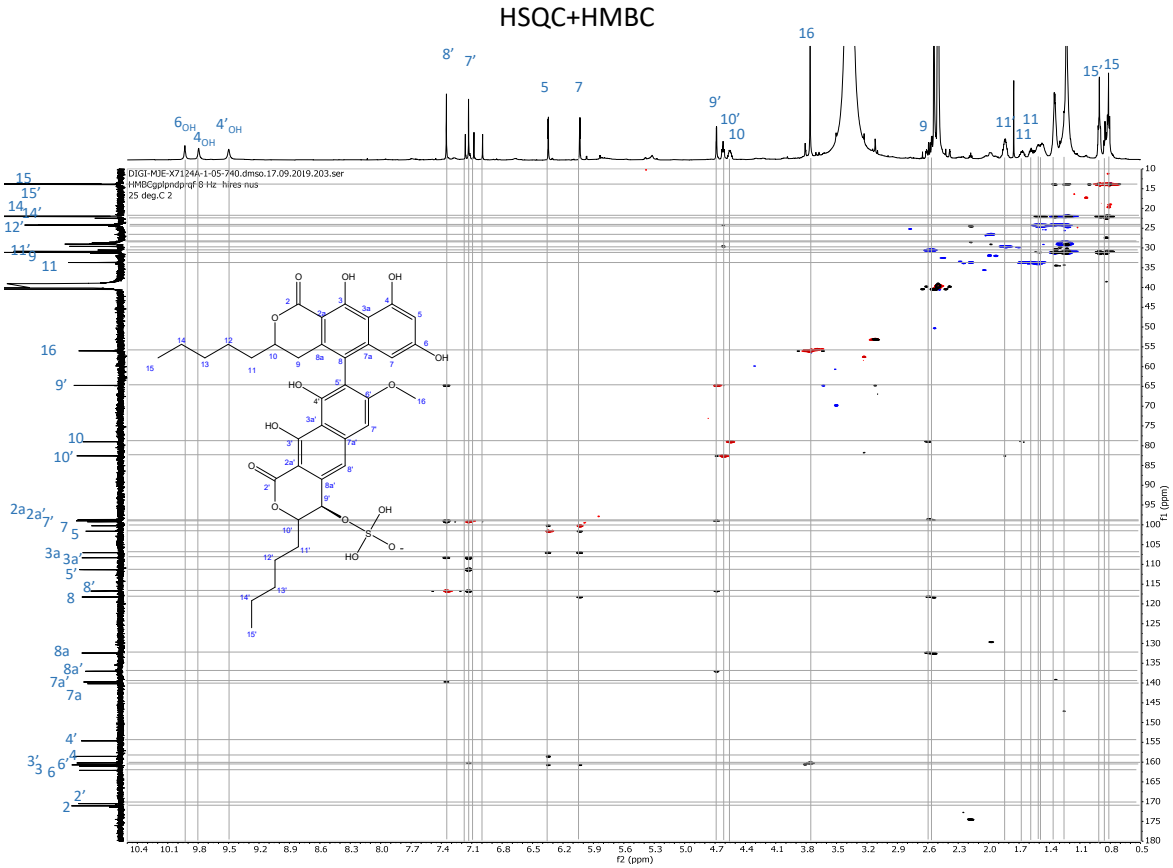

Supplementary Figure 6: Superimposed HSQC and HMBC of **2**.

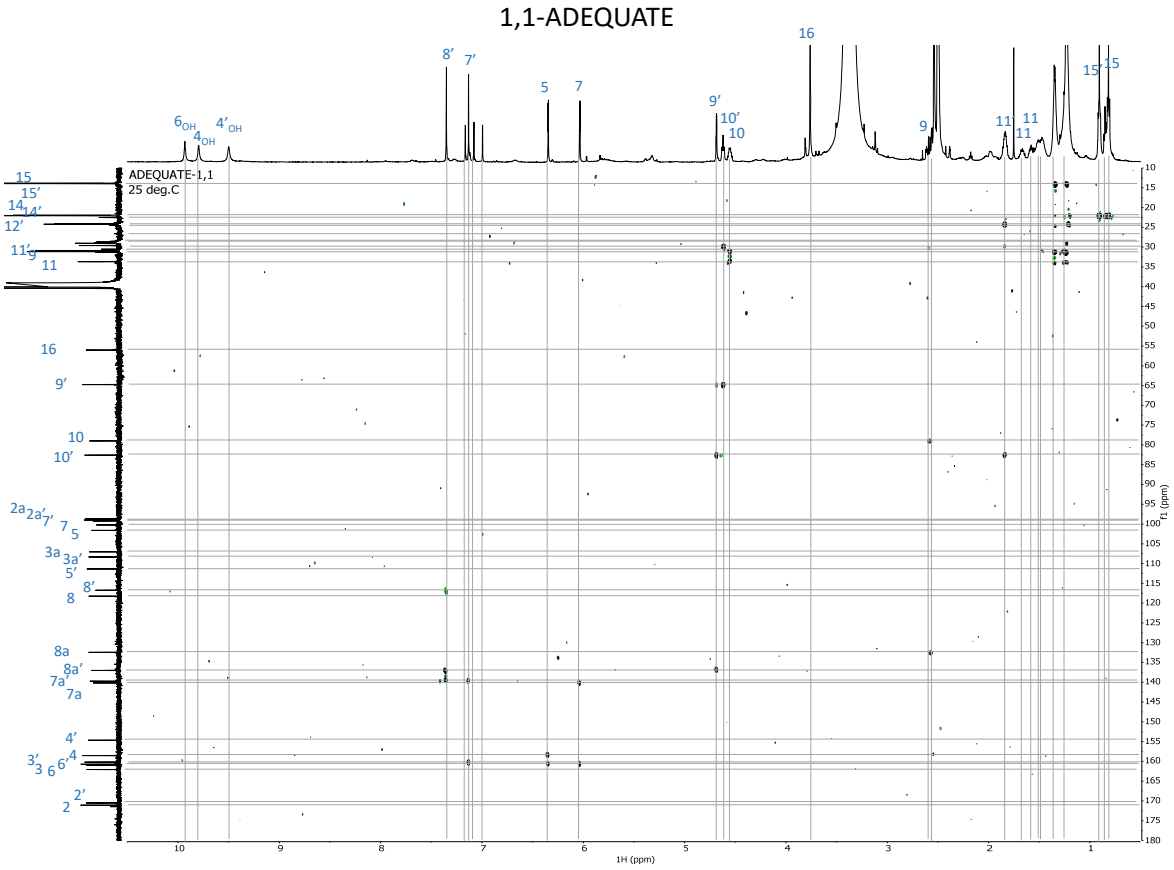

Supplementary Figure 7: 1,1-ADEQUATE of **2**.

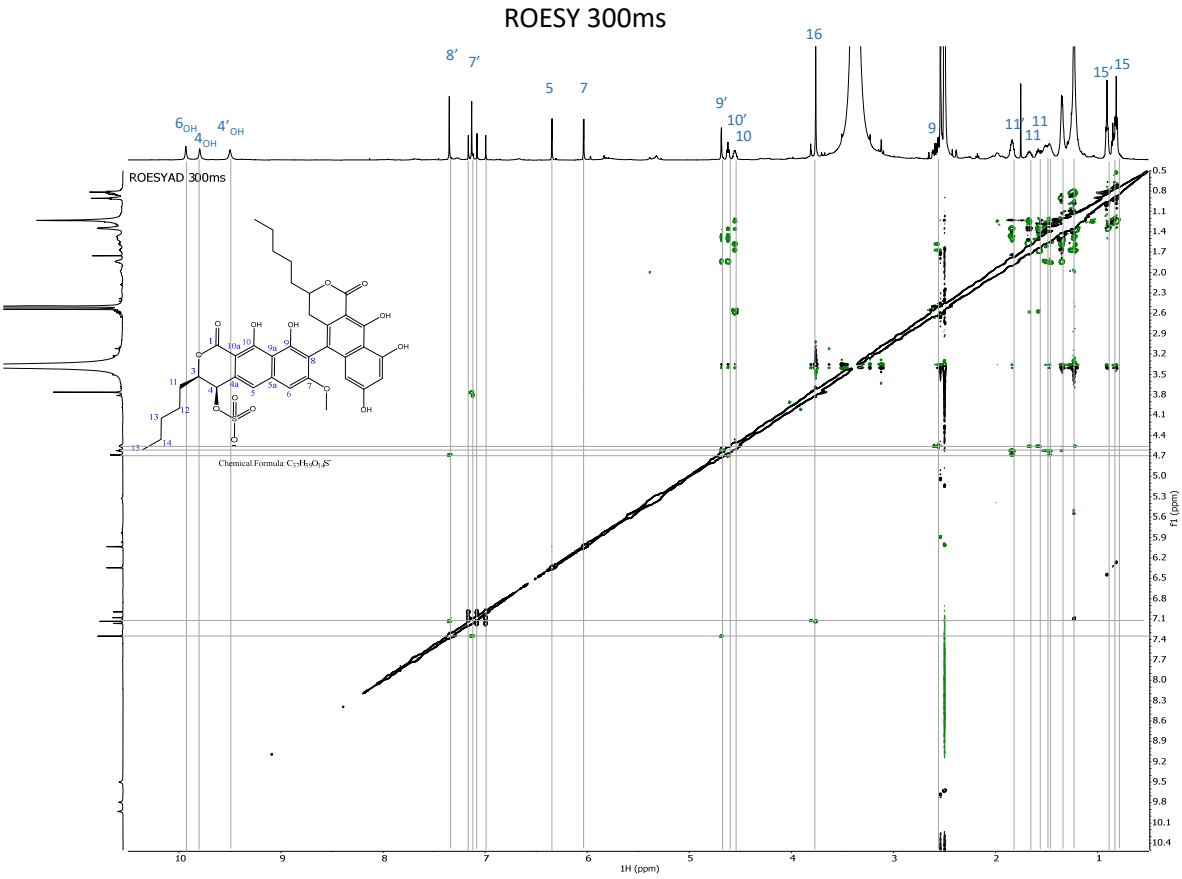

Supplementary Figure 8: ROESY (300 ms mixing time) of **2**.

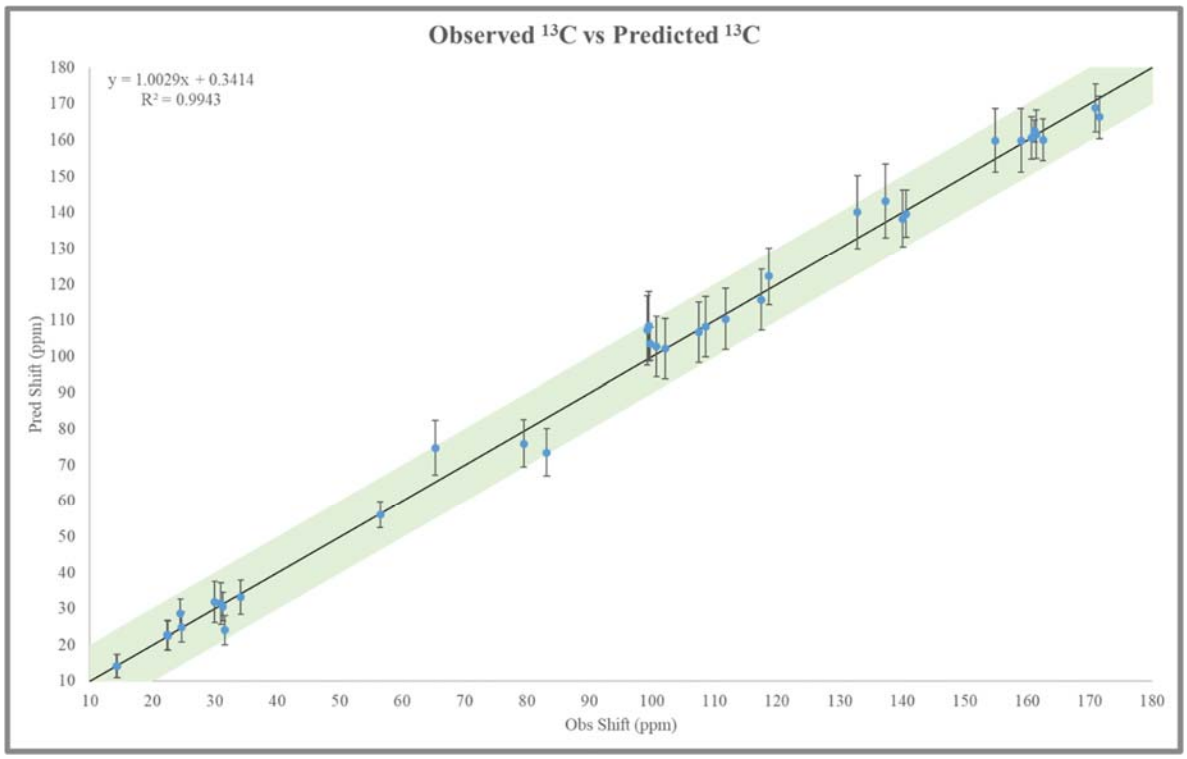

Supplementary Figure 9: Predicted vs observed ^{13}C chemical shift comparison. Average error of 2.79 ppm, R2 of 0.9943. Green region is equivalent to an error of +/- 10 ppm, black line y = x. Errors for prediction given by MestreNova Modgraph desktop prediction.

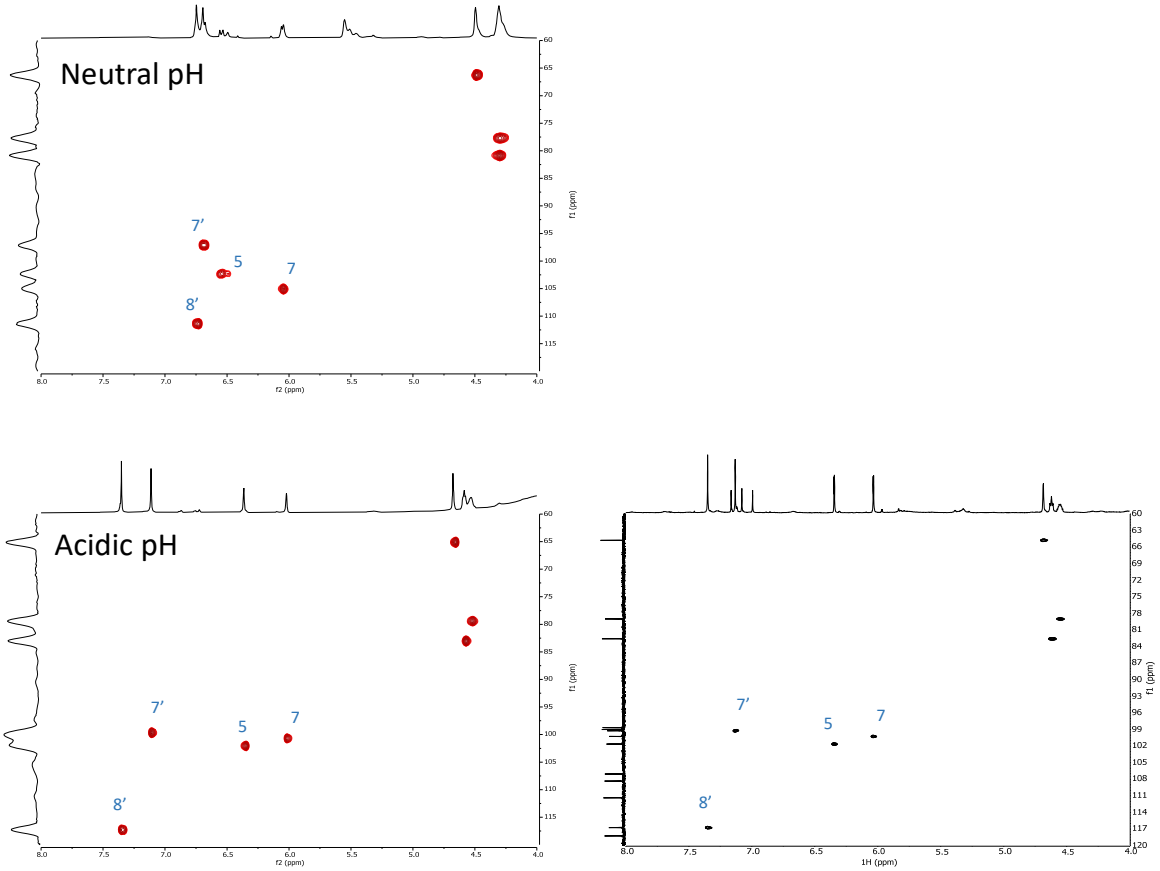

Supplementary Figure 10: The HSQC peaks of the aromatic region of the second preparation of **1** (red) at neutral (top) and after addition of acid (bottom), compared to the initial preparation of **2** in the presence of formic acid (black).

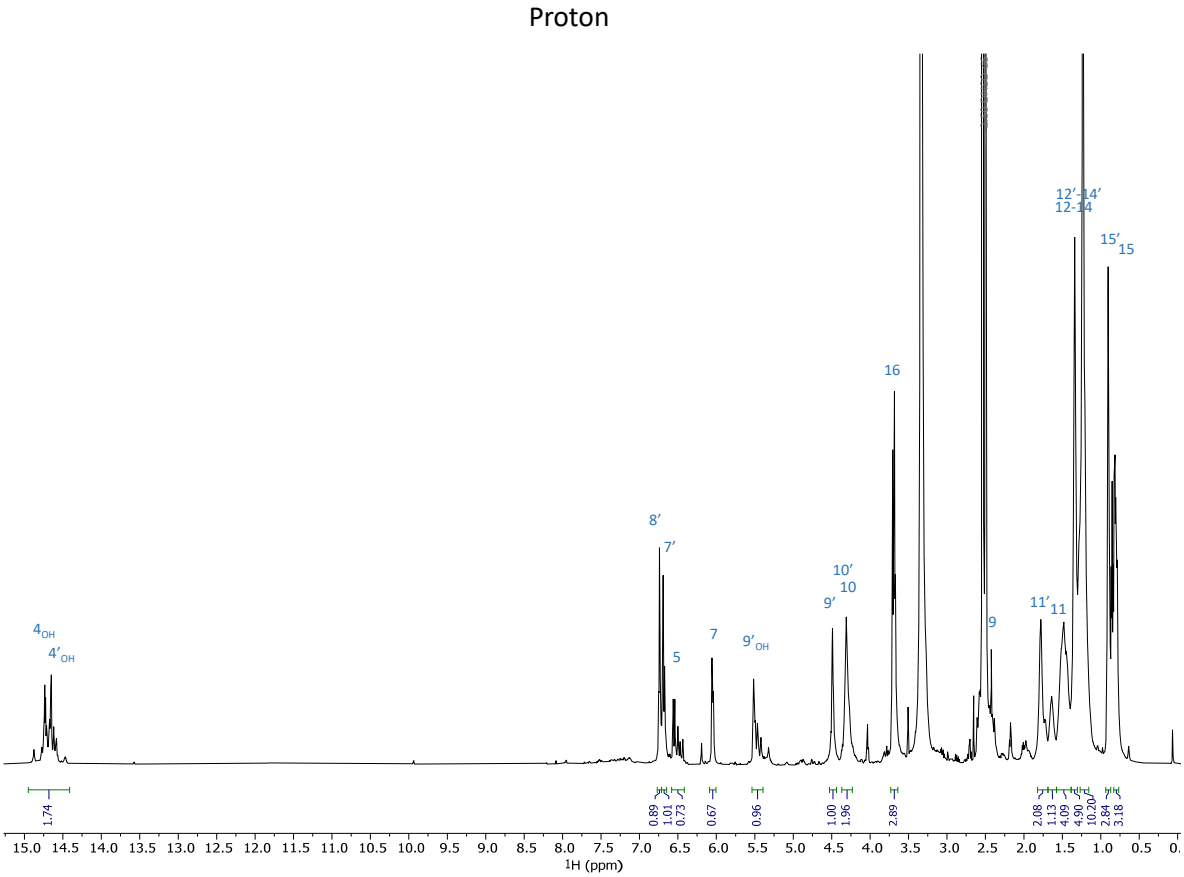

Supplementary Figure 11: Proton spectrum of **1** in DMSO-d6.

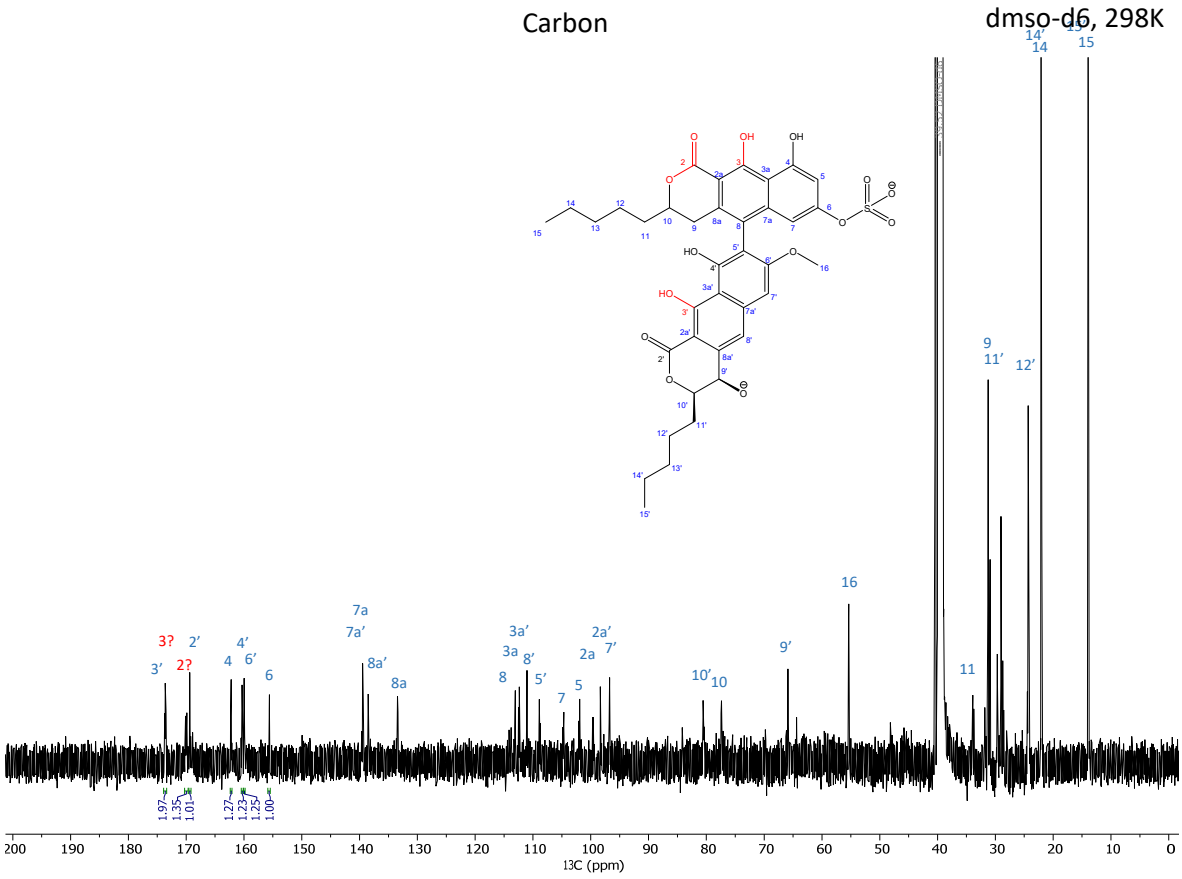

Supplementary Figure 12: Carbon spectrum of **1** in DMSO-d$_6$.

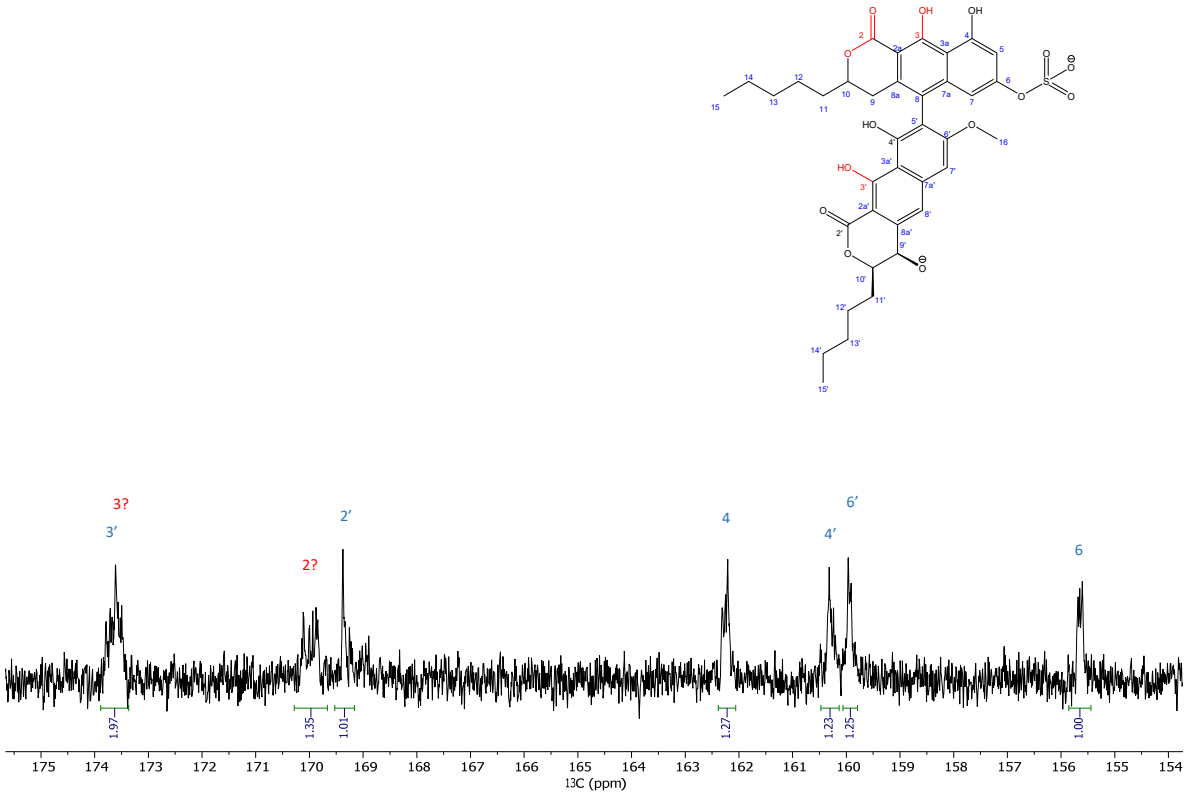

Supplementary Figure 13: Expansion of the carbonyl/deep aromatic region of the carbon spectrum in Supplementary Figure 12. Compared to **2**, **1** only has 4 carbons in the 160-165 range, and instead has 4 carbons in the 169-175 range. Integrals should be interpreted conservatively as it is ill advised to integrate carbon signals, but in this case we only qualitatively compare quaternary carbons to each other where the stead state noe enhancement is expected to be low and their T1 relaxation times are expected to be similarly slow. Without reading too much into it, it appears that C3 and C3' are not hidden among the other carbons in the 160-165 range but have indeed shifted to the more deshielded region normally associated with carbonyl resonances.

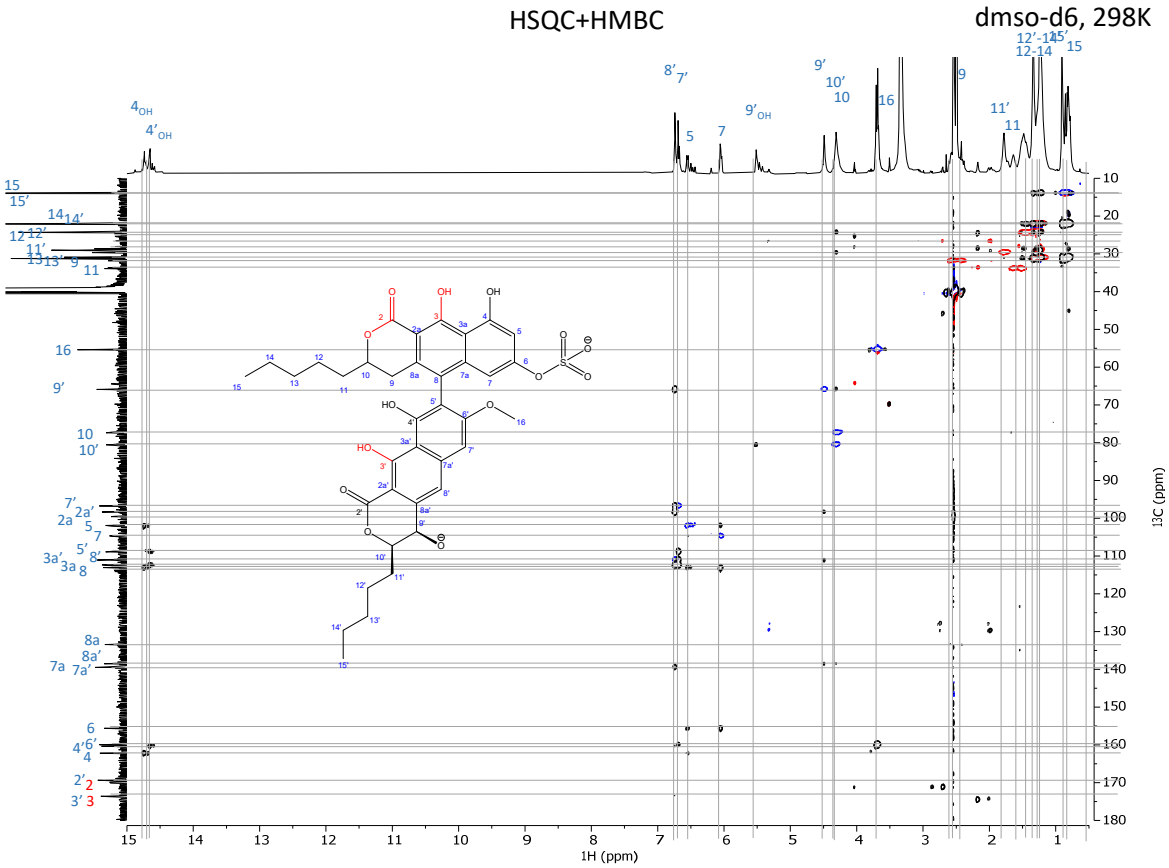

Supplementary Figure 14: Superimposed HSQC (red/blue) and HMBC (black) of **1** in DMSO-d_6.

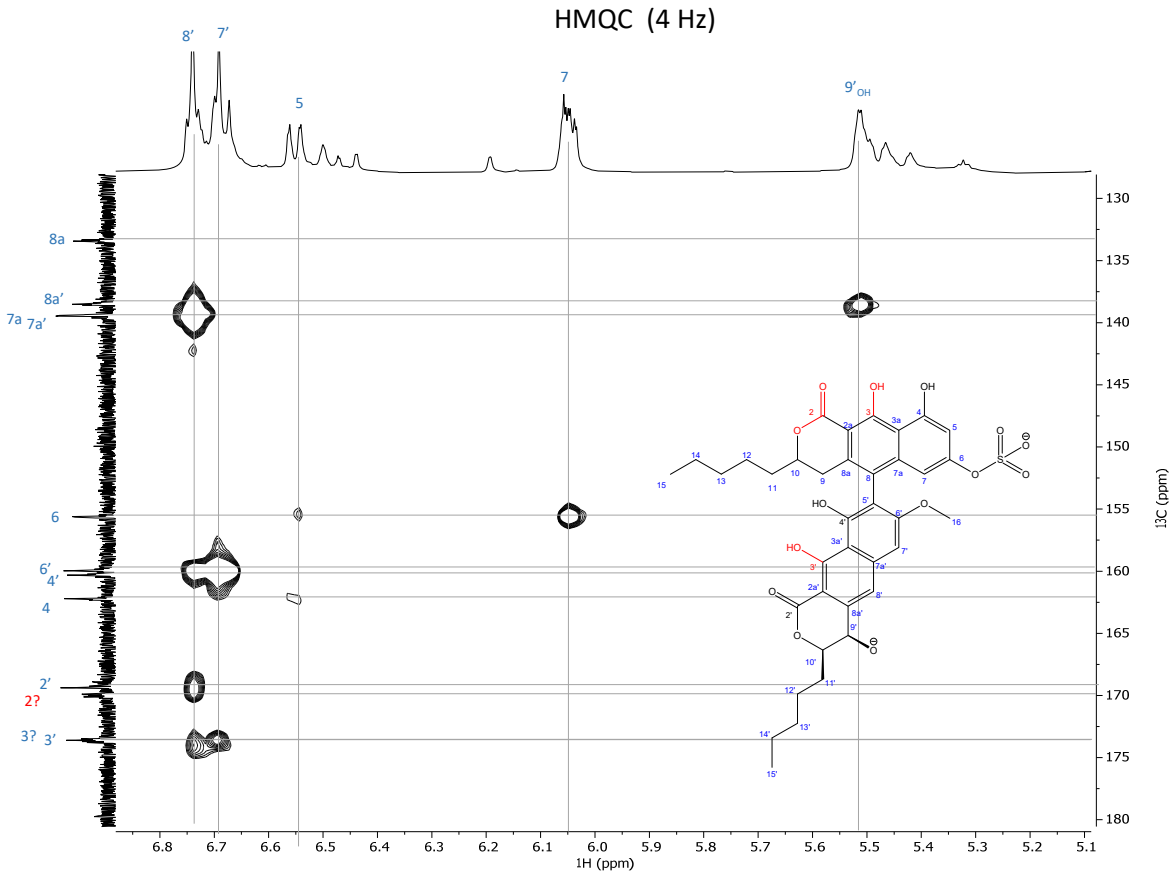

Supplementary Figure 15:HMQC optimized for 4 Hz $^{n}J_{CH}$ displays some of the important $^{4}J_{CH}$ for assignment.

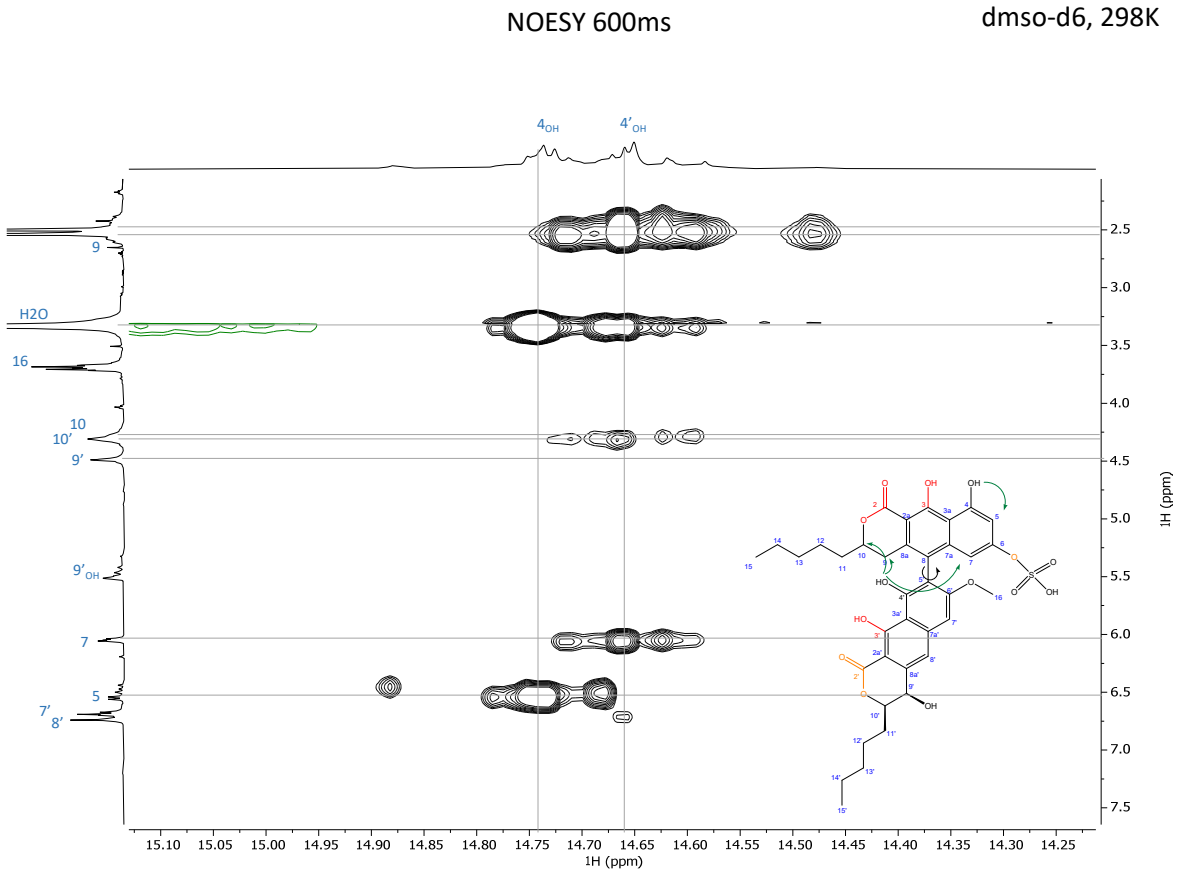

Supplementary Figure 16: NOESY (600 ms mixing time) of **1**. OH-4' displays NOE correlations with both H7 and H9, showing that the two ring systems are either rotating quickly, exist in several conformations, or are offset relative to each other allowing one interaction on top of OH-4' and the other below OH-4'.

PAPER IV

MDPI

Article

Lulworthinone: *In vitro* mode of action investigation of an antibacterial dimeric naphthopyrone isolated from a marine fungus.

Eric Juskewitz [1,*], Ekaterina Mishchenko [1], Vishesh K. Dubey [1], Marte Jenssen [2], Martin Jakubec [3], Philip Rainsford [3], Johan M. Isaksson [3], Jeanette H. Andersen [2] and Johanna U. Ericson [1,*]

[1] Research Group for Host Microbe Interactions, Department of Medical Biology, Faculty of Health Sciences, UiT the Arctic University of Norway, 9019 Tromsø, Norway
[2] Marbio, The Norwegian College of Fishery Science, Faculty of Biosciences, Fisheries and Economics, UiT the Arctic University of Norway, 9019 Tromsø , Norway
[3] Department of Chemistry, Faculty of Science and Technology, UiT the Arctic University of Norway, 9019 Tromsø, Norway
* Correspondence: eric.juskewitz@uit.no; johanna.e.sollid@uit.no

Abstract: Treatment options for infections caused by antimicrobial-resistant bacteria are rendered ineffective, and drug alternatives are needed - either from new chemical classes or drugs with new modes of action. Historically, natural products have been important contributors to drug discovery. In a recent study, the dimeric naphthopyrone lulworthinone produced by an obligate marine fungus in the family *Lulworthiaceae* was discovered. The observed potent antibacterial activity against gram-positive bacteria, including several clinical methicillin-resistant *Staphylococcus aureus* (MRSA) isolates, prompted this follow-up mode of action investigation. This paper aimed to characterize the antibacterial mode of action (MOA) of lulworthinone by combining *in vitro* assays, NMR experiments and microscopy. The results point to a MOA targeting the bacterial membrane, leading to improper cell division. Treatment with lulworthinone induced an upregulation of genes responding to cell envelope stress in *Bacillus subtilis*. Analysis of the membrane integrity and membrane potential indicated that lulworthinone targets the bacterial membrane without destroying it. This was supported by NMR experiments using artificial lipid bilayers. Fluorescence microscopy revealed that lulworthinone affects cell morphology and impedes the localization of the cell division protein FtsZ. Surface plasmon resonance and dynamic light scattering assays showed that this activity is linked with the compound's ability to form colloidal aggregates. Antibacterial agents acting at cell membranes are of special interest as the development of bacterial resistance to such compounds is deemed more difficult to occur.

Keywords: marine natural product; antimicrobial agents; mode of action; *B. subtilis*; MRSA; FtsZ ; colloidal aggregate

Citation: Lastname, F.; Lastname, F.; Lastname, F. Title. *Journal Not Specified* **2022**, *1*, 0. https://doi.org/

Received:
Accepted:
Published:

1. Introduction

Antimicrobial resistant bacterial pathogens have emerged as a serious threat to public health and there is an urgent need for new antibiotics. In 2019, infections caused by antimicrobial resistant (AMR) bacteria were the third leading cause of death [1]. Patients infected by *Staphylococcus aureus* were 64 % more likely to die if the strain was methicillin-resistant than if it was susceptible. As a result, methicillin-resistant *S. aureus* (MRSA) alone killed over 100.000 patients globally in 2019 [1]. Thus, the World Health Organisation (WHO) has declared MRSA as one of their priority pathogens to develop treatments against. Since AMR mechanisms are known to evolve and protect against related drug iterations, there is an urgent need for compounds with either a new mode of action (MOA) or from new chemical classes. Currently, 32 antibiotics targeting the WHO priority pathogens

are under development. But only six of them fulfil innovative criteria (absence of cross-resistance, new chemical class, new target or new mode of action). [2,3]. The last truly new antibiotic class discovered were acid lipopeptides in 1987 [4].

Still, unexplored parts of nature can provide new molecules with novel antibacterial properties. Bioprospecting has the potential to supply the drug development pipeline with new compounds. Through history, natural products have contributed the most to the development of drugs in clinical use [5]. Either they contain the antibacterial activity themselves (e.g., aminoglycosides, β-lactams, macrolides, tetracyclines) [6] or their molecule scaffolds have been adapted for drug development [7]. The focus on marine bioprospecting has increased in the last decades. Due to the dilution processes occurring in seawater, the antimicrobial compounds produced by marine organisms should be highly potent in order to be effective against their targets.

The strictly marine clades of fungi are less explored in natural product discovery [8,9]. Lulworthinone was the first bioactive compound to be published from the strictly marine fungal family *Lulworthiaceae* [10]. The compound was shown to have potent activity against several clinical MRSA isolates and displayed antiproliferate activity against three human cell lines (melanoma, hepatocellular carcinoma and non-malignant lung fibroblasts) at higher concentrations. During purification, acid-induced degradation was observed, forming a structural isomer [10]. This structural isomer was identical to lulworthinone, differing only in the position of the sulphate group (Figure 1). Lulworthinone appeared to form aggregates in DMSO and methanol, which was not observed for its isomer. The compound fits structurally in the class of naphthopyrones, which have been previously isolated from different sources, including filamentous fungi. Antibacterial activity against gram-positive bacteria has been reported for several naphthopyrones [11–14]. The well-studied naphthopyrone viriditoxin has minimal inhibitory concentrations (MICs) in the range of 4 - 8 µg/mL against different *Staphylococcus* isolates, by inhibiting cell division through blocking of FtsZ polymerization [15]. Another antibacterial fungal naphthopyrone, cephalochromin, inhibits the bacterial enoyl-acyl carrier protein reductase FabI, involved in fatty acid synthesis [12].

Target identification and mode of action studies are essential steps in natural product drug discovery and development, to facilitate further optimization by medicinal chemistry efforts. In this paper, the MOA of the published antibacterial natural product lulworthinone and its acidified form was investigated. The MOA was characterized using biosynthetic pathway markers, quantifying membrane permeability with water/ion NMR detected - phospholipid vesicle permeability assay (WIND-PVPA), *in vitro* membrane integrity assays and membrane potential assays, time-kill curves, pharmacodynamic calculations, surface plasmon resonance (SPR), fluorescence microscopy and quantitative phase microscopy. The combined results suggest that lulworthinone is a membrane active antibacterial compound - effective against MRSA, meanwhile its acidified form loses this ability.

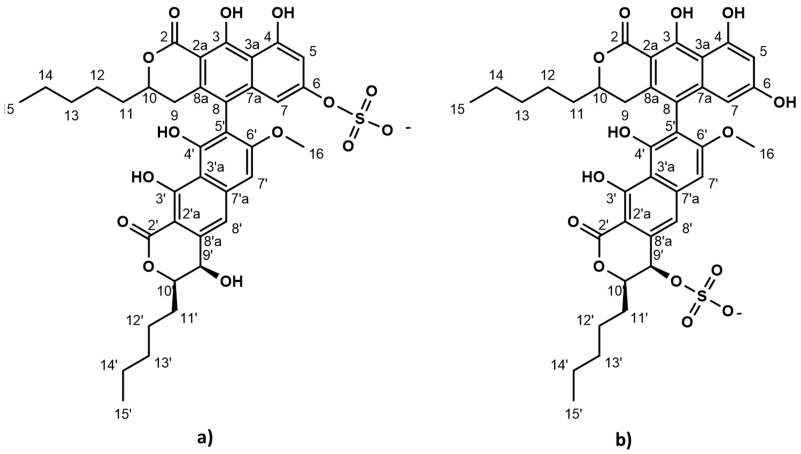

Figure 1. Chemical structure of lulworthinone (**a**) and acidified lulworthinone (**b**); under acidic conditions the sulphate group migrates from C6 to C9'.

2. Results

2.1. Lulworthinone induces transcription from promoters known to respond to cell envelope stress

Induction of gene expression from selected cellular pathways (i.e., DNA replication, transcription, translation, fatty acid, folic acid, cell wall and membrane) was assayed after addition of increasing concentrations of lulworthinone. Strains of *B. subtilis* 168 containing reporter-gene constructs of relevant promoters fused to the luciferase-gene are listed in Table 1. The relative luminescence activity was measured for concentrations ranging from 0 - 8 x MIC for either reference antibiotics or lulworthinone (Table 1 and 5) (Figure 2). *B. subtilis* 168 EM13, harboring the *ypuA* promoter-fusion (responding to cell wall biosynthesis inhibiton or general cell envelope stress) and *B. subtilis* 168 HMB67, carrying the *liaI* promoter-fusion (responding to general cell envelope stress) produced an increasing amount of luminescence in response to lulworthinone between 0.5 - 2 x MIC (Figure 2 a and c). At 4 x and 8 x MIC the luminescence was almost completely abolished, which indicates cell death. The control antibiotic, Bacitracin induced luciferase production at 0.125 - 2 x MIC from the *yupA* promoter and from the *liaI* promoter at all concentrations tested. This suggests that lulworthinone generates a general stress response in bacteria and is likely targeting the cell envelope.

Table 1. Bacterial strains sensing stress on key molecular pathways.

Bacteria	Strain number	Target pathway	Promotor	Control antibiotic	MIC in µg/ml
Bacillus subtilis 168	EM10	DNA replication	*yorB*	Ciprofloxacin	0.031
B. subtilis 168	EM11	Transcription	*belD*	Rifampicin	0.5
B. subtilis 168	EM12	Translation	*yheI*	Erythromycin	0.125
B. subtilis 168	EM13	Cell wall and membrane	*yupA*	Bacitracin	16
B. subtilis 168	HMB62	Viability control	*laiG*	all antibiotics	*
B. subtilis 168	HMB67	Cell wall and membrane	*liaI*	Bacitracin	16
B. subtilis 168	HMB69	Fatty acid synthesis	*fabJB*	Triclosan	4
B. subtilis 168	HMB70	Folic acid synthesis	*panB*	Tromethoprim	1

Abbreviations : MIC - minimal inhibitory concentration; * MICs are equivalent to the other strains

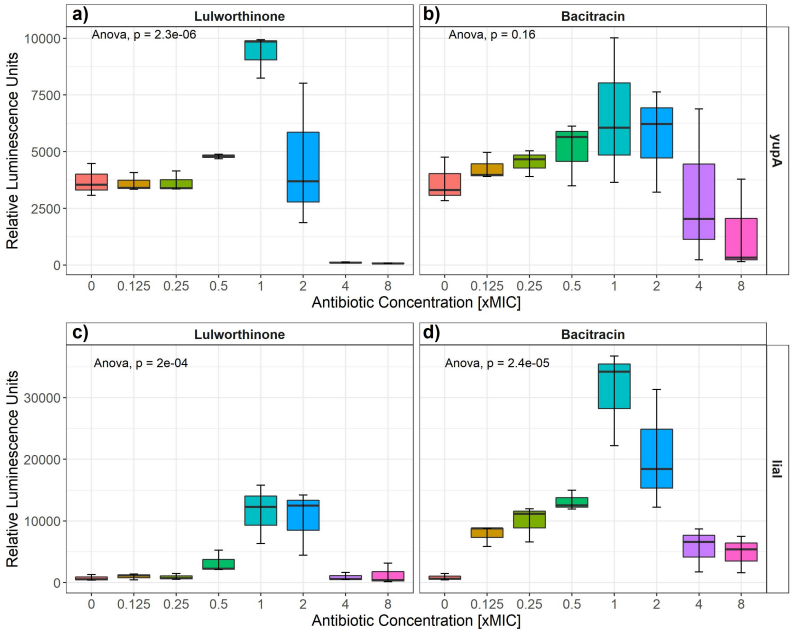

Figure 2. Luminescence units induced by either lulworthinone (**a** and **c**) or bacitracin (**b** and **d**) per tested concentration from 0 - 8 x MIC for *yupA* (**a** and **b**) and *liaI* (**c** and **d**) promoter fusions. Statistics performed by two-sided Anova, comparing data of each drug concentrations and biological replicates (n=3).

2.2. Lulworthinone alters membrane permeability without influencing membrane integrity

2.2.1. Lulworthinone interacts with membrane lipids

SPR was used to determine the affinity of lulworthinone and its isomer towards an inert lipid bilayer composed of 1,2-dimyristoyl-sn-glycero-phosphocholine (DMPC) vesicles and its subsequent rate of dissociation (Table 2). A high partitioning of lulworthinone into lipid layers was observed with a K_P reaching up to $44.81 \pm 2.47 * 10^3$ with a dissociation rate of $4.2 \pm 0.5 * 10^{-2}$ s^{-1}. Such values are typically encountered by very good lipid interactors (like AMC-109 [16], see Table 2). However, there was no observable decrease in the signal (RU) after lulworthinone dissociation from bilayer. This suggests that the lipid layer stayed intact, and that lulworthinone was able to self-aggregate on top of lipid bilayer without disturbing it. In addition, there was no observable binding of lulworthinone to lipid layer in concentrations < 30 µM (3 x MIC) (Figure S 12). Only in higher concentrations of lulworthinone a measurable increase in resonance units was observed. Thus, measured K_p for lulworthinone seems to represent both partitioning into lipid layer and self-aggregation on top of the membrane. On the other hand, acidified lulworthinone partitioning into lipid layer is much smaller with K_p – 0.76 ± 0.04 and with much faster dissociation rate k_{off} – 5.185 ± 1.594 s^{-1}. This suggest that the isomer lost its ability to bind to the lipid layer.

Table 2. Lulworthinone and acidified lulworthinone affinity towards and subsequent dissociation rate from an inert lipid bilayer. Positive and negative [17] controls are included.

Treatment	$K_p * 10^3$	$k_{off} s^{-1}$
Lulworthinone	44.81 ± 2.47	0.042 ± 0.005
acid. Lulworthinone	0.76 ± 0.04	5.185 ± 1.594
pos. control - AMC 109	14.97 ± 0.99	0.174 ± 0.007
neg. control - LWwNKr	0.40 ± 0.02	1.746 ± 0.162

K_p - partitioning constant, K_{off} - dissociation rate

2.2.2. Lipid bilayer permeability is not affected by lulworthinone

The ability of lulworthinone and its isomer to disrupt lipid bilayer was explored using WIND-PVPA to determine the P_{app} of water and Mg^{2+} and Ca^{2+} ions across packed lipid vesicles [18]. The PVPA barriers were exposed to 100 µM of lulworthinone, acidified lulworthinone, and Triton X-100, the latter as positive control. Figure 3 shows that neither water (Figure 3 a) nor ion (Figure 3 b) permeability was affected by lulworthinone. The P_{app} of Mg^{2+} in the presence of lulworthinone and the isomer were slightly lower relative to the blank (Blank: 0.42 x 10^{-6} cm/s; lulworthinone: 0.37 x 10^{-6} cm/s; acidified lulworthinone: 0.37 x 10^{-6} cm/s) but these differences were not statistical relevant (t-test, $p > 0.05$). In comparison, the detergent, Triton X-100 higher permeability was observed for both water and ions (water: 69 x 10^{-6} cm/s; Ca^{2+}: 0.41 x 10^{-6} cm/s; Mg^{2+}: 0.49 x 10^{-6} cm/s). Thus, concentrations of 100 µM lulworthinone or acidified lulworthinone did not disrupt the lipid layer of membranes.

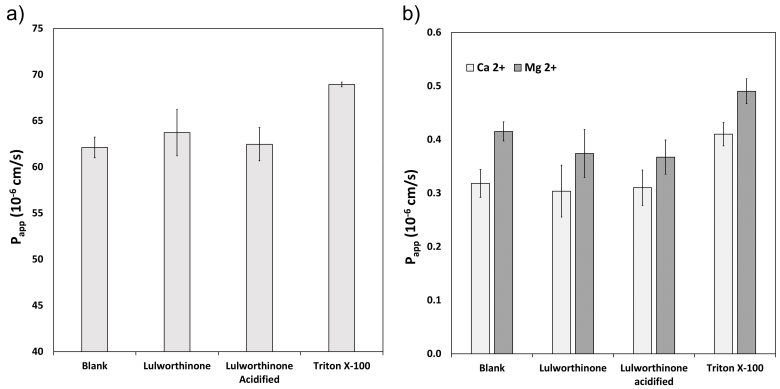

Figure 3. Permeability P_{app} of water (**a**) and Ca^{2+} and Mg^{2+} (**b**) measured under the influence of lulworthinone, acidified lulworthinone, and Triton X-100.

2.2.3. Lulworthinone increases the permeability of biological membranes while membrane intergity is not affected

The effect of lulworthinone on membrane integrity was investigated on bacterial cells, *B. subtilis* 168, carrying the pCSS962 plasmid from which luciferase is constitutively expressed. From this strain, bioluminescence is emitted once the bacterial cell membrane is affected and D-luciferin from the growth medium is allowed to enter the cell. A change in membrane permeability is detected by a rise in luminescence due to substrate influx. A strong drop of luminescence is detected either after cell death or complete membrane disruption due to a fast consumption of cellular ATP needed for the enzymatic process. Bioluminescence was recorded in the presence of 0.5 - 4 x MIC of lulworthinone or ciprofloxacin (CIP, negative control).

After 270 seconds cells that survived the first treatment were lysed by injecting a membranolytic dosage of chlorhexidine (CHX, positive control). The relative luminescence was recorded for 300 seconds, including the CHX injection at 270 seconds (Figure 4). Each concentration of lulworthinone increased the luminescence production in comparison to the basal water values (Figure 4 a). The decrease of luminescence at 4 x MIC after 30 seconds suggests ATP depletion or cell death, as to the fast drop after CHX injection.

In contrast, CIP did not influence the membrane integrity and the luminescence stayed at basal values of the water control until CHX injection (Figure 4 b). This implies that the membrane permeability is increasingly affected by rising lulworthinone concentrations and seemingly destroying the membrane at 4 x MIC.

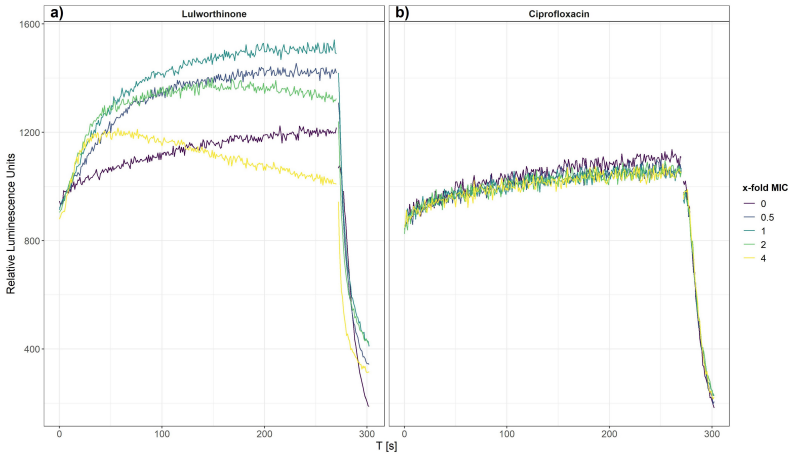

Figure 4. Membrane integrity of *B. subtilis* 168, carrying the pCSS962 plasmid, monitored as relative luminescence units, in the presence of different concentrations of lulworthinone (**a**) or ciprofloxacin (**b**). In both experiments membranolytic chlorhexidine was injected at 270 s. Data presented are the means of 3 biological replicates.

2.3. Lulworthinone affects the membrane potential

Changes in the membrane potential after exposure to concentrations of 0.25 - 4 x MIC of lulworthinone was measured by $DiOC_2(3)$ membrane depolarisation assay. *S. aureus* ATCC 29213 cells were stained with the membrane potential sensitive dye 3,3-diethyloxacarbocyanine iodide ($DiOC_2(3)$) and analysed by flow cytometry. The dye fluorescence shifts from green to red by self-aggregation if the membrane potential is maintained [19]. A decrease in the ratio of red by green signals indicates a change in membrane potential. Water (positive control) and carbonylcyanide 3-chlorophenylhydrazone (CCCP, negative control) were included in each assay. At 0.25 x MIC the membrane potential decreased by a half, whereas concentration from 0.5 - 4 x MIC depleted the potential close to levels of the potential inhibitor CCCP (Figure 5); an overview of all measured samples is provided in supplementary Figure S 13). This suggests that lulworthinone has a strong influence on the membrane potential.

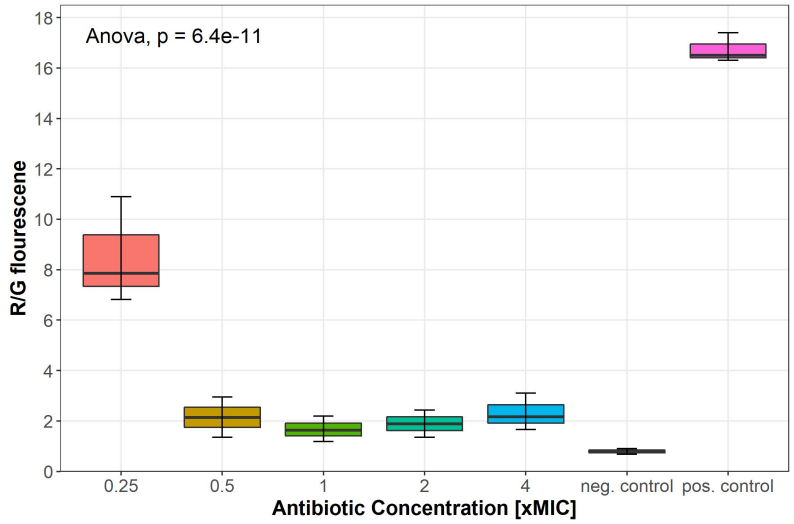

Figure 5. Membrane potential after exposure to increasing concentrations of lulworthinone measured by 3,3-diethyloxa- carbocyanine iodide ($DiOC_2(3)$) membrane depolarisation assay. Water (pos. control) and carbonylcyanide 3-chlorophenylhydrazone (CCCP, neg. control) were included in each assay. Statistics performed by two-sided Anova, comparing data of each drug concentrations and biological replicates (n=3).

2.4. Lulworthinone influences cell morphology and localization of the cell division protein FtsZ

Bacterial cell morphology in the presence of either lulworthinone or the membrane acting antibiotic daptomycin (DAP) was analysed using fluorescence microscopy. Cells were stained with membrane dye FM4-64 and DNA dye DAPI. A concentration of 1 x MIC lulworthinone affected the morphology as shown in Figure 6. When comparing the lulworthinone treated cells (Figure 6 e) to the control (Figure 6 a) an increased number of bacterial filaments was observed, indicating an effect on the division process. Also, the altered FM4-64 distribution shown as patches of strong signal and regions of nearly no staining at all (as seen in Figure 6 g) points to membrane perturbations. Changes in cell size after lulworthinone treatment was further analysed by Quantitative Phase Microscopy (QPM). Figure 7 shows an example of a quantitative phase map (a), and the measured cell length (c), width (d) and volume (e). Data based on a total of 6700 cells from each sample, untreated or treated with 1 x MIC lulworthinone (Figure 7 c-e) showed that the average cell length was extended from 4.974 to 6.763 µm while the average width was increased from 1.898 to 2.048 µm. Accordingly, the mean volume increased from 4.788 μm^3 to 6.649 μm^3. Cell localisation of the cell division protein FtsZ is known to be influenced by membrane potential [20]. Thus, a reporter strain *B. subtilis* 2020 (expressing FtsZ::GFP fusion protein) was used to study the influence of lulworthinone on the membrane structure. Normally FtsZ forms the Z-ring that defines the next septum formation and cell division site in the bacteria. The fluorescence micrographs (Figure 8) shows FtsZ localisation without treatment (a-b), in the presence of lulworthinone (c-d) and with the positive control DAP (e-f). In the control (a-b), FtsZ was localized in the middle of bacteria, forming the Z-ring preceding cell division. Treatment with lulworthinone led to the elongated cells or filaments and appearance of multiple Z-rings or FtsZ patches along the cells (c-d). daptomycin treatment (e-f) had a severe effect on FtsZ localisation and resulted in some bacteria with additional "spots" and "rings" of FtsZ. Few elongated cells and very few chains were observed. This suggests that lulworthinone has an influence on cell division supposedly via its effect on membrane structure.

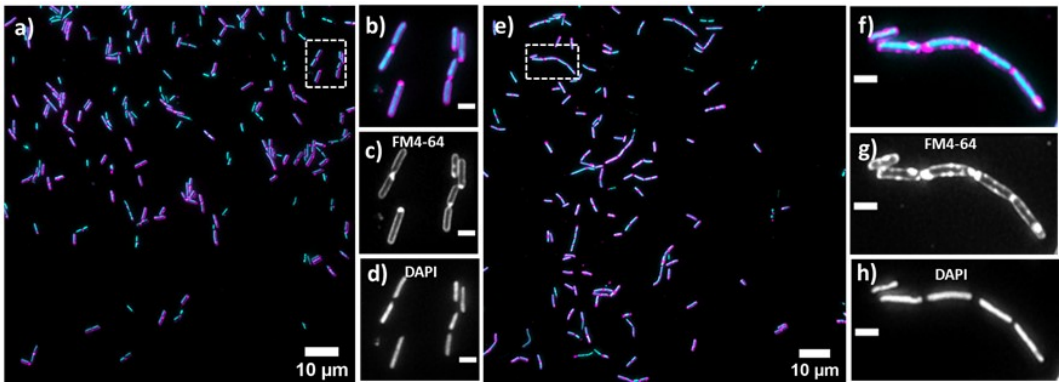

Figure 6. Cell morphology of *Bacillus subtilis* 168, membrane staining (FM4-64; magenta; **c & d**) and DNA staining (DAPI; blue; **d & h**) without treatment **a-d**) or in the presence of 1 x MIC lulworthinone **e-h**; 60 x magnification in **b-d**) and **f-h**), respectively).

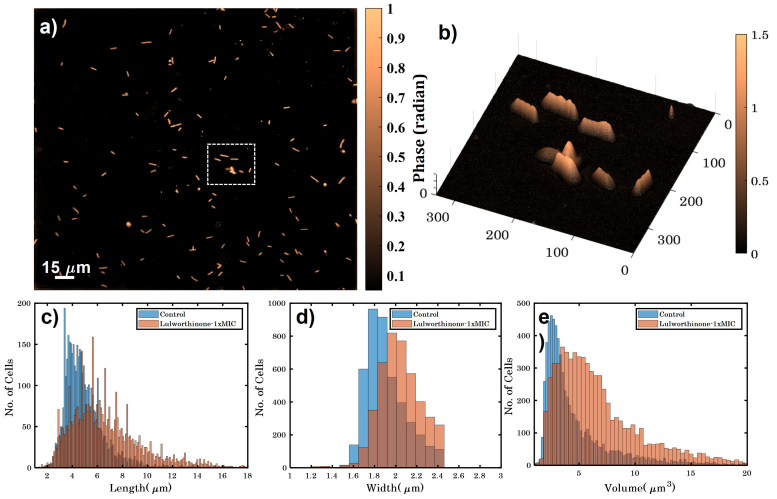

Figure 7. a) Quantitative phase map of *B. subtilis* 168 cells (scale bar is 15 µm and colorbar is in radian). **b**) 3D phase map of the zoomed area enclosed by white dotted box shown in (**a**). **c-e**) show the variation in height, width and volume for untreated and bacteria treated with 1 x MIC lulworthinone.

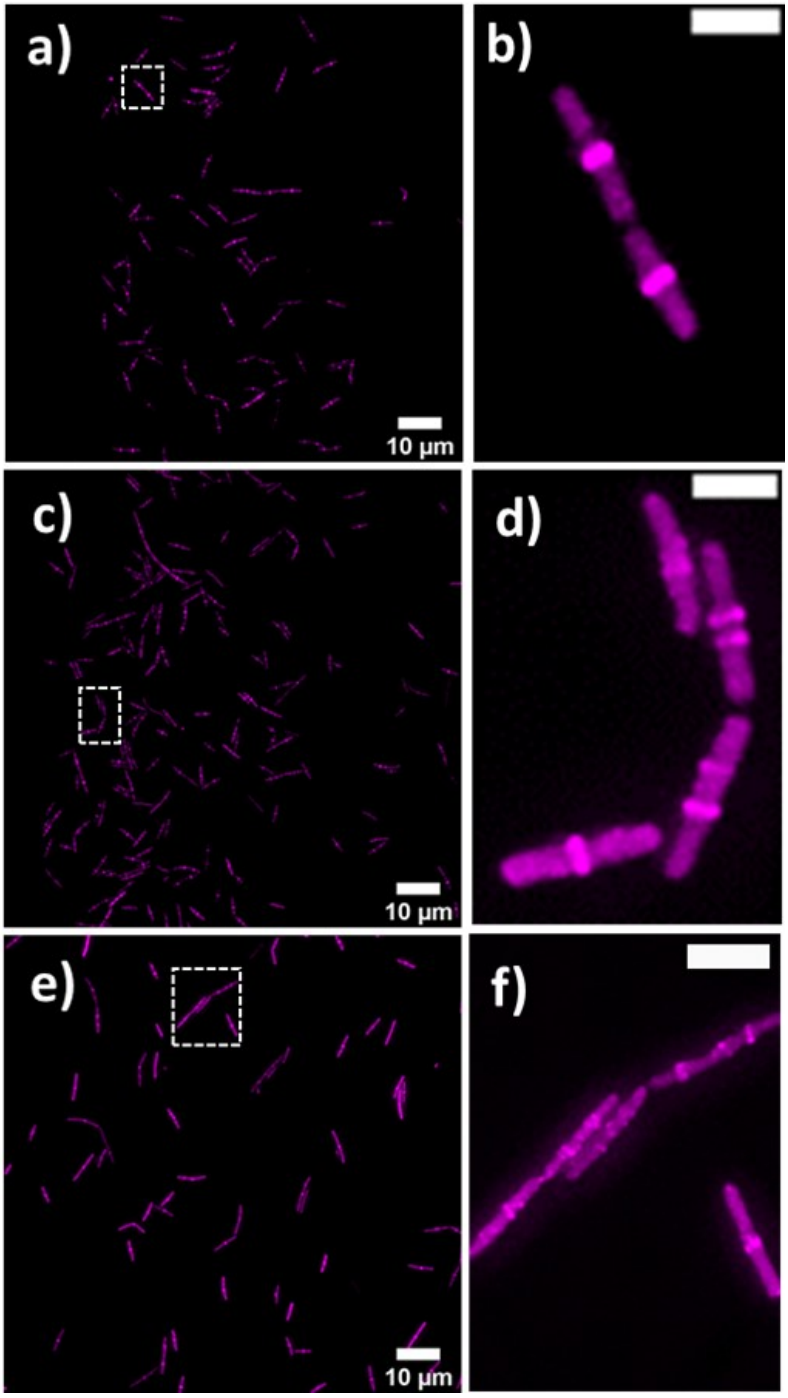

Figure 8. FtsZ localisation in *B. subtilis* 2020 with GFP labeled FtsZ **a**) without treatment **b**) 1 x MIC lulworthinone or **c**) 1 x MIC daptomycin, 60 x magnification in **b**), **d**), **f**), respectivly.

2.5. Lulworthinone has a strong bactericidal effect on B. subtilis

2.5.1. Time-kill curves reveal a fast bacterial killing

The kill kinetics of lulworthinone was determined by measuring bacterial survival over time at multiple concentrations ranging from 64 to 0 µg/mL (4 - 0 x MIC) (Figure 9). Using *B. subtilis* 168, it is shown that lulworthinone (Figure 9 a) was bactericidal at concentrations $\geq$ 1 x MIC. Higher concentrations (2 - 4 x MIC) led to rapid killing and cell counts fell below the detection limit (50 CFU/ml) and at 4 x MIC this was observed within 30 minutes. Sub-MIC concentrations induced a lag-phase of 30 and 120 minutes at 0.25 and 0.5 x MIC, respectively before growth was restored to rates comparable to the control. This suggest

that some kind of adaption is required before growth continues. Time-kill curves for CHX were prepared in parallel (Figure 9 b). Like lulworthinone, CHX was bactericidal above MIC and at highest concentration (4 x MIC) cell counts dropped below detection limit. These data suggest that lulworthinone has a strong and fast bactericidal mode of action.

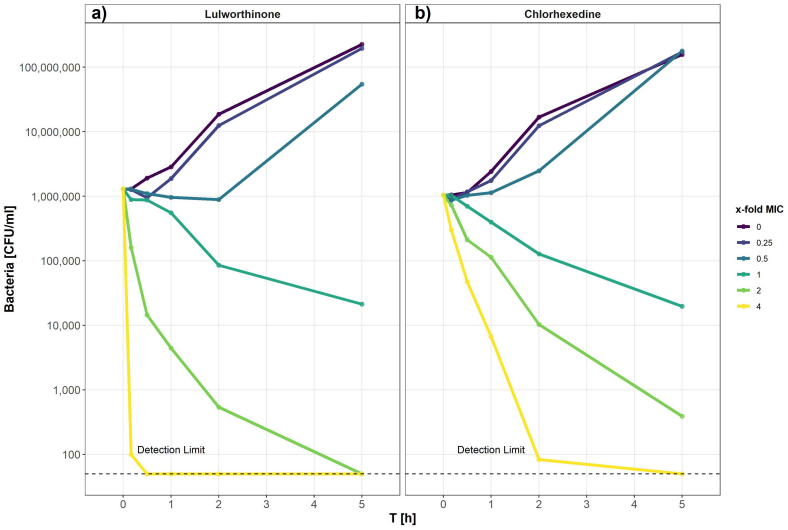

Figure 9. Time-kill curve of *B. subtilis* 168 of lulworthinone (**a**) and chlorhexidine (**b**).

2.5.2. Pharmacodynamic calculations reveal an unusual dose-response curve

Using the data from the time-kill curves the pharmacodynamic parameters of lulworthinone were calculated using the *pharmacodynamic function* according to Regoes *et al.* (2004) [21]. The bacterial growth rates (ψ) were estimated by calculating linear regressions to logarithm of the colony count for each concentration respectively.
The pharmacodynamic function was then fitted to the estimated ψ per concentration (Figure 10). The maximal growth rate ψ max, at 0 x MIC, was 0.6492 h^{-1}. Compound lulworthinone induced a strong bactericidal effect with a minimal growth rate, at 4 x MIC, of ψ min -7.88 h^{-1}. This led to a steep hill coefficent (κ) of 3.72. The estimated zMIC of 9.59 µg/mL agreed with the experimentally aquired MIC of 8 µg/mL. It was not possible to generate the typical sigmoidal "S"-shape for the drug response curve. This suggests that lulworthinone forms colloidal aggregates [22].

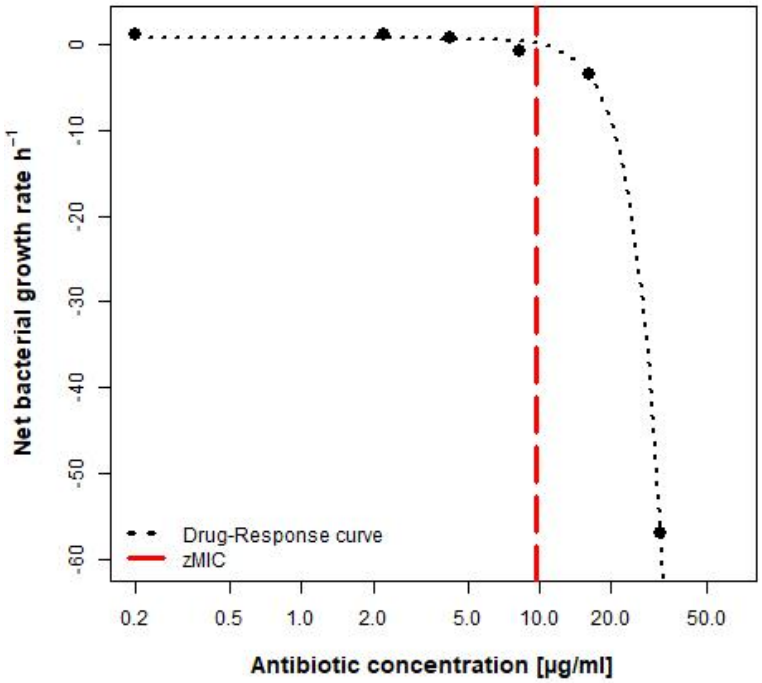

Figure 10. Pharmacodynamic model of lulworthinone against *B. subtilis* 168 with predicted MIC (zMIC).

2.6. Lulworthinone is a self-aggregating molecule

2.6.1. Confirmation of aggregation

To monitor the aggregation of lulworthinone and its isomer the molecules were assayed using dynamic light scattering (DLS). DLS is a common technique to determine particle sizes in solute by using coherent and monochromatic source of light – laser beam. Brownian motion of particles causes time-dependent fluctuation of local concentration which correspond to fluctuations of intensity of scattering light. These fluctuations of intensity can be transformed into auto correlation function from which hydrodynamic radius can be determined using Stokes-Einstein equation (1).

$$R\_h = kT/6\pi\eta D \quad (1)$$

Where R_h is hydrodynamic radius, k is the Boltzmann's constant, T is absolute temperature, η is shear viscosity of solvent and D is the translational diffusion coefficient. It has been previously shown that DLS can be used to estimate critical micellar concentrations [23]. We have used changes in intensity counts of particles > 10 nm in diameter to estimate critical colloidal concentration, as shown in Table 3. Compound lulworthinone showed variety of aggregates at two major diameter range of 192.7 $\pm$ 70.80 and 1319 $\pm$ 611.7 nm (Figure 11). To investigate if lulworthinone is a self-aggregating colloidal aggregate we included a non-ionic detergent (Tween 80) as proposed by Ganesh *et al.* (2018) [24] to reverse this kind of interaction. In the presence of detergent the aggregates vanished and we could detect only the typical Tween 80 micelles at 10 nm as shown in Figure 11 b. This suggests that lulworthinone forms colloidal aggregates.

Table 3. Aggregate sizes determined by DLS.

Treatment	Environment	critical aggregation concentration (CAC)	Prevalent size of aggregates at CAC
Lulworthinone	37 °C	53.71 µM	117.4 ± 25.9 d.nm
Lulworthinone with 0.025 % Tween 80	37 °C	no aggregation	no aggregation

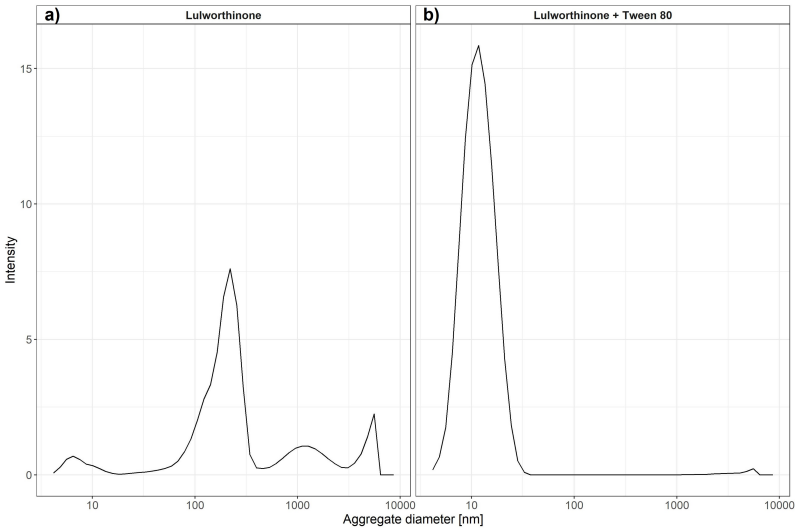

Figure 11. Average aggregate sizes of lulworthinone in concentration range 0.625 µM – 320 µM in MiliQ water with 1 % DMSO and without (**a**) or with 0.025 % Tween 80 (**b**); measured by dynamic light scattering.

2.6.2. The antibacterial activity is dependent on aggregation

To determine if the antibacterial activity of lulworthinone is altered by the presence of detergent (indicating that the compound is a colloidal aggregator), Tween 80 was included in our MIC assays as proposed by Ganesh *et al.* (2018) [24].
Addition of detergent resulted in a strong attenuation of the antibacterial activity from 6.15 µg/mL to >128 µg/mL against *S. aureus* ATCC 25923 (Table 4). This indicates that lulworthinone antibacterial activity is based on aggregation, as the compound also lost its antimicrobial activity after acidification.

Table 4. Antibacterial activity of lulworthinone.

Bacterial strain	Treatment	MIC
Staphylococcus aureus ATCC 25923	Lulworthinone	6.15 µg/mL
S. aureus ATCC 25923	Lulworthinone + Tween 80	>128 µg/mL
S. aureus ATCC 25923	acidified Lulworthinone	>128 µg/mL

3. Discussion

Antibiotic resistance is making the treatment of bacterial infections difficult, and new drugs with new modes of action are needed to tackle this increasing problem. The cell membrane is a promising target for new antibiotics, as resistance is coupled to a high fitness cost for the bacterium [25]. Identifying the bacterial target and establishing the mode of action are essential steps in natural product drug discovery. This information is essential to identify promising hit compounds that can be further altered by medicinal chemistry on the road to becoming marketed drugs.

In the current study, an antibacterial compound, lulworthinone, isolated from an obligate marine fungus was studied for its MOA. The compound's MOA includes the following key elements: (1) stress or influence on the bacterial envelope, (2) membrane permeabilization and membrane potential dissipation without destroying the membrane integrity, (3) changes in cell morphology, including increased length and width, lead to extended cells or filament formation, (4) FtsZ, a key protein for cell division, is delocalized within the bacterial cells, (5) the antibacterial activity is based on aggregation.

As several naphthopyrones have antibacterial activity against *S. aureus* and other gram-positive bacteria [11–14], it was not surprising to find that also lulworthinone has similar activity. This indicated that the naphthopyrone backbone might be a so-called privileged structure [26,27], with the ability to interact with a bacterial target common for some gram-positive bacteria. The lack of activity against gram-negative species might also be caused by the outer membrane barrier. Lulworthinone generates a general stress response in bacteria by targeting the cell envelope. The cell envelope is rather conserved among many bacterial species and the potential for resistance development towards membrane active compounds is low as they are known to have multiple MOA targets. Taken together, this makes the cell envelope an interesting target for new antibacterial drugs (e.g., lipepopeptides (daptomycin [28]), lipoglycopeptides (teicoplanin [29]) and cyclopeptides (polymyxin B [30]). Most membrane-active molecules interact with lipophilic targets in the membrane (disrupting the lipid composition or the functional architecture), change the conformation or localisation of membrane embedded proteins, or cause alteration in the proton motif force (PMF) [25].

However, lulworthinone does not seems to alter structural integrity of membrane bilayers or change the permeability of the lipid barrier. SPR indicated that lulworthinone has a high affinity towards lipids but it also showed that there is no observable retention of lulworthinone in the lipid bilayer – as the lipid bilayer was completely recovered after experiment. This was not expected as good lipid associators either intercalate into the lipid bilayer and increase the overall measured signal or disrupt the layer and release vesicles and lipid matter from the surface of the chip [31]. In addition, there was no observable association of lulworthinone with DMPC vesicles at concentrations < 30 µM. Indeed, SPR results suggested that rather than disrupting lipid layer, lulworthinone can use it as a scaffold for aggregation. This fact was further confirmed by permeability results from WIND-PVPA [18]. Neither lulworthinone nor its acidified form showed any changes in water or ion transmission in artificial lipid barriers. In contrast, an increase in permeability was detectable in bacterial membranes, albeit without the loss of envelope integrity marked by cell death (as sharp drop in fluorescence was observed only at highest MIC concentration). Combination of these results suggest that even though lulworthinone is able to bind to lipid bilayer, it does not disrupt artificial models, but it is still able to increase permeability in live cells. Either disruption effect of lulworthinone is very mild and below detection limits used in aritifical models or lulworthinone needs other membrane components present in live cells to be active.

Additionally, the dissipation of the membrane potential was detected. This can be an indication, that lulworthinone interacts with surface proteins (e.g. transporters or ion channels) and inactivates them. Strahl and Hamoen (2010) [20] have shown that the membrane potential is a crucial factor for the localisation for proteins forming the cytoskeleton. Over 20 proteins involved in cell morphology, division and cell division regulation are delocalised shortly after the membrane potential is dissipated. Indeed, compound lulworthinone changed cell morphology and led to cell widening and elongation, filaments and membrane perturbation (Figure 6 and 7). Signs of incomplete cell division or separation were observed.

The changes on cell morphology were accompanied by delocalisation of FtsZ (Figure 8), a key protein for cell division as it forms the Z-ring, a molecular structure that divides cells after DNA multiplication. FtsZ was found to be delocalised into patches all over the cell or multiple Z-rings at unusual sites in the cell. As a key element for cell division, FtsZ is a focus

target for antibacterial treatments [32–36]. As an explanation for the delocalisation, Strahl and Hamoen (2010) showed that the FtsZ guiding proteins FtsA and MinD are inactivated after loss of the membrane potential. Both have a C-terminal alpha helix structure used for membrane binding. Thus, membrane potential depletion might prevent the FtsZ guiding proteins from binding and correctly directing Z-ring formation. Without a functional Z-ring formation cell division is affected and filaments are formed. At sub-MIC concentrations of lulworthinone this effect could be compensated or overcome during the observed lag phase observed for 30 and 120 minutes at 0.25 and 0.5 x MIC, respectively in the time-kill curves. The current study indicates that the antibacterial activity of lulworthinone is based on self-aggregation. Compound aggregation was initially observed in the NMR experiments conducted during the structure elucidation of the compound [10]. Follow-up studies (SPR, DLS, Time-kill curves, pharmacodynamics) supported the notion of aggregation. MIC testing in the presence of detergent strongly suggested that the aggregation is necessary for antibacterial activity. The structural isomer, did not aggregate, and was also not active against *S. aureus* 29523 (Table 3). Thus, it was concluded that lulworthinone is a colloidal aggregate and the aggregation is necessary for its antibacterial activity. The role of aggregation in antimicrobial compounds is currently unexplored venue as most colloidal aggregators are viewed as undesirable new drug leads due to their non-specifc protein adsorbtion and inhibitions of enzymes [24,37]. To our knowledge this is the first time that aggregation is mentioned for compounds in the napthopyrone class. But to what extent lulworthinone is representative for the chemical class or an individual actor remains to be investigated.

4. Conclusions

In this study, we investigated the MOA of a dimeric naphthopyrone isolated in high yields from an obligate marine fungus. The naphthopyrone chemical class has previously been investigated for several types of bioactivities, among them antibacterial activity against gram-positive isolates. The results from this study shows that lulworthinone exerts its activity towards the bacterial membrane, without disrupting it. The membrane potential is influenced, and changes in FtsZ localization indicating an impaired cell division. Several experiments (NMR, SPR and DLS) indicate that the compound has the ability to form aggregates with itself, a property which is usually regarded as undesirable for new drug leads. To investigate if the aggregation affected the antibacterial activity, the compounds MIC was tested in the presence of detergent. In the presence of detergent, all antibacterial activity was lost, indicating that the aggregation was necessary for the compound's bioactivity. The study provides extended information about the target and MOA of naphthopyrones towards gram-positive bacteria. The study also describes the effect of aggregation, and to the best of our knowledge, this is the first study in which compound aggregation has been published for naphthopyrones.

5. Materials and Methods

5.1. Bacterial strains and material

All bacterial strains used are listed in Table 5. Overnight cultures were grown in cationic-adjusted BD BBL™ Mueller Hinton II Broth (MHB II, 212322, Becton, Dickson and Company, MD, USA) if not indicated otherwise. Lulworthinone was isolated using FLASH cromatography [10].

Table 5. Bacterial strains.

Strain	Relevant characteristics	MIC in µg/ml Lulworthinone	acid. lulworthinone	CHX	CIP	DAP	References
Bacillus subtilis 168	-	8	-	0.5	-	-	ATCC 23857
B. subtilis 168	pCSS962	8	-	0.5	0.00195	-	[38]
B. subtilis 168 EM10	$P_{yorB}luxABCDE$	8	-	-	-	-	[39–41]
B. subtilis 168 EM11	$P_{belD}luxABCDE$	8	-	-	-	-	[39–41]
B. subtilis 168 EM12	$P_{yheI}luxABCDE$	8	-	-	-	-	[39–41]
B. subtilis 168 EM13	$P_{yupA}luxABCDE$	8	-	-	-	-	[39–41]
B. subtilis 168 HMB62	$P_{liaG}luxABCDE$	8	-	-	-	-	[39–41]
B. subtilis 168 HMB67	$P_{liaI}luxABCDE$	8	-	-	-	-	[39–41]
B. subtilis 168 HMB69	$P_{fabHB}luxABCDE$	8	-	-	-	-	[39–41]
B. subtilis 168 HMB70	$P_{panB}luxABCDE$	8	-	-	-	-	[39–41]
B. subtilis 2020	*amyE::spc Pxyl-gfp-ftsZ*	-	-	-	-	2	[20]
Echerichia coli Top10	*pBS3Clux*	-	-	-	-	-	[39,40]
Staphylococcus aureus 29213	-	6.25	-	-	-	-	ATCC 29213
S. aureus 25923	-	6.25	>128	-	-	-	ATCC 25923

[1] Abbreviations : MIC - minimal inhibitory concentration; CHX - chlorhexedine; CIP - ciprofloxacin; DAP - daptomycin.

5.2. Promoter-based biosensor assay

A biosensor assay was used to correlate the activity of lulworthinone with previously known MOAs. Interaction of lulworthinone with DNA replication, transcription, translation, cell envelope, fatty and folic acid synthesis was determined using *B. subtilis* 168 derivates containing *luc*-genes fused to the *yorB*, *belD*, *yheI*, *yupA*, *liaI*, *fabHB*, *panB* or *liaG* promoters (Table 1). The biosensor constructs were cloned using building blocks directly from, or PCR products adapted to the cloning enzymes used by the Bacillus BioBrick Box [40]. The plasmid pBS3Clux was used as a vector during cloning in *E.coli* Top10. The promoter regions used were either directly applied from the BioBrick Box as digestible plasmid constructs provided through the Bacillus Genetic Stock Center or adapted and amplified from Urban *et al.* (2007) [39] and patent US20020164602A1 by the respective primers. The promotor regions were digested with *EcoRI* and *PstI* and subsequently ligated into the vector cut with the same combination of restriction enzymes. *B. subtilis* 168 was finally transformed with the *ScaI* linearized plasmids under 5 µg/mL chloramphenicol selection and verified by colony PCR of the disrupted *sacA* locus. Fresh colonies from agar plates were transferred to 5 ml MH medium containing 5 µg/mL chloramphenicol and incubated at 37 °C. Over night cultures were diluted to an OD_{600} = 0.1 and grown to an OD_{600} = 0.2 before addition to the assay plates already containing the analytes. The analytes and control antibiotics were diluted in two-fold dilution series, with the highest concentration representing 8 x of the respective MIC. 5 µL of each dilution series and 45 µL bacterial suspensions were added to the wells of the 386 well plates (6007490, PerkinElmer, Ma, USA) and covered by breatheasy sealing membrane (Z380059, SIgma-Aldrich, Germany) to reduce evaporation. The plates were kept in the plate reader (EnVision$^{(R)}$, PerkinElmer, Ma, USA) at 35 °C. Peak luminescence of the controls was compared to luminescence of cells treated with lulworthinone. Luminescence and OD_{595} were recorded every 30 minutes for a total of ten hours. The experiment was conducted three times, data analysis and code can be found at the data repository [42].

5.3. Lipid interactions using Surface Plasmon Resonance

The SPR experiments were performed at room temperature using the T200 Biacore instrument (GE Healthcare, Il, USA) and L1 chip. Chip treatment, cleaning, regeneration and flowrate settings are the same as in Jakubec *et al.* (2021) [43]. Briefly, extruded DMPC liposomes (100 nm diameter, 1 mM in 10 mM HEPES buffer pH 7.4 with 150 mM NaCl) were immobilised on a clean surface using flowrate 2 µL/min for 2400 seconds. Successful immobilisation and stabilisation was tested by injection of 0.1 mg/ml of bovine serum

albumin (BSA, A7030, Sigma-Aldrich, MO, USA) for 1 minute at 30 µL/min; change of < 400 RU indicated sufficient coverage. Dilution of lulworthinone and its isomer from 4 to 128 µM in HEPES buffer were injected over immobilised vesicles. Due to the possibility of sample retention, injections were made from low to high concentration with 200 seconds contact time and 400 seconds dissociation phase. Between runs, liposomes were regenerated by three subsequent injections of 10 mM NaOH at 30 µL/min for 30 seconds each. The control flow cell was treated the same way as sample cells, except 1 injection were replaced by HEPES buffer. The results were processed using in-laboratory written MATLAB scripts (MATLAB R2020a; scripts are available at - https://github.com/MarJakubec). We have obtained both partitioning constant (K_p) and dissociation rate (k_{off}) using the method developed by Figueira *et al.* (2017) [31]. K_p was evaluated from steady-state affinity in 190-second time mark after injection and fitting obtained curve into (Equation 2)

$$\frac{RU_S}{RU_L} = \frac{\gamma_L K_P \frac{M_S}{M_L}[S]_W}{1 + \sigma_{\gamma_L K_P \frac{M_S}{M_L}[S]_W}} \tag{2}$$

Where RU_S and RU_L are the relative response of solute (lulworthinone) and total lipid deposition response, respectively, γL is the molar volume of the lipids, M_S and M_L are the molecular mass of solute and lipid respectively, and $[S]_W$ is the concentration of solute in water. K_p and σ are obtained from fit and are respectively, partitioning constant and lipid to solute ratio. K_{off} rate was obtained by fitting the first 200-seconds of the dissociation run. We have identified the contribution of two populations in dissociation response, which led us to use adapted formalism from Figuera *et al.* [31] (Equation 3) to obtain the average k_{off} response (Equation 4).

$$S_L(t) = \alpha e^{-koff,\alpha^t} + \beta e^{-koff,\beta^t} + SL,r \tag{3}$$

$$k_{off} = \frac{\alpha k_{off},\alpha + \beta k_{off,\beta}}{\alpha + \beta} \tag{4}$$

Where S_L is the linearised ratio of responses of solute and lipid which is plotted against time of dissociation; α and β are individual populations, and $S_{L,r}$ is retained solute fraction.

5.4. Cell membrane integrity as determined by bioluminescence

A bioluminescence-based assay developed by Virta *et al.* (1995) [38] was used to investigate membrane disruptive properties of lulworthinone. Upon the disruption of the membrane, the intracellular produced Luciferase would interact with its extracellular provided substrate - D-luciferin - and emit luminescence in real time. For this, a *Bacillus subtilis* 168 strain expressing Luciferase - encoded on the pCSS962 plasmid was used. Concentration ranging from 0 - 4 x MIC, including chlorhexidine as a membranolytic control (200 µg/mL) and ciprofloxacin as a non-membrane active negative control was tested. Overnight cultures were grown in MHB II containing 5 µg/mL chloramphenicol (220551, Calbiochem, CA, USA). The bacteria were pelleted and resuspended in fresh MHB II to OD_{600} of 0.1 D-luciferin potassium salt (pH 7.4, SynChem Inc, Il, USA) was added for a final concentration of 1 mM. 96 well plates (655209, Greiner Bio-One, Kresmmuenster, Austria) containing 20 µL of compound dilutions were prepared and loaded into a plate reader (Synergy H1 Hybrid reader, BioTek, VT, USA). For each test well, 180 µL bacterial inoculums were injected by an automatic injector. The bioluminescence was measured for 270 seconds before 35 µL chlorhexidine (vnr 007214, Fresenius Kabi Norge AS, Halden, Norway) was added at a membranolytic concentration (30 µg/mL). The luminescence was measured for additional 30 seconds. The light emission with CHX would indicate the lysis of bacterial cells that are still alive after the first treatment. The experiment was performed three times,data, analysis and code at can be found in the datarepository [42].

5.5. $DiOC_2(3)$ cytoplasmic membrane depolarization assay

To characterize the influence of lulworthinone on the cytoplasmic membrane potential, the fluorescence of a membrane potential indicator dye was meassured with flow cytometry. The *Bac*Light™ Bacterial Membrane Potential Kit (B34950, Invitrogen, CA, USA), which includes a fluorescent membrane potential indicator dye, 3,3-Diethyloxacarbocyanine iodide ($DiOC_2(3)$), and carbonyl cyanide m-chlorophenyl hydrazone (CCCP) as a membrane potential inhibitor [19] was used. In low abundance, $DiOC_2(3)$ emits green fluorescence in bacterial cells, when cells maintain their membrane potential they accumulate more dye, which self-associates and the fluorescence shifts into the red spectrum. The assay was performed according to the manufacturer. *B. subtilis* 168 was replaced by *S. aureus* ATCC 29213, since it showed much clearer detectable differences in potential change. In short, inoculum of 1 x 10^6 CFU/ml was prepared in sterile filtered (0.22 µm pore size) PBS (P4417, Sigma-Adrich, MO, USA). For each sample, 1 ml inoculum was transferred in flow cytometer tubes (352054, Corning Science, Mexico), additional tubes for a depolarized control (CCCP, 10 µL of 500 µM stock) and unstained control were included. lulworthinone was added for concentrations ranging from 0.25 - 4 x MIC. Samples were vortexed and added 10 µL of $DiOC_2(3)$ (to each tube besides the unstained control), mixed and incubated for 30 minutes. Samples were exited at 480 nm and fluorescence collected with with 530/30 nm and 616/23 nm emission filters using the BD LSRFortessa™ Cell Analyser (647794,BD Bioscience, Switzerland). Samples were gated on the bacterial cell seize, with a set threshold at 1500 side ward scatter, 10.000 events were collected. The data was analysed using the FlowJoe™ software (v10.8.0, FlowJo, LLC, OR, USA) and the gated population Mean Fluorescence Intensity (MFI) was obtained in a red vs green florescence dot plot. The ratio of red MFI divided by green MFI reflecting the membrane potential. The experiment was performed three times; data, analysis, and code can be found in the datarepository [42].

5.6. Cell morphology and biomarker detection using microscopy

B. subtilis 168 was grown in MHB II at 37 °C under agitation. Reporter strain 2020 was grown in MHB II supplemented with 100 µg/mL spectinomycin (S9007, Sigma-Aldrich, MO, USA) and 0.5 % xylose (PHR2102-500MG, Merck Ag, Germany) at 30 °C under agitation. Additionally, MHB II was supplemented with 1.25 mM $CaCl_2$ for all experiments with daptomycin (DAP, Cubicin, Novartis, UK) [44]. For *B. subtilis* 168, aliquots from the overnight cultures were diluted 1:50 in prewarmed MHB II and incubated at 37 °C under agitation until an OD_{600} of 0.3. The cultures were diluted 1:1 with the solutions of lulworthinone and the reference antibiotic DAP in the wells of a 96-well microtiter plate (249943 Nunc™, Thermo scientific, UK). The final concentration of all compounds in the wells was 1x MIC. In parallel, a 1:1 combination of the cultures with sterile Milli-Q H_2O or 1.25 mM $CaCl_2$ for DAP, were used as untreated controls. Bacteria were incubated for 90 minutes at 37 °C with agitation and pelleted at 13.5 x g for 5 minutes and carefully suspended in prewarmed 0.9 % NaCl. Subsequently, bacteria were stained with 12 µg/mL FM 4-64 (T13320, Invitrogen, MA, USA) and 2 µg/mL DAPI (D9542, Sigma-Aldrich, MO, USA) for 25 minutes at 37 °C with agitation. Cells were pelleted again and carefully resuspended in preheated 0.9 % NaCl. Aliquots of the bacterial suspensions were applied to the bottom of 35 mm Confocal Dishes (75856-742, VWR, PE, USA) and covered by 2.4 % agarose pads prepared in 0.9 % NaCl. For *B. subtilis* 2020 the sample preparation was like the one described above, with following modifications. Aliquots from the overnight cultures were incubated in presence of 0.5 % xylose. Samples were treated for a total of 45 minutes prior to microscopy. No washing steps were included. Incubation at all steps was performed at 30 °C with agitation. Aliquots of the stained suspensions were applied to the round 1.5 coverslips (631-0161, VWR, PE, USA). The fluorescence images of the bacteria were acquired via DeltaVision Elite Deconvolution Microscope (GE Healthcare, IL, USA). For wide field deconvolution imaging of bacteria, an oil immersion 60X (1.42NA) objective lens was utilized. or DAPI, the excitation wavelength range was 381-401 nm, and the emission was in 409-456 nm range. The excitation and emission wavelength range

for FM 4-64 were 425-495 nm and 652-700 nm, respectively. For GFP, the excitation and emission wavelength range were 425-495 nm and 500-550 nm, respectively. To achieve a superior contrast and resolution in images, a volume stack of 12 planes over 3 µM depth are acquired and deconvolved. For each treatment, 10 - 20 imaging fields were viewed. Experiments were done in three biological replicates. Pictures can be found at the data repository [42].

5.7. Cell morphology determination with Quantitative Phase Microscopy

Digital holography based quantitative phase microscopy (QPM) has been developed to obtain quantitative information about the bacteria in a label free manner. QPM improves the image contrast of transparent cells while quantifying parameters such as: optical thickness (sample thickness x refractive index (n)), refractive index variation, cell dry mass and other morphological parameters [45,46]. *B. subtilis* 168 were cultivated in MHB II at 37 °C until an OD_{600} = 0.3 was reached. The cultures were diluted 1:1 with the solutions of lulworthinone for 90 minutes. 90 µL samples were pelleted at 13.5 x g for 5 minutes and carefully suspended in 200 µL PHEM (pH 7.3) buffer containing 2 % paraformaldehyde (PFA) and 1 % glutaraldehyde (GA). For QPM measurements the bacterial cells were placed in a polydimethylsiloxane (PDMS) chamber on a reflective Si substrate and covered with standard 1.5 thickness coverslip. Before sample preparation, the surface of Si substrate was treated with 0.1 % poly-L-lysin for 10 minutes to enhance cell attachment. The interferograms were acquired with 60 x (1.2NA) objective lens and further post-processed in MATLAB to get the phase map of the bacteria. The individual bacteria are segmented for the quantative assesment of lenght, width, volume and other morphological parameters of the bacteria.

5.8. Kill kinetics using Time-Kill curves

The kill kinetics of lulworthinone can be expressed as rate over time with a fixed drug concentration - so called Time-Kill curves [47]. Time-kill curve analyses were performed by culturing *B. subtilis* 168 in MHB II, at antimicrobial concentrations ranging from 4 × MIC to 0.25 × MIC. The MICs were determined according to CLSI guidelines [48], presented in Table 5). The antimicrobials examined were lulworthinone and chlorhexidine (17850, Sigma-Adrich, MO, USA). Cultures were inoculated from MH agar plates and grown in MHB II for 18 – 20 hours at 37 °C, reinoculated and grown to mid-log phase for 3 hours in MHB II, before diluting them to 1 x 10^6 CFU/mL in pre-warmed MHB II (37 °C). For the test setup, the two-fold drug concentrations were prepared in 750 µL MHB II each, an antibiotic free growth control was included and prepared in a 24-well polypropylene plate (SKU:1300-00312, Bellco Glass Inc., NJ, USA). For each drug concentration 750 µL inoculum were added to each well. The plates were incubated for 5 hours at 37 °C and sampled at 10, 30, 60, 120 and 300 minutes. Sample for the start time point (T_0) was taken from the inoculum, diluted 1:1 with MHB II. Each sample was diluted seven times in PBS and 20 µL of each dilution was plated out in a run-streak on MH agar plates. Samples were plated in duplicates; each experiment was performed three times. Data, analysis and code at can be found in the data repository [42].

5.9. Pharmacodynamic parameters

The data of the time-kill curves were used to model the pharmacodynamic parameters of lulworthinone. The bacterial net growth rates (ψ) were estimated from the surviving bacteria (CFU/ml) over time between 0 and 300 minutes, as described above. The phramacodynamic function [21], was fitted to ψ present at different drug concentrations. In this model, the top asymptote (ψ_{max}) and the bottom asymptote (ψ_{min}) indicate the maximal and minimal bacterial net growth rate in relation to the drug concentration. The slope of the curve (κ or the Hill coefficient) represent the relationship between bacterial growth and antimicrobial concentration. The antimicrobial concentration that results in a ψ of zero is the pharmacodynamic MIC (zMIC). Data analysis was done in R [49] and the *censReg*

package [50] was used to calculate for concentrations containing censored data points. Data and code is available at the data repository [42].

5.10. Aggregation formation detection with Dynamic Light Scattering

We have tested the ability of lulworthinone to form oligomers by Zetasizer Nano ZS (Malvern Ins., Malvern, UK). Lulworthinone was dissolved in 5 % DMSO in MiliQ and then diluted to obtain a concentration range from 320 µM - 0.625 µM in 1 % DMSO. We have tested its ability to form oligomers at 37 °C with or without the presence of 0.025 % Tween 80.

5.11. Influence of detergent on antibacterial activity

To determine if lulworthinone forms colloidal aggregates that affect its antimicrobial activity, a MIC assay including a non-ionic detergent was used. The antibacterial activity of a colloidal aggregate should be heavily attenuated in the presence of non-ionic detergents [24,51]. MIC assay was performed according to CLSI guidelines [48] using *S. aureus* ATCC 25923, MIC values used are from the previous study [10]. Overnight cultures were grown in MHB (275730, BD Difco^{TM}, France) at 37 °C. Two-fold dilution series of lulworthinone ranging from 128 µg/mL - 0.25 µg/mL with or without 0.025 % (v/v) Tween 80 (P8074, Sigma-Aldrich, MO, USA) were tested.

Assay was conducted in 96-well plates (Nunclon^{TM} Δ 734-2073, VWR, PA, USA). OD_{600} values were recorded by a plate reader (Victor multilabel counter, PerkinElmer, MA, USA) at 37 ∘C for 24 hours. Each test run included a growth control (media + inoculum), a sterility control (media + water) and for quality assurance *S. aureus* ATCC 25923 was tested against gentamicin (A2712, VWR). Tests were performed in triplicates with three technical replicates, median MIC values are displayed.

5.12. Data analysis

Data handling, analysis, statistics and presentation were done using R 4.1.0 [49], the *tidyverse* package [52], the *ggplot2* package [53], the *ggpubr* package [54] and the *cowplot* package [55]. Data documentation was done using the *bookdown* package [56].

Supplementary Materials: The following are available online at https://www.mdpi.com/article/10.3390/1010000/s1, Figure S1: SPR sensogram for (**A**) lulworthinone and (**B**) acidified lulworthinone, Figure S2: Membrane potential shift in the presence of lulworthinone.

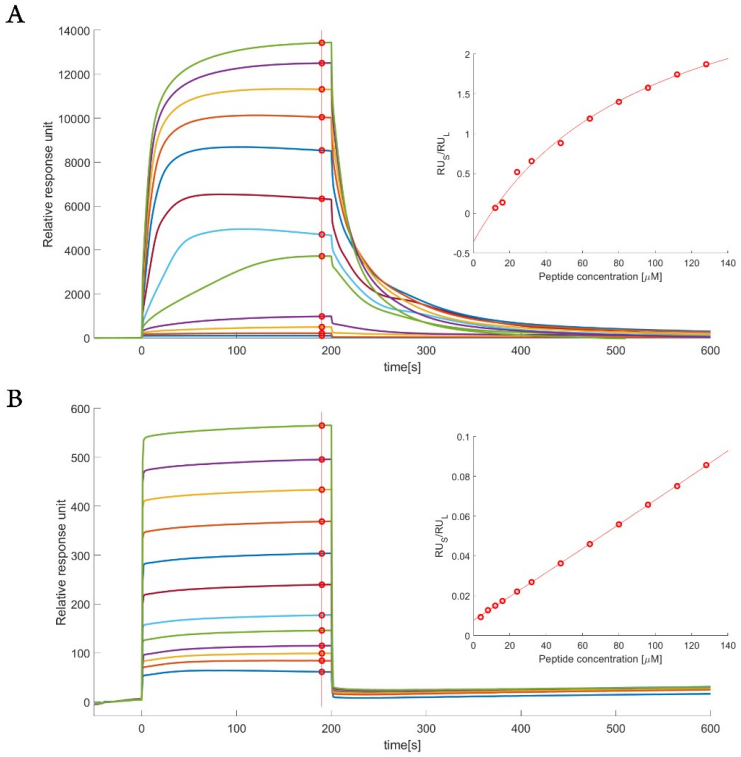

Figure 12. SPR sensogram for (**A**) lulworthinone and (**B**) acidified lulworthinone. Red line points to a steady state where relative response was read. Values were fitted (inset) to obtain K_P. Please note the different range in relative response units for both compounds.

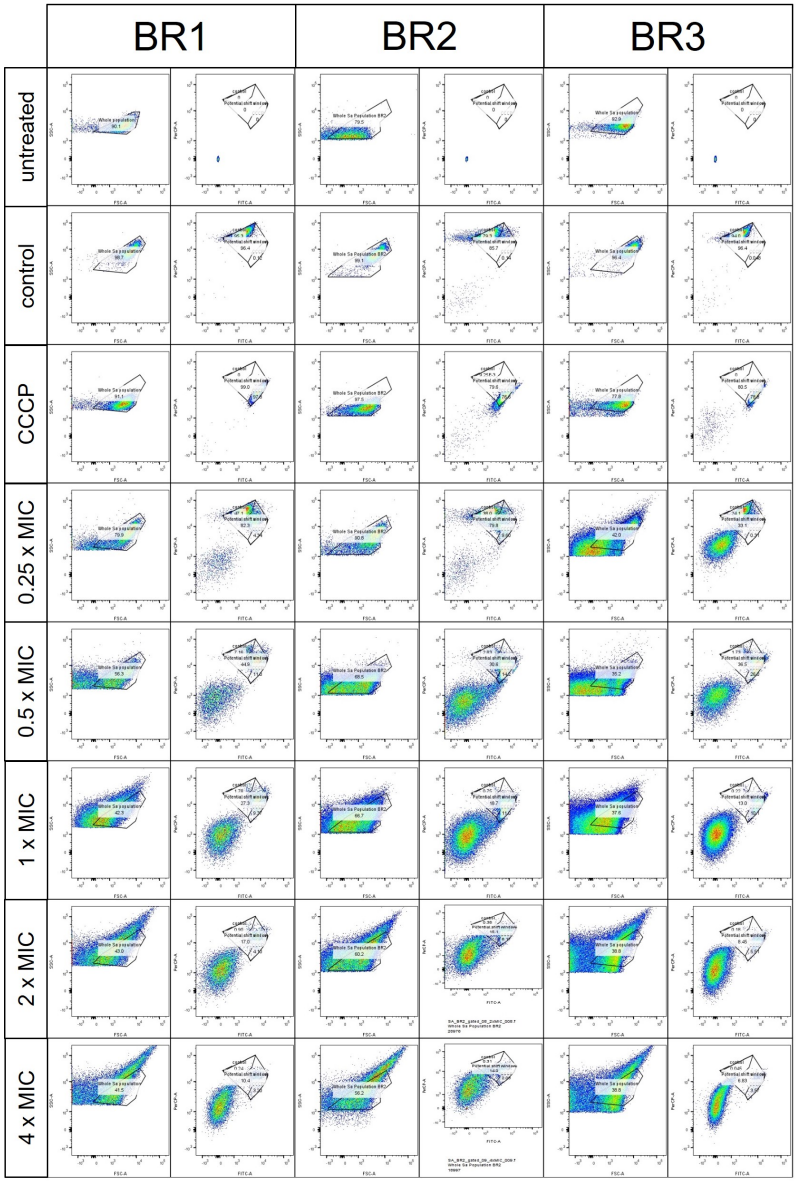

Figure 13. Membrane potential shift in the presence of lulworthinone. Red cultures have a membrane potential, while green cultures show a dissipation the membrane potential.

Author Contributions: Conceptualization, EJ and JE; data curation, EJ; formal analysis, EJ, VK, MJA; investigation, EJ, EM, VD, MJA and PR, project administration, EJ; resources, MJE and HMB; software, EJ, VK, MJA; supervision, EM and JE; visualization, EJ; writing - original draft preparation, EJ; writing review and editing, EJ, EM, MJE, MJA, PR, JA, JI and JE. All authors have read and agreed to the published version of the manuscript

Funding: The project was funded by The Research Council of Norway (RCN) grant no. 269425. The APC was covered by the open access publishing fund, UiT

Data Availability Statement: The data presented in this study are openly available in DataverseNO at https://doi.org/10.18710/6Z0VJX.

Acknowledgments: The authors would like to acknowledge the technical support by Mikal E. Fitsum, Marte Albrigsten and Theresa Wagner for *in vivo* experimental lab work. Antal Martinecz and Fabrizio Clarelli for advise one pharmacodynamic modelling. Roland Regoes for providing the pharmacodynamic workflow. We would also like to acknowledge Michaela Wenzel for providing the *B. sutilis* 2020 strain. Kine Østnes Hansen for providing the SMILES structure of lulworthinone. Deanna Wolfson for suggestions to optimize the microscopy methods used. We thank the Advanced Microscopy Core Facility (AMCF) of the UiT the Arctic University of Norway for the access to their

devices. Furthermore, we a grateful for the formal education and training provided by the Digital Life Norway research school and National Graduate School in Infection Biology and Antimicrobials (IBA, project number: 249062).

Conflicts of Interest: The authors declared no potential conflicts of interest with respect to the research, authorship, and/or publication of this article.

References

1. Murray, C.J.; Ikuta, K.S.; Sharara, F.; Swetschinski, L.; Aguilar, G.R.; Gray, A.; Han, C.; Bisignano, C.; Rao, P.; Wool, E.; et al. Global Burden of Bacterial Antimicrobial Resistance in 2019: A Systematic Analysis. *The Lancet* **2022**, *0*. doi:10.1016/S0140-6736(21)02724-0.
2. World Health Organization. *2019 Antibacterial Agents in Clinical Development: An Analysis of the Antibacterial Clinical Development Pipeline*; World Health Organization: Geneva, 2019; chapter x, 35 p.
3. Theuretzbacher, U.; Bush, K.; Harbarth, S.; Paul, M.; Rex, J.H.; Tacconelli, E.; Thwaites, G.E. Critical Analysis of Antibacterial Agents in Clinical Development. *Nature Reviews Microbiology* **2020**, *18*, 286–298. doi:10.1038/s41579-020-0340-0.
4. Silver, L.L. Challenges of Antibacterial Discovery. *Clinical Microbiology Reviews* **2011**, *24*, 71–109. doi:10.1128/CMR.00030-10.
5. Newman, D.J.; Cragg, G.M. Natural Products as Sources of New Drugs over the Nearly Four Decades from 01/1981 to 09/2019. *Journal of Natural Products* **2020**, *83*, 770–803. doi:10.1021/acs.jnatprod.9b01285.
6. Cushnie, T.P.T.; Cushnie, B.; Echeverría, J.; Fowsantear, W.; Thammawat, S.; Dodgson, J.L.; Law, S.; Clow, S.M. Bioprospecting for Antibacterial Drugs: A Multidisciplinary Perspective on Natural Product Source Material, Bioassay Selection and Avoidable Pitfalls. *Pharmaceutical Research* **2020**, *37*, 125. doi:10.1007/s11095-020-02849-1.
7. Davison, E.K.; Brimble, M.A. Natural Product Derived Privileged Scaffolds in Drug Discovery. *Current Opinion in Chemical Biology* **2019**, *52*, 1–8. doi:10.1016/j.cbpa.2018.12.007.
8. Imhoff, J.F. Natural Products from Marine Fungi—Still an Underrepresented Resource. *Marine Drugs* **2016**, *14*, 19. doi:10.3390/md14010019.
9. Overy, D.P.; Bayman, P.; Kerr, R.G.; Bills, G.F. An Assessment of Natural Product Discovery from Marine (Sensu Strictu) and Marine-Derived Fungi. *Mycology* **2014**, *5*, 145–167. doi:10.1080/21501203.2014.931308.
10. Jenssen, M.; Rainsford, P.; Juskewitz, E.; Andersen, J.H.; Hansen, E.H.; Isaksson, J.; Rämä, T.; Hansen, K.Ø. Lulworthinone, a New Dimeric Naphthopyrone From a Marine Fungus in the Family Lulworthiaceae With Antibacterial Activity Against Clinical Methicillin-Resistant Staphylococcus Aureus Isolates. *Frontiers in Microbiology* **2021**, *12*, 2862. doi:10.3389/fmicb.2021.730740.
11. Suzuki, K.; Nozawa, K.; Nakajima, S.; Udagawa, S.i.; Kawai, K.i. Isolation and Structures of Antibacterial Binaphtho-α-pyrones, Talaroderxines A and B, from Talaromyces Derxii. *Chemical & Pharmaceutical Bulletin* **1992**, *40*, 1116–1119. doi:10.1248/cpb.40.1116.
12. Zheng, C.J.; Sohn, M.J.; Lee, S.; Hong, Y.S.; Kwak, J.H.; Kim, W.G. Cephalochromin, a FabI-directed Antibacterial of Microbial Origin. *Biochemical and Biophysical Research Communications* **2007**, *362*, 1107–1112. doi:10.1016/j.bbrc.2007.08.144.
13. Boudesocque-Delaye, L.; Agostinho, D.; Bodet, C.; Thery-Kone, I.; Allouchi, H.; Gueiffier, A.; Nuzillard, J.M.; Enguehard-Gueiffier, C. Antibacterial Polyketide Heterodimers from Pyrenacantha Kaurabassana Tubers. *Journal of Natural Products* **2015**, *78*, 597–603. doi:10.1021/np5003252.
14. Rivera-Chávez, J.; Caesar, L.; Garcia-Salazar, J.J.; Raja, H.A.; Cech, N.B.; Pearce, C.J.; Oberlies, N.H. Mycopyranone: A 8,8'-Binaphthopyranone with Potent Anti-MRSA Activity from the Fungus Phialemoniopsis Sp. *Tetrahedron Letters* **2019**, *60*, 594–597. doi:10.1016/j.tetlet.2019.01.029.
15. Wang, J.; Galgoci, A.; Kodali, S.; Herath, K.B.; Jayasuriya, H.; Dorso, K.; Vicente, F.; González, A.; Cully, D.; Bramhill, D.; et al. Discovery of a Small Molecule That Inhibits Cell Division by Blocking FtsZ, a Novel Therapeutic Target of Antibiotics *. *Journal of Biological Chemistry* **2003**, *278*, 44424–44428. doi:10.1074/jbc.M307625200.
16. Isaksson, J.; Brandsdal, B.O.; Engqvist, M.; Flaten, G.E.; Svendsen, J.S.M.; Stensen, W. A Synthetic Antimicrobial Peptidomimetic (LTX 109): Stereochemical Impact on Membrane Disruption. *Journal of Medicinal Chemistry* **2011**, *54*, 5786–5795. doi:10.1021/jm200450h.
17. R. Silk, M.
18. Rainsford, P.; Sarre, R.B.; Brandsdal, B.O.; Falavigna, M.; Flaten, G.E.; Jakubec, M.; Isaksson, J. WIND-PVPA: Water/Ion NMR Detected PVPA to Assess Lipid Barrier Integrity in Vitro through Quantification of Passive Water- and Ion Transport.
19. Novo, D.; Perlmutter, N.G.; Hunt, R.H.; Shapiro, H.M. Accurate Flow Cytometric Membrane Potential Measurement in Bacteria Using Diethyloxacarbocyanine and a Ratiometric Technique. *Cytometry* **1999**, *35*, 55–63. doi:10.1002/(SICI)1097-0320(19990101)35:1<55::AID-CYTO8>3.0.CO;2-2.
20. Strahl, H.; Hamoen, L.W. Membrane Potential Is Important for Bacterial Cell Division. *Proceedings of the National Academy of Sciences* **2010**, *107*, 12281–12286. doi:10.1073/pnas.1005485107.
21. Regoes, R.R.; Wiuff, C.; Zappala, R.M.; Garner, K.N.; Baquero, F.; Levin, B.R. Pharmacodynamic Functions: A Multiparameter Approach to the Design of Antibiotic Treatment Regimens. *Antimicrobial Agents and Chemotherapy* **2004**, *48*, 3670–3676. doi:10.1128/AAC.48.10.3670-3676.2004.
22. Shoichet, B.K. Interpreting Steep Dose-Response Curves in Early Inhibitor Discovery. *Journal of Medicinal Chemistry* **2006**, *49*, 7274–7277. doi:10.1021/jm061103g.

23. Topel, Ö.; Çakır, B.A.; Budama, L.; Hoda, N. Determination of Critical Micelle Concentration of Polybutadiene-Block-Poly(Ethyleneoxide) Diblock Copolymer by Fluorescence Spectroscopy and Dynamic Light Scattering. *Journal of Molecular Liquids* **2013**, *177*, 40–43. doi:10.1016/j.molliq.2012.10.013.
24. Ganesh, A.N.; Donders, E.N.; Shoichet, B.K.; Shoichet, M.S. Colloidal Aggregation: From Screening Nuisance to Formulation Nuance. *Nano Today* **2018**, *19*, 188–200. doi:10.1016/j.nantod.2018.02.011.
25. Mingeot-Leclercq, M.P.; Décout, J.L. Bacterial Lipid Membranes as Promising Targets to Fight Antimicrobial Resistance, Molecular Foundations and Illustration through the Renewal of Aminoglycoside Antibiotics and Emergence of Amphiphilic Aminoglycosides. *MedChemComm* **2016**, *7*, 586–611. doi:10.1039/C5MD00503E.
26. Yet, L. *Privileged Structures in Drug Discovery: Medicinal Chemistry and Synthesis*; 2018, March.
27. Zhang, L.; Zhang, G.; Xu, S.; Song, Y. Recent Advances of Quinones as a Privileged Structure in Drug Discovery. *European Journal of Medicinal Chemistry* **2021**, *223*, 113632. doi:10.1016/j.ejmech.2021.113632.
28. Sauermann, R.; Rothenburger, M.; Graninger, W.; Joukhadar, C. Daptomycin: A Review 4 Years after First Approval. *Pharmacology* **2008**, *81*, 79–91. doi:10.1159/000109868.
29. Bernareggi, A.; Borghi, A.; Borgonovi, M.; Cavenaghi, L.; Ferrari, P.; Vékey, K.; Zanol, M.; Zerilli, L.F. Teicoplanin Metabolism in Humans. *Antimicrobial Agents and Chemotherapy* **1992**, *36*, 1744–1749. doi:10.1128/AAC.36.8.1744.
30. Cochrane, S.A.; Vederas, J.C. Lipopeptides from Bacillus and Paenibacillus Spp.: A Gold Mine of Antibiotic Candidates. *Medicinal Research Reviews* **2016**, *36*, 4–31. doi:10.1002/med.21321.
31. Figueira, T.N.; Freire, J.M.; Cunha-Santos, C.; Heras, M.; Gonçalves, J.; Moscona, A.; Porotto, M.; Salomé Veiga, A.; Castanho, M.A.R.B. Quantitative Analysis of Molecular Partition towards Lipid Membranes Using Surface Plasmon Resonance. *Scientific Reports* **2017**, *7*, 45647. doi:10.1038/srep45647.
32. Tripathy, S.; Sahu, S.K. FtsZ Inhibitors as a New Genera of Antibacterial Agents. *Bioorganic Chemistry* **2019**, *91*, 103169. doi:10.1016/j.bioorg.2019.103169.
33. Kusuma, K.D.; Payne, M.; Ung, A.T.; Bottomley, A.L.; Harry, E.J. FtsZ as an Antibacterial Target: Status and Guidelines for Progressing This Avenue. *ACS Infectious Diseases* **2019**, *5*, 1279–1294. doi:10.1021/acsinfecdis.9b00055.
34. Silber, N.; de Opitz, C.L.M.; Mayer, C.; Sass, P. Cell Division Protein FtsZ: From Structure and Mechanism to Antibiotic Target. *Future Microbiology* **2020**. doi:10.2217/fmb-2019-0348.
35. Chai, W.C.; Whittall, J.J.; Song, D.; Polyak, S.W.; Ogunniyi, A.D.; Wang, Y.; Bi, F.; Ma, S.; Semple, S.J.; Venter, H. Antimicrobial Action and Reversal of Resistance in MRSA by Difluorobenzamide Derivatives Targeted at FtsZ. *Antibiotics* **2020**, *9*, 873. doi:10.3390/antibiotics9120873.
36. Pradhan, P.; Margolin, W.; Beuria, T.K. Targeting the Achilles Heel of FtsZ: The Interdomain Cleft. *Frontiers in Microbiology* **2021**, *12*.
37. McLaughlin, C.K.; Duan, D.; Ganesh, A.N.; Torosyan, H.; Shoichet, B.K.; Shoichet, M.S. Stable Colloidal Drug Aggregates Catch and Release Active Enzymes. *ACS Chemical Biology* **2016**, *11*, 992–1000. doi:10.1021/acschembio.5b00806.
38. Virta, M.; Åkerman, K.E.O.; Saviranta, P.; Oker-Blom, C.; Karp, M.T. Real-Time Measurement of Cell Permeabilization with Low-Molecular-Weight Membranolytic Agents. *Journal of Antimicrobial Chemotherapy* **1995**, *36*, 303–315. doi:10.1093/jac/36.2.303.
39. Urban, A.; Eckermann, S.; Fast, B.; Metzger, S.; Gehling, M.; Ziegelbauer, K.; Rübsamen-Waigmann, H.; Freiberg, C. Novel Whole-Cell Antibiotic Biosensors for Compound Discovery. *Applied and Environmental Microbiology* **2007**, *73*, 6436–6443. doi:10.1128/AEM.00586-07.
40. Radeck, J.; Kraft, K.; Bartels, J.; Cikovic, T.; Dürr, F.; Emenegger, J.; Kelterborn, S.; Sauer, C.; Fritz, G.; Gebhard, S.; et al. The Bacillus BioBrick Box: Generation and Evaluation of Essential Genetic Building Blocks for Standardized Work with Bacillus Subtilis. *Journal of Biological Engineering* **2013**, *7*, 29. doi:10.1186/1754-1611-7-29.
41. Hansen, K.Ø.; Hansen, I.K.Ø.; Richard, C.S.; Jenssen, M.; Andersen, J.H.; Hansen, E.H. Antimicrobial Activity of Securamines From the Bryozoan Securiflustra Securifrons. *Natural Product Communications* **2021**, *16*, 1934578X21996180. doi:10.1177/1934578X21996180.
42. Juskewitz, E. Replication Data for: "Lulworthinone: In Vitro Mode of Action Investigation of an Antibacterial Dimeric Naphthopyrone Isolated from a Marine Fungus., in submission. doi:10.18710/6Z0VJX.
43. Jakubec, M.; Bariås, E.; Furse, S.; Govasli, M.L.; George, V.; Turcu, D.; Iashchishyn, I.A.; Morozova-Roche, L.A.; Halskau, Ø. Cholesterol-Containing Lipid Nanodiscs Promote an α-Synuclein Binding Mode That Accelerates Oligomerization. *The FEBS Journal* **2021**, *288*, 1887–1905. doi:10.1111/febs.15551.
44. Müller, A.; Wenzel, M.; Strahl, H.; Grein, F.; Saaki, T.N.V.; Kohl, B.; Siersma, T.; Bandow, J.E.; Sahl, H.G.; Schneider, T.; et al. Daptomycin Inhibits Cell Envelope Synthesis by Interfering with Fluid Membrane Microdomains. *Proceedings of the National Academy of Sciences* **2016**, *113*, E7077–E7086. doi:10.1073/pnas.1611173113.
45. Dubey, V.; Ahmad, A.; Singh, R.; Wolfson, D.L.; Basnet, P.; Acharya, G.; Mehta, D.S.; Ahluwalia, B.S. Multi-Modal Chip-Based Fluorescence and Quantitative Phase Microscopy for Studying Inflammation in Macrophages. *Optics Express* **2018**, *26*, 19864–19876. doi:10.1364/OE.26.019864.
46. Dubey, V.; Popova, D.; Ahmad, A.; Acharya, G.; Basnet, P.; Mehta, D.S.; Ahluwalia, B.S. Partially Spatially Coherent Digital Holographic Microscopy and Machine Learning for Quantitative Analysis of Human Spermatozoa under Oxidative Stress Condition. *Scientific Reports* **2019**, *9*, 3564. doi:10.1038/s41598-019-39523-5.

47. Clinical and Laboratory Standards Institute. M26-A - Methods for Determining Bactericidal Activity of Antimicrobial Agents; Approved Guideline.
48. Clinical and Laboratory Standards Institute. M7-A7: Methods for Dilution Antimicrobial Susceptibility Tests for Bacteria That Grow Aerobically; Approved Standard—Seventh Edition, 2006.
49. R Core Team. *R: A Language and Environment for Statistical Computing*; R Foundation for Statistical Computing: Vienna, Austria, 2021.
50. Henningsen, A. censReg: Censored Regression (Tobit) Models, 2020.
51. Shoichet, B.K. Screening in a Spirit Haunted World. *Drug Discovery Today* **2006**, *11*, 607–615. doi:10.1016/j.drudis.2006.05.014.
52. Wickham, H.; RStudio. Tidyverse: Easily Install and Load the 'Tidyverse', 2021.
53. Wickham, H.; Chang, W.; Henry, L.; Pedersen, T.L.; Takahashi, K.; Wilke, C.; Woo, K.; Yutani, H.; Dunnington, D.; RStudio. Ggplot2: Create Elegant Data Visualisations Using the Grammar of Graphics, 2021.
54. Kassambara, A. Ggpubr: 'ggplot2' Based Publication Ready Plots, 2020.
55. Wilke, C.O. Cowplot: Streamlined Plot Theme and Plot Annotations for 'Ggplot2', 2020.
56. Xie, Y.; cre.; Allaire, J.J.; Kim, A.; Samuel-Rosa, A.; Oles, A.; Yasumoto, A.; Frederik, A.; Quast, B.; Marwick, B.; et al. Bookdown: Authoring Books and Technical Documents with R Markdown, 2021.

PAPER V

Isolation and characterization of St-CRPs: Cysteine-rich peptides from the Arctic marine ascidian *Synoicum turgens*.

Ida K. Ø. Hansen [1,*], Philip B. Rainsford [2], Johan Isaksson [2], Kine Ø. Hansen [3], Klara Stensvåg [1], Anastasia Albert [4], Terje Vasskog [5] and Tor Haug [1,*]

[1] The Norwegian College of Fishery Science, Faculty of Biosciences, Fisheries and Economics, UiT The Arctic University of Norway, Breivika, N-9037 Tromsø, Norway; klara.stensvag@uit.no (K.S.)

[2] Department of Chemistry, Faculty of Science and Technology, UiT The Arctic University of Norway, Breivika, N-9037 Tromsø, Norway; philip.rainsford@uit.no (P.B.R.); johan.isaksson@uit.no (J.I.)

[3] Marbio, UiT The Arctic University of Norway, N-9037, Tromsø, Norway; kine.o.hanssen@uit.no

[4] Norce, Siva Innovasjonssenter, Sykehusveien 21, 9019 Tromsø; anastasia.albert@norut.no (A.A.)

[5]Department of Pharmacy, Faculty of Health Sciences, UiT The Arctic University of Norway, Breivika, N-9037 Tromsø, Norway; terje.vasskog@uit.no (T.V.)

[*] Correspondence: ida.k.hansen@uit.no; Tel.: +47-77-64-92-66 (I.K.Ø.H.), tor.haug@uit.no; Tel.: +47-77-64-60-71 (T.H.)

Abstract

Ascidians are a group of marine invertebrates where most are sessile and soft bodied. Their absence of an adaptive immune system makes them rely on innate immune responses to detect and eliminate invading microbes. Antimicrobial peptides (AMPs) play an essential part in this process. In this paper, we present the isolation, structure elucidation and bioactivities of two new cysteine-rich peptides (CRPs) from the Arctic marine ascidian *Synoicum turgens*. The sequences and structures of the peptides were solved with Edman degradation sequencing, mass spectrometry, and NMR analysis. This revealed two novel 2 kDa peptides, St-CRP-1 and St-CRP-2, with neutral net charge. St-CRP-1 consisted of 18 amino acids and inhibited growth of two Gram-positive bacterial strains (*Bacillus subtilis* and *Corynebacterium glutamicum*) at 24.6 µM, whereas St-CRP-2 consisted of 19 amino acids and inhibited the growth of *B. subtilis* at 49.2 µM. St-CRP-1 had no effect on two mammalian cell lines or the brine shrimp *Artemia salina* at the highest concentration tested. Structural analysis of the St-CRPs indicated a Cys1-Cys6, Cys2-Cys4, and Cys3-Cys5 disulfide connectivity, which is also found in alpha-defensins. The results from this study show that Arctic marine ascidians are a rich source of novel bioactive peptides.

1. Introduction

Peptides are ubiquitous natural products, widely abundant and found in all living organisms, from prokaryotes to mammals. Many small peptides (<50 amino acids) are bioactive, displaying various activities such as analgetic, anticancer, antihypertensive, antimicrobial, antioxidative, antiviral and immunomodulatory properties [1]. Many peptides also show high potency and selectivity, and low toxicity against normal human cells [2]. Furthermore, most peptides are usually less allergenic compared to larger proteins when administered in mammals [3]. Natural peptides are therefore interesting candidates for pharmaceutical research by serving as templates for developing new therapeutic drugs. There are currently around 60 peptide drugs on the global market, and more than 400 different peptides are in clinical development or in preclinical studies, many of which are derived from natural sources [4].

Antimicrobial peptides (AMPs), also referred to as host defense peptides, are produced by all living organisms, in eukaryotes - as an important part of their innate immune system [5,6]. Because of their natural properties as antibiotic agents, AMPs are promising candidates to overcome the growing problem of antibiotic resistant pathogenic bacteria. AMPs are considered particularly favorable due to their broad-spectrum antimicrobial properties and the low-tendency of resistance development towards them [7]. One group of diverse AMPs are called the defensins. Defensins are a family of cysteine-rich AMPs, and are found in vertebrates, invertebrates, plants and fungi. They consist of a characteristic β-sheet core structure, and are most often stabilized with six disulfide-linked cysteines [8]. Defensins exhibit a broad-spectrum antimicrobial activity, displaying effects against both bacteria, fungi and viruses [9].

While linear peptides show limited promise as both orally and parentally administered drugs because of poor *in vivo* stability (due to e.g. proteolytic degradation) and limited membrane permeability [2], cysteine-rich peptides (CRPs) are emerging as a promising class of drug lead candidates and/or templates for drug development [10]. Introduction of disulfide bonds in peptides seems to be among nature´s solutions to the problem of proteolytic degradation. Disulfide bonds effectively constrains peptide topology, resulting in increased structural rigidity and proteolytic resistance [11,12]. Cysteine knot peptides (defined by its three disulfide bridges) and small cysteine-rich proteins are a special sort of peptides containing diverse structures and displaying a wide variety of bioactivities [13].

Marine invertebrates are an increasingly interesting source of novel bioactive peptides because of their ability to thrive in the bacteria-rich-environment without the presence of an adaptive immune system [14-16]. Ascidians (also known as sea squirts) belong to the phylum of Chordata and the subphylum Urochordata (tunicates), and have been a prolific source of bioactive peptides [14]. A variety of bioactive peptides showing anticancer, antineoplastic, antiviral, antidiabetic, antioxidant, and immunomodulatory properties,

have been isolated from ascidians. Several of these peptides have been explored as drugs candidates including a few in clinical trials [17].

As part of our ongoing search for novel AMPs from Arctic marine organisms, two novel cysteine-rich AMPs, turgencin A and turgencin B, were isolated from the colonial ascidian *Synoicum turgens* [18]. The peptides were 35-36 amino acids in length (3.5-3.7 kDa), containing 3 disulfide bridges with an unusual disulfide connectivity of Cys1-Cys6, Cys2-Cys5, and Cys3-Cys4. During the isolation of these peptides, we recognized a series of 2 kDa peptides in the same extract, with putative antimicrobial properties. Preliminary mass spectrometric analysis indicated the presence of multiple cysteines in these peptides. In this study, two small AMPs (18-19 amino acids in length) having 3 disulfide bridges, were isolated from *S. turgens*. St-CRP-1 was sequenced using Edman degradation and LC-MS/MS fragmentation and its structure was confirmed by NMR analysis. The sequence and structure of St-CRP-2 was solved solely with LC-MS/MS. This revealed, for both peptides, a disulfide connectivity similarity to alpha-defensins, a Cys1-Cys6, Cys2-Cys4, and Cys3-Cys5 connectivity.

2. Materials and Methods

2.1. Materials

The colonial sea squirt *S. turgens* (Phipps, 1774) was collected off the coast of Svalbard in August 2016 (79°33′ N, 18°37′ E) by divers at 20-30 m depth. The sample was identified by Robert A. Johansen, Marbank, Norway (http://www.imr.no/marbank/en), and subsequently frozen at -20 °C at sea. The biomass was lyophilized and kept frozen until further processing.

2.2. Extraction

Lyophilized samples of the ascidian (100 g) were pulverized and extracted with 5 volumes (v/w) of 60% acetonitrile (MeCN, HPLC-grade, Sigma-Aldrich, Steinheim, Germany) containing 0.1% trifluoroacetic acid (TFA, HPLC-grade, Sigma-Aldrich) dissolved in Milli-Q H_2O (Millipore, Burlington, MA, USA) for 24 hours at 4 °C. The mixture was centrifuged, and the supernatant was collected and stored at 4 °C before the residue was extracted once more under the same conditions. Supernatants were pooled and incubated at -20 °C for 1-2 h, causing the formation of two liquid phases, an organic MeCN-rich phase and an aqueous salt-rich phase. The aqueous phase was dried in a ScanSpeed 40 vacuum centrifuge (Labogene ApS, Lillerød, Denmark), and afterwards dissolved in 0.05% TFA/ H_2O (v/v) to a concentration of 100 mg/mL. To remove salt form the sample, solid phase extraction (SPE) was performed using reversed-phase C18 35 cc Sep-Pak Vac cartridges (Waters, Milford, MA, USA), as described by Haug et al. [19] with some modifications. Briefly, the cartridge was conditioned in MeCN and equilibrated with 0.05% TFA/H_2O (v/v)

before adding the aqueous phase. After washing the loaded extract with acidified water, a five-step elution was done with 10, 20, 30, 40, and 80% (v/v) MeCN containing 0.05% TFA (v/v). The collected SPE eluates were dried in a ScanSpeed 40 vacuum centrifuge and kept frozen at -20 °C until further analysis.

The SPE fractions were resuspended in Milli-Q H_2O to a concentration of 10 mg/mL. Non-dissolved material was removed by centrifugation, and the supernatant was tested for antibacterial activity.

2.3. Peptide Purification and Identification

Active SPE fractions were submitted to purification by preparative reversed-phase high-performance liquid chromatography (RP-HPLC). The separation was performed using an Agilent 218 Preparative gradient LC system coupled to an Agilent 1260 infinity DAD and an Agilent 440-LC fraction collector (Matriks, Oslo, Norway). The column used was an XBridge BEH C18 Prep column (10 × 250 mm, 5 µm, Waters). The mobile phase consisted of A: H_2O with 0.05% TFA and B: MeCN with 0.05% TFA, where the method was set to run mobile phase A for 10 min, then a gradient of 0-60% of mobile phase B from 10-70 min, with a flow rate of 6 mL/min. One-minute fractions were collected throughout the analysis, vacuum dried separately and redissolved in 500 µL Milli-Q H_2O, before testing for antibacterial activity. All SPE fractions, and the active HPLC fractions were submitted to high-resolution mass spectrometry (HR-MS) analysis, using an Agilent 1290 Infinity UHPLC-DAD system and an Agilent 6540B quadrupole time-of-flight (Q-ToF) mass spectrometer coupled with a dual electrospray ionization (ESI) source. The data was acquired and analyzed by using the Agilent MassHunter software (Data Acquisition B.06.01, SP1, and Qualitative Analysis B.07.00, SP2)) (all instruments and software were from Matriks). A standard method was used, running a gradient from 5-100% MeCN with 0.1% formic acid over 8 min with a flow rate of 0.3 mL/min. The separation was done using an Agilent Zorbax Eclipse Plus C18 column (2.1 × 50 mm , 1.8 µM, Matriks).

The HR-MS analysis confirmed the presence of the small (ca. 2 kDa) peptides in some of the antibacterial HPLC fractions, derived from the 40% MeCN SPE fraction. In order to isolate these peptides, the SPE fraction was repeatedly injected on the preparative RP-HPLC system, using an optimized RP-HPLC method. The mobile phase consisted of the same constituents as described above, However, elution was performed by running 20% of mobile phase B for 5 min, then a gradient of 20-45% of mobile phase B from 5-35 min, with a flow rate of 6 mL/min. The peptides were isolated by triggering collection at predetermined timepoints during the run. Each fraction was analyzed using the Agilent HR-MS system, and fractions containing pure peptides were pooled, lyophilized, and kept frozen at -20 °C until further analysis.

2.4. Sequence Analysis

Primary structure determination of St-CRP-1 was performed with Edman degradation sequencing at Eurosequence (Groningen, The Netherlands, www.eurosequence.nl). For *de novo* MS sequencing of St-

CRP-2, 2 µL 0.5 mM peptide was added 20 µL 0.1 M Tris[2-carboxyethyl] phosphine (TCEP, Sigma-Aldrich, St. Louis, MO, USA) and 50 µL 1 mM ammonium format buffer adjusted to pH 3 with formic acid. The solution was incubated at room temperature for one hour for full reduction of the peptide. The reduced peptide was analyzed on an Acquity I-class UPLC with a Waters Xevo QToF G2 mass spectrometer (Waters). The separation was performed using an Acquity BEH C18 column (2.1 × 100 mm, 1.7 µm, Waters), and a mobile phase gradient consisting of A: water + 0.1% formic acid and B: MeCN + 0.1% formic acid. Fragmentation spectra were obtained by CID fragmentation with a collision energy ramp of 20-50 eV. The fragment spectra gave full coverage of the peptide sequence, and for confirmation, the proposed sequence was inserted in MS-product from UCSF (http://prospector.ucsf.edu/prospector/cgi-bin/msform.cgi?form=msproduct) to induce peptide fragmentation. Isoelectric points (pI) were calculated using Innovagen's peptide property calculator app (http://www.innovagen.com). Sequence similarity searches were performed using the Basic Local Alignment Search Tool (BLAST, https://blast.ncbi.nlm.nih.gov/Blast.cgi), provided by the National Centre for Biotechnological Information (NCBI).

2.5. NMR Spectroscopy and Calculations

NMR experiments were acquired on an Avance III HD spectrometer equipped with an inverse four-channel probe with cryogenic enhancement for ^{1}H, ^{2}H and ^{13}C (TCI) operating at 600 MHz for ^{1}H (Bruker Biospin, Fällanden, Switzerland).

The sample of St-CRP-1 was prepared by dissolving 0.8 mg of material in 120 µL of H_2O/D_2O solution (95/5) in a D_2O matched 3 mm Shigemi tube. The following experiments were acquired for the elucidation of St-CRP-1: ^{1}H (excitation sculpting), ^{13}C, ^{15}N-HSQC, ^{13}C-HSQC, HMBC (including selective carbonyl HMBC), HSQCTOCSY (80 ms DIPSI), NOESY (100, 200, 300 ms mixing time), ROESY (100 ms spinlock), DQF-COSY, E.COSY and TOCSY (60, 100 ms DIPSI). Where applicable, gradient-selection and adiabatic pulse sequences were used. Acquisition and processing were done in Topspin 3.5pl7 using standard pulse sequences (Bruker Biospin). Spectral assignment and integration were done in CARA 1.8.4.2.

Starting structures were created as extended chains and folded using standard simulated annealing protocol (2000 K, 20000 cooling steps *in vacuo*) using observed NMR parameters, and with an absence of disulfide connectivity. Low energy folds from the previous step were used to generate disulfide connected starting structures for the final refinements. Finally, production runs of 500 cycles of simulated annealing generated the reported structure ensemble. Structures were generated using XPLOR-NIH 2.52 and secondary structure prediction made in TALOS+ (https://spin.niddk.nih.gov/NMRPipe/talos/). The NMR data is available at the Biological Magnetic Resonance Data Bank (https://bmrb.io/) under accession number 50547.

2.6. Reduction and Alkylation of the Peptides

To determine the disulfide connectivity in the peptides a reduction and alkylation method by Albert et al. was employed [20]. All chemicals used in this method were purchased from Sigma-Aldrich. The protocols for St-CRP-1 and St-CRP-2 were optimized individually, using the described method as a template. An overview of the analytical method and details on the reduction and alkylation procedures will be given here.

St-CRP-1: The SPE column (Empore C18, 3M, St. Paul, MN, USA) was activated with 250 µL MeCN and subsequently equilibrated with 500 µL ammonium formate buffer (50 mM, pH 3). The peptide was dissolved in the same buffer to a concentration of 0.5 mM and a volume of 500 µL was applied to the column. A volume of 100 µL 0.1 M TCEP was loaded onto the column to selectively reduce available cysteine bridges and the mixture on the column was incubated for 1 min before the column was washed 3 times with 300 µL of ammonium formate buffer/MeCN 90:10 (v/v), and once with 250 µL of the same buffer. Immediately after, the peptide was alkylated by adding 20 µL 0.5 M *N*-methylmaleimide (NMM) dissolved in buffer and the solution was left to incubate for 1 hour. The sample was eluted from the column with 300 µL 80% MeCN, and MeCN was removed under a gentle stream of nitrogen at 55 °C. To remove excess NMM, 100 µL of 0.5 M thiosalicylic acid (TA) was added and left to react with remaining NMM for 30 min. The sample was loaded onto a freshly equilibrated SPE column and washed 3 times with 300 µL 10% MeCN and once with buffer. For the second reduction, 100 µL of 0.1 M TCEP was again added and left to incubate for 1 min before the column was washed 3 times with 300 µL 10% MeCN and once with 300 µL buffer. The peptides were alkylated for the second time by adding 20 µL of a 0.5 M solution of *N*-ethylmaleimide (NEM) and the solution was left to incubate for 1 hour before the column was washed, as described above. Excess NEM was removed with TA as described for NMM and after washing and eluting from the column 20 µL of 0.1 M TCEP was added to the solution and left to incubate for 1 hour. The final alkylation was performed by adding 20 µL 0.12 M *N*-cyclohexyl maleimide (NCM) and the solution was left to incubate for 3 hours.

St-CRP-2: In general, the same alkylation protocol was used for St-CRP-2, but with some modifications. The peptide was dissolved in the same buffer, but 450 µL of a 0.5 mM peptide solution was added to the column. A volume of 50 µL 0.1 M TCEP was added to the column to selectively reduce available cysteine bridges. After incubation, the column was washed with 500 µL 20% MeCN. Immediately afterwards, 10 µL of a 0.5 M NMM solution was added to alkylate the reduced cysteines and the solution was incubated for 1 hour. To remove excess NMM the column was washed 5 times with 500 µL 20% MeCN. The second reduction and alkylation were done by adding 50 µL of 0.1 M TCEP to the peptide solution before incubation for 1 min. The column was then washed with 500 µL 20% MeCN and immediately loaded with 10 µL 0.5 M NEM which was left to incubate for 1 hour. A volume of 50 µL 0.5 M TA was added to the column and

left to incubate for 0.5 hour to react with excess NEM before the column was washed 3 times with 500 µL 20% MeCN. The third and final reduction and alkylation was done in solution by eluting the peptide from the column with 300 µL 80% MeCN before 20 µL 0.1 M TCEP was added and left to incubate for 1 hour to reduce the remaining disulfide bridges. Then 20 µL of a 0.12 M NCM solution was added to complete the alkylation of the last cysteines.

Reduced and alkylated peptides were analyzed using the same MS instrument, column and mobile phase as described in the sequence analysis method. Mass spectrometric identification parameters were similar as for Albert et al. [20]. For both peptides a collision energy ramp of 26-58 eV was used for optimal fragmentation.

2.7. Antibacterial Activity Assay

All MeCN SPE fractions and HPLC fractions collected from the 40% MeCN SPE, as well as the isolated St-CRPs were screened for activity against *Escherichia coli* (ATCC 25922), *Pseudomonas aeruginosa* (ATCC 27853), *Staphylococcus aureus* (ATCC 9144), *Corynebacterium glutamicum* (ATCC 13032) and *Bacillus subtilis* (ATCC 23857). All isolates were grown in Mueller-Hinton (MH) broth (Difco Laboratories, Detroit, MI, USA) at room temperature. The assays were performed in 96 microwell plates (Thermo Fisher Scientific, Roskilde, Denmark) as previously described [21], but with a few exceptions; the cultures were diluted in MH broth to a concentration of 2.5-3.0×10^4 bacteria/mL, and 50 µL was added to each well in a plate preloaded with 50 µL of either SPE in a dilution series, HPLC fractions, or a dilution series of St-CRPs and controls. The purified peptides (>95% purity based on UHPLC-DAD-MS analysis) were dissolved in DMSO (Sigma-Aldrich), vortexed, and added MQ-H_2O to end up with a stock solution of 500 µg/mL containing 2.5% DMSO. The stock solution was diluted in MQ-H_2O to obtain final test concentrations ranging from 2.5-100 µg/mL. Oxytetracycline (Sigma-Aldrich) was used as a positive (antibacterial) control (0.04-40 µM), MQ-H_2O as a negative (growth) control, and a DMSO control was made using the highest tested concentration of DMSO (0.25% DMSO). All experiments were done in technical triplicates. The bacterial growth at 35 ˚C was monitored with an EnVision Multilable Reader (PerkinElmer, Llantrisant, United Kingdom), where the optical density (OD_{595}) was measured every hour for 24 hours. The minimum inhibitory concentration (MIC) was defined as the concentration resulting in >90% reduction in OD_{595} after 24 hours compared to the negative (bacterial growth) control.

2.8. Human Cell Viability Assay

The cytotoxic activities of St-CRP-1 was tested on two cell lines: A2058 (a human melanoma cancer cell line, ATCC CRL-11147TM) and MRC-5 (a non-malignant human fibroblast cell line, ATCC CCL-171). The peptides were assayed using a two-fold dilution series, ranging from 5-100 µg/mL. The assays were performed as previously described [22]. Cell viability calculation: cell survival (%) = (absorbance treated

wells − absorbance positive control)/(absorbance negative control − absorbance positive control) × 100. Both assays were performed in technical triplicates in two independent experiments.

2.9. Brine Shrimp Lethality Assay

St-CRP-1 was tested for toxic effect against *Artemia salina* nauplii as previously described by Haug et al. [23], with some modifications. Sterile filtered (0.22 µm) seawater was added to an illuminated petri dish with a teaspoon of dried brine shrimp eggs and incubated at 22-24 ˚C. After 48 hours of incubation, 100 µL of seawater containing 10-20 freshly hatched nauplii was added to separate wells in 96 microwell plates (Thermo Fisher Scientific). Three dilutions of the peptide were added to the wells (in duplicates) at final concentrations of 100, 50 and 25 µg/mL. The plates were incubated with illumination at 22-24 ˚C, and dead nauplii were counted after 6 (acute toxicity) and 24 hours (chronic toxicity). MQ-H_2O was used as negative control, and potassium dichromate ($K_2Cr_2O_7$, Sigma, 10-1000 ppm) was used as a positive control.

3. Results and Discussion

3.1. Peptide Purification and Mass Spectrometry Analysis

Colonies of *S. turgens*, collected from the coast of Svalbard, were lyophilized, crunched, and extracted with 60% acidified MeCN. After removing the sediment, the extract was separated into an organic phase and an aqueous phase (containing a high concentration of salt). The aqueous phase was subjected to SPE to remove the salt content, and to gain a rough compound separation based on their polarity. Antibacterial screening was done on the organic phase and the 5 fractions obtained after solid phase extraction. All fractions tested displayed antibacterial activity, but the 40% MeCN SPE fraction was the most potent fraction, but mainly against the Gram-positive strains *C. glutamicum* and *B. subtilis* (Table S1 in the SI). This fraction was therefore subjected to further fractionation by preparative RP-HPLC, and the collected one-minute HPLC fractions were tested against the same panel of bacteria as the SPE fractions to get a pointer towards which fractions/compounds might be causing the antibacterial effect. Such bioassay-guided purification has proven effective when discovering and isolating novel marine AMPs [21,24,25]. Several of the obtained HPLC fractions (fractions 40-52), containing compounds eluting at approximately 30-40% MeCN, displayed antibacterial activity against several of the test strains (Figure 1).

HR-MS analysis of the active fractions proved that many of them (fractions 42-43 and 47-51) contained the previously described AMPs turgencin A and B, both also having various oxidized versions (Figure 1) [18]. The turgencins (3.5-3.7 kDa) was originally isolated from the 80% MeCN SPE fraction due to much higher abundance of these peptides in that SPE fraction [18]. In the present study, HPLC fraction 44 (displaying

activity against all test strains), contained only minor amounts of the previously described AMP turgencin A_{Mox1} [18], indicating that another compound or compounds might be responsible for the activity observed. The most abundant molecule in this fraction was a smaller peptide that we later named, St-CRP-1. Mass-to-charge (*m/z*) ions recorded for this peptide were *m/z* 1019.8 and *m/z* 680.2, corresponding to $[M + 2H]^{2+}$ and $[M + 3H]^{3+}$, respectively. The monoisotopic mass of St-CRP-1 was determined to be 2037.67 Da by doing deconvolution of the isotopes.

Another peptide with similar size as St-CRP-1 was discovered in the broad-spectrum antibacterial HPLC fraction 48 (Figure 1). This peptide was named St-CRP-2. *m/z* ions recorded for this peptide were *m/z* 1003.9 and *m/z* 669.6, corresponding to $[M + 2H]^{2+}$ and $[M + 3H]^{3+}$, respectively. The monoisotopic mass of St-CRP-2 was determined to be 2005.75 Da. However, the most abundant molecule in this active HPLC fraction was the AMP turgencin B_{Mox2}. The peaks containing the St-CRPs are marked in bold in the RP-HPLC-DAD chromatogram in Figure 1.

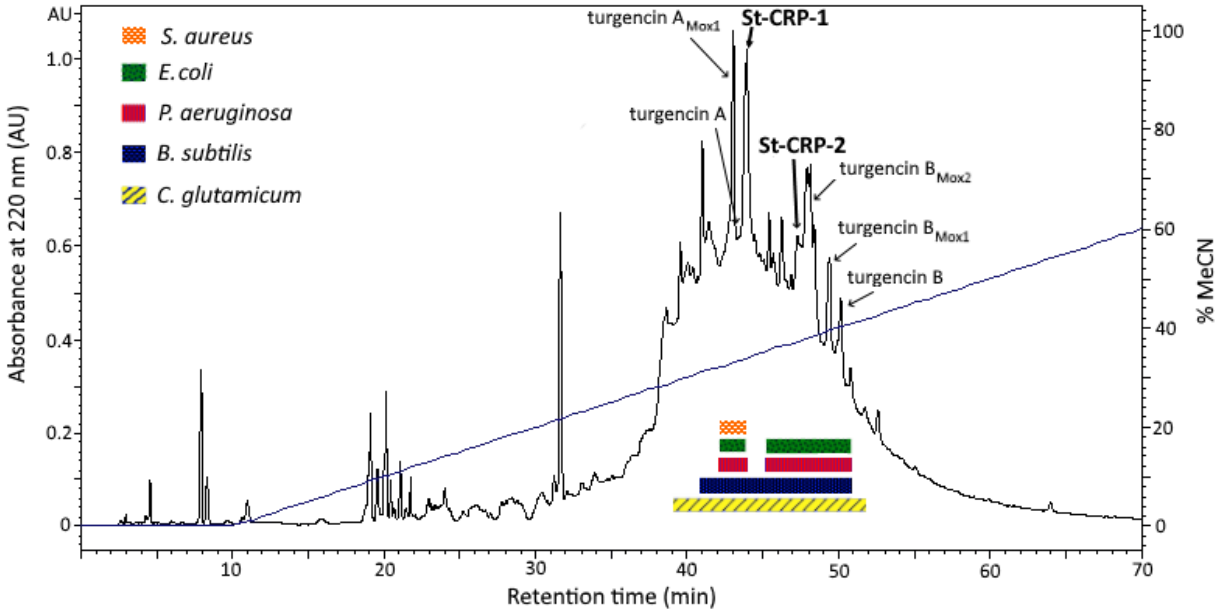

Figure 1. Preparative RP-HPLC-DAD chromatogram (recorded at 220 nm) of the 40% MeCN SPE fraction of *Synoicum turgens*. The peak fractions containing the St-CRP peptides and the turgencins are marked with arrows. HPLC fractions displaying antibacterial activity are marked with colored boxes below the chromatogram. The blue line shows the linear gradient (0-60%) of MeCN containing 0.05% TFA.

The St-CRPs proved to be challenging to purify as they coeluted with several other peptides with similar hydrophobicity. Another obstacle was the poor solubility after drying the isolated peptides. A prolonged process of optimizing the RP-HPLC method provided enough material of St-CRP-1 (1.2 mg) for nuclear

magnetic resonance (NMR) and bioactivity analysis. The amount of pure St-CRP-2 (0.6 mg) was only sufficient for the antibacterial assays and MS analysis. UPLC-DAD analysis of the isolated peptides indicated a purity of >95% for both the St-CRPs (Figure S1 and S2 in the SI).

3.2. Sequence Analysis

Edman degradation analysis of St-CRP-1 revealed an 18-residue N-terminal sequence (CCDQCYGFCRLVDNCCNS). The calculated monoisotopic mass of this sequence, assuming the six cysteines forms three disulfide bridges, is 2038.70 Da. The mass difference between measured and calculated mass of around -1 Da can be explained by a C-terminally amidated serine. C-terminal amidation occurs in all previously sequenced peptides from *S. turgens* [18], and is a known feature in antimicrobial peptides from eukaryotic organisms [26]. The sequence was confirmed by NMR analysis.

The sequence of St-CRP-2 was obtained by *de novo* sequencing using MS/MS. The peptide was treated with TCEP in acidic pH to break the disulfide bonds and subsequently analyzed on a UPLC-QToF-MS apparatus. This analysis resulted in a good sequence coverage, providing a 19-residue sequence (SCCEYCSXSCXVSGXXCCQ) with a C-terminally amidated glutamine (Figure S3 in the SI). The proposed fragments from MS-product (UCSF, ProteinProspector v.6.3.1, http://prospector.ucsf.edu) corresponded to the observed fragments in the MS/MS analysis and confirmed the sequence. Four amino acids in the MS/MS spectra were determined to be either leucine or isoleucine (both having a monoisotopic mass of 113.08 Da), but the method used could not distinguish between them, hence the X positions noted in the sequence. The calculated monoisotopic mass of this sequence, assuming three disulfide bridges, C-terminal amidation, and replacing X with leucine, is 2005.75 Da – the same mass as measured HR-MS.

Sequence alignment of the St-CRPs illustrates the similarities between the two peptides (Figure 2). They share the same cysteine pattern (CC-C-C-CC), are both C-terminally amidated, and neutrally charged with a calculated pI of 6.94 (St-CRP-1) and 6.58 (St-CRP-2). NCBI BLAST analyses revealed no sequence similarities to other known peptides or proteins. In addition, no similarities were found to any of the major AMP families present in the $CAMP_{R3}$ database by using the CAMPSign tool [27]. Furthermore, only 191 of the 3346 antimicrobial peptides registered at APD3 have a net charge of 0, whereof 41 have structures with 3 disulfide bonds. Most of these cysteine rich neutral peptides comes from plants (38 out 41), and their size differs between 26-46 amino acids [28].

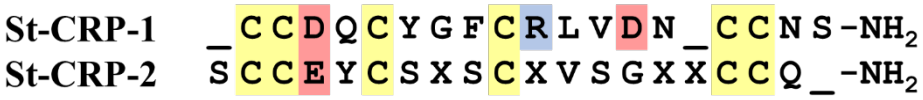

Figure 2. Sequence alignment of St-CRP-1 and St-CRP-2. Gaps (_) are introduced to maximize the alignment. Residues: yellow = Cys, red = acidic amino acids, blue = basic amino acid, X = Ile/Leu.

Knowledge obtained of the structures gave some clues about the solubility obstacles. Prior to this current information, the peptides were subjected to be dissolved in pure water, but with variable result. The solubility of the peptides improved when adding a small amount of DMSO first, before diluting the DMSO concentration considerately with water. DMSO at high concentrations has been known to interfere with bioassays, and the final concentration needs be kept at a minimum, with appropriate controls, to avoid false positives [29].

3.3. Structure Determination

The water-suppressed ^{1}H spectra of St-CRP-1 was clean, with no impurities above 5 mol%, and well-resolved. ^{15}N-HSQC and TOCSY spectra enabled the unambiguous assignment of all 18 amino acid residues (Table S2 and S3 in the SI). The sequence was assigned by NOE hopping supported by high resolution HMBC correlations through the backbone carbonyls where possible. In total 69 inter-residue backbone-backbone and backbone-sidechain through-space correlations could be extracted from the collected 100, 200 and 400 ms mixing time NOESYs. These NOEs were consistent with the sequence for St-CRP-1 (Figure 3).

Figure 3. Inter-residual NOEs for St-CRP-1 between adjacent residues extracted from 100, 200, and 300 ms NOESY NMR experiments. The line thickness for the 'i, i+1' couplings indicate the strength of the correlation: the thicker the line, the stronger the crosspeak. For 'i, i+2' and greater, the lines indicate which two residues dipolar couplings can be identified between specified backbone residues.

An additional 144 non-sequential inter- and intra-residual NOEs were extracted, to a combined total of 213 unique NOEs. The NOEs were qualitatively classified as one of four categories: Strong, Medium, Weak, Very Weak based on their intensities and correspond with upper limit distance constraints of 2.7, 3.5, 5.0, and 6.0 Å respectively.

Three dimensional structures were generated by simulated annealing protocols to produce a series of energetically minimized structures. First, structures were generated from an extended chain without any designation of disulfide bonds, applying only the distance constraints to fold the peptide. Three iterations were calculated, where any violations of interatomic distances due to overlaps or other sources of erroneous input were resolved to refine the fold. A batch production run of 500 structures was generated using the iterated constraints, and the 10 most energetically favorable structures were selected, and the sulfur-sulfur interatomic distances were plotted (Figure 4). By comparing the distances between each cysteine sulfur, the nearest and therefor most likely bonding partners were identified. The determined disulfide bridge partners were Cys1-Cys16, Cys2-Cys9, Cys5-Cys15, giving a C1-C6/C2-C4/C3-C5 disulfide pattern.

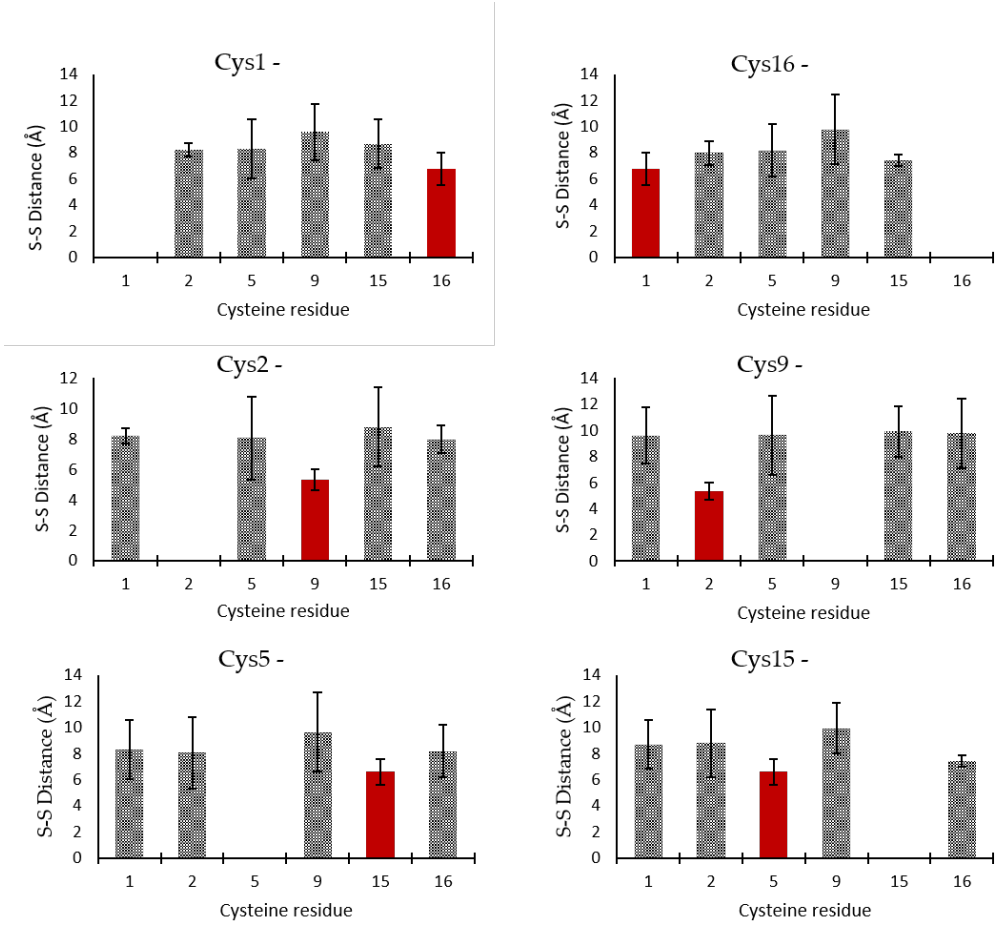

Figure 4. Average inter-sulfur distances for the six cysteines identified in St-CRP-1. The shortest distance is highlighted in red, being consistent with a C1-C6/C2-C4/C3-C5 disulfide pattern.

A final production batch was calculated with the C1-C6/C2-C4/C3-C5 disulfide pattern, using the same simulated annealing protocol together with the refined distance constraints, adding also dihedral bond angle constraints predicted from the H, N, C, CA, CB, HA and HB chemical shifts using TALOS+. The lowest energy structures (energies below 2 kcal) were selected for analysis, representing 38 of the 500 structures. Evaluation of the structures revealed that the structures adopt one of two energetically equivalent conformations – an open fold with a small stretch of helix (Figure 5a and b – 21/38 structures), and a knot conformation (Figure 5c and d – 17/38 structures).

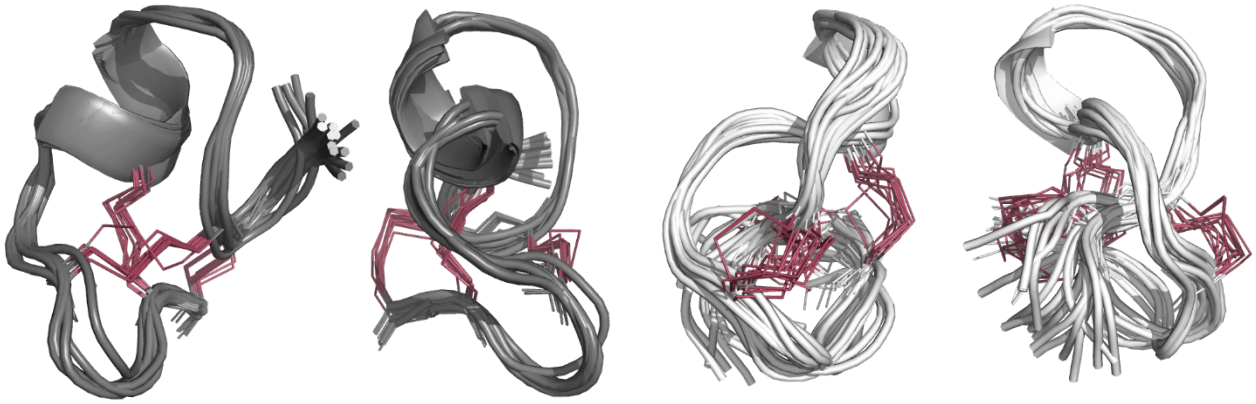

(a) (b) (c) (d)

Figure 5. The lowest energy structures generated from the simulated annealing of St-CRP-1 with a defined disulfide bridge pattern of C1-C6/C2-C4/C3-C5 in combination with NOE constraints and TALOS+ predicted dihedrals. The open structure (a), and the 90-degree rotated view (b), compared to the knot structure (c) and its rotated view (d).

Both these structures satisfied the experimental constraints equally well. The structures were evaluated for correlations that would be expected according to the conformation adopted but were absent in the data set – indicating if one conformation is more or less supported by the acquired data. The knot structure is more condensed and if this conformation was populated one would expect to observe a range of correlations between the C-terminus and residues 6-9 where the knot is formed. The clearest example was between HA-Tyr6 and HA-Cys16 (a distance of 4 Å). Since this correlation was not observed in the data and no clear inconsistencies with the open conformation could be found, we introduced a repulsion between HA Tyr6 and HA Cys16 and recalculated the structures. This abolished the knot conformation and resulted in a final structure ensemble presented in Figure 6. Three out of the 31 lowest energy structures had a backbone RMSD of more than 2.5 Å from the lowest energy structure and these were omitted from the graphical representation as a minor outlying conformation for visual clarity. The backbone RMSD of the other 28 structures were all 1.0 Å or less (Table S4 in the SI).

A short alpha-helical loop stretches between Cys9 and Val12 could be identified and was amply represented in the calculated structure ensemble (15 out of 19 in the final ensemble). Strong NH(i)-NH(i+1), and medium strength αH(i)- NH(i+1) NOEs were recorded for this stretch, which is consistent with an alpha-helical conformation being populated. Furthermore, two NH(i)-NH(i+3) correlations were also identified from residues 8 to 11 and 10 to 13, which is consistent with an alpha helix.

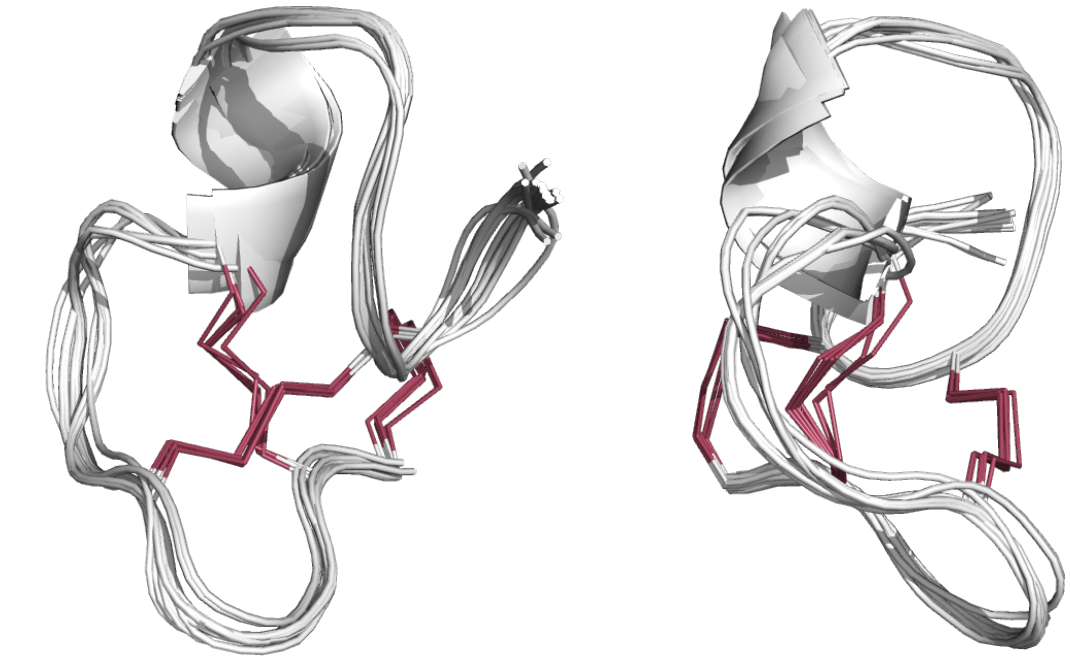

(a) (b)

Figure 6. The 19 lowest energy structure ensembles generated from the simulated annealing of St-CRP-1 with the defined disulfide bridge pattern of C1-C6/C2-C4/C3-C5 in combination with NOE constraints and TALOS+ predicted dihedrals (a), and the 90-degree rotated view (b).

The disulfide bridge pattern for both peptides was confirmed with LC-MS/MS by using a sequential alkylation method, introduced by Albert et al. [20]. The peptides were reduced and alkylated with different maleimides on solid phase before sequencing. The reduction and alkylation process resulted in a mixture of different alkylation patterns where the number of cysteines with different alkylating agents were 2xNMM + 4xNEM, 4xNMM + 2xNEM, 2xNMM + 4xNCM, 4xNMM + 2xNCM, 2xNEM + 4xNCM, 4xNEM + 2xNCM, 2xNMM + 2xNEM + 2xNCM, 2xNMM and 4xNMM without further alkylation, and 6xNMM for both peptides. In addition, St-CRP-1 got a pattern of 2xNMM+ 2xNEM without further reduction and alkylation that was not seen for St-CRP-2. Several of the alkylation patterns could be used to determine the disulfide connectivity, but the most convenient pattern was the 2xNMM + 2xNEM + 2xNCM, where each

bridge results in a pair of cysteines with the same alkylating agent. The other alkylating patterns were used to confirm the findings from this pattern.

To determine cysteine connectivity by MS/MS analysis, the $[M+2H]^{2+}$ ion and the corresponding acetylated ion was used for both peptides. The m/z value of this ion differs depending on the alkylation pattern, but for the 2xNMM + 2xNEM + 2xNCM pattern the St-CRP-1 peptide gave m/z = 1438.04 (acetylated m/z = 1459.05 (Figure 7) and the St-CRP-2 peptide gave m/z = 1422.08 (acetylated m/z = 1443.09) (Figure 8). The observed b- and y-ions of the acetylated $[M+2H]^{2+}$ of St-CRP-1 indicates that Cys1 and Cys16 are alkylated with maleimide NEM, Cys2 and Cys9 with NMM, and Cys5 and Cys15 with NCM (Figure 7). This verifies the C1-C6/C2-C4/C3-C5 connectivity for St-CRP-1 obtained by NMR.

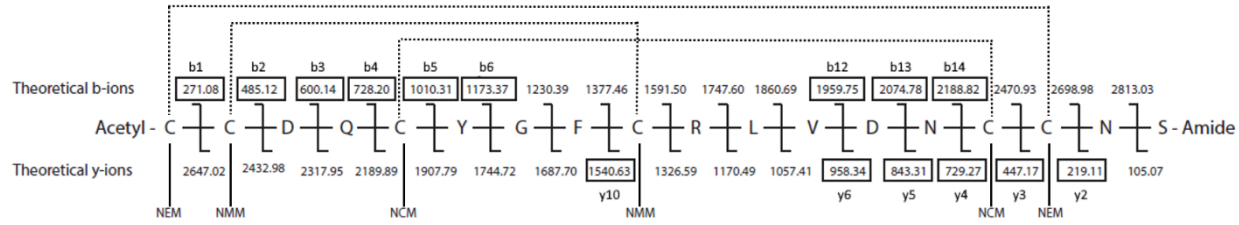

Figure 7. The alkylation pattern 2xNEM + 2xNMM + 2xNCM of the acetylated doubly charged $[M+2H]^{2+}$ molecular ion of St-CRP-1. The framed masses are b- and y-ions identified in the MS/MS spectra. The dotted lines illustrate the disulfide bridges.

St-CRP-2 showed the same disulfide bridge pattern as St-CRP-1. From the acetylated $[M+2H]^{2+}$ ion of St-CRP-2, two spectra showed the 2xNMM + 2xNEM + 2xNCM pattern. The observed b-ions, b-ions with water loss, y-ions, and y-ions with ammonia loss identified Cys1 and Cys16 to be alkylated with maleimide NCM, Cys2 and Cys9 with NEM, and Cys5 and Cys15 with NMM (Figure 8).

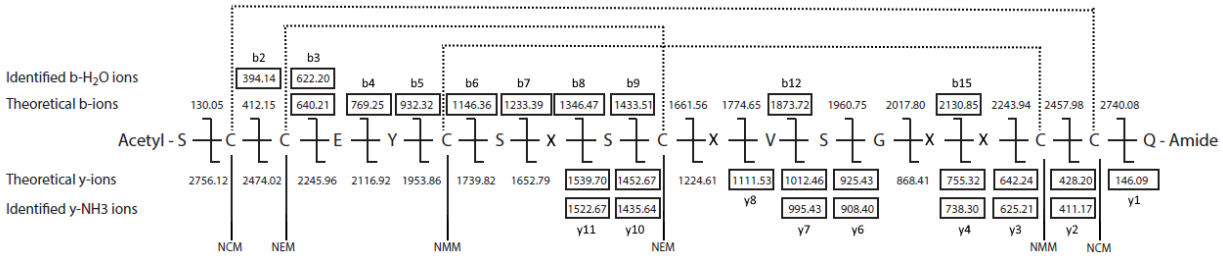

Figure 8. The alkylation pattern 2xNCM + 2xNEM + 2xNMM of the acetylated doubly charged $[M+2H]^{2+}$ molecular ion of St-CRP-2. The framed masses are b-, b-H_2O, y- and y-NH_3 ions identified in the MS/MS spectra. The dotted lines illustrate the disulfide bridges. The X in the sequence is either I or L.

The same cysteine connectivity was confirmed in another spectrum of St-CRP-2, where the identified fragments showed Cys1 and Cys16 to be alkylated with maleimide NEM, Cys2 and Cys9 with NMM, and Cys5 and Cys15 with NCM (Figure S4 in the SI). This gave the same cysteine pattern as for St-CRP-1, a C1-C6/C2-C4/C3-C5 connectivity. In contrast, the turgencins have a C1-C6/C2-C5/C3-C4 connectivity [18]. The St-CRPs share the same cysteine connectivity as mammalian alpha-defensins [8], and other AMPs such as aurelin from the jellyfish *Aurelia aurita* [30] and damicornin from the coral *Pocillopora damicornis* [31]. Other than the cysteine connectivity, these peptides share few similarities with the St-CRPs. They are all cationic peptides (damicornin with as much as 9 charges) and bigger in size (<30 amino acids), while the St-CRPs have a neutral net charge and less than 20 amino acids.

Another peptide family that has a C1-C6/C2-C4/C3-C5 connectivity is the M2 family of the conotoxins. In addition, the majority of the entire M family share the same cysteine pattern (CC-C-C-CC) as the St-CRPs [32]. These cysteine pattern similarities are interesting, but other than that, no relations can be drawn between the M2-family and the St-CRPs based on the information that is available. Many conotoxin families are well described in literature, but there are limited published data on the biological targets and mechanism of action of the peptides coming from the M2 branch. It has been reported that some of these peptides gives a strong excitatory behavior in mice [32].

3.4. Biological Activity

As the HPLC-fractions containing the St-CRPs possessed antibacterial properties (Figure 1), the purified peptides were tested against the same panel of bacteria to verify the antibacterial activity. In addition, St-CRP-1 was tested for toxicity against the brine shrimp *A. salina*, and for cytotoxic activity against a human melanoma cancer cell line A2058, and a non-malignant human fibroblast cell line MRC-5. The St-CRPs showed only moderate activity against a few bacterial strains. St-CRP-1 displayed a MIC-value of 50 µg/mL (24.6 µM) against *C. glutamicum* and *B. subtilis*, whereas St-CRP-2 displayed a MIC-value of 100 µg/mL (49.2 µM) *B. subtilis* (Table 1). None of the peptides were active against the Gram-negative bacterial strains at the highest concentration tested (100 µg/mL), which equals to 49.1 µM for St-CRP-1 and 49.2 µM for St-CRP-2, respectively. Also, St-CRP-1 showed no activity in any of the toxicity assays at the highest concentration tested. This conforms well with other neutral CRPs found in the APD3, whereof half of these peptides have unknown bioactivity [28]. In some cases, like with the varv peptides from the plant *Viola arvensis*, the plant produces several neutral CRPs with both known bioactivity (varv peptide A – anticancer, and varv peptide E – antiviral and hemolytic) and unknown bioactivity (varv peptide C and D) [33,34].

Table1. Antimicrobial and cytotoxic activity of St-CRPs.

	Antimicrobial activity (MIC; µg/mL)					Brine shrimp toxicity (LC_{50}; µg/mL)	Cytotoxic activity (IC_{50}; µg/mL)	
Peptide	**Cg**	**Bs**	**Sa**	**Ec**	**Pa**	**As**	**A2058**	**MRC-5**
St-CRP-1	50	50	>100	>100	>100	>100	>100	>100
St-CRP-2	>100	100	>100	>100	>100	N.t	N.t	N.t

Cg - *Corynebacterium glutamicum*, Bs - *Bacillus subtilis*, Sa - *Staphylococcus aureus*, Ec - *Escherichia coli, Pa – Pseudomonas aeruginsa,* As - *Artemia salina*. N.t : Not tested

Compared to some of the turgencins [18], which in general showed much higher antibacterial activity against the same panel of bacteria, one could assume that the main function of the St-CRPs is not to interfere with (inhibit the growth of or kill) bacteria directly. Here we have tested purified peptides alone *in vitro* against standard laboratory bacteria. It is plausible that the peptides would be more potent towards marine pathogenic bacteria, which is a bigger threat to the animal than the terrestrial strains tested. This have been observed in other studies of marine derived antimicrobial peptides [24]. However, the peptides might also have other host defense functions *in vivo*. Perhaps the St-CRPs generates a synergistic effect together with the turgencins or other compounds from the ascidian. The HPLC-fraction containing St-CRP-1 was active against all bacteria tested, and the fraction containing St-CRP-2 was active against 4 out of 5 strains tested. The St-CRPs was the dominant compounds in their respective HPLC-fractions. Since the St-CRPs showed no activity at 100 µg/mL against the Gram-negative bacterial strains tested (*E. coli* and *P. aeruginosa*) as well as against *S. aureus*, the activity had to come from other compounds in the fractions or be due to synergistic effect between the St-CRPs and other compounds. Many organisms produce cocktails of different AMPs to fight for their survival, and the main function of many of these peptides are yet to be explored [34].

4. Conclusions

The world-wide spread of antibiotic resistance has fueled the search for and discovery of novel antibacterial molecules. AMPs are promising candidates because of their broad-spectrum antimicrobial properties and fewer cases of antimicrobial resistance developed towards them. In addition, cysteine-rich AMPs (or CRPs) are generally also less prone to proteolytic degradation. In the present study, two novel cystine-rich peptides, St-CRP-1 and St-CRP-2, were isolated from the Arctic ascidian, *S. turgens*. The peptides consist of 18-19 amino acids, are neutrally charged, and share the same cysteine connectivity as alpha-defensins and M2 family of the conotoxins, a C1-C6/C2-C4/C3-C5 connectivity. A gene characterization of the St-CRPs could reveal the evolutionary relationship between them and other CRPs. The St-CRPs showed moderate

antibacterial activity, and no cytotoxicity against mammalian cells. Ascidians have proven to be a promising resource for finding novel peptides - potential templates for drug development.

Acknowledgments: This work was supported by grant from UiT, The Arctic University of Norway. The technical assistance provided by Hege Devold is much appreciated. The crew and divers of the research vessel Helmer Hansen are acknowledged for collection of animals.

Conflict of Interest: The authors declare no conflict of interest.

References

1. Cheung, R.C.F.; Ng, T.B.; Wong, J.H. Marine peptides: Bioactivities and applications. *Mar. Drugs* **2015**, *13*, 4006-4043, https://doi.org/10.3390/md13074006
2. Fosgerau, K.; Hoffmann, T. Peptide therapeutics: current status and future directions. *Drug Discov. Today* **2015**, *20*, 122-128, https://doi.org/10.1016/j.drudis.2014.10.003
3. Høst, A.; Halken, S. Hypoallergenic formulas – when, to whom and how long: after more than 15 years we know the right indication! *Allergy* **2004**, *59*, 45-52, https://doi.org/10.1111/j.1398-9995.2004.00574.x
4. Lau, J.L.; Dunn, M.K. Therapeutic peptides: Historical perspectives, current development trends, and future directions. *Bioorgan. Med. Chem.* **2018**, *26*, 2700-2707, https://doi.org/10.1016/j.bmc.2017.06.052
5. Ganz, T. The role of antimicrobial peptides in innate immunity. *Integr. Comp. Biol.* **2003**, *43*, 300-304, http://dx.doi.org/10.1093/icb/43.2.300
6. Hancock, R.E.W.; Sahl, H.-G. Antimicrobial and host-defense peptides as new anti-infective therapeutic strategies. *Nat. Biotechnol.* **2006**, *24*, 1551-1557, http://dx.doi.org/10.1038/nbt1267
7. Hancock, R.; Patrzykat, A. Clinical development of cationic antimicrobial peptides: from natural to novel antibiotics. *Curr. Drug. Targets. Infect. Disord.* **2002**, *2*, 79-83, https://doi.org/10.2174/1568005024605855
8. Ganz, T. Defensins: antimicrobial peptides of innate immunity. *Nat. Rev. Immunol.* **2003**, *3*, 710-720, https://doi.org/10.1038/nri1180
9. Raj, P.A.; Dentino, A.R. Current status of defensins and their role in innate and adaptive immunity. *FEMS Microbiol. Lett.* **2002**, *206*, 9-18, https://doi.org/10.1111/j.1574-6968.2002.tb10979.x
10. Muttenthaler, M.; King, G.F.; Adams, D.J.; Alewood, P.F. Trends in peptide drug discovery. *Nat. Rev. Drug Discov.* **2021**, *20*, 309-325, https://doi.org/10.1038/s41573-020-00135-8
11. Wang, C.K.; Craik, D.J. Designing macrocyclic disulfide-rich peptides for biotechnological applications. *Nat. Chem. Biol.* **2018**, *14*, 417-427, https://doi.org/10.1038/s41589-018-0039-y
12. Tombling, B.J.; Wang, C.K.; Craik, D.J. EGF-like and other disulfide-rich microdomains as therapeutic scaffolds. *Angew. Chem. Int. Edit.* **2020**, *59*, 11218-11232, https://doi.org/10.1002/anie.201913809
13. Schwarz, E. Cystine knot growth factors and their functionally versatile proregions. *Biol. Chem.* **2017**, *398*, 1295-1308, https://doi.org/10.1515/hsz-2017-0163
14. Wu, R.; Patocka, J.; Nepovimova, E.; Oleksak, P.; Valis, M.; Wu, W.; Kuca, K. Marine invertebrate peptides: Antimicrobial peptides. *Front. Microbiol.* **2021**, *12*, 785085, https://doi.org/10.3389/fmicb.2021.785085

15. Casertano, M.; Menna, M.; Imperatore, C. The ascidian-derived metabolites with antimicrobial properties. *Antibiotics* **2020**, *9*, 510, https://doi.org/10.3390/antibiotics9080510
16. Pavlicevic, M.; Maestri, E.; Marmiroli, M. Marine bioactive peptides-An overview of generation, structure and application with a focus on food sources. *Mar. Drugs* **2020**, *18*, 424, https://doi.org/10.3390/md18080424
17. Arumugam, V.; Venkatesan, M.; Ramachandran, S.; Sundaresan, U. Bioactive peptides from marine ascidians and future drug development–A review. *Int. J. Pept. Res. Ther.* **2018**, *24*, 13-18, https://doi.org/10.1007/s10989-017-9662-9
18. Hansen, I.K.Ø.; Isaksson, J.; Poth, A.G.; Hansen, K.Ø.; Andersen, A.J.C.; Richard, C.S.M.; Blencke, H.-M.; Stensvåg, K.; Craik, D.J.; Haug, T. Isolation and characterization of antimicrobial peptides with unusual disulfide connectivity from the colonial ascidian *Synoicum turgens*. *Mar. Drugs* **2020**, *18*, 51, https://doi.org/10.3390/md18010051
19. Haug, T.; Kjuul, A.K.; Stensvåg, K.; Sandsdalen, E.; Styrvold, O.B. Antibacterial activity in four marine crustacean decapods. *Fish Shellfish Immunol.* **2002**, *12*, 371-385, http://dx.doi.org/10.1006/fsim.2001.0378
20. Albert, A.; Eksteen, J.J.; Isaksson, J.; Sengee, M.; Hansen, T.; Vasskog, T. General approach to determine disulfide connectivity in cysteine-rich peptides by sequential alkylation on solid phase and mass spectrometry. *Anal. Chem.* **2016**, *88*, 9539-9546, https://doi.org/10.1021/acs.analchem.6b02115
21. Solstad, R.G.; Li, C.; Isaksson, J.; Johansen, J.; Svenson, J.; Stensvåg, K.; Haug, T. Novel antimicrobial peptides EeCentrocins 1, 2 and EeStrongylocin 2 from the edible sea urchin *Echinus esculentus* have 6-br-trp post-translational modifications. *PloS One* **2016**, *11*, e0151820, https://doi.org/10.1371/journal.pone.0151820
22. Hansen, K.Ø.; Andersen, J.H.; Bayer, A.; Pandey, S.K.; Lorentzen, M.; Jørgensen, K.B.; Sydnes, M.O.; Guttormsen, Y.; Baumann, M.; Koch, U.; Klebl, B.; Eickhoff, J.; Haug, B.E.; Isaksson, J.; Hansen, E.H. Kinase chemodiversity from the Arctic: The breitfussins. *J. Med. Chem.* **2019**, *62*, 10167-10181, https://doi.org/10.1021/acs.jmedchem.9b01006
23. Haug, T.; Stensvåg, K.; Olsen, Ø.M.; Sandsdalen, E.; Styrvold, O.B. Antibacterial activities in various tissues of the horse mussel, *Modiolus modiolus*. *J. Invertebr. Pathol.* **2004**, *85*, 112-119, https://doi.org/10.1016/j.jip.2004.02.006
24. Moe, M.K.; Haug, T.; Sydnes, M.O.; Sperstad, S.V.; Li, C.; Vaagsfjord, L.C.; de la Vega, E.; Stensvåg, K. Paralithocins, antimicrobial peptides with unusual disulfide connectivity from the red king crab, *Paralithodes camtschaticus*. *J. Nat. Prod.* **2018**, *81*, 140-150, https://doi.org/10.1021/acs.jnatprod.7b00780
25. Stensvåg, K.; Haug, T.; Sperstad, S.V.; Rekdal, Ø.; Indrevoll, B.; Styrvold, O.B. Arasin 1, a proline–arginine-rich antimicrobial peptide isolated from the spider crab, *Hyas araneus*. *Dev. Comp. Immunol.* **2008**, *32*, 275-285, https://doi.org/10.1016/j.dci.2007.06.002
26. Merkler, D.J. C-terminal amidated peptides: production by the in vitro enzymatic amidation of glycine-extended peptides and the importance of the amide to bioactivity. *Enzyme Microb. Tech.* **1994**, *16*, 450-456, https://doi.org/10.1016/0141-0229(94)90014-0
27. Waghu, F.H.; Barai, R.S.; Idicula-Thomas, S. Leveraging family-specific signatures for AMP discovery and high-throughput annotation. *Sci. Rep.* **2016**, *6*, 24684, https://doi.org/10.1038/srep24684
28. Wang, G.; Li, X.; Wang, Z. APD3: the antimicrobial peptide database as a tool for research and education. *Nucleic Acids Res.* **2015**, *44*, D1087-D1093, https://doi.org/10.1093/nar/gkv1278
29. Ansel, H.C.; Norred, W.P.; Roth, I.L. Antimicrobial activity of dimethyl sulfoxide against *Escherichia coli*, *Pseudomonas aeruginosa*, and *Bacillus megaterium*. *J. Pharm. Sci.* **1969**, *58*, 836-839, https://doi.org/10.1002/jps.2600580708
30. Ovchinnikova, T.V.; Balandin, S.V.; Aleshina, G.M.; Tagaev, A.A.; Leonova, Y.F.; Krasnodembsky, E.D.; Men'shenin, A.V.; Kokryakov, V.N. Aurelin, a novel antimicrobial peptide

from jellyfish *Aurelia aurita* with structural features of defensins and channel-blocking toxins. *Biochem. Bioph. Res. Co.* **2006**, *348*, 514-523, https://doi.org/10.1016/j.bbrc.2006.07.078

31. Vidal-Dupiol, J.; Ladrière, O.; Destoumieux-Garzón, D.; Sautière, P.-E.; Meistertzheim, A.-L.; Tambutté, E.; Tambutté, S.; Duval, D.; Fouré, L.; Adjeroud, M.; Mitta, G. Innate immune responses of a scleractinian coral to vibriosis. *J. Biol. Chem.* **2011**, *286*, 22688-22698, https://doi.org/10.1074/jbc.M110.216358
32. Jacob, R.B.; McDougal, O.M. The M-superfamily of conotoxins: a review. *Cell. Mol. Life Sci.* **2010**, *67*, 17-27, https://doi.org/10.1007/s00018-009-0125-0
33. Svangård, E.; Göransson, U.; Hocaoglu, Z.; Gullbo, J.; Larsson, R.; Claeson, P.; Bohlin, L. Cytotoxic cyclotides from *Viola tricolor*. *J. Nat. Prod.* **2004**, *67*, 144-147, https://doi.org/10.1021/np0301011
34. Göransson, U.; Luijendijk, T.; Johansson, S.; Bohlin, L.; Claeson, P. Seven novel macrocyclic polypeptides from *Viola arvensis*. *J. Nat. Prod.* **1999**, *62*, 283-286, https://doi.org/10.1021/np9803878

Supporting information

Isolation and characterization of St-CRPs: Cysteine-rich peptides from the Arctic marine ascidian *Synoicum turgens*

Ida K. Ø. Hansen [1], Philip B. Rainsford [2], Johan Isaksson [2], Kine Ø. Hansen[3], Klara Stensvåg [1], Anastasia Albert [4], Terje Vasskog [5] and Tor Haug [1,*]

[1] The Norwegian College of Fishery Science, Faculty of Biosciences, Fisheries and Economics, UiT The Arctic University of Norway, Breivika, N-9037 Tromsø, Norway; klara.stensvag@uit.no (K.S.)

[2] Department of Chemistry, Faculty of Science and Technology, UiT The Arctic University of Norway, Breivika, N-9037 Tromsø, Norway; philip.rainsford@uit.no (P.B.R.); johan.isaksson@uit.no (J.I.)

[3] Marbio, UiT The Arctic University of Norway, N-9037, Tromsø, Norway; kine.o.hanssen@uit.no

[4] Norce, Siva Innovasjonssenter, Sykehusveien 21, 9019 Tromsø; anastasia.albert@norut.no (A.A.)

[5]Department of Pharmacy, Faculty of Health Sciences, UiT The Arctic University of Norway, Breivika, N-9037 Tromsø, Norway

[*] Correspondence: ida.k.hansen@uit.no; Tel.: +47-77-64-92-66 (I.K.Ø.H.), tor.haug@uit.no; Tel.: +47-77-64-60-71 (T.H.)

Table of contents

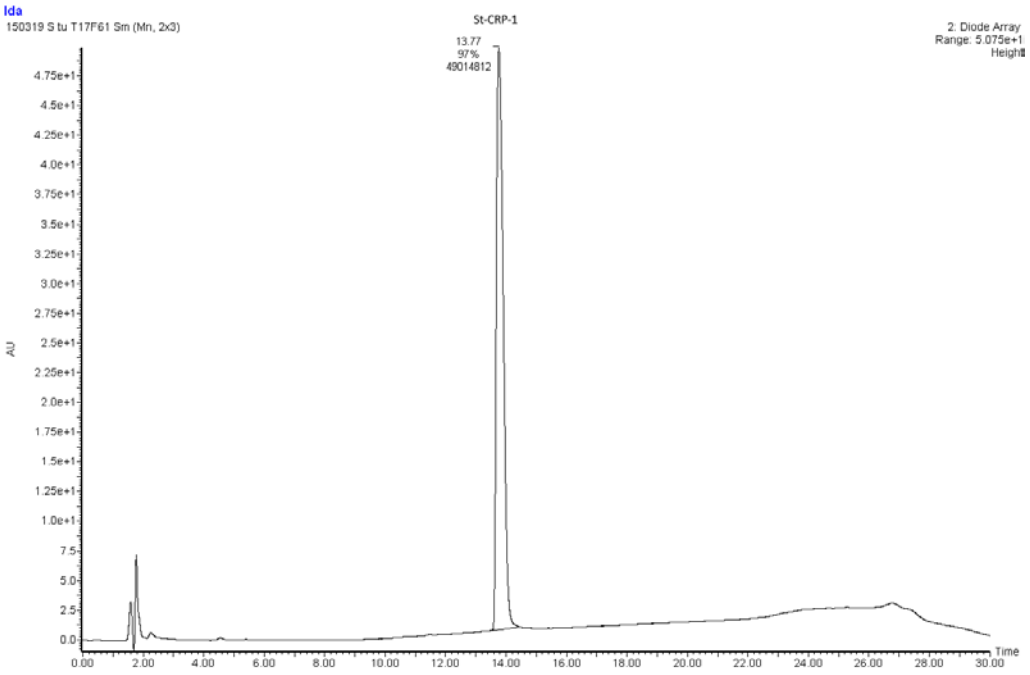

Figure S.1. UPLC-PDA chromatogram (detection wavelength, 280 nm) to determine the purity (97%) of St-CRP-1 isolated from *S. turgens*.

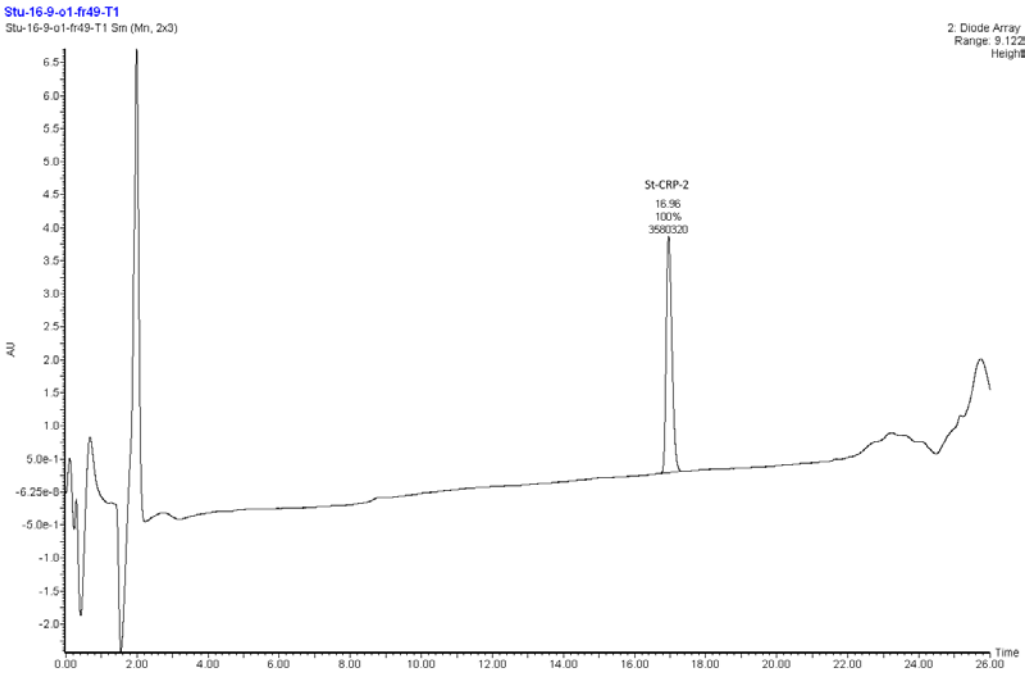

Figure S.2. UPLC-PDA chromatogram (detection wavelength, 280 nm) to determine the purity (100%) of St-CRP-2 isolated from *S. turgens*.

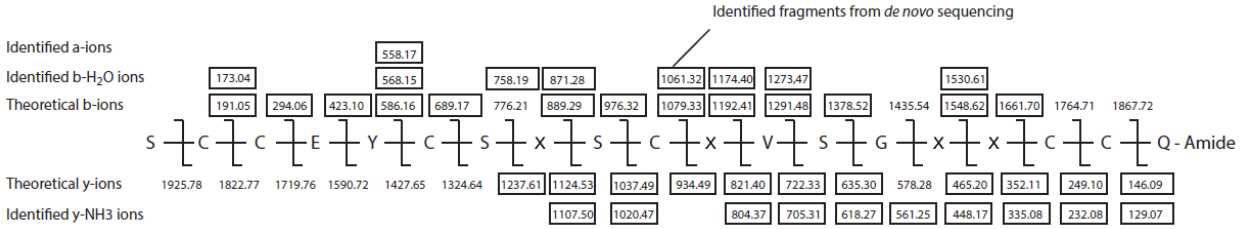

Figure S3. *De novo* sequencing of St-CRP-2 isolated from *S. turgens*, showing the identified a-, b-, b-H_2O, y- and y-NH_3 ions in frames. X = I/L. The sequencing was done on a Xevo G2-XS QToF MS (Waters).

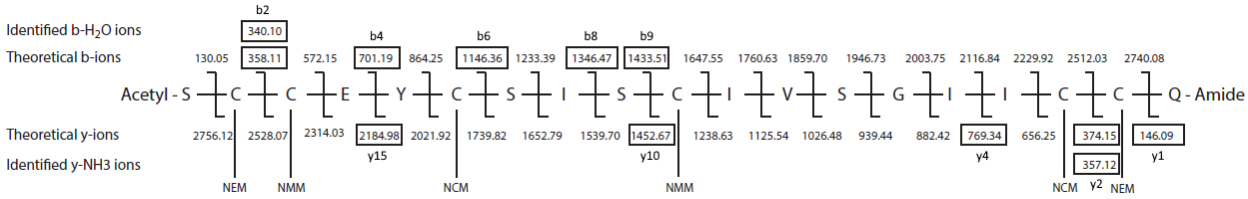

Figure S4. The alkylation pattern 2xNEM + 2xNMM + 2xNCM of the acetylated $[M+2H]^{2+}$ of St-CRP-2, isolated from *S. turgens*. The framed masses are b-, b-H_2O, y- and y-NH_3 ions identified in the MS/MS spectra. The X in the sequence is either I or L. The sequencing was done on a Xevo G2-XS QToF MS (Waters).

Table S1. Antimicrobial activity given as minimal inhibitory concentrations (MIC) of solid phase extract (SPE) fractions and the organic extract of *S. turgens*. The measurements were end point values of OD_{595} after 24 h at 35˚C. Bacterial test strains: *C. g. - Corynebacterium glutamicum, B. s. - Bacillus subtilis, S. a. - Staphylococcus aureus, E. c. - Escherichia coli, P. a. - Pseudomonas aeruginosa*.

	Antimicrobial activity (MIC; mg/mL)				
Extract	***C. g.***	***B. s.***	***S. a.***	***E. c.***	***P. a.***
10% SPE	1.25	5.00	5.00	10.00	5.00
20% SPE	2.50	2.50	5.00	5.00	5.00
30% SPE	0.16	0.16	2.50	5.00	5.00
40% SPE	0.04	0.08	2.50	5.00	2.50
80% SPE	0.31	0.31	2.50	5.00	2.50
Organic	2.50	2.50	10.00	>10.00	>10.00

Table S2. Proton (^{1}H) NMR and chemical shift assignments for St-CRP-1, isolated from *S. turgens*.

Residue	N^{1}H (ppm) 600 MHz, H_2O	α^{1}H (ppm) 600 MHz, H_2O	β^{1}H (ppm) 600 MHz, H_2O	γ^{1}H (ppm) 600 MHz, H_2O	other ^{1}H (ppm) 600 MHz, H_2O
CYS*1*	8.80	4.349	3.038, 2.875	-	-
CYS*2*	9.003	4.835	3.323	-	-
ASP*3*	9.028	4.262	2.698	-	-
GLN*4*	7.866	4.347	1.884, 1.944	2.229	6.785, 7.416
CYS*5*	8.793	4.676	2.895, 3.018	-	-
TYR*6*	7.581	4.596	2.812, 3.027	-	εCH: 6.772 δCH:6.926
GLY*7*	8.686	3.703, 3.849	-	-	-
PHE*8*	8.766	4.108	2.928, 3.182	-	εCH: 7.196 δCH: 7.233 ζCH: 7.147
CYS*9*	8.244	3.985	3.075, 3.371	-	-
ARG*10*	6.803	4.031	1.348, 1.632	1.439, 1.463	δCH_2: 3.060 εNH: 7.046
LEU*11*	7.712	3.963	1.585, 1.598	1.487	δCH_3: 0.780, 0.810
VAL*12*	7.234	4.226	2.188	0.470, 0.569	-
ASP*13*	7.743	4.438	2.639, 4.438	-	-
ASN*14*	8.222	5.150	2.293, 2.777	NH_2: 6.760, 7.355	-
CYS*15*	8.656	4.814	3.228, 3.257	-	-
CYS*16*	8.716	4.426	2.585, 3.155	-	-
ASN*17*	8.750	4.639	2.673, 2.752	NH2: 6.792, 7.504	-
SER*18*	8.199	4.295	3.758, 3.826	-	-

*Bruker Avance III HD spectrometer operating at 600 MHz for protons, equipped with an inverse detected TCI probe cryogenically enhanced for 1H, 13C and 2H.

Table S3. Carbon (^{13}C) NMR and chemical shift assignments for St-CRP-1, isolated from *S. turgens*.

Residue	^{13}C (ppm) 150 MHz, H_2O	$\alpha^{13}C$ (ppm) 150 MHz, H_2O	$\beta^{13}C$ (ppm) 150 MHz, H_2O	$\gamma^{13}C$ (ppm) 150 MHz, H_2O	Other (^{13}C (ppm) 150 MHz, H_2O)
CYS*1*	-	51.05	38.73	-	-
CYS*2*	-	51.38	42.86	-	-
ASP*3*	-	53.25	36.64	-	-
GLN*4*	-	51.97	25.81	30.69	177.75
CYS*5*	-	51.25	32.72	-	-
TYR*6*	-	53.52	37.87	127.02	δC: 130. 58 εC: 115.47 ζC: 154.94
GLY*7*	-	43.56	-	-	-
PHE*8*	-	58.57	36.21	135.21	δC: 128.86 εC: 127.55 ζC: 129.01
CYS*9*	-	56.47	41.35	-	-
ARG*10*	-	55.58	27.39	24.30	δC: 40.625 ζC: 156.651
LEU*11*	-	54.93	39.24	23.92	δC: 21.079, 21.601
VAL*12*	-	57.88	27.79	15.74, 18.32	-
ASP*13*	-	51.06	36.53	-	-
ASN*14*	-	48.63	37.87	-	-
CYS*15*	-	53.28	35.99	-	-
CYS*16*	-	52.66	36.50	-	-
ASN*17*	-	50.47	36.09	-	-
SER*18*	174.32	55.59	61.02	-	-

* Bruker Avance III HD spectrometer operating at 600 MHz for protons, equipped with an inverse detected TCI probe cryogenically enhanced for 1H, 13C and 2H

Table S4. RMSD of top St-CRP-1 structures generated through final simulated annellation constraints

Structure Name	All atom RMSD	Backbone RMSD	Carbon RMSD	Heavy atom RMSD
SA_252	0	0	0	0
SA_463	1.215	0.323	0.217	0.675
SA_6	1.624	0.355	0.258	0.628
SA_37	1.725	0.63	0.793	0.936
SA_372	1.749	0.526	0.513	0.852
SA_487	1.776	0.527	0.546	0.816
SA_48	1.793	0.658	0.75	0.963
SA_401	1.802	0.355	0.249	0.628
SA_382	1.872	0.531	0.517	0.869
SA_202	1.874	0.602	0.73	1.003
SA_495	1.885	0.512	0.502	0.867
SA_78	1.899	0.737	0.691	1.078
SA_238	1.927	0.541	0.519	0.905
SA_20	1.967	0.924	0.917	1.182
SA_113	1.974	1.004	1.111	1.412
SA_199	1.985	0.706	0.838	0.989
SA_100	2.074	0.533	0.48	0.925
SA_11	2.101	0.781	0.704	1.028
SA_462	2.178	0.532	0.506	0.906
SA_215	2.214	0.531	0.551	0.815
SA_80	2.215	0.538	0.552	0.802
SA_221	2.239	0.612	0.668	1.025
SA_76	2.259	0.766	0.854	0.948
SA_427	2.309	0.665	0.665	0.87
SA_97	2.374	0.635	0.686	0.932
SA_226	2.433	0.732	0.815	1.03
SA_412	2.509	0.87	0.968	1.059
SA_367	3.521	2.788	3.216	2.919
SA_488	3.726	2.88	3.347	3.047
SA_338	3.989	3.211	3.657	3.364
SA_436	4.13	3.192	3.645	3.307